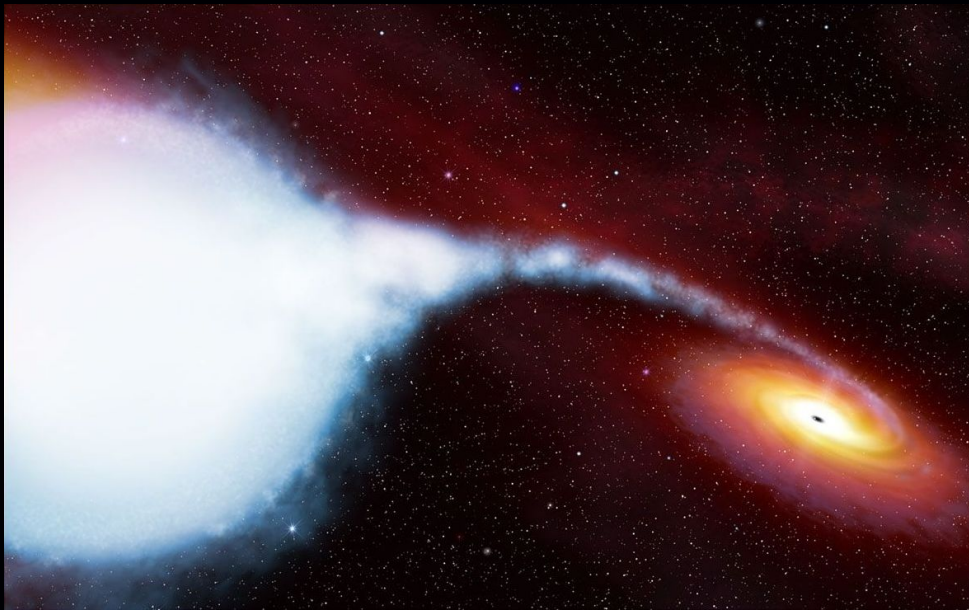


High-resolution
X-ray Spectroscopy
of the Black Hole Cygnus X-1
with
the *Chandra* X-ray Observatory



DIPLOMA THESIS
of
Manfred Hanke

from Wasserburg (Inn), Germany

performed at the

Dr. Karl Remeis-Sternwarte Bamberg

(Astronomical Institute of the University of Erlangen-Nuremberg)

Sternwartstr. 7, 96049 Bamberg

supervisor:

Prof. Dr. Jörn Wilms

July 2007

The image on the title page shows an artist's impression of the X-ray binary Cygnus X-1 with the stellar wind of the supergiant star heating while spiraling towards the black hole.

© 2004 European Space Agency,
from http://www.spacetelescope.org/goodies/posters/html/cygnus_x1.html

*“To anybody who may know as little as I do...
... and who is as curious as well.”*

Abstract

Cygnus X-1 was the first X-ray binary with a compact object that was identified as a black hole. Accretion of the focussed stellar wind of its supergiant companion star, HDE 226868, in the black hole’s gravitational potential releases a great amount of energy in form of X-rays. Due to its persistent brightness, Cygnus X-1 is the best studied stellar black hole X-ray binary and is therefore often called the ‘canonical example’ for such an object. Nevertheless, the accretion geometry and the detailed mechanisms leading to the observed spectrum are not yet understood and are still the subject of numerous investigations. This work contributes the analysis of one high-resolution observation of Cygnus X-1 where the source itself literally “X-rays” the accretion stream and unveils its chemical composition, especially, since absorption dips from clumps in the focussed wind are seen during part of the observation.

The first chapter is intended to give a comprehensible introduction for everyone, even if unexperienced in the field of X-ray astronomy and black holes – just as I started 9 months ago. Of course, special emphasis was placed on Cygnus X-1, which is the central object of investigation in this work. Furthermore, the *Chandra* X-ray observatory is described, since one of its instruments obtained the spectrum for this analysis.

The second chapter compiles the theory of spectral line analysis needed for this work. It is, in large parts, known from classical astronomy and stellar atmospheres, but can, in the context of this high-resolution X-ray spectroscopy of Cygnus X-1, also be transferred to the high energy regime. The chapter also explains how X-ray spectra are analyzed in general, since this requires some techniques which are not that often encountered in optical astronomy.

The third chapter summarizes the adoption of the concepts described in the previous chapter, i.e., their implementation as computer programs. There is the reduction tool for *Chandra* data, CIAO, and the very general and flexible analysis software ISIS. Their basic components are described and user-developed ISIS functions, allowing for modelling pile-up in the detector and analyzing absorption line series of specific ions, are presented.

The actual data analysis is reported in the fourth chapter of this diploma thesis. First the relevant *Chandra* observation is discussed in general. Then the detailed high-resolution spectroscopy of the non-dip spectrum is presented, which is in the following repeated for the dip(s). Plenty of absorption lines of the focussed stellar wind are detected, fitted and identified. Changes between dip and non-dip phases are discussed.

Finally, the outlook in the last chapter gives an overview of other *Chandra* observations of Cygnus X-1. This includes plans for my own future work to extend this investigation of the accretion flow in the system.

The appendix includes tables of atomic data, especially transition wavelengths, file format listings, complete lists of the line parameters that were obtained by the analysis and plots of those spectra themselves.

Contents

1	Introduction	4
1.1	X-ray astronomy	4
1.1.1	X-rays	4
1.1.2	History	4
1.1.3	The recent satellite missions	5
1.2	Black holes and X-ray binaries	6
1.2.1	Stellar evolution of massive stars	6
1.2.2	General relativity and black holes	8
1.2.3	Accretion and X-ray binaries	10
1.3	Cygnus X-1	13
1.3.1	The binary system	13
1.3.2	Accretion	17
1.3.3	The X-ray spectrum	18
1.3.4	Transient X-ray dips	19
1.4	The <i>Chandra</i> X-ray observatory	20
1.4.1	The spacecraft	21
1.4.2	The mirrors	22
1.4.3	The gratings	23
1.4.4	The ACIS detector	24
1.4.5	The PCAD-system	26
2	Spectral analysis	28
2.1	Absorption of light by atoms	28
2.1.1	Photoionization: bound – free transitions	29
2.1.2	Atomic physics	30
2.1.3	Line strength of bound-bound transitions	32
2.1.4	The cross section and its profile	34
2.1.5	The curve of growth	35
2.2	Analysis of X-ray spectra	39
2.2.1	Formalism	39
2.2.2	Spectral fitting and χ^2 statistics	40
3	Data reduction and analysis software	44
3.1	Reduction of <i>Chandra</i> /HETGS data with CIAO	44
3.1.1	Data files	44
3.1.2	Data reprocessing	44
3.1.3	Extraction of light curves	46
3.1.4	Extraction of spectra	46
3.2	Spectral analysis with ISIS	46
3.2.1	General overview	46
3.2.2	A model for pile-up in grating observations	49
3.2.3	Description of absorption lines	51
4	High-resolution analysis of the <i>Chandra</i> observation # 3814	53
4.1	The observation	53
4.1.1	Observational parameters and data reduction	53
4.1.2	The light curve	55
4.2	The ‘non-dip’ spectrum	57
4.2.1	Consistency checks	57
4.2.2	Description of the spectral continuum	58
4.2.3	Description and identification of absorption and emission lines	61
	Overview	63

	List of lines – sorted by ion	78
4.2.4	Spectral analysis with absorption line series	79
4.3	The ‘dip’ spectrum	88
4.3.1	Consistency checks	88
4.3.2	Description of the continuum	88
4.3.3	Lines in the spectrum	95
	Overview	95
	List of lines – sorted by ion	105
4.4	Comparison of ‘dip’ and ‘non-dip’ spectrum	108
4.5	Outlook	108
5	Other observations of Cygnus X-1	109
5.1	Comparison of all <i>Chandra</i> observations	109
5.1.1	Overview	109
5.1.2	Summary of published results	109
5.2	Miller’s <i>Chandra</i> observation # 2415	111
5.3	Future work	112
5.3.1	The joint <i>XMM-Chandra</i> observation (# 8525)	112
5.3.2	Outlook	112
5.3.3	Final conclusions	113
	References	114
A	Appendix	117
I	Atomic data	117
I.1	Bound-free transition edge-energies and ISM abundances	117
I.2	Bound-bound line-transition wavelengths	118
II	Data files from the CXC	122
II.1	Primary and secondary data files	122
II.2	High level data files	124
III	The <i>Chandra</i> observation # 3814	126
III.1	Flux-ratios of the sub-spectra	126
III.2	Spectral analysis of the ‘non-dip’ spectrum	126
III.3	Dependencies of the continuum-parameters	126
	Plots of the ‘non-dip’ spectrum	137
III.3	Dependencies of the continuum-parameters	145
III.4	Spectral analysis of the ‘dip’ spectrum	155
	Plots of the ‘dip’ spectrum	159
	Acknowledgments	167
	List of Figures	169
	List of Tables	171
	Declaration	173

1 Introduction

1.1 X-ray astronomy

1.1.1 X-rays

X-rays are electromagnetic waves with much higher frequency ν than visible light. Although there is no sharp distinction from ultraviolet light on the low energy side and γ -rays on the high energy side, X-rays are often defined as photons with energies between ≈ 0.1 keV (1 keV = 1.6×10^{-16} J) and 512 keV, which is the electron's rest mass energy $m_e c^2$. According to

$$E = h\nu = \frac{hc}{\lambda} \approx \frac{12.4 \text{ keV}}{\lambda/\text{\AA}} \quad (hc = 12.39842 \text{ keV} \cdot \text{\AA}) \quad (1.1)$$

the corresponding wavelengths are in the Ångström regime ($1 \text{ \AA} = 10^{-10} \text{ m} = 0.1 \text{ nm}$) and even below.

X-rays have been discovered¹ and extensively studied by the German scientist W. C. Röntgen² in 1895. Investigating cathode rays, Röntgen noticed fluorescent visible light that was caused on a barium platinocyanide screen from X-rays penetrating through the tube of glass and the cardboard shielding. The X-rays have been produced as bremsstrahlung from the electron beam being stopped at the anode. (Accelerated charges produce electromagnetic radiation.) The maximum photon energy is thus given by the kinetic energy of the electrons and thus simply by the accelerating voltage in cathode ray tube.

But X-rays can also be produced, e.g., as blackbody radiation of extremely hot objects with 10^7 K or via inverse Compton-scattering of low energy photons off hot electrons (see section 1.2.3).

Although X-rays can easily penetrate low density bodies (a fact which is used by physicians evaluating fractures of bones), the Earth's atmosphere shields most of the (especially low energy) cosmic X-rays. This is due to photoionization (cf. Section 2.1.1) of air molecules. The atmosphere has an effective height of ≈ 8.5 km, corresponding to an atom column density of $N \sim 10^{23} \text{ cm}^{-2}$! Figure 1.1 shows the atmospheric penetration depth of electromagnetic waves. The line indicates the height in which half of the radiation from space has been absorbed. One recognizes the small window of visible light, which is – besides radio waves – basically the only radiation that can pass through the atmosphere. Higher energies suffer gravely from photoabsorption; ground-based X-ray astronomy is thus almost impossible. To do so, one has instead to go to space!

In fact, if one continues to investigate electromagnetic radiation at even higher energies (“TeV γ -astronomy”), ground based observations become possible again. Imaging atmospheric Cherenkov telescopes like H.E.S.S. use the whole atmosphere as an air shower detector.

1.1.2 History

Experiments well above the atmosphere had become possible for the first time in 1946 with V-2 rockets from World War II (Golian et al., 1946). The sun was discovered to be also a bright source of X-rays. But this radiation was too weak in order to be detected in the distance of the other stars. Therefore, scientists did not believe in extra-solar X-ray astronomy, which has finally just started in 1962 with a rocket-experiment, where 3 Geiger counters with 20 cm^2 collecting area were brought for 350 s above 80 km altitude. This was enough to detect a very strong cosmic X-ray source which was later called Sco X-1 (Giacconi et al., 1962).³

¹In fact, Ivan Pulyui had first discovered them almost 15 years before (Wiener Berichte, 1880, 81, pp. 864-923; 1881, 83, pp. 402-420 and pp. 693-708; 1882, 85, pp. 871-881).

²Röntgen (1845–1923) obtained the first Nobel prize in 1901 “in recognition of the extraordinary services he has rendered by the discovery of the remarkable rays subsequently named after him” (http://nobelprize.org/nobel_prizes/physics/laureates/1901) – X-rays are called “Röntgen-Strahlen” in German.

³40 years later, in 2002, the Nobel prize was awarded to Giacconi “for pioneering contributions to astrophysics, which have led to the discovery of cosmic X-ray sources”. (http://nobelprize.org/nobel_prizes/physics/laureates/2002)

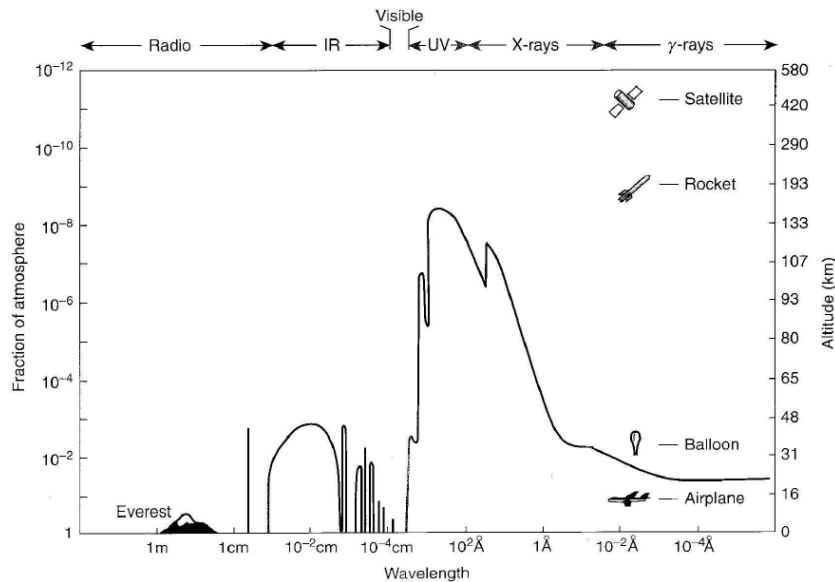


Figure 1.1: The penetration depth of electromagnetic waves in the Earth's atmosphere. (from Charles & Seward, 1995, Fig. 1.12)

After more experiments of this kind and the discovery of ~ 50 extra-solar X-ray sources (Friedman et al., 1967; Fisher et al., 1968), most of them in the galactic bulge, X-ray satellites were developed. This greatly improved the situation, as a satellite in a constant orbit above the atmosphere allows much longer observations than the rockets – days per source instead of seconds! The first of those, *Uhuru*, was launched in December 1970. It contained proportional counters with honeycomb collimators to determine the location of the X-ray sources. While spinning, it scanned the whole sky. The results of this more than 4 years lasting survey, 339 sources, are listed in the 4U catalogue (Forman et al., 1978). Many more satellites dedicated to X-ray astronomy followed in the 1970s, including *Copernicus* in 1972, the first pointing X-ray telescope, and the *Einstein* observatory in 1978, the first satellite mission allowing to take true images. *Einstein* also provided a larger sensitivity by more than 2 orders of magnitude than any mission before. The next major improvement in X-ray astronomy was obtained with the European X-ray Observatory SATellite *EXOSAT*, which was launched in 1983 into an extremely eccentric orbit, such that continuous observations for up to 3 days became possible. Then, the German ROentgen SATellite *ROSAT*, launched in 1990, performed the first all sky survey with an imaging telescope of a sensitivity comparable to the *Einstein* observatory.

For a more detailed introduction, see the book of Charles & Seward (1995) or the review article of Charles & Fabian (2001). A good overview of active and past missions is also available online from the High Energy Astrophysics Science Archive Research Center HEASARC.⁴

1.1.3 The recent satellite missions

NASA's *Rossi X-ray Timing Explorer RXTE* has been launched on 1995, December 30 on a low-Earth orbit (≈ 600 km altitude). It carries 3 different instruments, which allow to obtain very broad band spectra from 2 to 200 keV: PCA (described in detail by Jahoda et al., 1996) is a Proportional Counter Array of five xenon gas detectors with the large collecting area of 6250 cm^2 . The PCA is sensitive at energies from 2 to 60 keV. The High Energy X-ray Timing Experiment HEXTE (see Gruber et al., 1996) consists of two clusters of 4 NaI(Tl) / CsI scintillation counters, sensitive from 15 to 250 keV, with a collecting area of $2 \times 800 \text{ cm}^2$ in total. The All Sky Monitor ASM (cf. Doty, 1994) finally contains shadow cameras with xenon proportional counters, which detect X-rays in 3 energy bands, namely 1.5... 3 keV, 3... 5 keV and 5... 12 keV. Its collecting area is 90 cm^2 . As ASM rotates, it covers 80% of the whole sky within every revolution of *RXTE* in 90 minutes. *RXTE*'s instruments have only moderate spectral resolution, but allow timing observations with millisecond accuracy.

⁴ <http://heasarc.gsfc.nasa.gov/docs/observatories.html>

The *Chandra* X-ray observatory (see Sect. 1.4 and CXC, 2006) was launched on 1999, July 23. Its most important feature is the best-quality mirror system allowing imaging observations with the highest angular resolution ($< 1''$) and, in combination with transmission gratings, grating observations of very high spectral resolution (up to 1 000 for both the High and the Low Energy Transmission Gratings) in the energy range from 0.1 to 10 keV. The elliptical high-earth orbit makes very long observations possible.

The European X-ray Multi Mirror satellite *XMM-Newton* (described by Ehle et al., 2006) has been launched on 1999, December 10, – less than half a year after *Chandra*. *XMM-Newton* has the largest collecting area of 4 300 cm² at 1.5 keV. Therefore, it has the best capability to do spectroscopy with even weaker sources, where one wants to detect as many photons as possible to obtain a good signal-to-noise ratio. *XMM* carries grazing-incidence reflection gratings, which produce additional X-ray spectra with a resolution of 200...800 from all (imaging) observations. It is the first X-ray observatory that includes a coaligned optical/UV telescope that allows the detection of light with wavelengths from 180 to 650 nm.

The INTErnational Gamma-Ray Astrophysics Laboratory *INTEGRAL*, also operated by ESA, has been up in space since 2002, October 17. Its spectrometer SPI (described by Vedrenne et al., 2003) investigates hard X-rays and gamma-rays from 20 keV to 8 MeV, while IBIS (Ubertini et al., 2003) is a coded mask imager the energy range of 15 keV...10 MeV. There is also an X-ray monitor (see Lund et al., 2003), sensitive to energies from 3 to 35 keV, and an Optical Monitoring Camera (Mas-Hesse et al., 2003) for visual light between 500 and 850 nm. *INTEGRAL*, as well as *XMM-Newton*, has a similar orbit as *Chandra*.

NASA's *Swift*, launched on 2004, November 20, was delegated to unveil the mystery of gamma-ray bursts. Its Burst Alert Telescope (BAT) with an effective area of 5 240 cm², sensitive to the energy range of 15...150 keV has the large field of view of 1.4 sr, but can nevertheless determine positions to 5'' accuracy. A detected burst triggers the autonomous orientation of the whole satellite, as the X-Ray Telescope (XRT), which is sensitive to 0.2...10 keV, and the UV/Optical Telescope (UVOT) for 170...650 nm light only have a usual field of view.

The most recent high energy observatory is the Japanese *Suzaku*, launched only on 2005, July 10, again into a low-Earth orbit in 565 km altitude. It is the first satellite to carry an X-ray micro-calorimeter, which would have provided the best energy resolution (of almost 1 000) for a non-dispersive instrument, but due to a design flaw, it has lost all its liquid helium during the first three weeks of the mission, such that it cannot be used for any measurements (Kelley, 2006). But there is still the Hard X-ray Detector (described by Takahashi et al., 2007), which is sensitive in the energy range of 10...600 keV.

1.2 Black holes and X-ray binaries

1.2.1 Stellar evolution of massive stars

The balance of a star's own gravity and its radiation pressure from the central nuclear fusion manifests itself by the stability of the star: During the largest part of its live, it stays in a steady state and radiates continuously. For these hydrogen-burning (main sequence) stars, the stellar parameters (like mass, radius, surface temperature and gravity, luminosity) are uniquely related. This leads to the main sequence in the Hertzsprung-Russell diagram (Fig. 1.2), which is a plot of (absolute) luminosity versus temperature or color. These energy-gaining processes can only be maintained as long as stocks last. The lifetime of a star depends on its mass; as the rate of nuclear fusion grows stronger with mass than the amount of "fuel" itself, more massive stars evolve faster. After this (long) phase of hydrogen burning, the star has to shrink. If its mass is then below Chandrasekhar's limit of 1.4 M_{\odot} (Chandrasekhar, 1931a,b; Shapiro & Teukolsky, 1983, Chapters 3.3 and 3.4.) a white dwarf can form, in which the degeneration pressure of the Fermi-gas of electrons withstands gravity.

A star with initially more than about 8 M_{\odot} does not lose enough mass (e.g., by stellar winds) during its evolution; the resulting collapsar has therefore a mass above this limit. First, the electrons have to combine with the protons and a neutron star is formed. The Fermi-

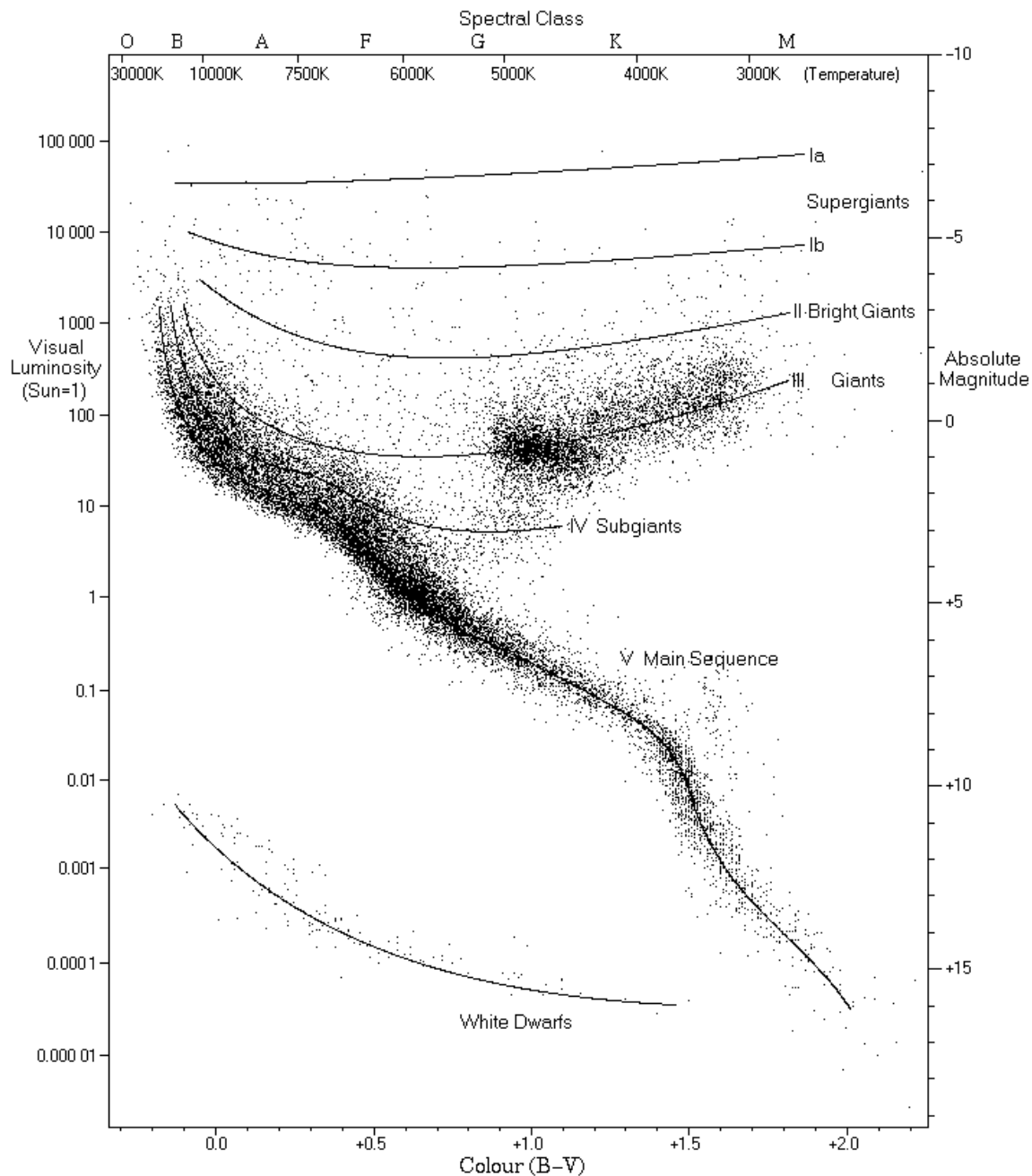


Figure 1.2: The Hertzsprung-Russell diagram.
 (from <http://www.atlasoftheuniverse.com/hr.html>)

degenerate neutrons can balance the gravitational force unless the mass of the compact object is again too high. The Oppenheimer-Volkoff threshold mass for neutron stars (Oppenheimer & Volkoff, 1939) is not as accurately known as Chandrasekhar's, due to uncertainties in our understanding of that extremely dense nuclear matter and its equation of state (The title of all the following publications of the last five years literally matches "maximum mass of neutron stars": Srinivasan, 2002; Burgio et al., 2002; Haensel, 2003; Lyford et al., 2003; Morrison et al., 2004; Brown et al., 2005; Schulze et al., 2006, hence there is still a lot of progress!), but it is definitely below $3 M_{\odot}$ (Shapiro & Teukolsky, 1983, Chapter 9.3). Massive stars lose much matter by stellar winds, but for very massive ones,⁵ there is no escape from the final collapse: Einstein's theory of general relativity (GRT) predicts that a black hole has to form inevitably if the gravity of such a large mass dominates all other forces.

⁵ It is hard to quantify, what "very massive" means; Postnov & Yungelson (2006) quote $25 \dots 60 M_{\odot}$ for solar metallicity. (The metallicity strongly influences the stellar evolution.) Stars (initially) even more massive will again form neutron stars, as their wind mass loss rate is very high.

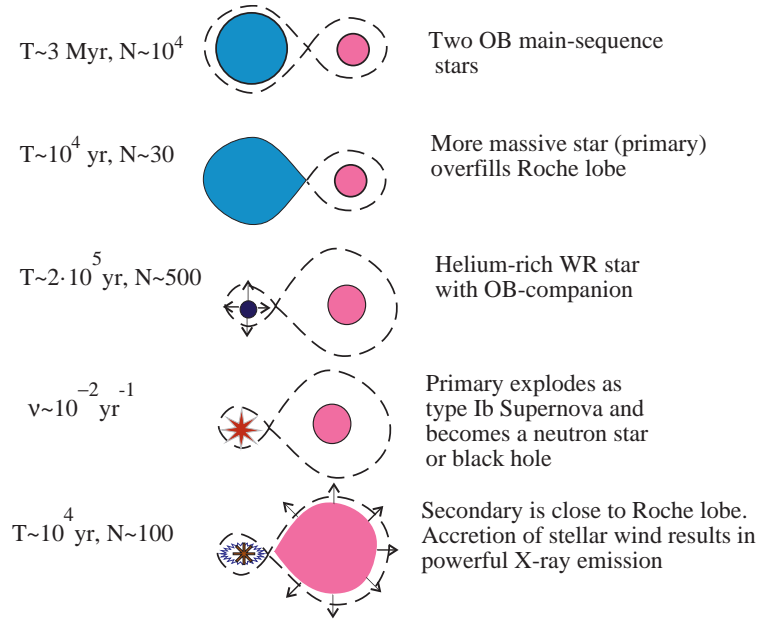


Figure 1.3: The evolution of a compact binary. (after Postnov & Yungelson, 2006, Fig. 4)

Evolution of massive binary systems

What has been described so far holds for single stars or stars in wide binaries, i.e., stars that do not influence each other significantly in their evolution. Close binaries, however, show mass transfers, especially by Roche lobe overflow. The Roche lobes are the surfaces separating the volume being bound gravitationally to one of the stars, see Sect. 1.2.3, Fig. 1.5. A possible scenario is shown in Fig. 1.3:

Due to this mass transfer, the initially more massive star, developing faster, results in the compact object, while the other becomes the companion star with finally the higher mass. A very good and detailed description of the evolution of compact binaries is given in a review article of Postnov & Yungelson (2006).

Ergma & van den Heuvel (1998) suggest that the evolution of a massive binary system in the range $20 \dots 50 M_{\odot}$, depends on further stellar parameters (magnetic fields or rotation) in the particular case and can both lead to a neutron star binary or a black hole binary. (Higher masses usually lead again to neutron stars, as the massive star loses very much material by stellar wind, cf. footnote 5.)

1.2.2 General relativity and black holes

A long public outreach article (in German) on black holes, which explains many things very comprehensibly, is available online from Müller (2007).

The theory of general relativity (Einstein, 1916) describes gravity as curvature of spacetime. This is finally expressed by the metric tensor $g_{\mu\nu}$, which allows to write the invariant line element ds^2 with the coordinate elements dx^{μ} as $ds^2 = \sum_{\mu,\nu} g_{\mu\nu} dx^{\mu} dx^{\nu}$. Special relativity corresponds thus to the Minkowski metric $ds_{\text{SRT}}^2 = d\vec{r}^2 - c^2 dt^2$ with $g_{\mu\nu} = \text{diag}(1, 1, 1, -c^2)$. The Einstein field equations

$$G_{\mu\nu} \left(:= R_{\mu\nu} - \frac{1}{2} R g_{\mu\nu} \right) = \frac{8\pi G}{c^4} T_{\mu\nu} \quad (1.2)$$

relate the Einstein tensor $G_{\mu\nu}$, which contains the metric and its derivatives⁶ with the stress-energy-momentum tensor $T_{\mu\nu}$, which contains the density and flux of energy and momentum, give thus (eventually coupled and eventually partial) differential equations for the $g_{\mu\nu}$.

⁶ $R_{\mu\nu}$ is the Ricci curvature tensor and $R = \sum_{\mu,\nu} R^{\mu\nu} g_{\mu\nu}$ is the Ricci scalar.

$R_{\mu\nu} = \sum_{\alpha} \left(\frac{\partial \Gamma_{\mu\nu}^{\alpha}}{\partial x^{\alpha}} - \frac{\partial \Gamma_{\mu\alpha}^{\nu}}{\partial x^{\nu}} \right) + \sum_{\alpha,\beta} \left(\Gamma_{\mu\nu}^{\alpha} \Gamma_{\alpha\beta}^{\beta} - \Gamma_{\mu\alpha}^{\beta} \Gamma_{\nu\beta}^{\alpha} \right)$ depends via the Christoffel symbols

$\Gamma_{\alpha\beta}^{\delta} = \frac{1}{2} \sum_{\gamma} g^{\gamma\delta} \left(\frac{\partial g_{\gamma\beta}}{\partial x^{\alpha}} + \frac{\partial g_{\alpha\gamma}}{\partial x^{\beta}} - \frac{\partial g_{\alpha\beta}}{\partial x^{\gamma}} \right)$ on the metric tensor $g_{\mu\nu}$ and its derivatives.

Black holes

A black hole is a singularity in spacetime that is fully characterized by its mass, spin, and electrical charge (Carter, 1971). This singularity is “hidden” in the sense that no matter, light, or information can escape from the region inside the (therefore) so called event horizon around the singularity. Although this region is somehow decoupled from the rest of the universe, the presence of the notable mass inside is still noticeable outside by its gravitational field.

Schwarzschild black holes. In the case of a non-rotating black hole with mass M , the event horizon is a sphere around the point-like singularity with Schwarzschild radius

$$R_S := \frac{2GM}{c^2} \approx 3 \text{ km} \cdot \frac{M}{M_\odot} . \quad (1.3)$$

Interestingly enough, this distance R_S can also be derived from pure classical mechanics, as below the event horizon, the Newtonian escape velocity extends the speed of light:

$$v_{\text{esc}} = \sqrt{\frac{2GM}{r}} \geq c \quad \text{for } r \leq R_S \quad (1.4)$$

In GRT, the spacetime around a black hole is described by the metric of Schwarzschild (1916):

$$ds^2 = \frac{dr^2}{1 - \frac{R_S}{r}} + r^2 (d\theta^2 + \sin^2 \theta d\varphi^2) - c^2 \left(1 - \frac{R_S}{r}\right) dt^2 \quad (\rightarrow ds_{\text{SRT}}^2 \text{ for } M \rightarrow 0) \quad (1.5)$$

Eq. (1.5) is a full solution of Einstein’s field equations – in fact the only static one with spherical symmetry and asymptotically flat spacetime in vacuum (Israel, 1967).⁷

Orbits. $r = 0$ is the only true singularity of the metric. The singularity at $r = R_S$ is only due to the choice of the frame of reference; there exist coordinate systems (Kruskal, 1960) to describe a particle crossing the event horizon while falling into the black hole (which is not possible in the other direction!) without any singularities.

The stable orbits around a (Schwarzschild) black hole can easily be derived from the effective potential (cf. Schutz 1985, Eq. 11.10; Shapiro & Teukolsky 1983, Eq. 12.4.25)

$$V^2(r) \sim \left(1 - \frac{R_S}{r}\right) \cdot \left(1 + \frac{L^2}{M^2 c^2 r^2}\right) \quad (1.6)$$

which follows from the conservation of angular momentum L due to the spherical symmetry. A stable circular orbit can only exist for $L \geq L_{\text{min}}$, as the conditions for a potential minimum

$$\frac{dV}{dr} \sim \frac{M^2 c^2 R_S \cdot r^2 - 2L^2 \cdot r + 3R_S L^2}{M^2 c^2 r^4} = 0 \quad \text{and} \quad \frac{d^2V}{dr^2} > 0 \quad (1.7)$$

require

$$r = \frac{L^2 + \sqrt{L^4 - 3M^2 c^2 R_S^2 L^2}}{M^2 c^2 R_S} \geq \frac{L_{\text{min}}^2}{M^2 c^2 R_S} \quad \text{with} \quad L \geq L_{\text{min}} = \sqrt{3} M c R_S . \quad (1.8)$$

A Schwarzschild black hole’s innermost stable circular orbit has thus the radius $r_{\text{ISCO}} = 3R_S$.

⁷ $T_{\mu\nu} = 0$ leads by the Einstein field equations to $R_{\mu\nu} = \frac{1}{2}R g_{\mu\nu}$, which can only be satisfied by $R_{\mu\nu} = 0$. Inserting $ds^2 = A(r) dr^2 + r^2 (d\theta^2 + \sin^2 \theta d\varphi^2) + B(r) dt^2$, which is the most general static ansatz with spherical symmetry, leads finally to $\frac{d}{dr}(A(r) \cdot B(r)) = 0$ and $r \frac{dA(r)}{dr} = A(r) \cdot (1 - A(r))$.

Rotating black holes. Kerr (1963) published a solution for the ‘Gravitational field of a spinning mass’, which describes in fact (uncharged) rotating black holes. (Newman et al. (1965) have also found another ‘Metric of a rotating, charged mass’, but its astrophysical significance is marginal.) Rotating black holes have some different properties compared to those of Schwarzschild type, which may finally even allow a discrimination by observational evidences: As space time is not static in the Kerr scenario, but rotates itself, everything close to the event horizon is forced to co-rotate with the black hole. This so called frame dragging effect depends on the black hole’s spin J , which can be parameterized by the dimensionless Kerr-parameter $a = Jc/(GM^2)$. Kerr’s solution requires $-1 < a < 1$, implies thus a maximum spin $J = GM^2/c$. The frame dragging effect causes the radius of the innermost stable circular orbit to decrease from $r_{\text{ISCO}}(0) = 3R_S$ for $a = 0$ (which is the static Schwarzschild solution) to $r_{\text{ISCO}}(a = 1) = R_S$ for a maximal spinning black hole. In the limiting case $a = 1$, the ISCO would be on the event horizon H , whose radius is given by Eq. (1.9). Particles can thus be accelerated very efficiently next to a fast rotating Kerr black hole. It can even be shown that energy can be transferred from the black hole within the ergosphere E (which is, in fact, an oblate ellipsoid), which is (for $a < 1$) still outside the event horizon (Penrose & Floyd, 1969, 1971; Müller, 2004):

$$r_H = R_S \cdot \left(1 + \sqrt{1 - a^2}\right) \leq r_E(\theta) = R_S \cdot \left(1 + \sqrt{1 - a^2 \cos^2 \theta}\right) \quad (1.9)$$

Types of black holes

One knows ‘galactic black holes’, which are stellar-mass black holes first discovered in our galaxy that formed through the collapse of massive stars as described above. But there are also ‘supermassive black holes’ with masses of $10^6 \dots 10^9 M_\odot$ in the center of most galaxies – just as Sgr A* in our Milky Way (Ghez et al., 2000; Eckart et al., 2002; Schödel et al., 2002).

1.2.3 Accretion and X-ray binaries

In the previous section, black holes have been introduced as passive (“black”) objects. Although it seems self-contradictory at first sight, they can, however, produce astronomically bright sources as well. Such accreting black holes will be described in this section.

A good overview on black hole X-ray binaries is given by Remillard & McClintock (2006).

Accretion

Accretion of matter in the gravitational potential of a massive compact object can produce more energy than nuclear fusion: The whole potential energy of an infinite distant mass m above a black hole’s Schwarzschild radius is

$$E_{\text{pot}}(\infty) - E_{\text{pot}}(R_S) = G \frac{mM}{R_S} = \frac{1}{2} mc^2, \quad (1.10)$$

of which a considerable fraction (from $\approx 0.1 mc^2$ for Schwarzschild-black holes up to $\approx 0.4 mc^2$ for fast rotating ($a \rightarrow 1$) Kerr-black holes) can be released: The velocity on a Kepler orbit is

$$v_{\text{Kepler}}(r) = \sqrt{\frac{GM}{r}}, \quad \text{such that} \quad \frac{1}{2} m v_{\text{Kepler}}(r)^2 = \frac{1}{2} (E_{\text{pot}}(\infty) - E_{\text{pot}}(r)). \quad (1.11)$$

(That the kinetic energy is half of the binding energy, is well known as the virial theorem.) Matter that is accreted to a distance $r_{\text{ISCO}}(0) = 6GM/c^2$ has therefore to dissipate the energy

$$E_{\text{pot}}(\infty) - E_{\text{pot}}(3R_S) - \frac{1}{2} m v_{\text{Kepler}}(3R_S)^2 = \frac{1}{2} \cdot \frac{1}{6} mc^2 \approx 0.083 mc^2. \quad (1.12)$$

As explained in the previous section, rotating black holes have a narrower innermost stable circular orbit and the co-rotation costs less kinetic energy – thus a very large fraction of $\frac{1}{2} mc^2$ can be released. Nuclear fission in the following usual way however gives ‘only’ $0.007 \cdot (4m_H)c^2$:



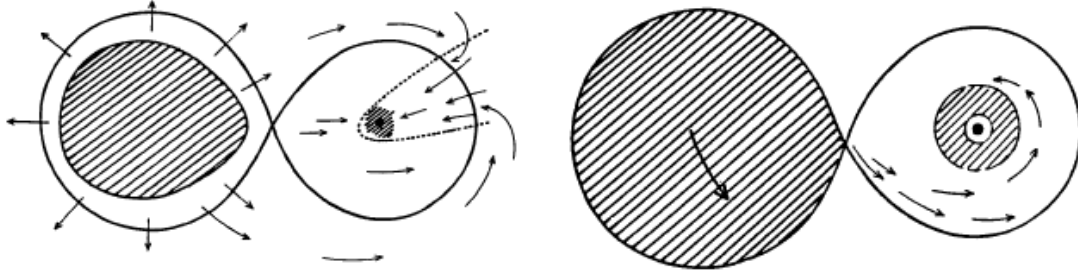


Figure 1.4: Mass transfer via focused stellar wind (left) and Roche lobe overflow (right).
(after Gleissner, 2004, Fig. 1.2)

X-ray binaries

This energy gain by accretion is realized in X-ray binaries (XRBs) with galactic black holes (or also neutron stars, which behave not very different, except in that they have a solid surface) and in active galactic nuclei (AGN) with supermassive black holes. It is believed that XRBs and AGN show essentially the same physics, and that all effects just scale with the mass of the powering black hole (see, for example, Wilms, 2006). Processes around galactic black holes evolve, for example, on much shorter time scales than those next to supermassive ones. This section is, however, solely dedicated to XRBs.

There are two scenarios of mass transfer in a binary system with a compact object:

- In a high mass X-ray binary (HMXB), a young, massive O- or B-star's strong stellar wind is focused towards the compact object and a small fraction is accreted. As the wind does not carry much angular momentum, no or just a small accretion disk is formed.
- In a low mass X-ray binary (LMXB), an old, late-type star has evolved to a giant and fills its Roche lobe, such that matter can pass via the Lagrangian point L_1 , see Fig. 1.4. Due to the conservation of angular momentum, the mass cannot fall directly onto the compact object, but forms an accretion disk.

The Roche lobes are those equipotential surfaces in a binary system (whose effective potential in the rotating coordinate system

$$\Phi(\vec{r}) = -\frac{GM_1}{|\vec{r} - \vec{r}_1|} - \frac{GM_2}{|\vec{r} - \vec{r}_2|} - \frac{1}{2}|\vec{r} \times \vec{\omega}|^2 \quad (1.14)$$

also includes the centrifugal force), that separate the region bound to the one star from that which is bound to the other one. They are connected at the inner Lagrangian point L_1 , which is the gravitational saddle point between the two members of the binary. In general, the Lagrangian points $L_1 - L_5$ are those points where the gravitational forces of both objects sum up to the necessary centripetal force for co-rotation.

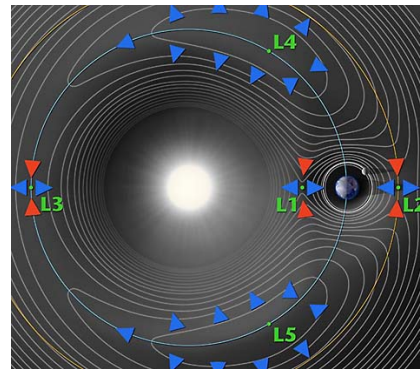


Figure 1.5: The 5 Lagrangian points.
(from http://map.gsfc.nasa.gov/m_mm/ob_techorbit1.html)

These accreting binaries emit X-rays due to their high luminosity $L = \eta \dot{m} c^2 \approx 10^{30}$ W (for realistic values $\eta \approx 0.1$, $\dot{m} \approx 10^{-9} M_\odot \text{ a}^{-1}$): The assumption of blackbody emission $L = 4\pi R^2 \sigma_{\text{SB}} T^4$ leads for stellar mass black holes (with $R \approx 100$ km) to temperatures $T \approx 5 \times 10^6$ K and therefore to photon energies $E = k_B T = 0.086 \text{ keV} \cdot T / (10^6 \text{ K}) \approx 0.5 \text{ keV}$ in the X-ray regime.

The Eddington luminosity L_{Edd} is the maximal luminosity L of a bright source which accretes a plasma of mostly ionized hydrogen. To derive its value, the gravitational force on a

proton is assumed to dominate the radiation pressure on the corresponding electron (which is coupled via the Coulomb-force) via classical Thomson-scattering:

$$F_{\text{grav}} = \frac{GMm_p}{r^2} > \frac{\sigma_T}{c} \frac{L}{4\pi r^2} = F_{\text{rad}} \quad (1.15)$$

Obviously, L cannot exceed the threshold L_{Edd} , which only depends on the central mass M :

$$L < L_{\text{Edd}} = \frac{4\pi G c m_p}{\sigma_T} \cdot M \approx 1.3 \times 10^{31} \text{ W} \cdot M/M_\odot = 3.4 \times 10^4 L_\odot \cdot M/M_\odot. \quad (1.16)$$

Soft and hard spectra, Comptonization

The spectrum of most X-ray binaries contains a (soft) thermal component, indicating the existence of a (relatively) cold accretion disk, and also a (hard) power law component. The latter can be explained by the process, where low energetic thermal photons gain energy by inverse Compton scattering off electrons of a very thin but hot plasma in a so called accretion disk corona (ADC), which is probably generated by magnetohydrodynamical instabilities (Balbus & Hawley, 1998).

‘Usual’ Compton scattering is the reaction $\gamma + e \rightarrow \gamma' + e'$ of a photon with an electron, which is assumed to be at rest. In this case, a photon with energy E has after a scattering at an angle of θ an energy (which follows directly from the conservation of 4-momentum)

$$E' = \frac{E}{1 + \frac{E}{m_e c^2}(1 - \cos \theta)} \leq E \Rightarrow \langle E' - E \rangle \approx -\frac{E^2}{m_e c^2} \quad \text{for } E \ll m_e c^2 \quad (1.17)$$

Photons that scatter with hot electrons, however, can gain energy. One can show that a Maxwellian distribution of electrons with temperature T leads on average to an up-scattering:

$$\frac{\langle E' - E \rangle}{E} \approx \frac{4k_B T - E}{m_e c^2} \quad (1.18)$$

(Rybicki & Lightman, 1979, Eq. 7.36). Now multiple scattering (Comptonization) produces roughly a power law spectrum with exponential cutoff at $E_0 \approx k_B T$, where the photon index Γ depends on the optical thickness of the electron plasma:

$$\frac{dN}{dE} \sim E^{-\Gamma} \cdot \exp\left(-\frac{E}{E_0}\right) \quad (1.19)$$

More details on Comptonization simulations are given by Sunyaev & Titarchuk (1985).

Another possibility to explain hard power law spectra is Synchrotron-radiation from jets, i.e., relativistic plasma outflows (Markoff et al., 2005). The base of the jets plays then the role of the Comptonizing corona.

States

Most X-ray binaries can be classified to be in one of the following ‘states’, which are mainly determined by the relative strength of the soft and the hard component and furthermore by the total luminosity and the radio spectrum. (A possible geometric explanation for Cyg X-1 is shown in Fig. 1.12.) The state of a source may change on timescales of minutes to months.

- The high/soft state is characterized by quite high luminosity L , only slightly below the Eddington luminosity L_{Edd} , which indicates a high accretion rate. The accretion disk reaches to the innermost stable circular orbit and the spectrum is therefore dominated by the thermal component. The photon index of the weaker power law component, if existing, is typically $\Gamma \approx 2.5$. There is usually no radio emission detected.
- The low/hard state is characterized by a relatively low luminosity $L \lesssim 0.05 L_{\text{Edd}}$ and an X-ray spectrum with dominating power law component or even absent thermal component. The photon index Γ is typically between 1.4 and 1.8. Some sources show in the hard state additionally considerable radio emission, which is assumed to be synchrotron radiation from a plasma outflow (jet).

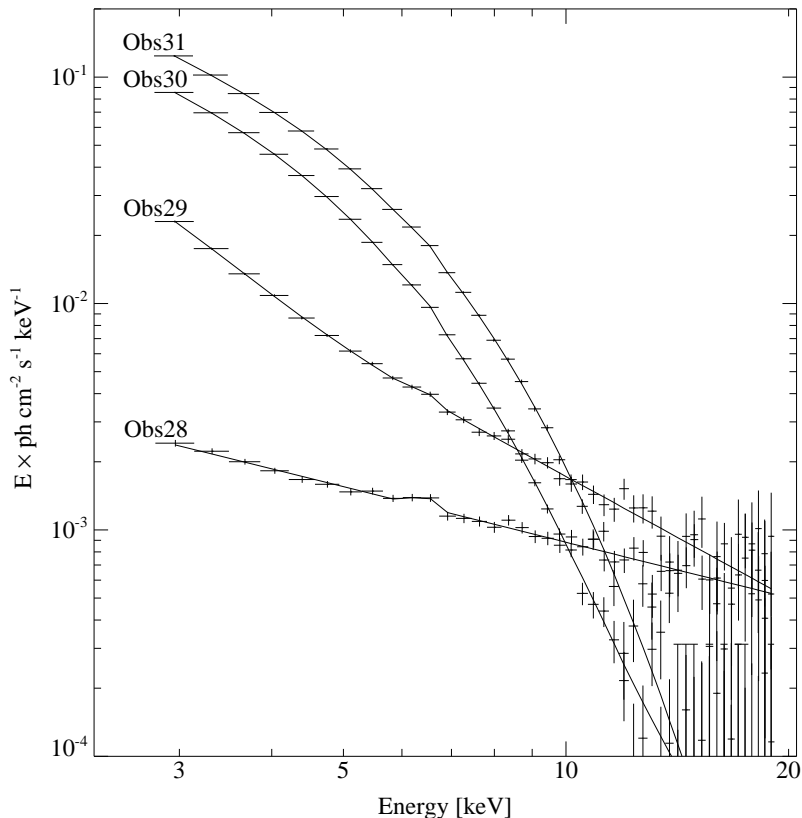


Figure 1.6: Spectrum of LMC X-3, showing a transition from the hard to the soft state. (Wilms et al., 2001, Fig. 4)

This list of states is not complete at all; there is, e.g., also the very high state, where a steep power law component contributes significantly to the high luminosity very close to L_{Edd} . The transition between soft and hard state usually occurs via another intermediate state. A more detailed discussion is given by Remillard & McClintock (2006).

As an example, the hard to soft transition of LMC X-3 is shown in Fig. 1.6: Obs. 28 was taken by Wilms et al. (2001) on 1998-05-29 in the hard state, while the final Obs. 31 only two and a half months later, on 1998-08-12, in a typical soft state. State transitions might be induced by changes in the accretion geometry and Compton cooling (cf. Eq. 1.17) of the hot electron corona, and they seem to be related to the jet formation (Kalemci et al., 2006), but all these effects are still discussed.

1.3 Cygnus X-1

1.3.1 The binary system

Cyg X-1 is a bright X-ray source that was discovered already in 1964 (Bowyer et al., 1965). The detection of a nearby radio flare in 1971 (Hjellming & Wade, 1971), which suggested the identification of Cyg X-1 with this radio source (Hjellming et al., 1971), allowed the accurate measurement of its position and furthermore the identification of the optical companion HDE 226868 (Murdin & Webster, 1971; Webster & Murdin, 1972; Bolton, 1972). Radial-velocity measurements of HDE 226868 have confirmed the binary behavior of the Cyg X-1 system (Webster & Murdin, 1972). As will be shown below, the compact object's mass is dynamically constrained to be above the Oppenheimer-Volkoff limit, so it was also the first object, which was believed to be a black hole. Because of the massive optical component, Cyg X-1 is a HMXB. In contrast to LMXB with black holes, which are transient X-ray sources, Cyg X-1 shows persistent X-ray activity – just as the other two black hole HMXBs that have been discovered yet, namely LMC X-3 and LMC X-1 (Remillard & McClintock, 2006).

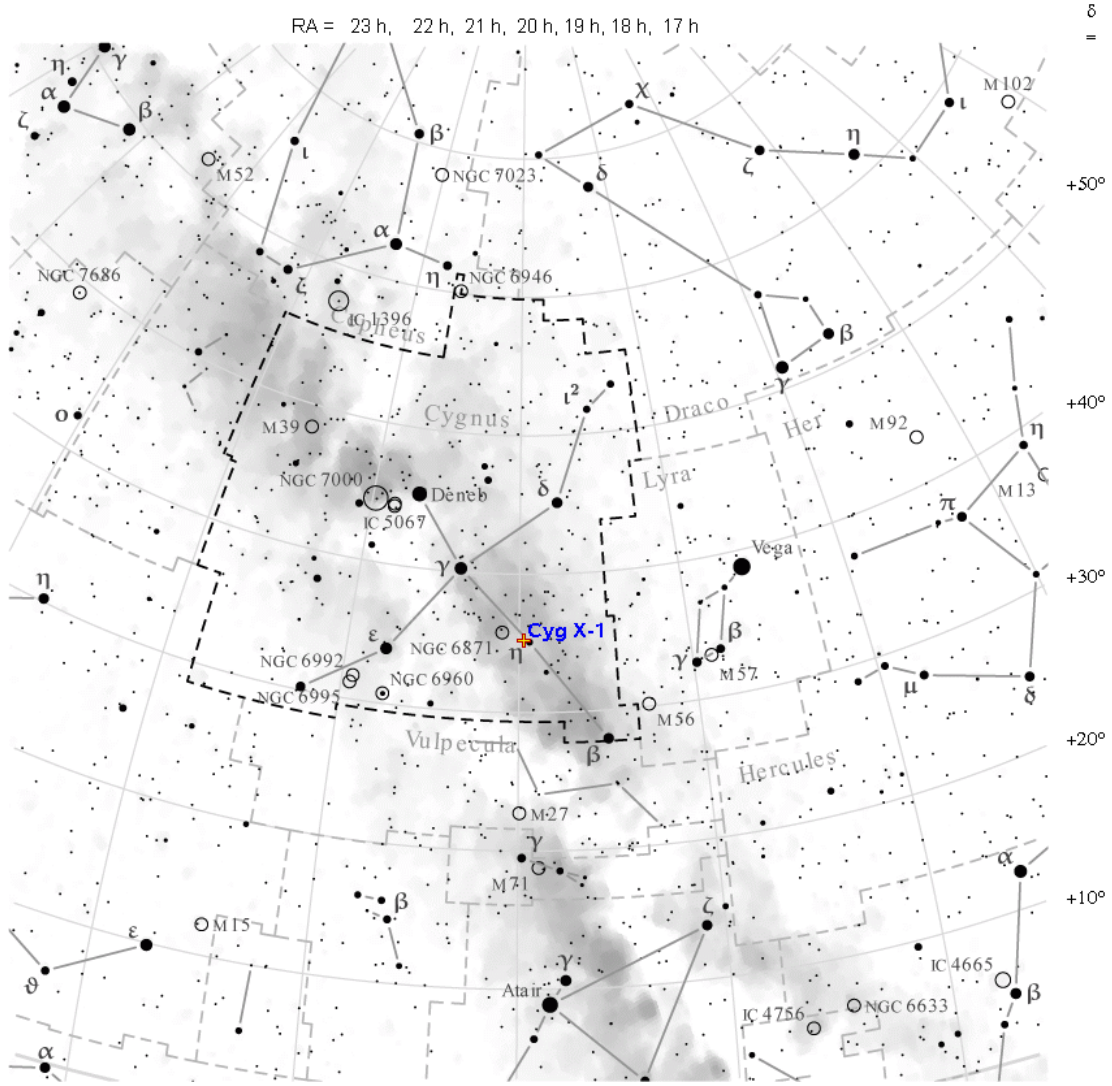


Figure 1.7: The constellation Cygnus with Cyg X-1 at $RA = 19^{\text{h}} 58^{\text{min}} 21.7^{\text{s}}$, $\delta = +35^{\circ} 12' 06''$. (after <http://ephemeriden.com/images/charts/cygnus.png>)

Location

Cyg X-1 is located near η Cyg at $RA = 19^{\text{h}} 58^{\text{min}} 21.7^{\text{s}}$, $\delta = +35^{\circ} 12' 06''$, corresponding to galactic coordinates $l_{\text{II}} = 71.3^{\circ}$, $b_{\text{II}} = +3.1^{\circ}$, thus near the galactic plane (Liu et al., 2006) at ~ 2.5 kpc ($1 \text{ kpc} = 3.085 \times 10^{19} \text{ m}$) distance (Bolton, 1972; Ninkov et al., 1987).

The optical companion

HDE 226868 is a $m_V = 8.84$ mag O9.7Iab supergiant (Walborn, 1973; Humphreys, 1978; Herrero et al., 1995). Hutchings (1978) fitted the orbital elements from the light curve and obtained a mass $M_{\star} = 14 \dots 19 M_{\odot}$ for HDE 226868. Gies & Bolton (1986) have tried to determine its mass from the rotational broadening of the absorption lines in its spectrum. As this not a conventional method, their result, $M_{\star} = 33 \pm 9 M_{\odot}$, is probably too high. The best analysis was probably performed by Herrero et al. (1995), who described the optical spectrum of HDE 226868 with unified models, which – in contrast to usual models for stellar atmospheres that only give the temperature and surface gravity – include the stellar wind as well. This gives, besides the mass loss rate and wind velocity,⁸ additionally the stellar radius without any further assumptions on the luminosity. The latter, as well as the mass, can be derived from the other parameters, which are listed in Table 1.1. The surface gravity has still

⁸The wind velocity is usually described as $v(r) = v_{\infty} \cdot \sqrt{1 - R/r}$, after the model of Castor et al. (1975).

Table 1.1: Parameters of stellar atmosphere and wind of HDE 226868 (Herrero et al., 1995)

		useful constants in SI-units	
effective temperature	$T_{\text{eff}} = 32\,000\text{ K}$		
(uncorrected) surface gravity	$g_{\star} = 10^{3.15}\text{ cm s}^{-2}$		
stellar radius	$R_{\star} = 17 R_{\odot}$		$(R_{\odot} = 7 \times 10^8\text{ m})$
mass loss rate	$\dot{M}_{\star} = 3 \times 10^{-6} M_{\odot} \text{ yr}^{-1}$		$(M_{\odot} = 1.98 \times 10^{30}\text{ kg})$
terminal wind velocity	$v_{\infty} = 2\,100\text{ km s}^{-1}$		

Derived parameters of HDE 226868:

luminosity	$L_{\star} = \sigma_{\text{SB}} \cdot 4\pi R_{\star}^2 \cdot T_{\text{eff}}^4$	$(\sigma_{\text{SB}} = 5.67 \times 10^{-8}\text{ W m}^{-2}\text{ K}^{-4})$
	$= 1.1 \times 10^{32}\text{ W} = 10^{5.4} L_{\odot}$	$(L_{\odot} = 3.827 \times 10^{26}\text{ W})$
(uncorrected) mass ^a	$M_{\star} = g_{\star} \cdot R_{\star}^2 / G$	$(G = 6.67 \times 10^{-11}\text{ m}^3\text{ kg}^{-1}\text{ s}^{-2})$
	$= 3 \times 10^{31}\text{ kg} = 15 M_{\odot}$	$(M_{\odot} = 1.98 \times 10^{30}\text{ kg})$

^aFurther corrections (see text) give even $17.8 M_{\odot}$.

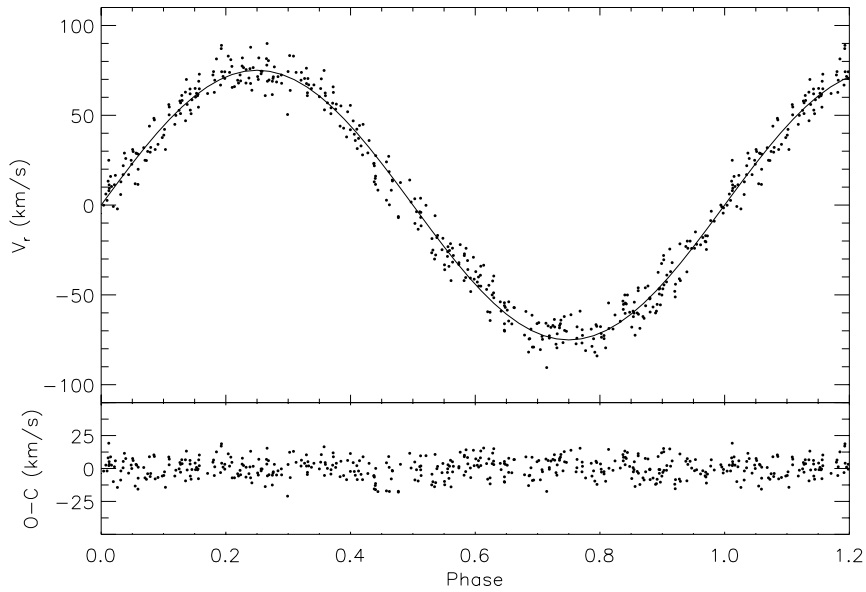


Figure 1.8: A velocity curve of HDE 226868, binned on the orbital phase. (Brocksopp et al., 1999b, Fig. 1)

Table 1.2: Orbital elements of the binary HDE 226868 / Cyg X-1 (Gies & Bolton, 1982)

orbital period	$P = 5.59974(8)\text{ days}$
velocity semi-amplitude	$K = 75.7(10)\text{ km s}^{-1}$
eccentricity	$e = 0.021(13)$
Derived orbital parameters of HDE 226868:	
semi major axis	$a_{\star} \sin i = P \cdot K / (2\pi)$ for $e \ll 1$
	$= 5.83(8) \times 10^6\text{ km}$
mass function	$f(M) := \frac{PK^3}{2\pi G}$
	$= 0.252(10) M_{\odot}$

Table 1.3: Recent ephemeris for HDE 226868 / Cyg X-1

reference	t_0 (MJD ^a)	P /days
LaSala et al. (1998)	50 234.79	5.5998
Brocksopp et al. (1999b)	41 874.207	5.599829
Gies et al. (2003)	51 729.949	5.599829

^aThe Modified Julian Date is $\text{MJD} = \text{JD} - 2\,400\,000.5$; thus 51 544 plus the number of days after 2000-01-01, 0 h, as the Julian Date JD is the number of days since -4712 Jan 1, 12 h.

to be corrected for the centrifugal force. From the assumption of synchronous rotation, an inclination $i = 35^\circ$ and a turbulence of 30 km s^{-1} in the atmosphere, [Herrero et al. \(1995\)](#) report finally $M_\star = 17.8 M_\odot$ for the mass of HDE 226868.

Yet a different result was obtained by [Ziólkowski \(2005\)](#), who considered the evolutionary status of HDE 226868 (another non-standard method) to derive a mass of $M_\star = 40 \pm 5 M_\odot$.

Orbital elements

A velocity curve (like in Fig. 1.8) can be established from measurements of the radial velocity via Doppler-shifted spectral lines of HDE 226868. Its analysis gives the orbital period and the (projected) velocity semi-amplitude $K = v_\star \sin i$. A detailed modeling of the velocity curve gives also the eccentricity of the orbit, which is zero unless the orbit is elliptical. From those parameters, one can easily determine the (projected) semi major axis $a_\star \sin i$, see Table 1.2, which summarizes the early result of [Gies & Bolton \(1982\)](#).

Together with a time t_0 of a given position in the binary orbit (e.g., when HDE 226868 is closest to us and its velocity just starts to turn positive, i.e., away from the observer – which is the superior conjunction of the invisible counterpart), the orbital period P allows the construction of an ephemeris: Provided that P is constant, the binary phase at any time t is

$$\phi(t) \equiv \frac{t - t_0}{P} \text{ mod } 1 \quad (\text{i.e., the fractional part of } \frac{t-t_0}{P}) \quad . \quad (1.20)$$

Although it was reported by [Ninkov et al. \(1987\)](#) that the binary period might increase with time, no change in period could be confirmed by following high resolution radial velocity measurements of [LaSala et al. \(1998\)](#), [Brocksopp et al. \(1999b\)](#) and [Gies et al. \(2003\)](#). Their ephemerides are shown in Table 1.3.

Constraints on the mass

With the knowledge of its projected radial velocity $K = v_\star \sin i \approx 76 \text{ km s}^{-1}$ and the binary's orbital period of $P = 5.6$ days (see Table 1.2; [Gies & Bolton, 1982](#)), Kepler's third law

$$\frac{P^2}{a^3} = \frac{4\pi^2}{G(M_\star + M_X)} \quad (1.21)$$

and the velocity $\frac{K}{\sin i} = v_\star = \frac{M_X}{M_X + M_\star} \frac{2\pi a}{P}$ of M_\star give the spectroscopic mass-function

$$f(M) := \frac{P K^3}{2\pi G} = 0.252 M_\odot = \frac{(M_X \sin i)^3}{(M_X + M_\star)^2} = \frac{M_X \cdot (\sin i)^3}{(1 + q)^2} \quad , \quad (1.22)$$

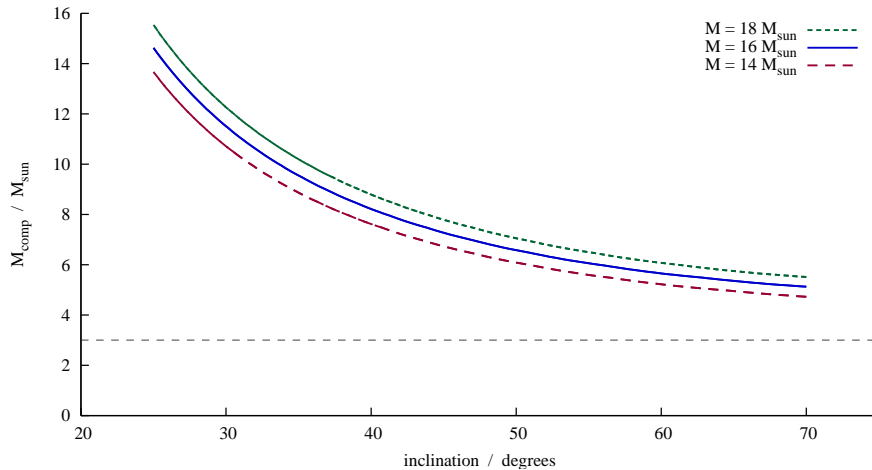


Figure 1.9: The mass of the compact object for $f(M) = 0.252 M_\odot$ and $M_\star = (16 \pm 2) M_\odot$.

which constrains the mass $M_X =: M_*/q$ of the compact object well above the Oppenheimer-Volkoff-limit for neutron stars, see Fig. 1.9. Cyg X-1 has therefore been the first convincing black hole. The estimated inclination $i \approx 35^\circ$ (Gies & Bolton, 1986) gives $M_X \approx 10 M_\odot$, if $M_* \approx 18 M_\odot$ is assumed (Herrero et al., 1995). (The earlier assumption of $M_* = (33 \pm 9) M_\odot$ lead even to $M_X \approx (16 \pm 5) M_\odot$.)

1.3.2 Accretion

As noted in Table 1.1, HDE 226868 drives a strong stellar wind (mainly by the UV-photons' radiation pressure) with a terminal velocity of 2100 km s^{-1} and a mass loss rate of $3 \times 10^{-6} M_\odot \text{ a}^{-1}$ (Herrero et al., 1995). 0.1...1% of this material is focused onto the black hole, which strongly influences the wind by its gravity and non-inertial forces, such that the focused wind is highly asymmetric. More precisely, Friend & Castor (1982) have calculated that the supergiant's mass loss rate in direction of the black hole is about 4.5 times the minimal value, see Fig. 1.10. (The wind is so extremely focused because HDE 226868 is almost filling its Roche lobe.) This is also in agreement with the fact that dips (Sect. 1.3.4) occur preferentially near superior conjunction (i.e., when the back hole is 'behind' HDE 226868 along our line of sight).

This accretion gives a luminosity of typically $L_X \approx 4 \times 10^{30} \text{ W} = 1.0 \times 10^4 L_\odot$. The fact that Cyg X-1 is continuously powered by wind accretion makes it a persistent X-ray source. In transient low mass X-ray binaries, which are fed by a disk formed of Roche lobe overflowing matter, the effective accretion rate depends on the viscosity in the disk. If enough material is available, the viscosity increases and so much energy will be dissipated that an X-ray outburst can be detected. But the black hole quickly absorbs the whole disk and the source falls into quiescence – until enough matter is collected again.

There is also evidence for a small accretion disk: Some (especially soft state) spectra show a soft excess at low energies, which can be explained by blackbody radiation from a standard accretion disk, and even most hard-state spectra contain the Fe $K\alpha$ line at 6.4 keV, which is thought to be the fluorescence in the disk from reflected X-rays.

As HDE 226868 is very close to filling its Roche lobe, there might be further matter transfers onto the black hole, induced by tidal effects of the black hole (Blondin et al., 1991): Already Petterson (1978) has showed that material leaves the companion star of many HMXB systems via the inner critical point (which only coincides with the Lagrange point L_1 , if the star is co-rotating). The trajectory of this stream, as well as the final accretion rate on the compact object, depends on the rotation of the companion and the binary separation, as the stream is deflected by the Coriolis force.

Petterson (1978) suggested that Cyg X-1, in the hard state, accretes only the stellar wind, whereas the stream might contribute in the high state. Nevertheless, the trailing stream can account for the enhanced absorption, as well as an increased number of dips, which is detected at orbital phases $\phi \approx 0.6$, even if this stream passes the black hole.

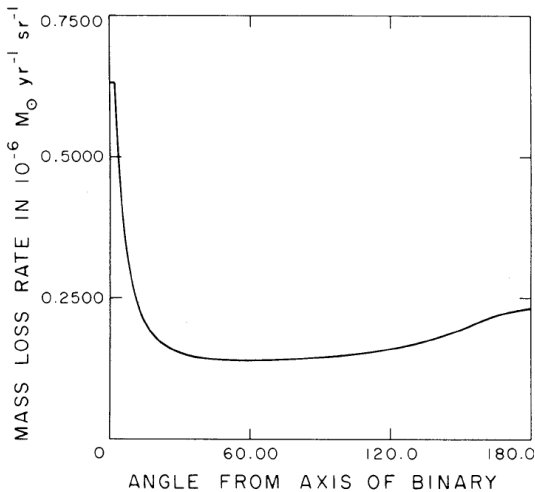


Figure 1.10: Mass loss rate of Cyg X-1, modeled by Friend & Castor (1982, Fig. 4).

The mass loss along the axis of the binary is higher by a factor of ≈ 4.5 . Therefore, this kind of mass transfer is called the “focussed wind scenario”.

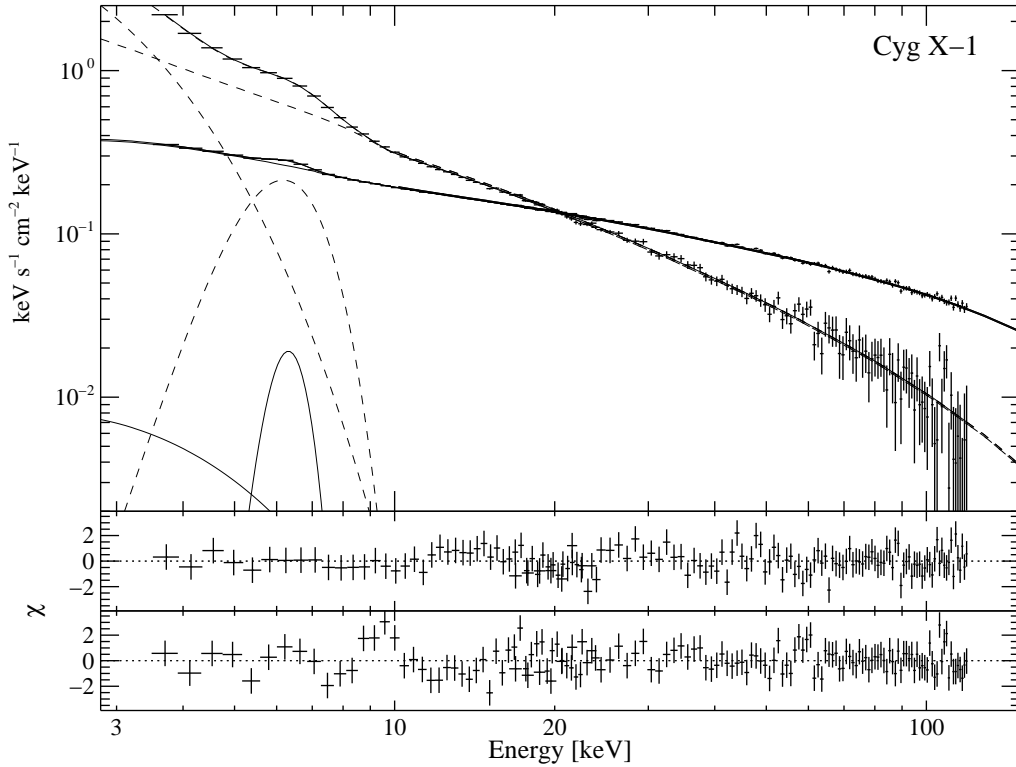


Figure 1.11: Unfolded spectra and residuals of Cyg X-1 in the hard and in the soft state. (on 2003-01-10 and 2003-07-23, respectively; from Wilms et al., 2006b, Fig. 12)

1.3.3 The X-ray spectrum

Cyg X-1 is hardly found in the soft state (see Sect. 1.2.3), namely, only at $\approx 30\%$ of the time (Wilms et al., 2006b). In these soft states, Cyg X-1 reaches its highest luminosity. Its spectrum is dominated by thermal emission from a standard accretion disk. There is also evidence of a fluorescence iron $K\alpha$ line at $E \approx 6.4$ keV (Ebisawa et al., 1996), which emerges when hard X-rays ionize the material in the disk. The strength of the iron line is thus another measure for the extent of the disk. Furthermore, there is a so called reflection hump from hard X-rays that lose energy by Compton-backscattering from the (relatively) cold disk (see Lightman & White, 1988 for AGN and Reynolds, 1998 for a review). The weak power law component has a larger photon index Γ (cf. Eq. 1.19) than in the hard state, i.e., the spectrum is softer. There is no radio emission detected.

In the hard state (which has first been distinguished by Tananbaum et al., 1972), the spectrum above $E = 2$ keV is a ($\Gamma \approx 1.4 \dots 1.7$)-power law with exponential cutoff at $E_0 \approx 150$ keV. If there is a soft-excess below $E = 1$ keV (i.e., above $\lambda = 12$ Å), it is still explained by a cold accretion disk with $k_B T \approx (0.1 \dots 0.3)$ keV. There is usually a spectrally flat radio emission of ~ 12 mJy (cf. Sect. 2) at 15 GHz (Wilms et al., 2006b).

In the top panel of Fig. 1.11, the (unfolded) F_E spectra (see Sect. 2) are shown both for a flat hard state spectrum from 2003, January 10, and for a steeper and much more curved spectrum of the subsequent soft state, on 2003, July 29. Very accurate models have been obtained for both spectra by Wilms et al. (2006b), as indicated by the residuals shown in the lower two panels. The disk- and iron line components additionally contributing to the Comptonization model `eqpair` are also shown separately in the top spectrum panel. It is obvious, that both disk and iron line hardly contribute to the hard state spectrum (solid lines), in contrast to those of the soft state spectrum (dashed lines), as the flux-axis is scaled logarithmically and spans 3 orders of magnitude.

The spectral features may be explained by an accretion disk corona (ADC), which underlies the theoretical Comptonization models (Sect. 1.2.3). Another possibility to explain the hard power law spectrum – a short overview of the discussion is given in the introduction of Wilms et al. (2006b) – is synchrotron self-Compton emission from relativistic electrons in a plasma

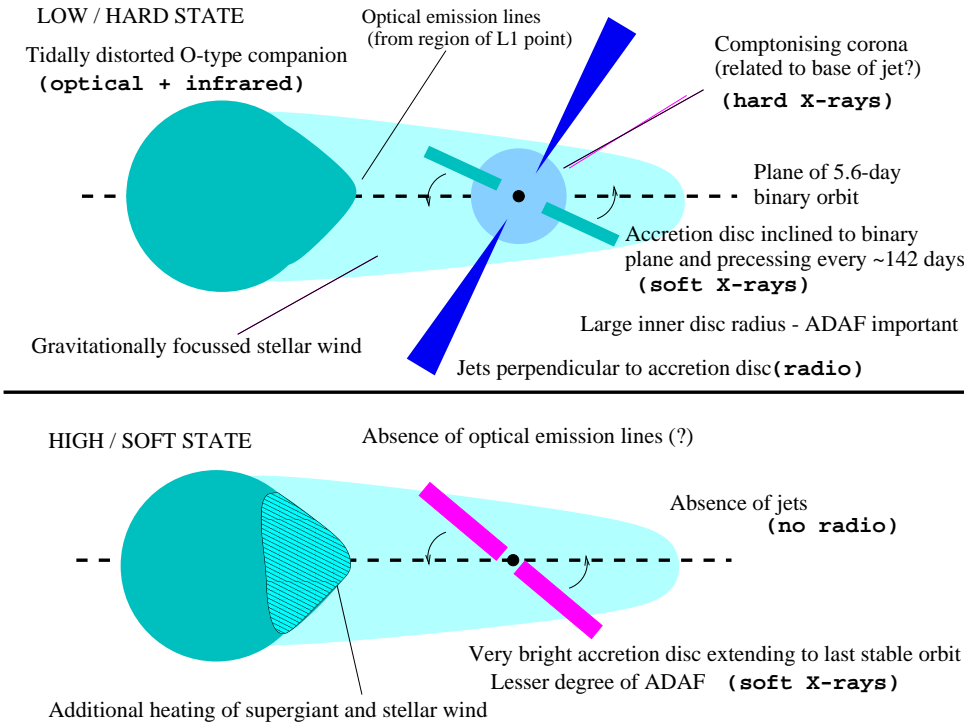


Figure 1.12: Sketched geometry for the hard (top) and soft (bottom) state of Cyg X-1. (from Brocksopp et al., 1999a, Fig. 7)

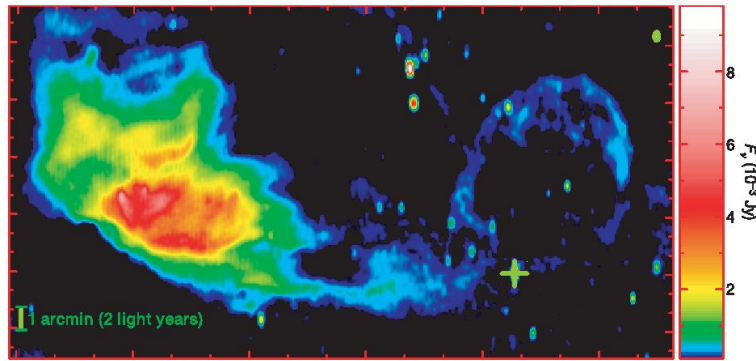


Figure 1.13: A jet blown ring around Cyg X-1 (cross) next to the H II region Sh2-101 (left). (observed for 60 h at 1.4 GHz; from Gallo et al., 2005, Fig. 1)

outflow (Markoff et al., 2005), see also Fig. 1.12. This jet, imaged by Stirling et al. (2001), who measured a velocity of $v > 0.6 c$, is also considered as the origin of the radio emission, which is thought to be synchrotron radiation (Fender et al., 2000). It was recently found that the jet (‘dark outflow’) has to carry a significant power – even comparable to the X-ray luminosity of Cyg X-1 itself. This was inferred from a ring of radio emission (Fig. 1.13) that might result from the shock of the jet hitting a nearby H II region (Gallo et al., 2005). Correlations between the radio and X-ray spectrum are shown, e.g., by Wilms et al. (2006b, Fig. 8).

1.3.4 Transient X-ray dips

It has already been found in early times of X-ray observations (Li & Clark, 1974; Mason et al., 1974), that Cyg X-1 shows sudden decreases of its X-ray intensity (“X-ray dips”), whose duration is usually only minutes, but which can last for up to 8 hours as well. The spectrum hardens during those dips, i.e., low energies are more strongly reduced than higher ones and the spectrum becomes flatter. This indicates that they may result from photoabsorption, which affects a spectrum dominantly at low energies. (The cross section is roughly $\sigma_{\text{ph.abs.}} \sim E^{-3}$, cf. Sect. 2.1.1.) The hardness is often also defined quantitatively as ratio of the fluxes in different energy bands. Therefore, dips can be identified as peaks in hardness curves – often

even better than in the light curves themselves. Bałucińska-Church et al. (1997) found that the flickering of the source is also reduced during the dips, in detail that the root mean square (rms) variability amplitude⁹ is proportional to the X-ray intensity. According to them, this shows on the one hand that the variability is intrinsic to the emission region of the source, and it suggests on the other hand that dips are phenomena of absorption. Pravdo et al. (1980), however, have already noticed that the dips cannot be explained solely by photoabsorption. (But Remillard & Canizares (1984) state again, that the data of Pravdo et al. cannot rule out absorption in partially ionized material.)

The investigation of the dips by timing observations helps thus to constrain the geometry of the source region. As the UV spectrum of Cyg X-1, which is dominated by the O star HDE 226868, remains unchanged during the dips (Pravdo et al., 1980), it is likely that the dips arise from clumps in the accretion flow. It was already known in the 1970s that dips occur mainly near superior conjunction $\phi = 0$, which was confirmed by the systematic analysis of their distribution with orbital phase by Bałucińska-Church et al. (2000). The distribution of dips in archived historical observations shows a clear peak at phases near $\phi = 0.95$, i.e., short before upper conjunction, with a full width at half maximum of 0.25. They show that the distribution follows the variation of the column density in the wind. The analysis of *RXTE*/ASM (see Sect. 1.1.3) data (where dips are identified via hardness ratios of the count rates in the different energy bands) re-verifies this result with a greatly improved statistic and reveals another peak at $\phi \approx 0.6$, see Fig. 1.14.

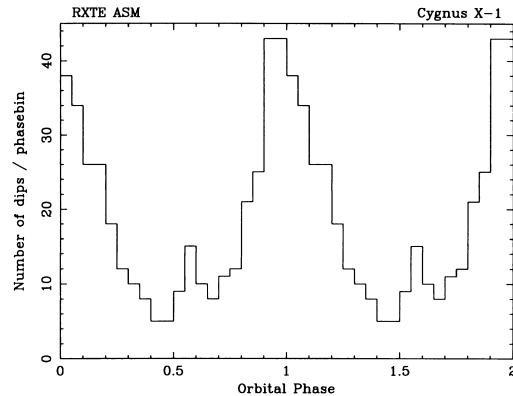


Figure 1.14: Phase distribution of dips. (Bałucińska-Church et al., 2000, Fig. 5)

Several scenarios for the origin of these dips have been proposed (see, for example, Remillard & Canizares, 1984; Bałucińska-Church et al., 2000). It is quite likely that the dips arise from clumps in the accretion flow. The focused stellar wind is highly ionized by the X-rays, which also suppresses the radiative driving force from HDE 226868. Bałucińska-Church et al. (2000) suggested that neutral material in the wind leads to the formation and – by shielding of X-rays – growth of dense blobs, whose density is enhanced by a factor of 100...1000. The occurrence of dips near $\phi = 0.6$ may indicate that there is also a stream produced by Roche lobe overflow which trails the black hole.

Feng & Cui (2002) have reported a new category of dips: What has been presented so far, holds only for ‘type A’ dips – according to their nomenclature. They found also (a minority of) ‘type B’ dips, where the flux is reduced almost independent of the energy. The following possibilities, which both agree with the fact that B-dips occur independent of orbital phase, are among their discussed explanations: 1. Parts of the extended emission region are suddenly fully obscured by a tidal stream close to the accretion disk itself. 2. The new dips could also result from Thomson scattering in extremely dense, but ionized blobs in the accretion flow, which are again very close to the X-ray source.

1.4 The *Chandra* X-ray observatory

As described in the very first Section 1.1, all these X-ray features of black holes in X-ray binary systems, and in particular of Cygnus X-1, discussed in the last sections can only be observed with space telescopes. The active satellite missions have been mentioned briefly in Sect. 1.1.3. In this section, the *Chandra* X-ray observatory, which performed the observation analyzed

⁹ This variability of Cyg X-1 is subject of many extensive studies, e.g., of Gleissner (2004), as it gives hints on the timescales and sizes of the system, but it is not a main issue of this work.

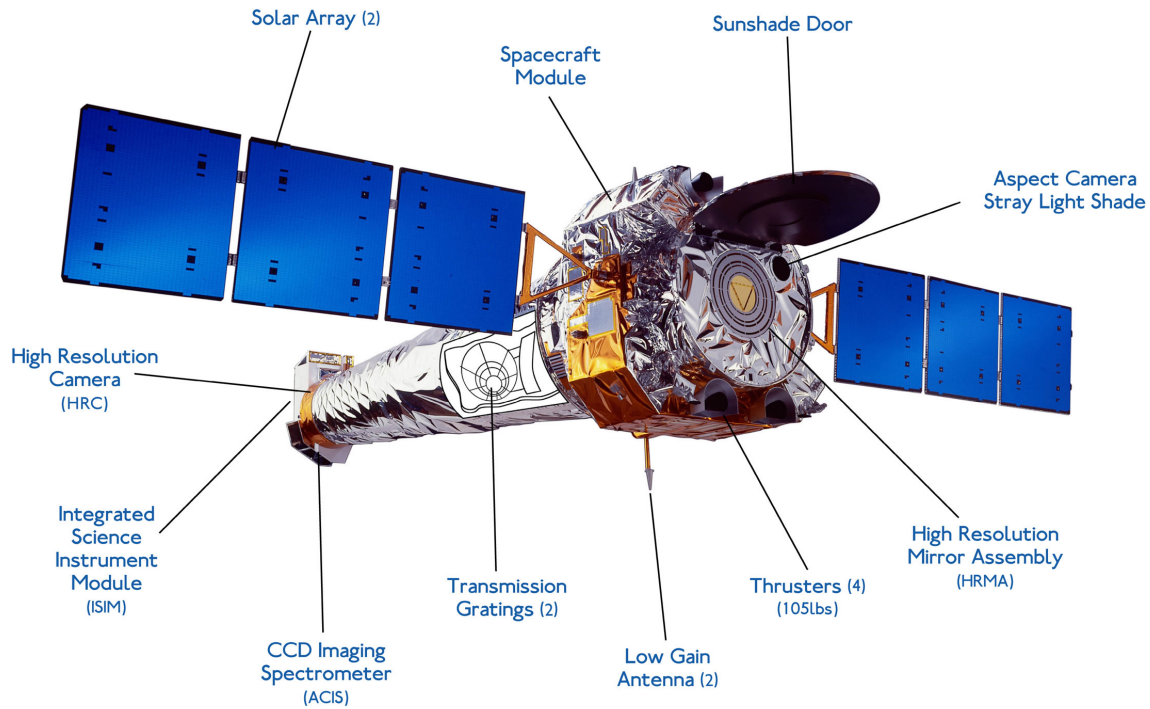


Figure 1.15: The *Chandra* spacecraft.
 (from <http://chandra.harvard.edu/about/spacecraft.html>)

in this work (Sect. 4), is discussed in detail. Some of the basic functionalities, however, can be transferred to *XMM-Newton*, which is also a grating observatory with a similar mirror system for X-rays. In contrast, the X-ray detection of *RXTE*, *INTEGRAL*, or *Suzaku* is quite different.

An excellent overview of grazing incidence X-ray telescopes is given by Aschenbach (1985).

1.4.1 The spacecraft

The *Chandra* X-ray observatory, which was originally called *Advanced X-ray Astrophysics Facility (AXAF)*, has been named after the Indian astronomer Subrahmanyan Chandrasekhar.¹⁰ *Chandra* is a NASA-satellite of mass 4.8 tons, which has been launched by the Space Shuttle *Columbia* on 1999, July 23.¹¹ Whereas some other X-ray satellites, e.g., *RXTE*, reside in a close-Earth orbit (which lasts 96 minutes in the case of *RXTE*) below the Van Allen belts – these are regions of charged particles deflected from Earth’s magnetosphere, and thus dangerous for X-ray detectors – *Chandra*’s orbit is highly elliptical: In December of 2006, its height above the Earth was 26 300 km in perigee, and 122 500 km in apogee (CXC, 2006), corresponding to an eccentricity of 0.98. It therefore spends most of its time ($\sim 75\%$) above the radiation belts. As the orbital period is about 64 hours, 160 ks long observations are possible without interruption. (Due to friction in the atmosphere, especially at the perigee passages, and due to gravitational torques from the higher multipole moments of the Earth’s mass distribution, the orbit itself varies with time: at the end of 2005, it reached its minimal eccentricity with 28 600 km distant perigee, 120 300 km distant apogee and a period of 63.5 hours.)

Chandra carries several high precision instruments, see Fig. 1.15, of which the most important ones will be described in the following subsections. A complete reference manual can be found in the Proposer’s Observatory Guide (CXC, 2006).

¹⁰ Chandrasekhar (1910–1995) won the Nobel prize in 1983 “for his theoretical studies of the physical processes of importance to the structure and evolution of the stars” (http://nobelprize.org/nobel_prizes/physics/laureates/1983).

¹¹ Due to the *Challenger* disaster in 1986, this was delayed by 9 years: Aschenbach (1985, Sect. 4.2.6) had expected AXAF to be launched in 1990.

1.4.2 The mirrors

Due to the large successes, *Chandra*'s mirror technology proceeds with what has already been implemented in the Einstein observatory (with half the mirror's diameter) and the ROSAT mission (see Sect. 1.1.2). The unique capability is largely due to its mirror: “*Chandra* was designed to provide order-of-magnitude advances over previous X-ray astronomy missions with regards to spatial and spectral resolution.” (CXC, 2006, POG). Its high resolving power is still unbeaten, even by the later mission *XMM-Newton*.

Before starting with *Chandra*'s mirror itself, it is appropriate to discuss the deflection of X-rays, which is only possible via total reflection if they graze a surface under a small angle – typically less than 1 degree. The critical angle α is given by the index of refraction, n , by

$$1 - \frac{\epsilon_r \mu_r - 1}{2} \approx \sqrt{\epsilon_r \cdot \mu_r} = n = \cos \alpha \approx 1 - \frac{\alpha^2}{2} \quad (1.23)$$

For frequencies ω much larger than any resonance in the material, the relative dielectric permittivity ϵ_r can be expressed by the electron density ZN (Jackson, 1975, Eqs. 7.59&7.60):

$$\epsilon_r = 1 - \frac{\omega_p^2}{\omega^2}, \quad \text{with the plasma frequency } \omega_p = \sqrt{\frac{4\pi ZN e^2}{m_e}}. \quad (1.24)$$

The magnetic permeability is $\mu_r \approx 1$. Expressing N by the mass density $\rho = Am_u \cdot N$ (with atomic mass number A and unit m_u) and inserting $\lambda = c \cdot 2\pi/\omega$, one obtains for $Z/A \approx 0.5$:

$$\alpha = \sqrt{\frac{1}{\pi} \frac{Z}{A} \frac{\rho}{m_u} \frac{e^2}{m_e c^2} \cdot \lambda^2} \approx 1.6 \text{ mrad} \cdot \sqrt{\frac{\rho}{\text{g cm}^{-3}}} \cdot \frac{\lambda}{\text{\AA}} \quad (1.6 \text{ mrad} = 5.6') \quad (1.25)$$

This result is also quoted by Aschenbach (1985, Eq. 2.7), who uses the classical electron radius $r_e = e^2/(m_e c^2)$, where $e^2 = e_{\text{SI}}^2/(4\pi\epsilon_0)$ in SI-units, and “Avogadro's number” $N_0 = m_u^{-1}$.

Chandra's high resolution mirror assembly (HRMA, see Fig. 1.16) is a Wolter I-type mirror system (Wolter, 1952) that consists of 4 pairs of (parts of) confocal paraboloids and hyperboloids. As the critical angle (Eq. 1.25) for total reflection scales with $\sqrt{\rho}$, metals like gold or iridium are favorable. In *Chandra*'s case, a 33 nm thick layer of iridium has been deposited on the surface of the mirrors. As the efficiency of a telescope depends on its collecting area and the effective area for grazing incidence is relatively small, 4 nested Wolter mirrors of diameters 1.23 m, 0.99 m, 0.87 m and 0.65 m have been combined. The HRMA's geometric aperture is 1 145 cm², but the final effective area is lower and strongly

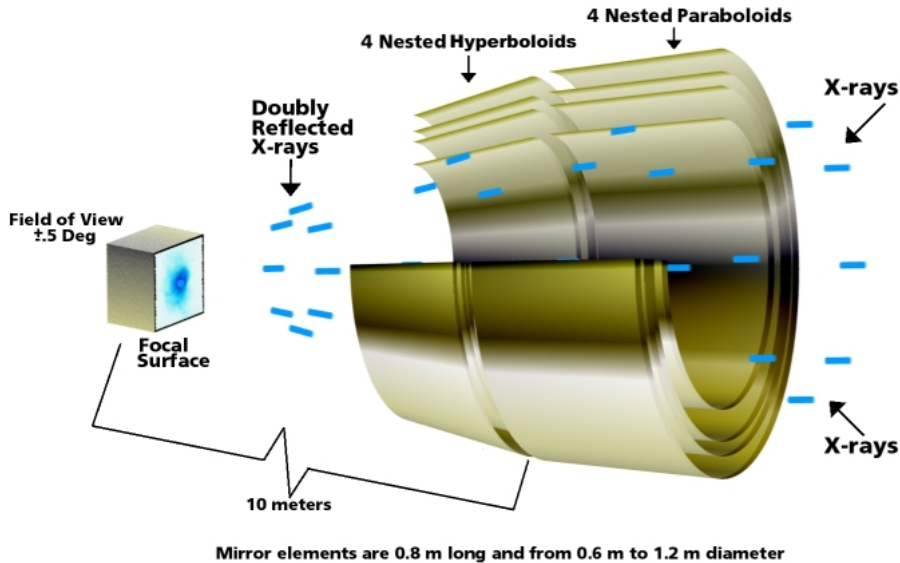


Figure 1.16: *Chandra*'s high resolution mirror assembly.
(from http://chandra.harvard.edu/about/telescope_system.html)

energy dependent (cf. Eq. 1.25 again) – it also depends on the detector efficiency (see ARFs, Sect. 2.2.1). One has also noticed a 2.2 nm thick contamination layer of hydrocarbons on the mirror which affects the efficiency near the Iridium M edges above 2.05 keV.

The focal length of the HRMA and therefore the whole telescope is 10 m, which was mainly limited by the transporting Space Shuttle. The mirror’s weight is almost 1.5 tons.

In comparison, *XMM-Newton* has 58 concentric Wolter mirrors and therefore a much larger collecting area of 4 300 cm² at 1.5 keV.

1.4.3 The gratings

Chandra can both be used for imaging analysis and grating spectroscopy. These two modes are realized by transmission gratings, which can either stay tilted or be flipped into the optical path. In the latter case, they produce dispersed images according to the grating equation

$$p \cdot \sin \theta = m \cdot \lambda , \quad (1.26)$$

where p is the grating period, θ the deflection angle, m the order and λ the wavelength.

There are two systems of transmission gratings available: the Low and High Energy Transmission Gratings (LETG and HETG). Both consist of Rowland gratings: Grating facets are mounted on a toroidal aluminum assembly. The Rowland geometry assures that photons (which are already focused by the mirror) being diffracted from different facets are focused again on the same point. This concept reduces optical aberrations. The Rowland circle is the intersection of the torus with the plane in the direction of dispersion and perpendicular to the focal plane, see Fig. 1.17. It contains the mirror’s focal point and also all the focal points of the Rowland grating, which can be seen from elementary geometry. The Rowland spacing (\approx diameter of the circle) is 8.63 m.

While the ACIS-S detector (mostly used with the HETG, see Sect. 1.4.4) is placed tangentially to the Rowland circle, parts of the HRC-S detector (mostly used with the LETG) are tilted to follow the circle, as low energies (large wavelengths) lead to a larger deflection, such that the curvature of the Rowland focus becomes more important.

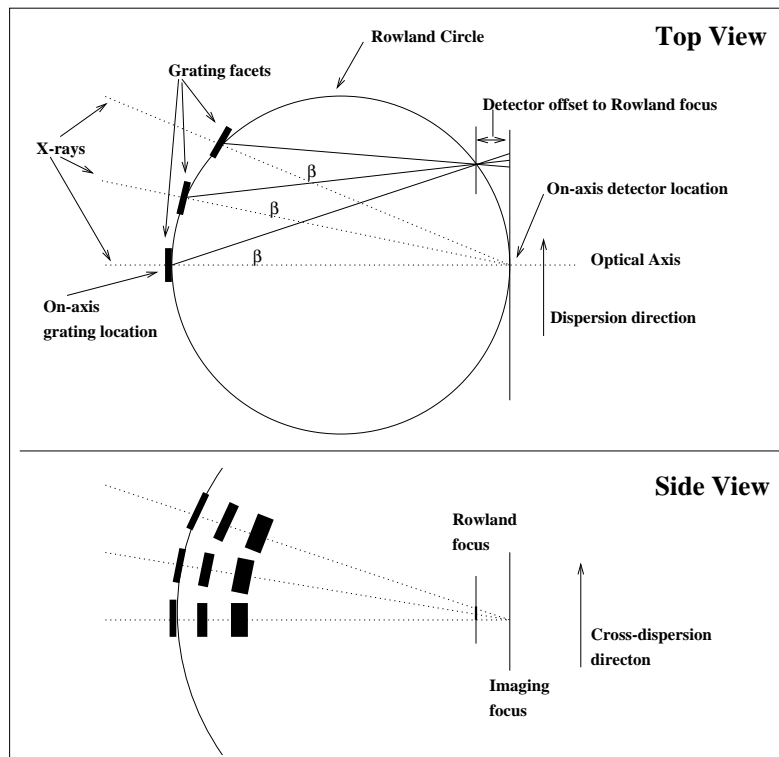


Figure 1.17: The Rowland geometry.

(from http://cxc.harvard.edu/proposer/POG/html/HETG.html#tth_fIg8.3)

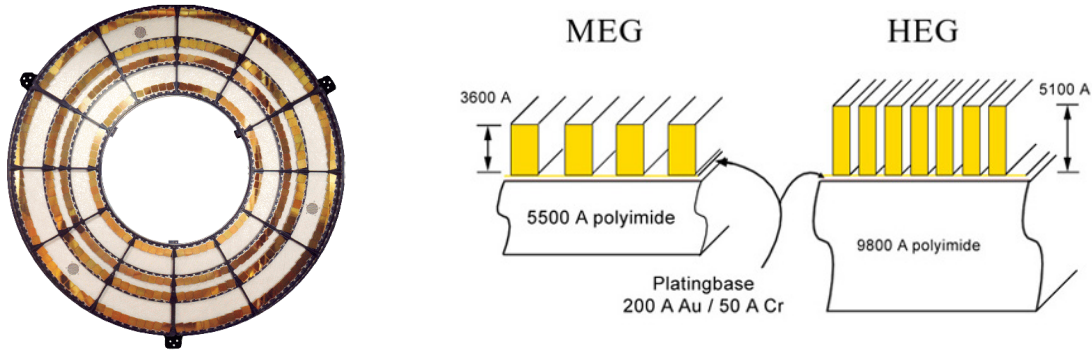


Figure 1.18: The High Energy Transmission Grating HETG.

Left: photography (from http://space.mit.edu/HETG/hetg_info.html), right: illustration of the gold bar grating (from http://chandra.harvard.edu/about/science_instruments3.html)

LETGS

The LETG has been developed at the SRON Laboratory for Space Research of the Netherlands, in collaboration with the Max-Planck-Institut für Extraterrestrische Physik in Garching (near Munich), Germany. It uses $0.5\ \mu\text{m}$ thick gold wires with $1\ \mu\text{m}$ period as its grating. Support structures in perpendicular and triangular directions with $25\ \mu\text{m}$ and $2\ \text{mm}$ period produce additional diffractions. In combination with the HRMA and the High Resolution Camera, the Low Energy Transmission Grating Spectrometer (LETGS) provides the high spectral resolution of $\Delta E/E = 1000$ in the low energy-range $0.08 \dots 0.2\ \text{keV}$.

HETGS

The HETG, which is used for high energies of $0.4 \dots 10\ \text{keV}$, where it also produces the high resolution of $\Delta E/E = 1000$, comprises two sets of gratings at once: the High and the Medium Energy Gratings (HEG and MEG), whose grating facets are realized by gold bars of specific periods. As the directions of dispersion of HEG and MEG differ by 10° , the image of a point source produced by the HETG is a crossed pair of arms (Figs. 3.1, 4.2 and 4.3). The HEG occupies the inner two rings of the Rowland torus on the support structure (see Fig. 1.18), which is $1.1\ \text{m}$ in diameter. The outer two rings form the MEG. While the HEG consists of 144 grating facets with gold bars of $1200\ \text{\AA}$ width and $2001\ \text{\AA}$ period on a thin polyimide substrate, the MEG has 192 facets with $2080\ \text{\AA}$ width and $4002\ \text{\AA}$ period; the almost 2:1 ratio of period and width of MEG's grating bars suppresses dispersion in even orders.

The HETG is usually used in combination with the HRMA and the Advanced CCD Imaging Spectrometer (see below); this is called the High Energy Transmission Grating Spectrometer (HETGS). The HEG has the larger spectral resolution of $5.5\ \text{m\AA}$ per ACIS detector pixel, while the MEG (with $11\ \text{m\AA}$ per ACIS pixel) covers a larger range of wavelengths.

1.4.4 The ACIS detector

The Science Instrument Module (SIM) in the focal plane contains two detectors. It can be moved to bring either the High Resolution Camera (HRC), which is a micro-channel plate detector, or the Advanced CCD Imaging Spectrometer (ACIS) into the focus. Both have two subsystems: a longish one for grating spectroscopy (-S) and another square-shaped one for imaging analysis (-I), see Fig. 1.19.

The ACIS (see Fig. 1.20) consists of 4 ACIS-I (in a 2×2 array) and 6 ACIS-S (in a 1×6 array) planar CCD chips. At most 6 chips can be operated simultaneously. The default chips in ACIS-I-mode are I1-I4 and S2-S3, but it is also possible to use ACIS-S in imaging-mode with S1-S4, I2-I3. ACIS-S in spectroscopy-mode uses S0-S5, of course.

Each CCD (charge coupled device) is a silicon solid-state detector with 1024×1024 pixels of each $24\ \mu\text{m}$ size. It operates at $-90 \dots -120^\circ\text{C}$, as electrons from the valence band shall not be excited thermally into the conduction band, but via the inner photo effect: absorbed

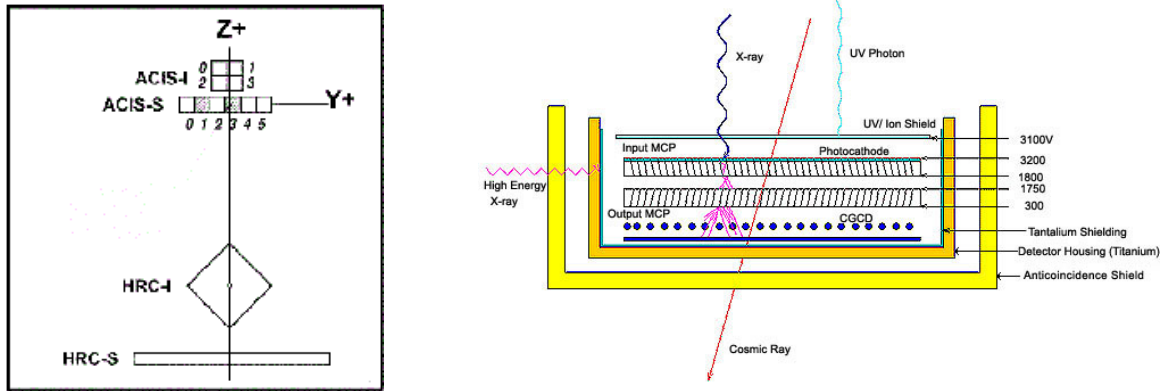


Figure 1.19: The Science Instrument Module SIM and the High Resolution Camera HRC. Left: SIM (from http://cxc.harvard.edu/proposer/POG/html/INTRO.html#tth_sEc1.6), right: HRC (from http://chandra.harvard.edu/about/science_instruments1.html).

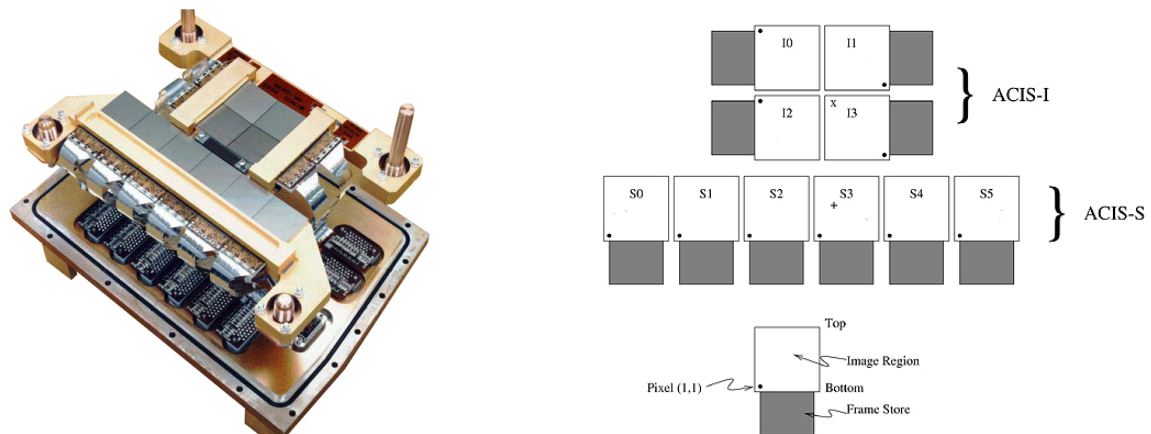


Figure 1.20: The ACIS CCD-chips: photography and sketch.

Left: photography (from http://chandra.harvard.edu/about/science_instruments.html), right: sketch (from http://chandra.harvard.edu/about/science_instruments2.html).

X-rays produce a large number of electron-hole pairs. This charge will be measured, and it is proportional to the X-ray energy: there is one pair for each 3.7 eV. This is different to optical CCDs, where each photon produces roughly only one electron and the number of electrons (after absorption of many photons) is therefore proportional to the intensity of the light. The additional entry of visible light is suppressed by the optical blocking filters (OBF), $\approx 3.5 \mu\text{m}$ thick layers of aluminum and polyimide, directly above the CCD chips.

There are different realizations of CCD chips in use: all but 2 of ACIS's chips are front-side-illuminated (FI), which means that charges are stored – and read out by the electronics, of course – on the front side, which is exposed to the radiation. For this reason, the FI chips unfortunately suffer from radiation damage from the very beginning of the *Chandra* mission: High-energetic cosmic protons, which are not sufficiently shielded, have been focused by the Wolter mirror just like the grazing X-rays during early passages through the radiation belts. Since this has been realized, the detector is removed from the mirror's focal plane during these passages. S1 and S3 (see Fig. 1.20) are, however, back-side-illuminated (BI), i.e., the charges are generated and read out at the back side, which is possible for such a detector, as the X-rays can penetrate the silicon crystal. Additionally, the ACIS efficiency has decreased slowly, but continuously, since *Chandra's* launch due to molecular contamination (predominantly carbon) on the optical blocking filters.

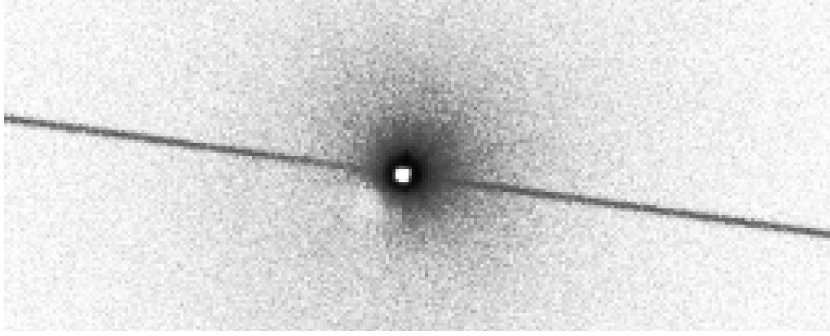


Figure 1.21:
A readout streak.

Readout modes

The charge produced by an X-ray photon in a CCD is usually confined to one pixel; only the neighboring pixels might be affected. If the latter is the case, the event can be rejected in the post-observational data-processing (see filtering for grade in Sect. 3.1.2).

When the CCD is read out, voltages are applied to each row in such a way that all electrons move one row towards the frame store register, which exists for each column. As this is possible in $40 \mu\text{s}$, the whole column can be read out in 41 ms.

In timed exposure (TE) mode, the CCD is exposed for some time t_{exp} , then its data is transferred in the frame store, which is read out during the next exposure. As the readout of the full frame store requires 3.2 s, this is also the optimal exposure time, unless only sub-arrays of each chip are used. The frame-time is important, as it defines the time resolution of the detector. If one wants to do timing analysis (e.g., Fourier transforms), one has to use integer multiples of the frame-time for the time-binning in order to avoid artefacts at the frame-frequency.

There might be new events during the readout process, especially if a very bright source is observed. This leads to an misidentification of the position, as the pixels might already have been shifted. The result is a streak in readout direction, as shown in Fig. 1.21. The (center of the) source itself appears to be very faint, but this is due to the rejection of piled events.

Pile-up occurs when two or more photons arrive at the same pixel in one frame time. Then, the photo-electrons produced by both events cannot be distinguished and are misinterpreted as one single event with higher energy (nearly the sum of the original events' energies). This leads to the rejection of events in the data-processing due to bad grades or the identification as higher order event, which both reduce the measured flux in the main (first order) spectrum.

One is therefore interested to have short frame times. In TE mode, it is not useful to use less than 3.2 s (the frame store readout time, see above). Another possibility is to use Continuous Clocking (CC) mode, where the columns are read out continuously, which means that no row coordinate Y can be assigned to an event. Each chip has now only a resolution of 1024×1 pixels, but the frame time is reduced to only 3 ms as well. Nevertheless, it is still necessary to separate counts from photon dispersed by the HE- or by the ME-Gratings, otherwise no flux calibration could be performed. To first order, this is no problem at all, as the dispersion is different (see Fig. 4.2) and the events can easily be distinguished by the internal energy resolution of the detector (Fig. 3.2). The fact that the MEG gratings have a 2:1 ratio of period and width assures that the second order MEG spectrum is suppressed and cannot be confused with the first order HEG spectrum, with which it overlaps.

1.4.5 The PCAD-system

As the ACIS detector has gaps between the chips of a width corresponding to 18 pixels, information would be lost, if a target would be focussed steadily. *Chandra*, however, dithers in a Lissajous-pattern (see Fig. 1.22) to spread the image over several detector pixels. This furthermore reduces the effect of bad pixels. As each single photon event is recorded with a time-stamp, the true image can easily be reconstructed by the post-observational data-processing (see Sect. 3.1.2). One just has to correct the effective area (used in the analysis) for the fact that there is less exposure in those parts of the image or spectrum resulting from

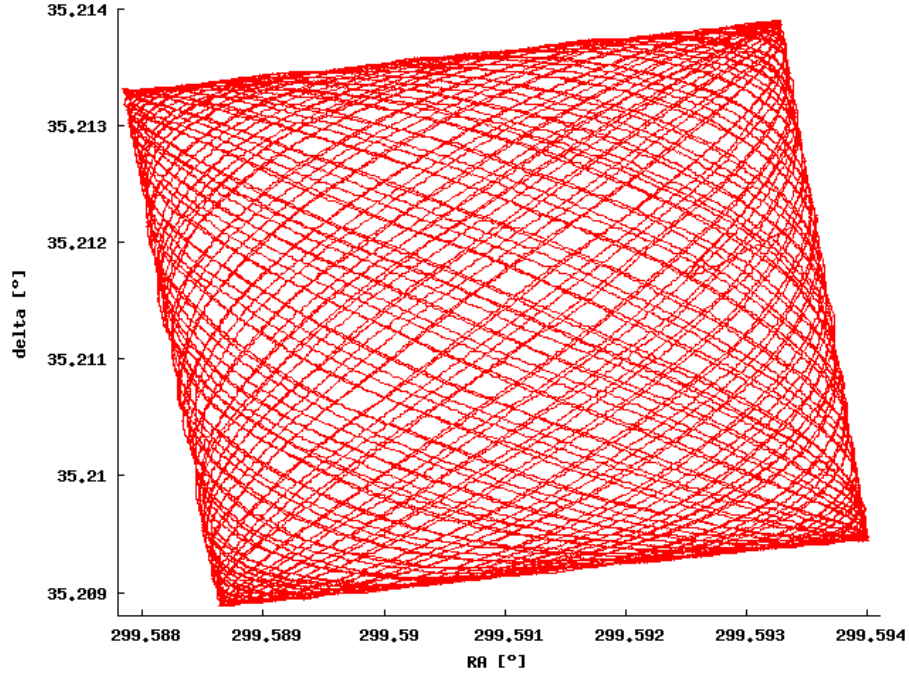


Figure 1.22: *Chandra*'s Lissajous dither pattern: time-evolution of the focused target-position.

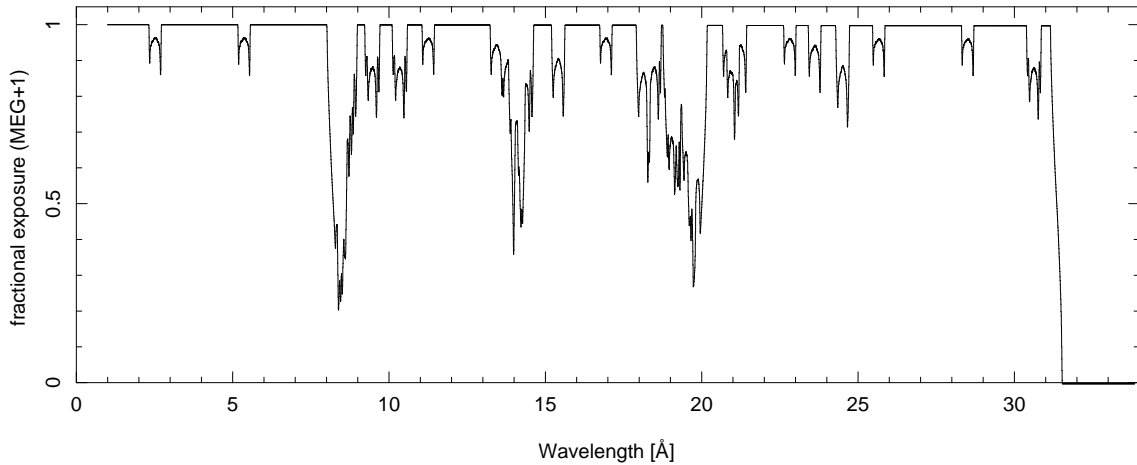


Figure 1.23: Fractional exposure of MEG+1 wavelength bins in a *Chandra* grating observation.

the pixels near the gaps or defect detector elements. Fig. 1.23 shows the fractional exposure in the MEG+1 wavelength bins (corresponding to the detector pixels). The chip gaps and bad pixels at λ_0 are smeared out over a range $\Delta\lambda$ with the following profile, which has the strongest effect at wavelengths λ at the dither's turning points, where $|\lambda - \lambda_0| = \Delta\lambda$:

$$\frac{1}{T} \int_0^T dt \delta(\lambda - [\lambda_0 + \Delta\lambda \cdot \cos(2\pi t/T)]) = \frac{1}{\pi \sqrt{1 - (\frac{\lambda - \lambda_0}{\Delta\lambda})^2}} \quad \text{for } |\lambda - \lambda_0| < \Delta\lambda \quad (1.27)$$

The effect of the dithering can also be seen quite nice in comparison of the (uncorrected) ‘detector image’ of an observation (Fig. 4.1) with the aspect-corrected ‘sky image’ (Fig. 4.2). There are some detector failures (several “hot columns” and two afterglow events), which are smeared in the corrected ‘sky-image’ and thus do not affect the analysis so strongly.

The dithering is achieved by the pointing control and aspect determination (PCAD) system. It carries both propulsion systems to orientate the *Chandra* observatory and detector instruments to measure the actual orientation precisely. The aspect camera array (ACA) including a 11.2 cm optical telescope and CCD-cameras with a 1.4 deg \times 1.4 deg field of view, and two inertial reference units (IRUs) with several gyroscopes serve for this latter purpose.

2 Spectral analysis

Everything that is known about stars, galaxies, black holes – and even the whole universe – is in the end inferred from the light we can collect from these sources. It is well known, that light consists of electromagnetic waves with different wavelengths λ and frequencies $\nu = c/\lambda$, and that the visible light only forms a very small part of the electromagnetic spectrum.

The spectrum

The basic quantity in astronomy is thus the spectrum S_λ , which gives the number of photons dN_{ph} which arrive per time dt , area dA and in a wavelength interval $[\lambda, \lambda + d\lambda]$. S is often equivalently expressed in terms of the frequency ν (\sim energy $E = h\nu$), which is related:

$$S_\lambda(\lambda) = \frac{dN_{\text{ph}}(\lambda)}{dt dA d\lambda} \Rightarrow S_\nu(\nu) = \frac{dN_{\text{ph}}(\nu)}{dt dA d\nu} = \left| \frac{d\lambda}{d\nu} \right| \cdot S_\lambda(\lambda(\nu)) = \frac{c}{\nu^2} \cdot S_\lambda(c/\nu) \quad (2.1)$$

Especially optical astronomers consider more often the energy flux spectrum $F_\nu(E) = \frac{dE(E)}{dt dA d\nu} = h\nu \cdot S_\nu(E/h)$, which is their basic observed quantity. (The difference of optical and X-ray CCDs was already mentioned in Sect. 1.4.4.) While the unit of $F_E(E)$ in X-ray astronomy is typically $\text{keV} (\text{s cm}^2 \text{keV})^{-1}$, radio astronomers use the unit Jansky for the energy flux $F_\nu(\nu) = \frac{dE(\nu)}{dt dA d\nu}$ per frequency interval $d\nu$: $1 \text{ Jy} = 10^{-26} \text{ W} (\text{m}^2 \text{Hz})^{-1}$.

The radiation field

While the spectrum S is the most convenient observational quantity for light, the basic quantity of the radiation field itself is the specific intensity, i.e., the energy dE_{ph} radiated per time dt , area dA , solid angle $d\Omega$ and in a frequency interval $[\nu, \nu + d\nu]$: $I_\nu = \frac{dE_{\text{ph}}}{dt dA d\Omega d\nu} = \frac{h\nu}{4\pi} S_\nu$. (The latter transformation holds for isotropic radiation.)

2.1 Absorption of light by atoms

It was stated in the introductory phrases that light brings information about the physical universe. This would not be true if there was no interaction of light with matter. But there are actually several ones: scattering, emission and absorption. The latter is the main topic of this section.

While a very comprehensible summary of radiative processes is given by Spitzer (1978, Chapter 3), a extremely detailed description can be found in Mihalas (1978, Chapter 4).

The transfer equation

The emissivity j_ν and the absorptivity κ_ν describe the specific energy transfer from matter to the radiation and vice versa. With the definitions of Eq. (2.2) (and $dV = dA \cdot ds$), the transfer equation for the change of the specific intensity I_ν with distance s is simply given as follows:

$$j_\nu = \frac{dE_{\text{em}}}{dt dV d\Omega d\nu}, \quad \kappa_\nu = \frac{1}{I_\nu} \frac{dE_{\text{abs}}}{dt dV d\Omega d\nu} \Rightarrow \frac{dI_\nu}{ds} = j_\nu - \kappa_\nu I_\nu \quad (2.2)$$

κ_ν can be expressed by the absorption cross section $\sigma(\nu)$ and the particle density n $\left[\frac{\text{atoms}}{\text{cm}^3} \right]$: $\kappa_\nu = \sigma(\nu) \cdot n$. For constant κ_ν along a path s , the optical depth $\tau_\nu = \int_0^s \kappa_\nu ds$, which measures the optical path backwards to the source ($d\tau_\nu = -\kappa_\nu ds$ and $\tau_\nu(\text{observer}) = 0$), is therefore $\tau_\nu = \kappa_\nu \cdot s = \sigma(\nu) \cdot N$, with the column density N , conventionally in units of atoms cm^{-2} .

For pure absorption ($j_\nu = 0$), the solution of the transfer equation 2.2 is just

$$I_\nu(\text{observer}) = I_\nu(\text{source}) \cdot e^{-\tau_\nu} = I_\nu(\text{source}) \cdot e^{-\sigma(\nu) \cdot N} \quad (2.3)$$

Photoabsorption processes

In contrast to light, atoms have discrete energy levels, which affect the interaction between light and matter, as far as inner-atomic transitions are involved: Bound-free transitions can only occur when the photon's energy is larger than the ionization threshold, leading to an edge in the spectrum (discussed in Sect. 2.1.1), and bound-bound transitions can even only be excited at sharp energies, which leads to discrete absorption or emission lines (Sections 2.1.4–2.1.5).

These spectral features can serve as a fingerprint for the involved atoms or ions, which allows the investigation of stellar atmospheres, stellar winds or the interstellar medium.

2.1.1 Photoionization: bound – free transitions

Photoionization is the reaction of a photon with a bound electron in an atom, which is released afterwards. As the energy levels of the free electron are not quantized any more, the interaction can take place with photons of any energy above ionization threshold E_{ion} . For $E > E_{\text{ion}}$, the photoionization cross section drops again quickly – approximately as $\sigma(E) \sim E^{-3}$ (see, for example, Wilms et al., 2000). This is sketched in Fig. 2.1. The strength of the photoabsorption is not only determined by the ionization cross section, but also by the column densities N_Z of the different atoms (Eq. 2.3). These are usually given as $N_Z = A_Z \cdot N_{\text{H}}$, with the equivalent hydrogen column density N_{H} and relative abundances A_Z . Table ?? on page ??, does not only list the edge energies, but also the abundances of the elements of astrophysical interest. The X-ray absorption in the interstellar medium was analyzed by Wilms et al. (2000) as well.

As a result, the strongest edge in an X-ray spectrum between 0.5 keV and 2 keV (corresponding to about 6...25 Å) results from the oxygen K-edge at $E = 0.53 \text{ keV} \equiv \lambda = 23.3 \text{ Å}$ (see Fig. 2.1). One can also recognize the iron L-edge at $E = 0.71 \text{ keV} \equiv \lambda = 17.5 \text{ Å}$ and the neon K-edge at $E = 0.87 \text{ keV} \equiv \lambda = 14.3 \text{ Å}$. Furthermore, there is the magnesium K-edge at $E = 1.31 \text{ keV} \equiv \lambda = 9.47 \text{ Å}$ and the silicon K-edge at $E = 1.85 \text{ keV} \equiv \lambda = 6.70 \text{ Å}$.

For detailed studies of the edge-structures of O, Ne and Fe, is given by Juett et al., 2004, 2006. The most recent modeling of the X-ray absorption by the interstellar medium (Wilms et al., 2006a) includes these features.

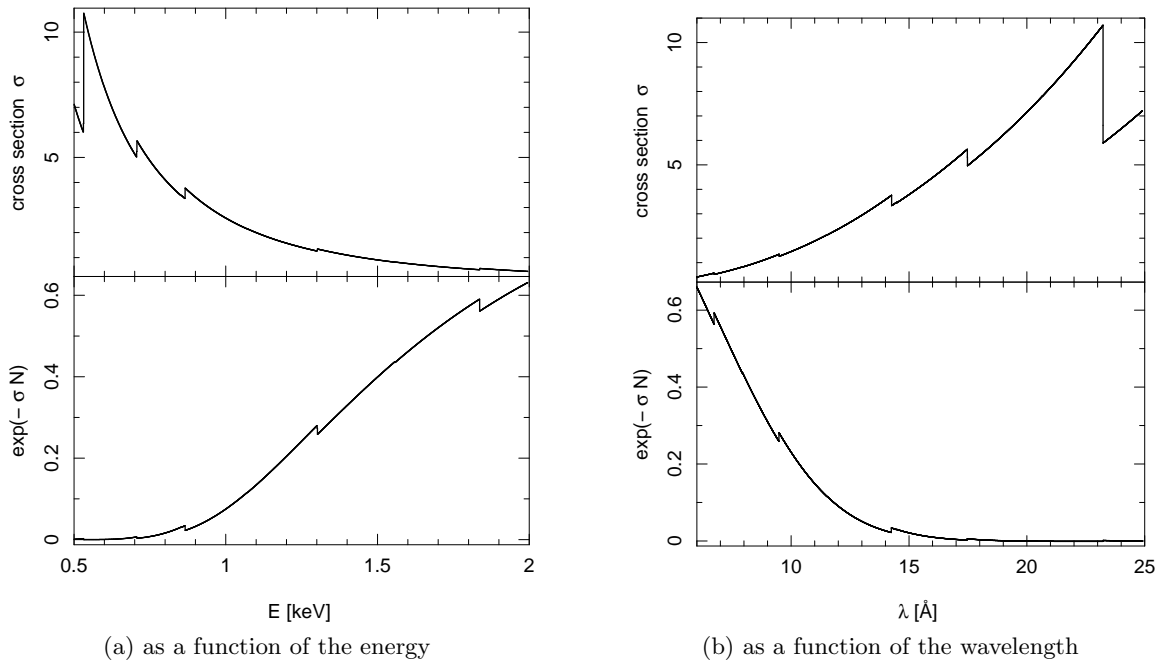


Figure 2.1: The photoionization cross section and the corresponding edges in the spectrum for a equivalent H-column density of 10^{22} cm^{-2} and typical composition.

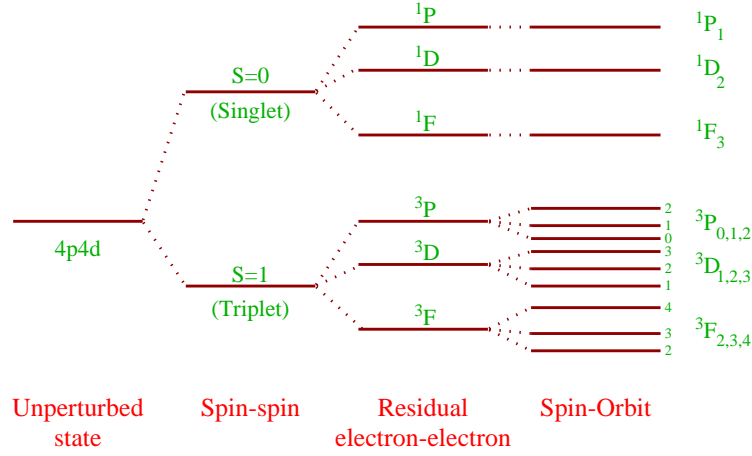


Figure 2.2: Breaking of the degeneracy of the energy levels in multi-electron systems. (from Rybicki & Lightman, 1979, Fig. 9.2a)

2.1.2 Atomic physics

Tables with transition wavelengths, mostly for the astrophysically relevant ions, are given in appendix ?? on page ?. They quote the atomic database ATOMDB from the Chandra X-ray Center,¹ which includes the Astrophysical Plasma Emission Database (APED) and output from the Astrophysical Plasma Emission Code (APEC), see also Smith et al. (2001). The ATOMDB² was used in large parts of this analysis.

The hydrogen atom and H-like ions

The discrete energy levels of the bound electron in a hydrogen atom (or a hydrogen-like ion with atomic number Z) are well known from quantum mechanics:

$$E_n = -\frac{(Z\alpha)^2 \cdot \mu c^2}{2 \cdot n^2} \approx -13.6 \text{ eV} \frac{Z^2}{n^2} \quad \text{with} \quad \alpha = \frac{e_{\text{SI}}^2}{4\pi\epsilon_0\hbar c}, \quad \mu = \frac{Zm_p + (A-Z)m_n}{Zm_p + (A-Z)m_n + m_e} \cdot m_e \quad (2.4)$$

($\alpha \approx 1/137$ is the electromagnetic fine-structure constant, expressed in SI-units with $e_{\text{SI}} = 1.6 \times 10^{-19} \text{ C}$. This is stated explicitly, as some formulas are quoted in the usual (historical) system of units, which uses $e^2 = e_{\text{SI}}^2 / (4\pi\epsilon_0)$. $\mu \approx m_e \approx 512 \text{ keV}/c^2$ is the electron's reduced mass and n is the principal quantum number.) There is a degeneracy of the angular momentum quantum number, as the energy level depends only on n . (It is finally broken by the hyperfine structure – resulting from the magnetic interaction of the nuclear and electron spin – and the Lamb shift, which is a result from the complete treatment in quantum electrodynamics.) The transition between those energy levels occurs thus at the energy differences $\Delta E_{ij} = E_i - E_j = h\nu_{ij}$. Table ?? lists the wavelengths of the transitions from the $n = 1$ ground state, which form the Lyman series. The Balmer series (Table ??) consists of the transitions from the first excited state $n = 2$.

Helium-like ions

He-like ions possess two electrons whose coupling (spin-spin, electron-electron and spin-orbit) breaks the degeneracy of the hydrogenic energy levels, see Fig. 2.2. In general, the spin-orbit coupled states are given in terms of $^{2S+1}[L]_J$, where S is the total spin, $[L]$ denotes the total orbital angular momentum L by its letter ($[L]=\text{'S'} \Rightarrow L=0$, $[L]=\text{'P'} \Rightarrow L=1$, $[L]=\text{'D'} \Rightarrow L=2$, ...) and J is the total angular momentum $L \oplus S$.

Two electrons with spin $s = 1/2$ can either couple to a total spin of $S = 0$ or $S = 1$. The singlet-states ($S = 0$) and the triplet states ($S = 1$) form – in first approximation – separate subsystems, as the usual electric dipole transitions cannot change the spin quantum

¹ The ATOMDB is available online at <http://cxc.harvard.edu/atomdb/>.

² At the time of this work, the ATOMDB was available in version 1.3.1.

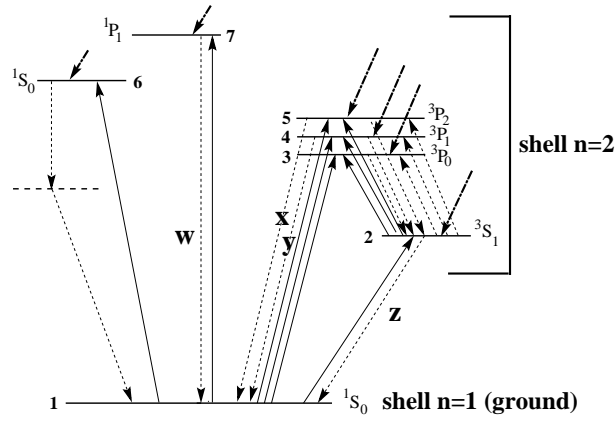


Figure 2.3: A simplified Grotrian diagram of He-like ions.
Dashed arrows denote radiative transitions, full arrows show collisional excitations.
(Porquet & Dubau, 2000, Fig. 1)

number S . (Transitions via other electromagnetic multipole radiation can, however, but their probability is much lower.) The three strongest lines, which occur at similar wavelengths, connect the ground states of those two subsystems, $1s^2$ (1S_0) and the meta-stable $1s2s$ (3S_1), with the corresponding first excitation in the $n = 2$ shell, namely $1s2p$, coupled as 1P or 3P , respectively (see also Fig. 2.3; Porquet & Dubau, 2000). Such a “He-like triplet” consists of

- the resonance (r) line, $1s^2$ (1S_0) \leftrightarrow $1s2p$ (1P_1),
which results from the usual dipole (also called w-) transition of the singlet-system,
- the intercombination (i) line, $1s^2$ (1S_0) \leftrightarrow $1s2p$ ($^3P_{1,2}$),
which comes from the unresolved x- and y-transitions (the magnetic quadrupole transition $^1S_0 \leftrightarrow ^3P_2$ contributes significantly for ions with charge ≥ 10 , Gabriel & Jordan, 1969) between the singlet’s ground state and the triplet’s first excited state,
- and the forbidden (f) line, $1s^2$ (1S_0) \leftrightarrow $1s2s$ (3S_1),
which arises from the magnetic dipole z-transition between the two ground states.

As there is no exact analytical solution for the quantum mechanical He-problem, the application of perturbation theory shows that the eigenstates of the many-body Hamiltonian are mixtures of singlet and triplet states (see, for example, Drake & Dalgarno, 1969; Laughlin, 1978). For this reason, intercombination transitions (e.g., $^3P_1 \rightarrow ^1S_0$), which are forbidden by standard dipole selection rules (given at the end of Sect. 2.1.3), become allowed. Their transition probability is, however, still smaller by ≈ 4 orders of magnitude.

It was first recognized by Gabriel & Jordan (1969) that He-like triplets can be used for the diagnostics of optically thin plasmas, where all three components of a triplet are emission lines, as the ratios of the line strengths r , i , f depend on the electron density and temperature: One usually defines (see, for example, Porquet et al., 2001, also for more details on the diagnostics)

$$R(n_e) = \frac{f}{i} \quad \text{and} \quad G(T_e) = \frac{f+i}{r} \quad (2.5)$$

It is already indicated by the notation that $R(n_e)$ depends on the plasma’s electron density, while $G(T_e)$ is sensitive to the electron temperature.

Plasmas with higher density become first optically thick ($\tau > 1$) in the resonance line which has a larger absorption cross section than the intercombination and particularly the forbidden line. Then, r turns into an absorption line, while i and f still remain emission lines.

The wavelengths of the He-like triplets and the transitions from the ground state are given in Tables ?? and ??.

Lithium-like ions

Being an alkali metal, Lithium has a single electron outside of a closed shell. The energy levels are thus similar to the hydrogenic ones, except for the fact that the electron-electron coupling lifts the degeneracy notably. Table ?? (listing the wavelengths of the transitions from the $[1s^2]2s$ ($^2S_{1/2}$) ground state) includes both the $^2P_{1/2}$ and the $^2P_{3/2}$ coupled state of $[1s^2]3p$, as the lines differ by 0.04 \AA in wavelength, which can be resolved in many cases.

Further iron ions

Being the final element of energy-gaining nucleosynthesis by fusion of lighter elements, iron has a relatively large abundance. Due to its large number of electrons, there are many strong transitions all over the X-ray spectrum, see Table ??.

The transitions from the singlet ground state of Fe XXIII, which consists of two closed s -shells ($[1s^2 2s^2] (^1S_0)$), are found relatively straight forward – one of the two $2s$ electrons will be excited into a np state ($n \geq 3$). Table ?? includes magnetic dipole transitions to triplets 3P_1 levels (after a spin flip) as well, as they may also be quite strong.

There are many transitions from the ground state of Fe XXII, which is $[1s^2 2s^2] 2p$. It is most probable that the lone $2p$ electron will be excited, as the s electrons are in closed s^2 shells. Dipole radiation can bring it either in a ns or a nd ($n \geq 3$) state. For the excitations of one of the $2s$ electrons to a $3p$ level, there are so many coupling-possibilities (resulting in many separate, but weak lines) that only the strongest transitions are included in Table ??.

The same holds for Fe XXI and its ground state $[1s^2 2s^2] 2p^2$: The strongest lines arise from $2p \rightarrow ns$ or nd ($n \geq 3$) transitions, see Table ??.

The strongest Fe XX lines – both according to the ATOMDB and the table of E1 transitions of Jonauskas et al. (2005) – are listed in Table ?. The last entry, at 8.82 \AA , stems from three blending lines, which are quite strong although they partly arise from transitions forbidden in the dipole approximation: $2s \rightarrow 5f$, $2s^2 \rightarrow 2p4d$ and $2s \rightarrow 5p$ (allowed).

The Tables ????-?? only list the strongest lines of Fe XIX–XVII. Transitions from the ground state of lower ionized iron $\leq \text{XVI}$ do not fall in the wavelength range below 25 \AA , as the $n \leq 2$ shells remain completely filled, namely, $[1s^2 2s^2 2p^6] \dots$.

2.1.3 Line strength of bound-bound transitions

At the end of the last section, different transition had been compared: there was talk of “the strongest lines”. According to Eq. (2.3), it is clear that the strength will both depend on the cross section and the number of atoms. Before these are discussed (in Sections 2.1.4 and 2.1.5), however, further quantities describing the ‘line-strength’, are introduced: The Einstein coefficients and the oscillator strength are directly related to quantum mechanical properties of the atomic transitions. Hilborn (2002) discusses different conventions of the definition of these parameters (and thus their relations) and points out common pitfalls.

Transitions between the atomic energy levels i and j (with populations N_i and N_j) involving the interaction with light can occur via the following three processes, whose rates are described by the Einstein (1917) coefficients A and B :

- Spontaneous emission of light from an excited state j

$$\left(\frac{dN_i}{dt}\right)_{\text{spont.}}^{j \rightarrow i} = -\left(\frac{dN_j}{dt}\right)_{\text{spont.}}^{j \rightarrow i} = N_j \cdot A_{ji} \quad (2.6)$$

- Stimulated emission of light from an excited state j by a photon with energy $h\nu_{ij}$

$$\left(\frac{dN_i}{dt}\right)_{\text{stim.}}^{j \rightarrow i} = -\left(\frac{dN_j}{dt}\right)_{\text{stim.}}^{j \rightarrow i} = N_j \cdot I_{\nu_{ij}} \cdot B_{ji} \quad (2.7)$$

- Stimulated absorption of light from a lower state i by a photon with energy $h\nu_{ij}$

$$\left(\frac{dN_j}{dt}\right)_{\text{stim.}}^{i \rightarrow j} = -\left(\frac{dN_i}{dt}\right)_{\text{stim.}}^{i \rightarrow j} = N_i \cdot I_{\nu_{ij}} \cdot B_{ij} \quad (2.8)$$

Stimulated absorption is in fact formally the same as stimulated emission with $i \leftrightarrow j$.

There are linear relations between the Einstein coefficients due to the principle of detailed balance; in a steady state, the net, i.e., $(i \rightarrow j) - (j \rightarrow i)$, transition rate must vanish:

$$N_j \cdot A_{ji} + N_j \cdot I_{\nu_{ij}} \cdot B_{ji} = N_i \cdot I_{\nu_{ij}} \cdot B_{ij} \quad (2.9)$$

In thermal equilibrium, the relative population N_j/N_i is given by Boltzmann statistics (g_i and g_j denote the multiplicities) and the intensity I_ν of the photon field by the Planck law:

$$\frac{N_j}{N_i} = \frac{g_j}{g_i} \exp\left(-\frac{h\nu_{ij}}{k_B T}\right), \quad I_\nu = \frac{8\pi h\nu^3}{c^3} \frac{1}{\exp\left(\frac{h\nu}{k_B T}\right) - 1} \quad (2.10)$$

This gives, together with Eq. (2.9), the desired Einstein relations:

$$A_{ji} = \frac{2h\nu_{ij}^3}{c^2} \cdot B_{ji} \quad \text{and} \quad g_i B_{ij} = g_j B_{ji} \quad (2.11)$$

In terms of these Einstein coefficients and the population densities $n_x = dN_x/dV$, the specific line emissivity and absorptivity (as defined in Eq. 2.2) read

$$j_\nu = h\nu_{ij} \cdot n_j \cdot A_{ji} \cdot \frac{1}{4\pi} \cdot \delta(\nu - \nu_{ij}) \quad \text{and} \quad \kappa_\nu = \frac{1}{I_\nu} \cdot \frac{h\nu_{ij} \cdot (n_j B_{ji} - n_i B_{ij})}{c} \cdot \delta(\nu - \nu_{ij}). \quad (2.12)$$

The classical damped oscillator and the quantum mechanical oscillator strength

Although emission or absorption (which are equivalent by detailed balance) of light are pure quantum processes, their classical analogue is considered first: The emission of light from an excited state in an atom is described in the classical picture by a harmonic oscillator with intrinsic frequency ω_0 and damping constant $\gamma_{cl} = 2e^2\omega_0^2/(3mc^3)$ (which will be shown below). The equation of motion for a driving electric field $E_0 \cos(\omega t)$ and its steady-state solution are

$$m\left(\ddot{x}(t) + \gamma_{cl} \dot{x}(t) + \omega_0^2 x(t)\right) = eE_0 \cos(\omega t) \quad \Rightarrow \quad x(t) = \Re e \left\{ \frac{e/m \cdot E_0}{\omega^2 - \omega_0^2 + i\gamma_{cl}\omega} e^{i\omega t} \right\}. \quad (2.13)$$

The damping force $F(t) = -m\gamma_{cl}\dot{x}(t)$ follows from energy-loss considerations: Larmor's formula gives the radiation power of an accelerated charge from classical electrodynamics: (Jackson, 1975, Eq. 14.22, for the electro-static unit system with $e^2 = \frac{e_{SI}^2}{4\pi\epsilon_0}$, also adopted here)

$$P_{cl}(t) = \frac{2e^2 \ddot{x}(t)^2}{3c^3} \quad (2.14)$$

Equating its time average with the mean of the energy loss by damping, $dE/dt = F \cdot v$,

$$\langle P_{cl} \rangle = \frac{2e^2 \omega^4 x_0^2}{3c^3} \cdot \langle \cos^2(\omega t) \rangle \stackrel{!}{=} m\gamma_{cl} x_0^2 \omega^2 \cdot \langle \cos^2(\omega t) \rangle = \langle F(t) \cdot \dot{x}(t) \rangle, \quad (2.15)$$

gives γ_{cl} (after substitution of ω by ω_0 , as the damping is most important near the resonance):

$$\gamma_{cl} = \frac{2e^2\omega_0^2}{3mc^3} \quad (2.16)$$

The emission oscillator strength f_{ji} is now per definition proportional to the A_{ji} :

$$f_{ji} := \frac{A_{ji}}{3\gamma_{cl}} = \frac{mc^3}{8\pi^2 e^2 \nu_{ij}^2} \cdot A_{ji} \quad (2.17)$$

This can be considered as an ‘‘effective number of classical oscillators’’: Absorption and emission oscillator strength, f_{ij} and f_{ji} , are related by the multiplicities $g_s = 2J_s + 1$ via

$$g_i f_{ij} = g_j f_{ji} =: ‘‘gf’’ , \quad (2.18)$$

such that an absorption oscillator strength $f_{ij} = 1$ for a transition from a state i with $J_i = 0$ to $J_j = 1$ means that A_{ji} equals the classical decay rate (damping constant) $\gamma_{cl} = |dE/dt|/E$.

Eqs. (2.17) and (2.18) give, with $e^2 = \frac{e_{SI}^2}{4\pi\epsilon_0} = 2.307 \times 10^{-28} \text{ J m}$ and $m = 9.11 \times 10^{-31} \text{ kg}$:

$$f_{ij} = \frac{g_j f_{ji}}{g_i} = \frac{mc}{8\pi^2 e^2} \cdot \lambda_{ij}^2 \cdot \frac{g_j}{g_i} A_{ji} = 1.4992 \times 10^{-16} \cdot \left(\frac{\lambda}{\text{\AA}}\right)^2 \cdot \frac{g_j}{g_i} \frac{A_{ji}}{\text{s}^{-1}} \quad (2.19)$$

Dipole approximation

Most radiative transitions are electric dipole transitions. The average radiation power of Eq. (2.15) can be expressed in terms of $\frac{e \cdot x_0}{2}$, which can be considered as mean dipole moment and is therefore replaced by the matrix element of the electric dipole operator $\hat{d} = e\hat{r}$ in the quantum mechanical description (Lang, 1999, Sect. 2.3). This gives an expression for A :

$$\langle P_{\text{cl}} \rangle = \frac{64\pi^4 \nu_{ij}^4}{3 c^3} \cdot \left(\frac{e x_0}{2}\right)^2 \stackrel{!}{=} h\nu_{ij} \cdot A_{ji} \Rightarrow A_{ji} = \frac{64\pi^4 \nu_{ij}^3}{3 h c^3} \cdot \left| \langle \psi_i | \hat{d} | \psi_j \rangle \right|^2 \quad (2.20)$$

These matrix elements vanish due to the symmetries of the wave functions $\psi_{m,n}$ unless the following so called ‘selection rules’ are fulfilled:

- total spin $\Delta S = 0$
- total orbital angular momentum $\Delta L \in \{0, \pm 1\}$
- orbital angular momentum of jumping electron $\Delta l \in \{\pm 1\}$
- total angular momentum $\Delta J \in \{0, \pm 1\}$, but no transitions from $J = 0$ to $J = 0$
- $\Delta M_J \in \{0, \pm 1\}$, but transitions from $M_J = 0$ to $M_J = 0$ are not allowed for $\Delta J = 0$

These lines are called allowed lines and have the largest transition probabilities. (There are also semi-forbidden and forbidden lines resulting from magnetic dipole and electric quadrupole transitions, which are subsequently suppressed by a factor of roughly 10^4 each.)

2.1.4 The cross section and its profile

This section deals with the cross section, which already has almost been derived, and its shape as a function of frequency.

If Eqs. (2.15) and (2.13) are combined, $\langle P_{\text{cl}} \rangle$ leads to the classical cross section:

$$\begin{aligned} \langle P_{\text{cl}} \rangle &= \frac{2 e^2}{3 c^3} \cdot \frac{\omega^4 (e/m)^2 E_0^2}{(\omega^2 - \omega_0^2)^2 + \gamma_{\text{cl}}^2 \omega^2} \cdot \frac{1}{2} =: \frac{c E_0^2}{8\pi} \cdot \sigma_{\text{cl}}(\omega) \\ \Rightarrow \sigma_{\text{cl}}(\omega) &= \frac{8\pi e^4 \omega^4}{3 m^2 c^4} \cdot \frac{1}{(\omega^2 - \omega_0^2)^2 + \gamma_{\text{cl}}^2 \omega^2} \stackrel{(\omega \approx \omega_0)}{\approx} \frac{\pi e^2}{m c} \cdot \frac{\gamma}{(\omega - \omega_0)^2 + (\gamma/2)^2} \end{aligned} \quad (2.21)$$

The second factor is, in usual frequency units $\nu = \frac{\omega}{2\pi}$, a normalized Lorentzian profile:³

$$\phi(\nu) = \frac{1}{\pi} \frac{\gamma/(4\pi)}{(\nu - \nu_0)^2 + [\gamma/(4\pi)]^2} \Rightarrow \int_{-\infty}^{\infty} d\nu \phi(\nu) = 1 \quad (2.22)$$

– with center ν_0 and full width at half maximum (FWHM) $\frac{\gamma}{2\pi}$, as $\phi(\nu_0 \pm \frac{\gamma}{4\pi}) = \frac{1}{2}\phi(\nu_0)$. The full quantum mechanical result is now parameterized in terms of the factors of Eq. (2.21) and the oscillator strength (either f_{ji} for emission or f_{ij} for absorption lines) from above:

$$\sigma(\nu) = f \cdot \frac{\pi e^2}{m c} \cdot \phi(\nu) \quad (2.23)$$

The Lorentzian profile from the description of excited states

The same line profile follows from the quantum mechanical description of an excited state, whose detection probability decays with the rate Γ , which consists in principle both of the Einstein coefficient A and an inverse mean free time between scatterings (leading to the pressure broadening of lines), implying the following time development of the wave function:

$$P(t) = \psi^*(0) \psi(0) e^{-\Gamma t} \Rightarrow \psi(t) = \psi(0) \cdot e^{-(i\omega_0 + \frac{\Gamma}{2})t} \quad (2.24)$$

³ Though stated differently in some textbooks, σ cannot be composed in (total cross section) \times (normalized profile), as the profile is not a dimensionless quantity (see, e.g., Eq. 2.22). The ‘total cross section’ would therefore not even have the dimension of a cross section and would depend on the chosen variable ($\omega, \nu, E, \lambda, \dots$).

The energy distribution amplitude is given by the Fourier transform of the time evolution:

$$\tilde{\psi}(\omega) = \int dt e^{i\omega t} \psi(t) \sim \int_0^\infty dt e^{(i(\omega_0 - \omega) - \frac{\Gamma}{2})t} = - \left[i(\omega - \omega_0) - \frac{\Gamma}{2} \right]^{-1} \quad (2.25)$$

As the corresponding probability is the modulus squared amplitude, $|\tilde{\psi}(\omega)|^2$, the line profile of Eq. (2.22) is also obtained from this consideration.

Doppler broadening – the Voigt profile

There are now several effects influencing the actual line profile. In this work, only the Doppler broadening will be discussed. The complete theory of line formation in stellar atmospheres is explained in detail in the book of Mihalas (1978, chapters 8 & 9).

In a thermal stellar atmosphere, the atoms move with (random) velocities ξ along the line of sight and notice Doppler shifted frequencies $(1 - \xi/c) \nu$ in their frame. The (one dimensional) Maxwellian probability distribution for a velocity component in the range $(\xi, \xi + d\xi)$ is

$$W(\xi) d\xi = \frac{1}{\sqrt{\pi}\xi_0} \exp\left(-\frac{\xi^2}{\xi_0^2}\right) d\xi, \quad \text{where } \xi_0 = \sqrt{\frac{2k_B T}{m}}. \quad (2.26)$$

Therefore, the combined line profile is given by the following convolution integral

$$\phi_{\text{tot}}(\nu) = \int \phi\left(\left(1 - \frac{\xi}{c}\right)\nu\right) W(\xi) d\xi =: \frac{1}{\sqrt{\pi}\Delta\nu_D} H\left(\frac{\Gamma}{4\pi\Delta\nu_D}, \frac{\nu - \nu_0}{\Delta\nu_D}\right) \quad (2.27)$$

for $\nu \approx \nu_0$. The Doppler width is $\Delta\nu_D = \frac{\xi_0}{c}\nu_0$, and the Voigt function H is defined as

$$H(a, v) := \frac{a}{\pi} \int_{-\infty}^{\infty} \frac{e^{-y^2} dy}{(v - y)^2 + a^2} = \Re\{w(v + ia)\} \quad (2.28)$$

The latter relation (Abramowitz & Stegun, 1972, Eq. 7.4.13) to the Faddeeva function $w(z) = e^{-z^2} \cdot \text{erfc}(-iz)$ is sometimes used for the numerical computation of the Voigt-function H .⁴ There is also an analytical approximation of H for the case $a \ll 1$ of astrophysical interest, which is derived in many textbooks, e.g., that of Mihalas (1978, p. 280):

$$H(a, v) \approx \begin{cases} e^{-v^2}, & \text{for } |v| \ll 1 \\ \frac{a}{\sqrt{\pi}v^2}, & \text{for } |v| \gg 1 \end{cases} \quad \text{for } a \ll 1 \quad (2.29)$$

These approximations uncover exactly the limiting cases of a Doppler-broadened Gaussian in the core and the damping Lorentzian at the wings of the normalized absorption profile:

$$\phi_{\text{tot}}(\nu) \approx \begin{cases} \frac{1}{\sqrt{\pi}\Delta\nu_D} \exp\left(-\left(\frac{\nu - \nu_0}{\Delta\nu_D}\right)^2\right), & \text{for } |\nu - \nu_0| \ll \Delta\nu_D \\ \frac{1}{\pi} \frac{\Gamma/(4\pi)}{(\nu - \nu_0)^2 + [\Gamma/(4\pi)]^2}, & \text{for } |\nu - \nu_0| \gg \Delta\nu_D \end{cases} \quad (2.30)$$

$\int \phi_{\text{tot}}(\nu) d\nu = 1$ holds true in any case, as ϕ_{tot} is the convolution of normalized functions.

2.1.5 The curve of growth

As already stated at the beginning of Sect. 2.1.3, finally only the dependence on the number of absorbing atoms remains to be discussed. This is now the aim of this section.

The simple (but comprehensible and quite accurate) approximations of the curve of growth in the next section follows the script of Dr. Lea, San Francisco State University, US (online at <http://www.physics.sfsu.edu/~lea/courses/grad/cog.PDF>). Though not used in this work, but anyway interesting – hints on the numerical integration of the curve of growth are given in Chapter 11 of the script on stellar atmospheres by Dr. Tatum, University of Victoria, Canada (available online at <http://orca.phys.uvic.ca/~tatum/stellatm.html>).

⁴ In ISIS (Sect. 3.2), the Voigt profile is computed from numerical code for the Faddeeva function.

The equivalent width is a measure for the total amount of energy removed from the continuum in an absorption line, which is easily accessible in observations – even if the exact line profile cannot be detected. If F_c and F_l denote the flux in the continuum and respectively in the line, the relative line depth $A(\nu)$, and the equivalent width W_ν , is defined as follows:

$$A(\nu) := \frac{F_{\nu,c}(\nu) - F_{\nu,l}(\nu)}{F_{\nu,c}(\nu)} = \frac{h\nu \cdot [S_{\nu,c}(\nu) - S_{\nu,l}(\nu)]}{h\nu \cdot S_{\nu,c}(\nu)} \Rightarrow W_\nu := \int A(\nu) d\nu \quad (2.31)$$

A similar definition exists for wavelength-spectra, namely $W_\lambda := \int \frac{F_{\lambda,c}(\lambda) - F_{\lambda,l}(\lambda)}{F_{\lambda,c}(\lambda)} d\lambda$, but both equivalent widths are related via

$$\frac{W_\nu}{\nu_0} = \frac{W_\lambda}{\lambda_0}, \quad \text{due to} \quad F_\nu |d\nu| = F_\lambda |d\lambda| \quad \text{and} \quad \left| \frac{d\lambda}{d\nu} \right| = \frac{\lambda}{\nu}. \quad (2.32)$$

The equivalent width has its name from the fact that W_X equals the line width $\int_{W_X} 1 dX$ of a rectangular line profile with $F_l = 0$ inside the line and $F_l = F_c$ outside of it. As a note, one should be careful as the convention that $W > 0$ for an emission line and $W < 0$ for an absorption line is often used as well. This would require to replace A by $-A$ in Eq. (2.31).

The curve of growth gives the dependence of a line's equivalent width on the number of absorbing atoms. Curves of growth in stellar atmospheres would require the full treatment of line formation (including the transfer equation for radiation through the atmosphere in local thermal equilibrium (LTE), the Milne-Eddington approximation for pure absorption lines without scattering contribution – which all is even just an early approach to the problem). This is beyond the scope of this work, but excellently described in the book of [Mihalas \(1978\)](#).

If the emissivity is negligible, however, the solution of the transfer equation (2.2) reduces to the simple absorption according to the optical depth (Eq. 2.3):

$$F_{\nu,l}(\nu) = e^{-\tau(\nu)} \cdot F_{\nu,c}(\nu) \quad \text{with} \quad \tau(\nu) = N_i \cdot \sigma(\nu) = N_i \cdot f_{ij} \cdot \frac{\pi e^2}{m c} \cdot \phi(\nu) \quad (2.33)$$

To obtain W_ν , the integration of Eqs. (2.33) and (2.31) with the general profile ϕ_{tot} (Eq. 2.27) cannot be performed analytically, but in three regions, specific approximations are reasonable:

- The linear part of the curve of growth

If few atoms absorb, $\tau \ll 1$, mainly the Doppler core of the line contributes to the equivalent width. The approximation $A(\nu) \approx \tau(\nu)$ gives the following simple result, where W is proportional to the absorbing column density N_i and independent of $\Delta\nu_D$:

$$(W_\nu)_{\text{lin}} \approx \int \tau(\nu) d\nu = N_i \cdot f_{ij} \cdot \frac{\pi e^2}{m c} \cdot \int \phi(\nu) d\nu = N_i \cdot f_{ij} \cdot \frac{\pi e^2}{m c} \quad (2.34)$$

- The flat saturation part of the curve of growth

If $\tau(\nu_0) \gtrsim 1$, but $\tau(\nu) \ll 1$ for $|\nu - \nu_0| > \Delta\nu_D$ (i.e., if the core saturates, but the line wings do not yet contribute), the core can still be described by $H(a, v) \approx e^{-v^2}$. The equivalent width is approximately $(W_\nu)_{\text{flat}} \approx 2 \cdot |\nu_1 - \nu_0|$, where $\tau(\nu_1) = \frac{(W_\nu)_{\text{lin}}}{\sqrt{\pi} \Delta\nu_D} \exp\left(-\left(\frac{\nu_1 - \nu_0}{\Delta\nu_D}\right)^2\right) \stackrel{!}{=} 1$:

$$(W_\nu)_{\text{flat}} \approx 2 \Delta\nu_D \sqrt{\ln\left(\frac{N_i f_{ij} \sqrt{\pi} e^2}{m c \Delta\nu_D}\right)} \quad (2.35)$$

As simple series expansion of $A(\nu) = 1 - e^{-\tau(\nu)}$, instead of this rough estimate, gives

$$(W_\nu)_{\text{flat}} = -\sqrt{\pi} \Delta\nu_D \cdot \sum_{n=1}^{\infty} \left(\frac{-(W_\nu)_{\text{lin}}}{\sqrt{\pi} \Delta\nu_D}\right)^n \cdot \underbrace{\int_{-\infty}^{\infty} \frac{\exp\left(-n\left(\frac{\nu - \nu_0}{\Delta\nu_D}\right)^2\right)}{\sqrt{\pi} \Delta\nu_D} d\nu}_{= 1/\sqrt{n}}, \quad (2.36)$$

which is a divergent series, the approximation (2.35) is thus indeed useful.

As a result, the dependence of $W_\nu \sim \sqrt{\ln N_i}$ on N_i in the saturation part is rather weak.

- The square-root part of the curve of growth

If there are enough absorbing atoms that the line wings contribute to the equivalent width, the approximation above can be repeated, but now with the Lorentzian profile:

$$\tau(\nu_1) = \frac{(W_\nu)_{\text{lin}}}{\pi} \frac{\Gamma/(4\pi)}{(\nu_1 - \nu_0)^2} \stackrel{!}{=} 1 \Rightarrow (W_\nu)_{\text{sqrt}} \approx 2 \cdot |\nu_1 - \nu_0| = \sqrt{\frac{N_i f_{ij} e^2 \Gamma}{\pi m c}} \quad (2.37)$$

Another, better, approximation for W_ν is obtained by directly integrating Eq. (2.33) with $\phi(\nu) = \frac{1}{\pi} \frac{\Gamma/(4\pi)}{(\nu - \nu_0)^2}$: (despite $\tau(\nu_0) \sim \phi(\nu_0) = \infty$, the profile $e^{-\tau(\nu)}$ remains finite)

$$(W_\nu)_{\text{sqrt}} \approx 2 \cdot \int_{\nu_0}^{\infty} \left[1 - \exp\left(-N_i f_{ij} \frac{\pi e^2}{m c} \frac{1}{\pi} \frac{\Gamma/(4\pi)}{(\nu - \nu_0)^2}\right) \right] d\nu = \sqrt{\frac{N_i f_{ij} e^2 \Gamma}{m c}} \quad (2.38)$$

For this calculation, the following integral was used:

$$\int_0^{\infty} \left[1 - \exp\left(-\frac{a^2}{x^2}\right) \right] dx = \left[x \cdot \left(1 - \exp\left(-\frac{a^2}{x^2}\right) \right) - 2a \cdot \int_0^{a/x} e^{-t^2} dt \right]_{x=0+}^{x=\infty} = \sqrt{\pi} \cdot a \quad (2.39)$$

W_ν is finally again independent of $\Delta\nu_D$, but grows now only with the square-root of N_i .

Inserting numerical values (noticing that $e^2 = e_{\text{SI}}^2/(4\pi\epsilon_0)$, i.e., $\frac{\pi e^2}{m c} = 2.6466 \times 10^{-6} \text{ m}^2 \text{ s}^{-1}$), one obtains for the linear (Eq. 2.34), flat (Eq. 2.35) and square-root part (Eq. 2.38):

$$\frac{W_\lambda}{\lambda_0} = \frac{W_\nu}{\nu_0} = \begin{cases} 8.828 \times 10^{-5} \cdot \frac{N_i \cdot f_{ij}}{10^{16} \text{ cm}^{-2}} \cdot \frac{\lambda_0}{\text{\AA}} & \text{(lin)} \\ 6.67 \times 10^{-6} \cdot \frac{v_{\text{therm}}}{\text{km s}^{-1}} \cdot \sqrt{\ln\left(14.93 \cdot \frac{N_i \cdot f_{ij}}{10^{16} \text{ cm}^{-2}} \cdot \frac{\lambda_0}{\text{\AA}} \cdot \left[\frac{v_{\text{therm}}}{\text{km s}^{-1}}\right]^{-1}\right)} & \text{(flat)} \\ 3.061 \times 10^{-6} \cdot \sqrt{\frac{N_i \cdot f_{ij}}{10^{16} \text{ cm}^{-2}} \cdot \frac{\Gamma}{10^{12} \text{ s}^{-1}}} \cdot \frac{\lambda_0}{\text{\AA}} & \text{(sqrt)} \end{cases} \quad (2.40)$$

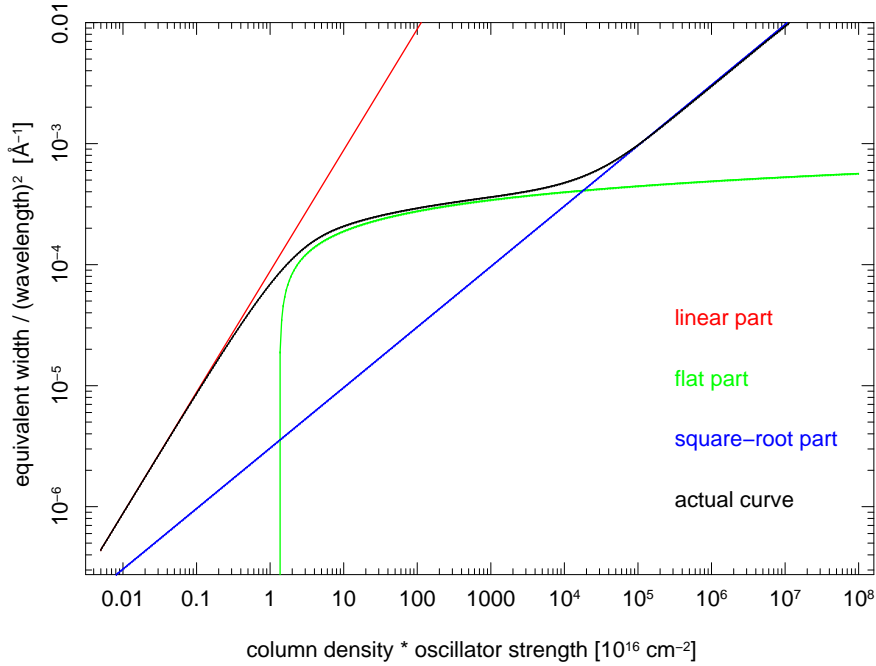


Figure 2.4: A curve of growth in the form W_λ/λ^2 vs. $N_i f_{ij}$. In this curve, the linear part is universal and the square-root part only scales with Γ . (Here, the parameters $\lambda = 5 \text{ \AA}$, $v_{\text{therm}} = 100 \text{ km s}^{-1}$ and $\Gamma = 10^{12} \text{ s}^{-1}$ were used.)

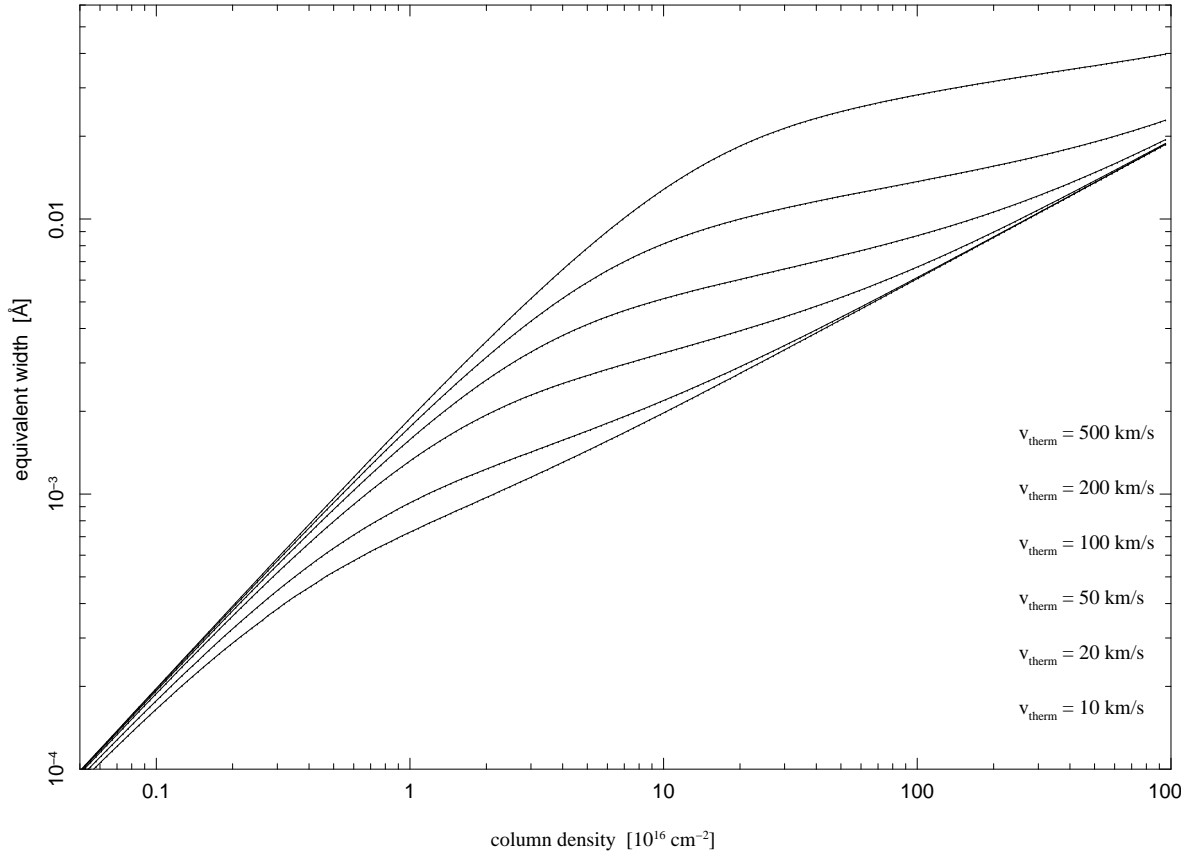


Figure 2.5: Curves of growth for S XVI Ly α in the form W_λ vs. $N_{\text{S XVI}}$. (Here, the parameters $\lambda_0 = 4.73 \text{ \AA}$ and $\Gamma = 8.3 \times 10^{13} \text{ s}^{-1}$ were used.)

As long as a line is on the flat part of the curve of growth, its ion's column density can be directly inferred from its equivalent width: Combining Eq. (2.40)_{lin} with Eq. (2.19), gives

$$N_i = 7.56 \times 10^{20} \text{ cm}^{-2} \cdot \left(\frac{(W_\lambda)_{\text{lin}}}{\text{m\AA}} \right) \cdot \left(\frac{\lambda_0}{\text{\AA}} \right)^{-4} \cdot \left(\frac{g_j}{g_i} \frac{A_{ji}}{10^{12} \text{ s}^{-1}} \right)^{-1}. \quad (2.41)$$

This result is also found in many textbooks, e.g., that of Spitzer (1978, p. 52).

In general, however, the complete curve of growth has to be considered. While some textbooks explain this rather theoretically than practically orientated, Kotani et al. (2000), for example, shows a worked example with all the required details in a comprehensive way.

For a single transition, the major uncertainty usually lies in the Doppler broadening. As an example, Fig. 2.5 shows the direct dependence of W_λ on N_i for the Ly α transition of S XVI at $\lambda_0 = 4.73 \text{ \AA}$ with $\Gamma = A = 8.3 \times 10^{13} \text{ s}^{-1}$ (and therefore $f = 0.28$, Eq. 2.19) for different values of v_{therm} . Unless the Doppler broadening can be constrained by other means, the column density may be uncertain by more than one order of magnitude if the line is saturated.

2.2 Analysis of X-ray spectra

2.2.1 Formalism

In the X-ray regime, the flux spectrum cannot be measured directly, which is in contrast to optical astronomy, where the resolution of the instrument is believed to be only a minor problem – although it has to be taken into account for a proper analysis. This is due to the different properties of X-rays especially what concerns their detection:

Redistribution of photon energies and detection efficiency

The detection of an X-ray photon generally gives the pulse height amplitude of the voltage signal from the read out charge of the photo-electrons. This PHA is binned by the pulse height analyzer into discrete channels, i.e., only the number of pulse heights in certain intervals are counted and finally transmitted from the satellite. As every detector has only a finite resolution, $\sigma \sim \sqrt{E}$, as the number of photo-electrons $N \sim E$ is Poisson distributed with $\sigma_N = \sqrt{N}$, a photon with energy E cannot always produce a signal corresponding to exactly this energy in the detector. The probability for detection in the discretized energy bin $B_i = [E'_i, E'_{i+1}]$ is described by the redistribution matrix function (RMF) $R(i, E)$. If one would measure energies E' continuously⁵ with redistribution function $\tilde{R}(E', E)$, the RMF would be $R(i, E) = \int_{E'_i}^{E'_{i+1}} dE' \tilde{R}(E', E)$. But one uses energy bins to achieve higher count rates (i.e., better signals) and to reduce telemetry data. $\tilde{R}(E', E)$ is roughly a Gaussian with center $E' = E$ and a width corresponding to the energy resolution of the detector. But there are also other effects which have to be considered, especially the fluorescent photon escape phenomenon: A photon with sufficient energy may also ionize an electron from an inner shell of an atom of the detector material. Although the recombination produces again photons, which could in principle ionize other atoms and contribute photo-electrons (which are finally read out) as well, it is more probable that these characteristic photons escape because the photoabsorption cross-section is lowest at and immediately below the absorption edges (Dolan, 1972). Therefore, $\tilde{R}(E', E)$ has also escape peaks at $E - E' = h\nu_{K\alpha}$ or $h\nu_{K\beta}$ or probably even $h\nu_{L\alpha}$ or $h\nu_{L\beta}$. Furthermore, there might be nonlinearities which finally make $R(i, E)$ a rather complicated function! Fig. 2.6 shows an example for a response matrix function.

⁵ In principle, the detection is anyway a discrete quantum process leading to a finite resolution, but the binning is usually much larger than this resolution.

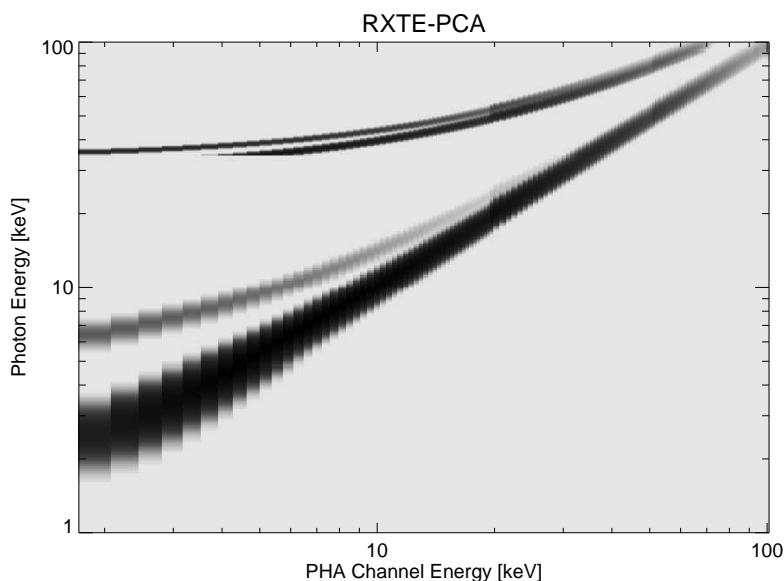


Figure 2.6: The response matrix of the xenon-gas Proportional Counter Array on *RXTE*.
 $R(i, E) \equiv R(\text{channel}, \text{photon energy})$ (from Wilms, 1998, Fig. 4.4)

The effective area of the detector is strongly energy dependent as well: The ancillary response function (ARF) $A(E)$ also includes the effective area of the mirror, the quantum efficiency of the detector, contamination effects, exposure effects due to dithering of the satellite and chip gaps (...).

The product $R(i, E) \cdot A(E)$ tells how many counts are detected in energy bin B_i resulting per unit incident photon flux at energy E . This is called response function (RSP) of the detector. RMFs and ARFs can be generated by software tools from the corresponding satellite's calibration teams. In the case of *Chandra*, these are included in the calibration database CALDB from the *Chandra* X-ray center, CXC.

After an exposure time t_{exp} , the number of counts $C(i)$ in a detector bin i is now given, including the background signal $B(i)$, by the following (see also [Arnaud et al., 2007](#)):

$$C(i) = B(i) + t_{\text{exp}} \cdot \int dE K(R(i, E), A(E), S_E(E)) \quad (2.42)$$

$K(R, A, S)$ is a kernel, that convolves RMF, ARF and the source spectrum $S_E(E)$,

$$\text{e.g., } K(R(i, E), A(E), S_E(E)) = R(i, E) \cdot A(E) \cdot S_E(E) , \quad (2.43)$$

i.e., forms just the product in the simplest case. See Sect. 3.2.2 for more complicated kernels.

Grating observations

Although energies can be detected much more accurately in a grating observation (via the position of an event in the dispersed spectrum, Eq. 1.26), the same formalism of RMF and ARF is also used in this case. Then, the RMF describes the probability that a photon is dispersed in a certain order (cf. order-sorting in Sect. 3.1.2). For *Chandra* observations, there are again CXC-tools to generate grating RMFs (gRMFs) and grating ARFs (gARFs).

2.2.2 Spectral fitting and χ^2 statistics

Equation (2.42) cannot successfully be solved for $S_E(E)$, as the redistribution matrix is almost singular ([Dolan, 1972](#)). One therefore uses model spectra, $M(E)$, determines the resulting count rates $C_M(i) = t_{\text{exp}} \cdot \int dE K(R(i, E), A(E), M(E))$ (forward-folding) and compares $C_M(i)$ to the detected count rate $C_0(i) = C(i) - B(i)$.

For an objective ‘comparison’, a quantitative measure for the goodness of the model is needed, which is often called a cost function. For this purpose, χ^2 is commonly used: χ^2 is the sum over all bins of the squared deviation of C_M and C_0 in terms of specific error σ ,

$$\chi^2 = \sum_i \left(\frac{C_0(i) - C_M(i)}{\sigma(i)} \right)^2 \quad (2.44)$$

The error σ is mostly assumed to be $\sqrt{C+B}$, in the Gaussian limit of Poisson statistics.⁶ It can be useful not to derive σ from the detected counts (which are actually measured, without any error), but from the mean counts predicted by the model: $\sigma(i) = \sqrt{C_M(i)}$.

The model usually contains several parameters. These are determined in the fitting procedure such that χ^2 is minimized. The final measure for the goodness of the fit is then the reduced χ^2 , which is $\chi_{\text{red}}^2 = \chi^2/\nu$, where the number of degrees of freedom ν is the difference of the number of considered bins i and the number of fit parameters. For a good fit, $\chi_{\text{red}}^2 \approx 1$, as every measured data point $C_0(i)$ should scatter on average within the statistical fluctuation $\sigma(i)$ around the “true” value $C_M(i)$, thus $\langle |C_0(i) - C_M(i)| \rangle \approx \sigma(i)$ and $\chi^2 \approx \nu$ (cf. Eq. 2.48). A ‘better’ χ_{red}^2 is usually a sign that one has overestimated the errors $\sigma(i)$.

Though not used in this work, it is noted that another standard cost function is the C-statistics of [Cash \(1979\)](#), which is directly derived from the Poisson distribution.

⁶ This may require the rebinning of the data to ≥ 20 counts/bin, to ensure that the Gaussian distribution can be applied. Otherwise, the proper statistics for the low counts limit has to be applied, see [Gehrels \(1986\)](#).

The χ^2 distribution

One can investigate how the values of χ^2 are distributed assuming that all data points $C_0(i)$ are normal distributed with mean $C_M(i)$ and standard deviation $\sigma(i)$, i.e., that each $Z_i := \frac{C_0(i) - C_M(i)}{\sigma(i)}$ is normal distributed with mean 0 and standard deviation 1:

$$f_i(z_i) dz_i := P(z_i \leq Z_i < z_i + dz_i) = \frac{1}{\sqrt{2\pi}} \exp\left(-\frac{z_i^2}{2}\right) dz_i \quad (2.45)$$

As $\chi^2 = \sum_i Z_i^2$, the probability distribution for the whole set \vec{Z} of the ν values Z_i is thus

$$f_{\vec{z}}(\vec{z}) d^\nu \vec{z} = \prod_i f_i(z_i) dz_i = (2\pi)^{-\nu/2} \exp\left(-\frac{\chi^2}{2}\right) d^\nu \vec{z} . \quad (2.46)$$

The distribution $f_{\chi^2}^\nu(\chi^2) d(\chi^2) := f_{\vec{z}}(\vec{z}) d^\nu \vec{z}$ follows now simply from the volume element $d^\nu \vec{z} = \frac{2\pi^{\nu/2}}{\Gamma(\nu/2)} |\vec{z}|^{\nu-1} d|\vec{z}|$ and $|\vec{z}| = \sqrt{\chi^2}$: (The cases $\nu = 1, 2$ and 3 are shown in Fig. 2.7.)

$$f_{\chi^2}^\nu(\chi^2) d(\chi^2) = (2\pi)^{-\nu/2} \exp\left(-\frac{\chi^2}{2}\right) \frac{2\pi^{\nu/2}}{\Gamma(\nu/2)} (\chi^2)^{\frac{\nu-1}{2}} \frac{d(\chi^2)}{2\sqrt{\chi^2}} = \frac{(\chi^2)^{\frac{\nu-2}{2}} \exp(-\frac{\chi^2}{2})}{2^{\nu/2} \Gamma(\nu/2)} \quad (2.47)$$

With the definition of the Γ -function, one can easily show that the mean of a $f_{\chi^2}^\nu$ -distributed χ^2 is just ν , i.e., that $\langle \chi_{\text{red}}^2 \rangle = 1$ holds exactly, as already expected above:

$$\Gamma(x) = \int_0^\infty t^{x-1} \exp(-t) dt \quad \Rightarrow \quad \langle \chi^2 \rangle = \int_0^\infty f_{\chi^2}^\nu(\chi^2) \chi^2 d(\chi^2) = \nu \quad (2.48)$$

The probability that χ^2 takes a value larger than X^2 , is given by the cumulative probability,

$$F_{\chi^2}^\nu(X^2) := \int_{X^2}^\infty f_{\chi^2}^\nu(\chi^2) d(\chi^2) . \quad (2.49)$$

For $\nu = 1, 2, 3$, it is shown in Fig. 2.8. Explicit formulae for $\nu = 1, 2$ are also listed in Table 2.1.

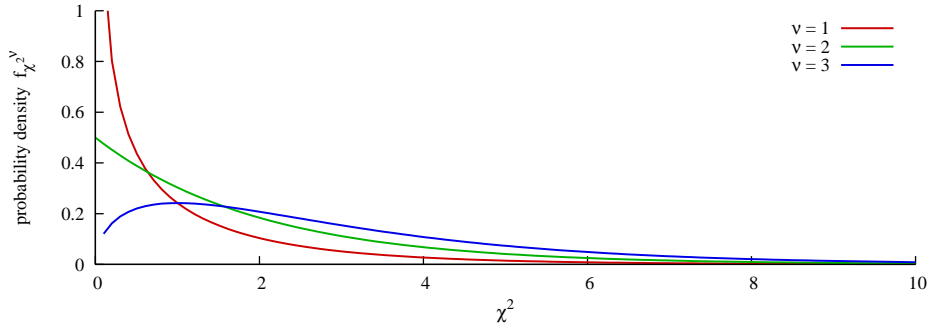


Figure 2.7: The probability density function $f_{\chi^2}^\nu$ of the χ^2 -distribution with $\nu = 1, 2, 3$ d. o. f..

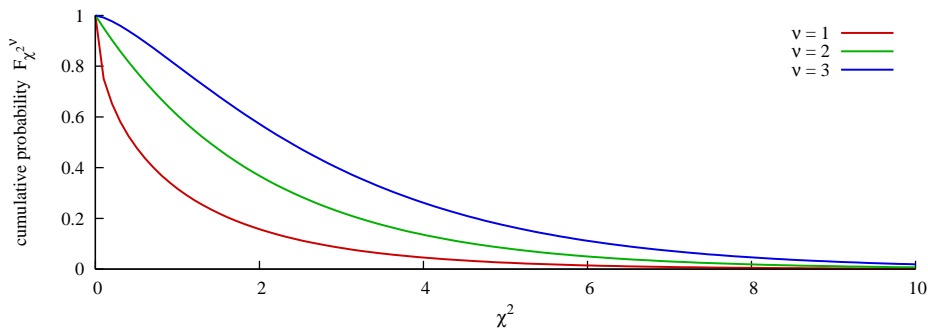


Figure 2.8: The cumulative probability $F_{\chi^2}^\nu$ of the χ^2 -distribution with $\nu = 1, 2, 3$ d. o. f..

Table 2.1: Explicit functions of $F_{\chi^2}^\nu(\chi^2)$ and confidence-level defining values of $\Delta(\chi^2)$ for $\nu = 1$ and $\nu = 2$ degrees of freedom

$$\begin{aligned} \nu = 1 &\Rightarrow F_{\chi^2}^1(\chi^2) = \frac{2}{\sqrt{\pi}} \int_{\sqrt{\frac{\chi^2}{2}}}^{\infty} \exp(-t^2) dt = 1 - \operatorname{erf}\left(\sqrt{\frac{\chi^2}{2}}\right) \\ \nu = 2 &\Rightarrow F_{\chi^2}^2(\chi^2) = \exp\left(-\frac{\chi^2}{2}\right) \end{aligned}$$

confidence level	$\Delta(\chi^2)_{\max}^{\nu=1}$	$\Delta(\chi^2)_{\max}^{\nu=2}$	$\Rightarrow F_{\chi^2}^\nu(\Delta(\chi^2)_{\max}^\nu)$ for $\nu = 1, 2$
1σ (68.269% CL)	1.000000	2.295749	0.31731
90% CL	2.705543	4.605170	0.1
99% CL	6.634897	9.210340	0.01

Confidence intervals of fit parameters

Functions obeying χ^2 -statistics are additive: If a function with m parameters is fitted to a set of N data points, such that the corresponding χ^2 -statistic $\chi^2(m)$ has $N - m$ degrees of freedom, and another function with $m + 1$ parameters leads to the statistic $\chi^2(m + 1)$ with $N - m - 1$ degrees of freedom, the difference $\Delta(\chi^2) = \chi^2(m) - \chi^2(m + 1)$ is again distributed according to a χ^2 -statistic, namely with 1 degree of freedom (Bevington & Robinson, 1992).

The $\Delta(\chi^2)(a)$ obtained by varying one fit parameter a , while re-fitting all the others, is distributed with the probability density function $f_{\chi^2}^1$. The restriction $\Delta(\chi^2)(a) < \Delta(\chi^2)_{\max}$ defines thus an interval $[a_-, a_+]$, whose confidence level (CL) is given by $1 - F_{\chi^2}^1(\Delta(\chi^2)_{\max})$ (c.f. Table 2.1 for typical CLs), e.g., the 90% CL is obtained from $\Delta(\chi^2)(a) \leq 2.7055$.

Further discussion can be found in the paper of Lampton et al. (1976).

An example. The example in Fig. 2.9 shows the χ^2 contours of two strongly coupled parameters c_3 and β_3 (cf. Sect. 4.2.2 for their actual meaning, which is, however, not important for what is discussed here). The confidence interval of c_3 must not be determined by simply varying c_3 and keeping the others fixed (see gray line from the minimum of χ^2 parallel to

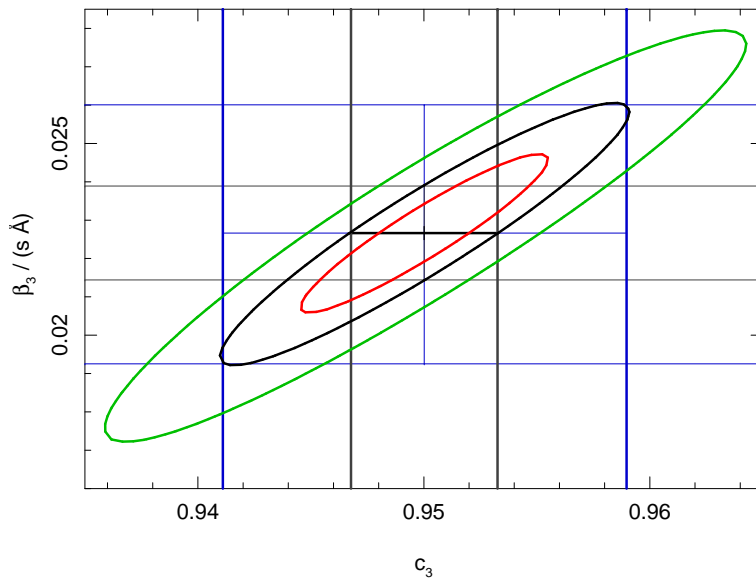


Figure 2.9: χ^2 contours for *single* parameter confidence levels.

Red: $\Delta(\chi^2) = 1$ (68.3% CL), black: $\Delta(\chi^2) = 2.71$ (90% CL), green: $\Delta(\chi^2) = 6.63$ (99% CL). The proper confidence interval for c_3 must not be determined by holding β_3 fixed (gray lines), but it has to be optimized as well (leading to the larger blue interval).

the c_3 -axis), but the optimal value of β_3 (and also all other parameters, which are not shown in this projection onto the c_3 - β_3 plane) has also to be determined in each step. The correct procedure gives the (larger) blue intervals with the result $c_3 = 0.9500^{+0.0090}_{-0.0089}$ on the 90% CL. In the same way, $\beta_3 = (0.0227^{+0.0033}_{-0.0034}) \text{ s} \cdot \text{\AA}$ is found.

Note that these are single parameter confidence intervals; the probability that both parameters are coincident in the quoted range is however less than 90%. If one was interested in this probability, one would have to use the $\Delta(\chi^2)$ threshold for $\nu = 2$ degrees of freedom, i.e., $\Delta(\chi^2)_{\max} = 4.605170$ (cf. Table 2.1).

Finding the minimum of the χ^2 function

The fitting of nonlinear functions requires a general algorithm to find the (absolute) minimum of a (complex) quadratic function (Eq. 2.44) $\chi^2 \equiv f(a_1, a_2, \dots, a_n)$ of many parameters a_i . There are two very basic methods, the gradient-search and the parabolic expansion, whose sophisticated combination results in the standard Marquardt-algorithm.

The gradient $\vec{\nabla} f = \left(\frac{\partial f}{\partial a_1}, \frac{\partial f}{\partial a_2}, \dots, \frac{\partial f}{\partial a_n} \right)$ points locally towards f 's steepest increase, as

$$f(\vec{a} + \Delta\vec{a}) = f(\vec{a}) + \vec{\nabla} f \cdot \Delta\vec{a} + \text{O}(\Delta a^2) = \max. \quad \text{for } \Delta\vec{a} \parallel \vec{\nabla} f \quad (2.50)$$

from Taylor expansion. The gradient-search method evaluates the gradient numerically $\left(\frac{\partial f}{\partial a_i} \approx \frac{f(a_1, \dots, a_i + \Delta a_i, \dots, a_n) - f(\vec{a})}{\Delta a_i} \right)$ and moves through the parameter space along $-\vec{\nabla} f$. If this could be done in a infinitely smooth way, one would certainly reach a local minimum of f . Besides the problem probably not to have found the global minimum, there are furthermore numerical instabilities, as $\vec{\nabla} f = \vec{0}$ at the minimum.

In the neighborhood of a minimum of f at \vec{a} , the parabolic expansion

$$f(\vec{a} + \Delta\vec{a}) \approx f(\vec{a}) + \sum_i \frac{\partial f}{\partial a_i} \Delta a_i + \frac{1}{2} \sum_{i,j} \frac{\partial^2 f}{\partial a_i \partial a_j} \Delta a_i \Delta a_j \quad (2.51)$$

may be a valuable approximation. Its variation $\delta/\delta(\Delta a_i)$ gives a set of linear equations

$$0 \approx 0 + \frac{\partial f}{\partial a_i} + \sum_j \frac{\partial^2 f}{\partial a_i \partial a_j} \Delta a_j, \quad (2.52)$$

which can be solved with the inverse of the curvature matrix:

$$\Delta\vec{a} = - \left(\frac{\partial^2 f}{\partial a_i \partial a_j} \right)_{i,j}^{-1} \cdot \vec{\nabla} f. \quad (2.53)$$

Computing the second derivatives and the inversion of a matrix gives the iteration $\vec{a} + \Delta\vec{a} \mapsto \vec{a}$.

The gradient-search method is efficient far away from the minimum, while the expansion method only works close to it. The Marquardt algorithm (Marquardt, 1963; Bevington & Robinson, 1992; Press et al., 1992, Ch. 15.5) provides a procedure to interpolate between these two methods by iterating

$$\Delta\vec{a} = - \left(\frac{\partial^2 f}{\partial a_i \partial a_j} \cdot (1 + \lambda \cdot \delta_{i,j}) \right)_{i,j}^{-1} \cdot \vec{\nabla} f, \quad (2.54)$$

where λ is adjusted according to the local success of minimizing f : Starting with a large λ , the matrix is dominated by its diagonal elements, and the algorithm is similar to the gradient-search. (The curvature factors take account for the fact that the gradient does not direct to the minimum, if the latter is very asymmetric.) Afterwards, with reduced λ , the parabolic expansion method is recovered.

Of course, this is just a basic guideline on fitting routines. There are several very subtle methods, e.g., the Nelder-Mead simplex algorithm (Nelder & Mead, 1965) or a variant, the subplex algorithm (Rowan, 1990).⁷

⁷The subplex algorithm can also be used in ISIS (see Sec. 3.2).

3 Data reduction and analysis software

What has been discussed in the previous chapters is consequently implemented by software tools. The reduction of *Chandra*'s raw data (a file of all X-ray events recorded by the detector) is performed with CIAO (Sect. 3.1). Finally, ISIS is used for spectral analysis (Sect. 3.2).

3.1 Reduction of *Chandra*/HETGS data with CIAO

Although some details in this chapter are also valid for *Chandra* LETGS (or even imaging) observations, most issues are specific for *Chandra* grating observations with the HETGS.

3.1.1 Data files

Primary and secondary data products from Standard Data Processing (SDP) can be downloaded from the the *Chandra* X-ray Center via the *CHandra* Archive SEArch and Retrieval interface *chaser*.¹ Their detailed structure is listed in appendix ??, page ??.

- The level 1-event file `...evt1.fits` contains a list of all X-ray events that have been registered by the detector and were not internally rejected. Each dataset includes basically a time-stamp, the ID of the activated chip and the position on it, the calculated position on the sky (which has been reconstructed from the aspect information of the PCAD system on the dithering of the satellite, see Sect. 1.4.5) and the photon energy internally determined by the CCD-detector. Table ?? gives a detailed listing.
- The aspect/PCAD file `pcad...fits` lists the time-evolution of the whole satellite's orientation, especially the focused target position (see Table ?? and cf. Fig. 1.22).
- The parameter-block file `...pbk0.fits` lists the active CCDs and how they were read out (see Table ??).
- bias files (see Table ??)
- The filter file `...flt1.fits` (see Table ??) contains the good time intervals of the observation.
- The mask file `...msk1.fits` tells if any masks were applied, i.e., if only events from a certain (spatial or energetic) window have been telemetered (see Table ??).
- The bad pixel file `...bpix1.fits` contains a list of bad pixels for an observation (see Table ??).

3.1.2 Data reprocessing

As the standard data processing (SDP) is done automatically, the high-level data products (i.e., spectra) are often not reliable (especially when the target position could not be determined properly, as the source has been blocked) or they are too general. One also wants to apply the most recent calibration files, which are in continuous development. The low-level data has therefore to be reprocessed manually making use of the *Chandra* Interactive Analysis of Observations software package CIAO (Fruscione et al., 2006),² following the analysis thread "Obtain Grating Spectra from HETG/ACIS-S Data".³

If the data was processed with a software version < DS 7.4.0, `acis_detect_afterglow` has been applied to the level 1-event file by SDP, a tool to identify residual charges from cosmic rays in CCD pixels. The relevant events are marked via their status flag (see Table ??). It is recommended to remove this identification (with the tool `dmtcalc`) and use the newer

¹ <http://cda.harvard.edu:9011/chaser/>

² For this work, CIAO 3.3 and CALDB 2.5 were used.

³ http://cxc.harvard.edu/ciao/threads/spectra_hetgacis/

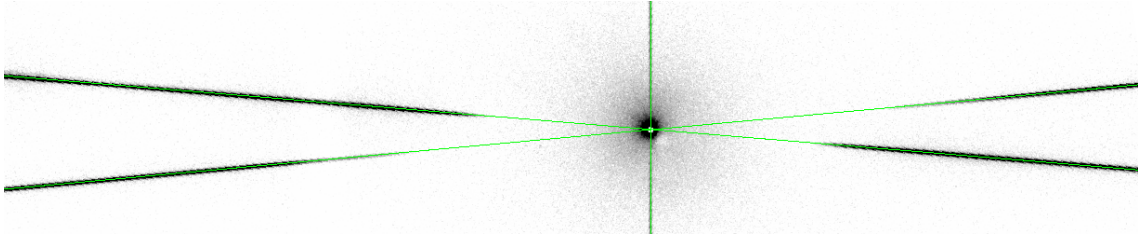


Figure 3.1: Finding the zero-order position with HEG and MEG arm and readout streak. In this observation (Sect. 4.1.1), the point source is surrounded by a scattering halo.

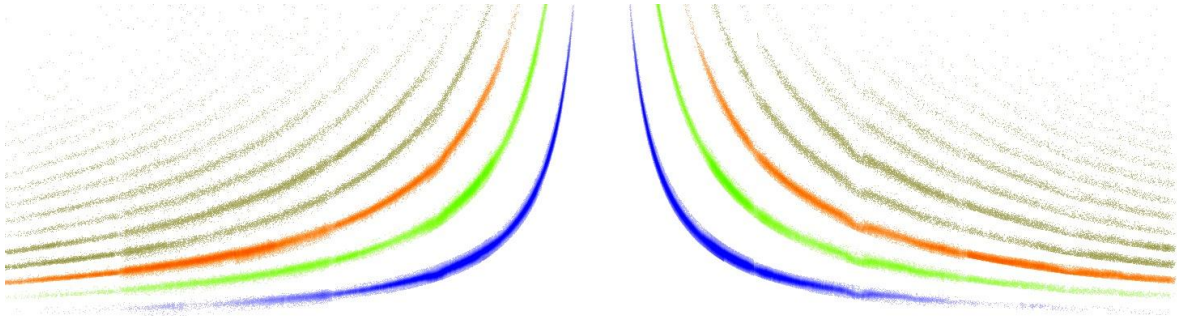


Figure 3.2: Order sorting in a plot of energy vs. position along the MEG-arm.

tool `acis_run_hotpix` (which marks afterglow-events in the bad pixel file) instead, as this produces less miss-identifications.

The tool `acis_process_events` is used to recompute the values of the detector (TDET, DET) and sky (SKY) coordinates, the energy values (ENERGY, PI), the GRADE and STATUS flags with the information from the bad pixel file. The grade is determined by the number and position of neighboring CCD pixels that contained charges at the same time. The status flag marks if the event is considered to result from a cosmic ray's afterglow.

The first crucial point in a grating observation is to determine the position of the zero-order image of the target, as this affects the wavelength calibration essentially. The tool `tgdetect` is used for this job, but there can be several problems causing `tgdetect` to fail: 1. The zero-order image of a bright source might have been blocked by a filter in order to avoid telemetry saturation. 2. The center of the zero-order image might show less events due to pile-up. 3. The observation might be in CC-mode.

Problems 1 and 2 can be solved by fitting lines to the HEG and MEG arm, which cross the readout streak (as in Fig. 1.21) and each other at the zero-order position of the source (see Fig. 3.1) There is an ISIS-script of Ishibashi (2006) for this job. Problem 3 is hard to be solved generally, it often needs many manual tries. (The goodness of the zero-order-position can be checked by comparing + and - orders of the same final spectrum.)

CIAO's `tg_create_mask` creates the extraction regions for HEG and MEG events based on the previously determined zero-order position. Afterwards, `tg_resolve_events` assigns grating orders and wavelengths to the events, which are stored in a new level 1.5-event file (for detailed structure see Table ??). From the grating equation $p \cdot \sin \theta = m \cdot \lambda$ follows that an event on a certain position of the detector (determined by $\sin \theta$) could result from a first-order diffracted photon with wavelength λ_1 as well as from a higher order ($|m| > 1$) spectrum's wavelength $\lambda_1/|m|$. As these photons differ in energy, the different orders can be discriminated by the internal energy information of the detector (see Sect. 1.4.4) – which is quite rough, but sufficient for this purpose (see Fig. 3.2). The order mapping is controlled by the order sorting and integrated probability (OSIP) file, which is part of the calibration database CALDB. But one can also apply a custom OSIP file. Only those events which have a good grade (i.e., there are no simultaneous events in neighboring pixels), do not result from bad pixels (see `acis_process_events`), and which are in good time intervals marked by the filter file (see Table ??) are copied to the level-2 event file by using the tool `dmcopy`.

At last, one can apply the `destreak`-tool, which is meant to remove events (wrongly) resulting from charge loss along a detector row while the readout process. These events produce a weak ‘readout streak’ similar to the strong readout streak from the zero-order image (Fig. 1.21). `destreak` looks for coincidences of events in adjacent pixels along a row.

3.1.3 Extraction of light curves

One can now extract light curves from the final level-2 event file `...evt2.fits`. The powerful tool `dmextract` allows similar selection filters as `dmcopy`, but does not produce a list of events but a table of count rates in user-defined bins. For the current issue, one is interested to bin for time-intervals. With the selection filters, one could for example restrict the events to a certain energy band. The additional option `ltc1` is especially useful for the extraction of light curves. The detailed data structure of a light curve file is listed in Table ??.

One might want to apply temporal filters to the level-2 event file, e.g., if the light curves or hardness (ratio of count rates in different energy bands) curves indicate a certain behavior of the source, such as outbursts or absorption dips, whose spectrum should probably be excluded or also be analyzed exclusively. This can be done with the tool `dmcopy`, just as the observational good time intervals have been applied at the end of Sect. 3.1.2.

3.1.4 Extraction of spectra

One starts in any case with a level-2 event file, from which the spectrum can be extracted with the tool `tgextract`. This produces a so called PHA2 file, which contains 12 tables with the spectra of the HEG and the MEG in $\pm 1^{\text{st}}$, $\pm 2^{\text{nd}}$ and $\pm 3^{\text{rd}}$ order each. The spectra contain the number of counts (which also determines the error from the Poisson distribution) and the count rate in wavelength bins of 2.5 mÅ width in case of the HEG and 5 mÅ for the MEG. There is also a number of background counts (see Table ??), that may be extracted to a separate file by the tool `tg_bkg` in order to be subtracted in the latter analysis.

As mentioned in Sect. 2.2.1, RMFs and ARFs are essential for the analysis of X-ray spectra. For grating observations, RMFs are generated by the tool `mkgrmf` and grating ARFs are generated by the CIAO script `fullgarf`, which essentially calls the tool `mkgarf`. The contents of the resulting files are shown in Table ?? and Table ??.

3.2 Spectral analysis with ISIS

The spectral analysis in this work is done with the Interactive Spectral Interpretation System ISIS⁴ (Houck & Denicola, 2000), which has been developed by the MIT Center for Space Research. The lead scientist and software engineer John C. Houck describes ISIS in his manual (Houck, 2006) as follows:

ISIS is intended to support the analysis of high resolution X-ray spectra by combining in one package tools to query a database of atomic data [...] with tools to manipulate and measure high resolution spectral data. [...] ISIS is also programmable and extensible [...]. S-Lang, the interpreted language which provides these features, also provides IDL-like array-based mathematical functions which greatly simplify common analysis operations.

3.2.1 General overview

The “flux-corrected spectrum”

Although it was stated in Sect. 2.2.1, that it is in general not possible to derive the flux spectrum directly from the detected count rates

$$C(i) = B(i) + t_{\text{exp}} \cdot \int dE K(R(i, E), A(E), S_E(E)) , \quad (2.42)$$

⁴ This work started with ISIS version 1.4.2, but further development lead to v. 1.4.7.

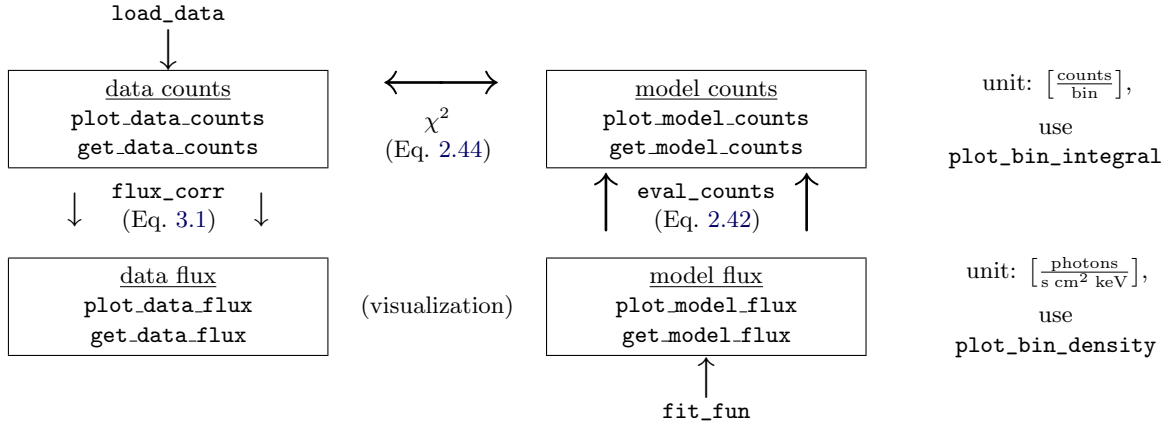


Figure 3.3: The main data structures for spectral analysis in ISIS and their interactions.

ISIS provides the possibility to calculate a “flux-corrected spectrum”

$$\tilde{S}_E(i) = \frac{C(i) - B(i)}{t_{\text{exp}} \cdot \int_{E_i}^{E_{i+1}} dE K(R(i, E), A(E), 1)}, \quad (3.1)$$

which would give the actual flux $S_E(E)$, if $\tilde{R}(E', E)$ was a δ -function, provided K is the standard product-kernel. \tilde{S}_E often produces useful results and may be used for visualizations, but is never used for any analysis. The advantage of this approach is that it describes “unfolded spectra” in a model-independent manner. For a brief discussion, see, for example, Nowak et al. (2005).

Data and model in counts- and flux-space

Using the results of the data reduction (Sect. 3.1.4), the spectra are read from the PHA2-file via `load_data`, the ARFs via `load_arf` and the RMFs via `load_rmf`.⁵ The background count rates (which are also loaded by `load_data`, but have to be scaled to the same collecting area⁶ and exposure time⁷) are subtracted from the signal, and the error is corrected according to propagation of Poisson-errors (in the Gaussian limit):

$$C_0 = C - B \Rightarrow \sigma_{C_0} = \sqrt{\sigma_C^2 + \sigma_B^2} = \sqrt{C + B} \quad (3.2)$$

The command `set_fit_statistic(chisqr;sigma=model)`; causes the errors σ for the χ^2 statistic (Eq. 2.44) to be calculated rather from the model than from the data counts.

After the ARFs and RMFs are assigned to the corresponding spectra via `assign_arf` and `assign_rmf`, one usually does not have to care about them any more. The whole complex count rate \leftrightarrow flux conversion (described in Section 2.2.1, Eq. 2.42) is now done by ISIS.

While the primary observed quantity are the number of counts, any model is defined via `fit_fun` as a function for the flux spectrum. The “flux-corrected spectrum” (3.1) has to be calculated explicitly via the function `flux_corr`, and the model has to be evaluated in counts space via `eval_counts` as well. This is sketched schematically in Fig. 3.3.

Fit functions for the definition of flux-models

All computations are carried out on a discrete grid of bins $B_i = [\lambda_i, \lambda_{i+1}]$. (ISIS generally uses wavelength-grids, but they can easily be converted into energy-grids $[E_i, E_{i+1}]$, of course.) Composed models are still first evaluated on the grid, before the operations are performed.

⁵ If one needs to assure, that the RMF is normalized as described in Sect. 2.2.1, one should apply `factor_rsp` to split additional factors off the RMF, which should rather be multiplied to the ARF, before assigning them.

⁶ The scale is given by $\frac{\text{BACKSCAL}}{\text{BACKSCUP} + \text{BACKSCDN}}$ with the keyword values additionally stored in the PHA2-file.

⁷ For *Chandra* grating observations, the background is determined directly during the observation and has thus the same exposure time.

It is thus essentially important to distinguish bin-integrated models on the one hand from models independent of the bin-size on the other hand, because ISIS does not check internally if a model is additive or multiplicative. For example, if the model $f = f_1 \cdot f_2 + f_3$ is composed from the models f_1 , f_2 and f_3 , all except of exactly one of f_1 , f_2 have to be bin-integrated. Assuming that f_2 is not bin-integrated, but rather evaluated at the bin-center or, even better, bin-averaged, the “correct” (though still approximative) result in a bin B_i will be obtained:

$$\begin{aligned} \tilde{f}(B_i) &= \int_{\lambda_i}^{\lambda_{i+1}} d\lambda \left(f_1(\lambda) \cdot f_2(\lambda) + f_3(\lambda) \right) \stackrel{!}{\approx} \tilde{f}_1(B_i) \cdot \tilde{f}_2(B_i) + \tilde{f}_3(B_i) \\ &= \left(\int_{\lambda_i}^{\lambda_{i+1}} d\lambda f_1(\lambda) \right) \cdot \left\{ \begin{array}{c} f_2\left(\frac{\lambda_i + \lambda_{i+1}}{2}\right) \\ \langle f_2(\lambda) \rangle_{[\lambda_i, \lambda_{i+1}]} \end{array} \right\} + \left(\int_{\lambda_i}^{\lambda_{i+1}} d\lambda f_3(\lambda) \right) \end{aligned} \quad (3.3)$$

It would neither make sense to multiply two bin-integrated quantities, as in general

$$\int_{\lambda_i}^{\lambda_{i+1}} d\lambda \left(f_1(\lambda) \cdot f_2(\lambda) \right) \neq \left(\int_{\lambda_i}^{\lambda_{i+1}} d\lambda f_1(\lambda) \right) \cdot \left(\int_{\lambda_i}^{\lambda_{i+1}} d\lambda f_2(\lambda) \right), \quad (3.4)$$

nor to add models of different type (i.e., bin-integrated ones with bin-averaged ones).

The ISIS-command `list_functions` lists all fit functions. (One might have to run `require("xspec")`; before the dynamically linked local models are shown.) In this section, only the most important models, which are also used in this work, will be described:

- **powerlaw** (with the fit parameters `norm` $\equiv S_E(1 \text{ keV})$ and `PhoIndex` $\equiv \Gamma$)

describes a power law spectrum $f(E) = S_E(1 \text{ keV}) \cdot \left(\frac{E}{1 \text{ keV}}\right)^{-\Gamma}$.

It is evaluated as bin-integrated quantity, i.e., $\tilde{f}(B_i) = \int_{E_i}^{E_{i+1}} f(E) dE$.

- **phabs** (with the single fit parameter `nH` $\equiv N_H$)

describes the photoelectric absorption $f(E) = \exp(-\sum_Z \sigma_Z(E) \cdot A_Z \cdot N_H)$ (cf. Eq. 2.3) for fixed elemental abundances A_Z and cross sections $\sigma_Z(E)$. This model is not evaluated bin-integrated, as **phabs** is thought to be a multiplicative model.

- **gauss** (with the fit parameters `area` $\equiv W$, `center` $\equiv \lambda_0$ and `sigma` $\equiv \sigma$)

describes a bin-integrated Gaussian in wavelength space,

$$f(\lambda) = W/(\sigma\sqrt{2\pi}) \cdot \exp\left(-\frac{(\lambda - \lambda_0)^2}{2\sigma^2}\right). \quad (3.5)$$

The width is parameterized by σ . The full width at half maximum (FWHM) is

$$\text{FWHM} = 2\sqrt{2 \ln 2} \sigma \approx 2.355 \sigma. \quad (3.6)$$

- **constant** (with the single fit parameter `factor` $\equiv c$)

describes (indeed) a multiplicative (not bin-integrated) constant $\tilde{f} \equiv f \equiv c$.

- **bin_width** (with no fit parameters at all)

returns the width of the wavelength bins $\tilde{f}(B_i) = \lambda_{i+1} - \lambda_i$.

Another work, performed by a guided trainee (quoted in Sect. 4.2.2), uses two further models:

- **bknpower** (with parameters `Norm`, `PhoIndx1` $\equiv \Gamma_1$, `BreakE` $\equiv E_{\text{break}}$ and `PhoIndx2` $\equiv \Gamma_2$) describes a bin-integrated continuous broken power law spectrum $f(E) \sim E^{-\Gamma(E)}$ with `Norm` = $f(1\text{keV})$ and

$$\Gamma(E) = \begin{cases} \Gamma_1 & \text{for } E \leq E_{\text{break}} \\ \Gamma_2 & \text{for } E \geq E_{\text{break}} \end{cases}. \quad (3.7)$$

- `highcut` (with the fit parameters `cutoffE` $\equiv E_{\text{cut}}$ and `foldE` $\equiv E_{\text{fold}}$) is a (multiplicative) high-energy cutoff above E_{cut} with folding energy E_{fold} :

$$f(E) = \begin{cases} 1 & \text{for } E \leq E_{\text{cut}} \\ \exp\left(-\frac{E-E_{\text{cut}}}{E_{\text{fold}}}\right) & \text{for } E \geq E_{\text{cut}} \end{cases} \quad (3.8)$$

The whole model is defined with the command `fit_fun("fit-function");`, where *fit-function* is an expression that may be formed from the models. There may be several independent instances of a model with separate parameters each, which are however shared by all datasets, e.g., `fit_fun("gauss(1)+gauss(2)+gauss(3)");`. There is also the possibility to use `Isis_Active_Dataset` as identifier, which means that every dataset is used with its own parameters. (The parameters of the corresponding model's first instance are used for dataset # 1, the second instance for dataset # 2, and so on.)

It is possible to provide user-defined fit-functions for the model spectra. Examples are given in the next sections.

Fitting of spectral models

One can fit for the parameters of a model defined by `fit_fun`. If not all parameters are allowed to vary, one has to `freeze` the others. (Afterwards, they can be `thawed` again.) The fitting is started with the command `fit_counts`. Unless changed by `set_fit_method`, the Marquardt-algorithm (Eq. 2.54, Sect. 2.2.2) is used. It was found that `set_fit_method("subplex");` is more appropriate (though rather slow) if the fitting routine is stuck in a very flat relative minimum of χ^2 , which is not yet the global optimum.

3.2.2 A model for pile-up in grating observations

As briefly mentioned in Sect. 1.4.4, pile-up reduces the number of detected counts in the first order spectra: Whenever two (or more) photons arrive at one single detector pixel within one exposure time, they cannot be separated in the following readout and are considered as one event. This might be rejected in the data processing (if neighboring pixels are affected by the larger charge in the CCD). In grating observation, it will otherwise be counted as an event of a higher order. (The energy of two photons of wavelength λ_1 diffracted in a first order spectrum is the same as the energy of a single photon of wavelength $\lambda_2 = \lambda_1/2$, which would arrive at the same place if dispersed in second order.) Therefore, the first order spectra are depleted, while higher order spectra gain photons.

Pixels with many counts are more affected by pile-up than others and the effect scales exponentially: If the number of counts C in the pixel with the most counts $\max_j\{C(j)\}$ is reduced by a factor $1 - p$ (p is called pile-up fraction), the general reduction is

$$C'(i) = C(i) \cdot (1 - p)^{\frac{C(i)}{\max_j\{C(j)\}}} \quad (3.9)$$

`simple_gpile`

The `simple_gpile` model of Nowak et al. (2007) can be used to describe pile-up reduction in the first order spectra of grating observations. It includes the pile-up of overlapping higher order ($m > 1$) spectra: photons with wavelength λ/m or respectively energy $m \cdot E$ hit the detector at the same position as those of the first order spectrum with wavelength λ .

In this pile-up model, an arbitrary model spectrum $M(E)$ is modified according to the pile-up formula (3.9); the number of counts C_M is estimated in the following simple way: The total number of counts in one readout cycle at a bin B_i is roughly given by the product of the flux M , the ARFs A_m (noting the shift of energies by a factor m for higher order spectra) and the frame time t_{frame} . In fact, not the frame time, but the bin dependent ratio $t_{\text{frame}}/t_{\text{exp}}(m, i)$ is used, which results in an effective count rate c_M instead of C_M . The fractional exposure $t_{\text{exp}}(m, i)/t_{\text{frame}}$, which is most easily available as array `fracexpo` in the structure returned

by the ISIS-function `get_arf_info`, is lower than 1 for pixels near chip gaps. (Due to the dithering of the satellite, there is no part of the spectrum which is always lost in a gap.) In these regions, the count rate is lower, but the pile-up reduction is not.

$$c_M^{\text{sim}}(i) = \sum_{m=1}^3 \frac{t_{\text{frame}}}{t_{\text{exp}}(m, i)} \cdot A_m(m \langle E \rangle_{[E_i, E_{i+1}]}) \cdot \int_{E_i}^{E_{i+1}} dE M(m E) \quad (3.10)$$

$$\rightarrow M'(i) = M(i) \cdot (1 - p)^{\frac{c_M^{\text{sim}}(i)}{\max_j \{c_M^{\text{sim}}(j)\}}}$$

As the pile-up fraction p applies to the bin with the maximal count rate (and the other bins are scaled with respect to this value), this model is not local. It is thus important that the `simple_gpile` model is always used for the whole spectrum to obtain a consistent description.

`simple_gpile2`

Especially when adding emission and absorption lines to a model spectrum, one is interested to have local models for the continuum, with which the value in one bin is not affected by local modifications of other (especially distant) bins. The non-locality of `simple_gpile` can be avoided by introducing other parameters than p for the pile-up reduction:

$$(1 - p)^{\frac{c_M^{\text{sim}}(i)}{\max_j \{c_M^{\text{sim}}(j)\}}} \equiv \exp(-\beta \cdot c_M^{\text{sim}}(i)) \quad \text{with} \quad -\beta = \frac{\log(1 - p)}{\max_i \{c_M^{\text{sim}}(i)\}} \quad (3.11)$$

The exponential scale $\beta \approx \frac{p}{\max_j \{c_M^{\text{sim}}(j)\}}$ is roughly proportional to the pile-up fraction p , i.e., a larger β means – just as a larger p – stronger reduction of the count rate by pile-up. The implementation of this pile-up model (which differs from the original `simple_gpile` only in the parameter β instead of p) is called `simple_gpile2` and will be used in this work's analysis.

Estimation of β :

If $C = c \cdot t_{\text{frame}} \cdot \Delta\lambda$ denotes the number of counts per frame time in one detector pixel,⁸ one would expect a pile-up reduction of e^{-C} from Poisson statistics. A first estimate for the exponential scale is therefore (cf. footnote 8)

$$\beta \approx t_{\text{frame}} \cdot \Delta\lambda, \quad \text{where } \Delta\lambda_{\text{MEG}} = 3 \cdot 11 \text{ m\AA} = 2 \cdot \Delta\lambda_{\text{HEG}}. \quad (3.12)$$

Use of `simple_gpile(2)` in ISIS

Before using these pile-up models, one has to assure that the factorization of the detector response functions into ARFs and RMFs is done as described in Sect. 2.2.1, i.e., the RMFs are normalized redistribution matrix functions and the ARFs include the effective area as well as the detector efficiency. To do so, additional factors have to be split off the RMFs with the command `factor_rsp` and multiplied to the original ARFs before ARFs and RMFs are assigned to the corresponding spectra.

`simple_gpile2` (as well as `simple_gpile` itself) is a convolution model, to be defined via

$$\text{fit_fun}(\text{"simple_gpil2(instance, fit-function)"}); , \quad (3.13)$$

where *instance* is typically `Isis_Active_Dataset`.

The parameters `data_indx`, `arf2_indx` and `arf3_indx` have to be set to the correct index for each dataset. (Therefore, one has to use `instance=Isis_Active_Dataset`.) As these are no fit parameters, they will stay frozen during the whole analysis.

⁸ As 3×3 pixel islands are considered to determine the grade of an event in the data processing (see Sect. 3.1), the length $\Delta\lambda$ of a unit cell that has to be considered to pile up is in fact three times the wavelength range covered by one ACIS-pixel. The MEG has a dispersion spread of 11 mÅ/detector pixel and the HEG has only the half of this value (see Sect. 1.4.3).

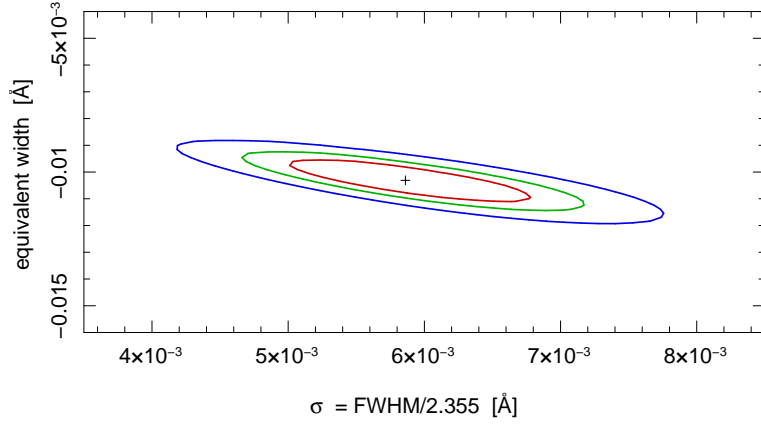


Figure 3.4: 68.3%, 90% and 99% 2-parameter confidence contours of a Gaussian's σ and E_λ for a very strong line, namely, Si XIV Ly α at 6.18 Å. Not even in this case, the width σ is very well constrained – in contrast to the equivalent width.

3.2.3 Description of absorption lines

The theory of absorption lines has been described in the Sections 2.1.2 – 2.1.5. Here, it will be shown how they can actually be fitted within ISIS.

Single Gaussian lines

It is sufficient to describe single absorption or emission lines just by Gaussian line profiles (which allow for an easy implementation and a fast computation as well),

- if the actual line profile is dominated by thermal broadening, as the appropriate Voigt-profile is asymptotically a Gaussian (cf. Sect. 2.1.4)
- if the profiles are not resolved anyway and only the equivalent widths can be inferred (cf. Sect. 2.1.5, see also Fig. 3.4)

As the equivalent width is defined via the relative line depth A which is given by the ratio of the flux of the line and of the continuum, respectively (Eq. 2.31), it is useful to parameterize the model for the line by a factor $(1 + A)$ times the model for the continuum,

$$S_l = S_c \cdot (1 + A). \quad (3.14)$$

A can now be defined by the fit-function `gauss` or the sum of several instances of it. As `gauss` is evaluated by ISIS as a bin-integrated quantity (see Sect. 3.2.1), it should be divided by the bin-width `bin_width` to obtain a bin-average: $A \stackrel{\text{“=”}}{=} \text{gauss}/\text{bin_width}$ is evaluated as

$$\tilde{A}(B_i) = \langle A(\lambda) \rangle_{[\lambda_i, \lambda_{i+1}]} = \frac{1}{\lambda_{i+1} - \lambda_i} \int_{\lambda_i}^{\lambda_{i+1}} d\lambda \frac{W_\lambda}{\sigma\sqrt{2\pi}} \exp\left(-\frac{(\lambda - \lambda_0)^2}{2\sigma^2}\right). \quad (3.15)$$

If there is no blend of multiple lines, this kind of bin-average is the appropriate choice.

The flux model in ISIS is defined by `fit_fun("fit-function")`; or as in (3.13), if the pile-up model of Sect. 3.2.2 is included as well, where *fit-function* is defined by

$$\text{fit-function} = (\text{continuum-function}) * \left(1 + \left(\sum_n \text{gauss}(n)\right)/\text{bin_width}\right). \quad (3.16)$$

The equivalent width E_λ of these lines is directly given by the norm `area`. For the analysis, a curve of growth (Sect. 2.1.5) has to be constructed to obtain the ions' column densities.

If confidence levels are fitted for multiple lines, the problem usually factorizes in the different lines: As long as there are no blends, it is sufficient to keep all parameters fixed, except those of the considered line, of course, which saves a considerable amount of computational time.

Absorption line series

As an alternative to using a curve of growth after the fitting, a whole series of an ion's lines, whose equivalent widths are coupled according to the transitions' oscillator strength, can be fitted simultaneously. In fact, the concept of equivalent widths is dispensable, if the proper line profiles are used, containing N directly as parameter (cf. Sect. 2.1.4; Eqs. 2.33 and 2.27):

$$M_l(\lambda) = M_c(\lambda) \cdot e^{-\tau(\lambda)}, \quad \text{with} \quad \tau(\lambda) = N_i f_{ij} \frac{\pi e^2}{m c} \frac{1}{\sqrt{\pi} \Delta\nu_D} H\left(\frac{\Gamma}{4\pi \Delta\nu_D}, \frac{\nu(\lambda) - \nu_0}{\Delta\nu_D}\right) \quad (3.17)$$

Therefore, the ISIS module `lineProfile` containing new fit-functions was developed.⁹ In order to provide the possibility of combining overlapping lines – both from the same series (e.g., unresolved multiplets from spin-orbit-coupling) and from different series or extra lines as well – this was organized by dummy fit-functions: `ls0` for line series and `lp0` for single line profiles. Both models evaluate only to $\tilde{f}(B_i) \equiv 0$, but put their line-data on an internal stack. The proper bin-average of all these lines is finally evaluated by the multiplicative convolution model `evallp` without any parameters at all. (The lines are stored on an internal stack.) For example, if a *continuum-function* is to be modified by two line series and one single line profile, the models can thus be used in the following way in ISIS:

$$\textit{fit-function} = (\textit{continuum-function}) * \textit{evallp}(0, \textit{ls0}(1)*\textit{ls0}(2)*\textit{lp0}(1)) \quad (3.18)$$

The model `ls0` has, besides the parameters `Z` and `ion` that will stay frozen, the fit-parameters `shift` [km s^{-1}], which is $\Delta\lambda/\lambda_0 \cdot c$, `vtherm` [km s^{-1}] and `N` [10^{16}cm^{-2}]. The required atomic data – namely wavelengths and Einstein A -coefficients of the lines in the series, and multiplicities of the involved quantum states – are provided by another feature¹⁰, `atomicData`, which just compiles the necessary data of the strongest lines from Verner et al. (1996) or the ATOMDB (cf. Sect. 2.1.2). The model `lp0` is independent of atomic data; it has the fit-parameters `lambda`, `vtherm`, `Gamma` and `Nf`. In the case of `ls0`, Γ is set to A , assuming an absorbing plasma with low density and negligible pressure broadening of the lines. $N \cdot f$ is, of course, set according to N and f , which is given by $g_j/g_i A_{ji}$ and λ_{ij} (Eq. 2.19). The convolution model `evallp` computes now, if the bin B_i is affected by a line (otherwise $\tilde{f}(B_i) \equiv 1$), the following average:

$$\tilde{f}(B_i) = \frac{1}{\lambda_{i+1} - \lambda_i} \int_{\lambda_i}^{\lambda_{i+1}} d\lambda \exp(-\tau(\lambda)) \quad (3.19)$$

The integration is performed with help of a Romberg-integrator after Press et al. (1992, Chapter 4.3). $\tau(\lambda)$ is given by Eq. (3.17) for all lines on the stack, which is numerically

$$\tau(\lambda) = \sum_l 6.1836 \times 10^{-4} \cdot \frac{N_l f_l}{10^{16} \text{cm}^{-2}} \cdot \frac{1 \text{keV}}{\Delta E_{D,l}} \cdot H\left(\frac{\Gamma_l \cdot h}{4\pi \Delta E_{D,l}}, \frac{E(\lambda) - E_{0,l}}{\Delta E_{D,l}}\right) \quad (3.20)$$

The Doppler-energy-width $\Delta E_{D,l}$ is simply $E_{0,l} \cdot v_{\text{therm},l}/c$, the Voigt-function H is implemented in the source code of ISIS (`voigt.c`), and Planck's constant is $h = 4.13567 \times 10^{-18} \text{keV s}$.

As already mentioned above, Eq. (3.20) is not evaluated for bins far away of any line, in order to save computational power. 'Far away' needs to be quantified, of course. But the width of a line can be estimated as done in Sect. 2.1.5 for the equivalent widths. It is easily checked whether the line is dominated by thermal broadening (Gaussian profile) or by radiation damping (Lorentzian profile). The larger width defines the scale on which the profile has to be evaluated exactly.

Examples for line profiles for series of some important ions are shown in Fig. 4.14.

⁹ It is available at <http://pulsar.sternwarte.uni-erlangen.de/hanke/diplomathesis/code/>.

¹⁰A 'feature' is, according to the ISIS manual (Houck, 2006), "an abstract quantity that is undefined here. The `require` function ensures that a specified 'feature' is present."

4 High-resolution analysis of obs. # 3814

As all necessary tools have been developed in the last chapters, this chapter presents the actual work of this thesis: the high-resolution spectroscopic analysis of a *Chandra*-observation of Cygnus X-1. It has been performed when the source was behind the companion star and the former literally “x-rayed” the focussed wind. This observation is thus eminently suited to analyze the accretion flow in the X-ray binary system.

4.1 The observation

The *Chandra* observation # 3814 of Cygnus X-1 had been proposed by Katja Pottschmidt et al. to analyze the X-ray absorption dips (see Sect. 1.3.4) and the distance (as well as the extent) of the scattering dust cloud producing a soft X-ray halo (see Figs. 3.1, 4.2, 4.3).

4.1.1 Observational parameters and data reduction

The observation was performed on 2003 April 19...20 for almost 50 ks, corresponding to the binary’s orbital phase $\phi \approx 0.93 \dots 0.03$, see Table 4.1. This time around $\phi = 0$ had been chosen, as the absorption dips preferentially occur at superior conjunction of the black hole.

This *Chandra* observation used the HETGS in timed exposure (TE) mode with a frame time of 1.741 s (Sects. 1.4.3 and 1.4.4). The use of only half of the nominal ACIS frame time is explained by the fact that only a 512 pixel sub-array was used. Additionally, an attempt was made to place a 40×40 pixel window over the zero-order image of the bright source to avoid telemetry saturation without blocking the scattering halo from the dust cloud between us and Cyg X-1, but the source was not fully covered (see detector-image, Fig. 4.1).

Figures 4.1 and 4.2 show the resulting image with color-coded photon energies: The 2.5...8 keV high energy band with the shortest wavelengths, which is mapped next to the zero-order image, is shown in blue; events of intermediate energy are shown in green and the 0.2...1.5 keV low energy band is shown in red. One can easily recognize the MEG arms with the lower dispersion from the upper left to the lower right corner and the HEG arms in the other diagonal direction. Note the two afterglow events and four hot columns which are at fixed detector-pixels and therefore at smeared sky-positions.

Most parts of the data reduction were performed as described in Sect. 3.1.2: the position of the zero-order image of the source was determined as $(X, Y) = (4099.919, 4024.862)$ (cf. Fig. 3.1), but the extraction region for the spectrum was limited to a 10 pixel box around the grating arms (see Fig. 4.3). The default width of more than 87 pixels would include the scattering halo to the background spectrum, see Fig. 4.4.

Starting with 6 724 131 events in the level 1-event file, 5 354 442 events are retained in the destreaked level-2 event file. The detailed assignment to the different grating orders is listed in Table 4.2.

To illustrate the wavelength range accessible within this observation with the *Chandra* HETGS, Figure 4.5 shows the number of counts in all spectra of the MEG and the HEG from this observation. As already shown in Table 4.2, the first order spectra (Fig. 4.5a) have the most counts and therefore the best signal to noise ratio. The second order MEG spectra are even weaker than the third order spectra (as expected, see Sect. 1.4.3), while the number of counts in the HEG spectra decreases monotonically with order.

Table 4.1: Time of observation # 3814 in various formats

	date	<i>Chandra</i> -time ^a	MJD ^b	ϕ ^c
start	2003-04-19, T16:47:31	167 158 051	52 748.69967	0.93
end	2003-04-20, T06:41:43	167 208 103	52 749.27897	0.03

^aThe *Chandra*-time is the number of seconds after 1998-01-01, T00:00:00 (MJD 50814).

^bThe definition of the modified Julian date is given in footnote *a* to Table 1.3.

^cThe binary’s orbital phase ϕ can be calculated by Eq. (1.20) with any ephemeris given by Table 1.3.

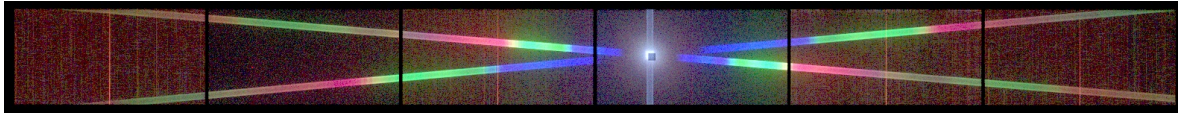


Figure 4.1: Detector-image of obs. ID 3814, color-coding the photon energies.

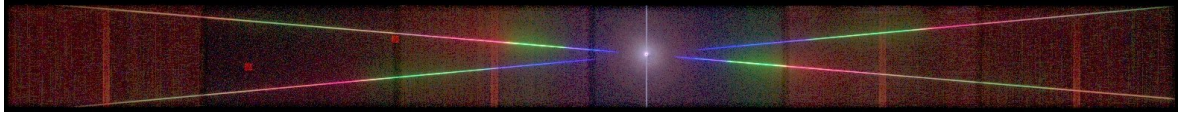


Figure 4.2: 'Sky'-image of obs. ID 3814, color-coding the photon energies.

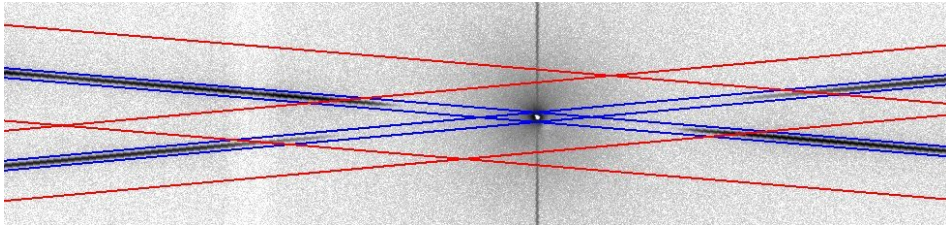


Figure 4.3: Default (red) and narrow (blue; excluding most of the halo) extraction regions.

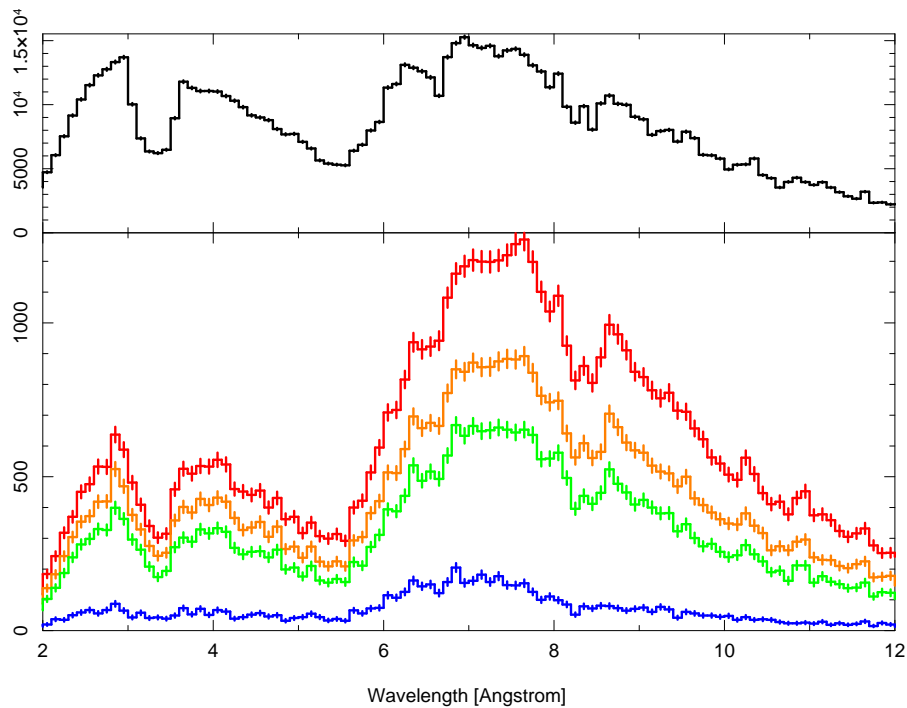
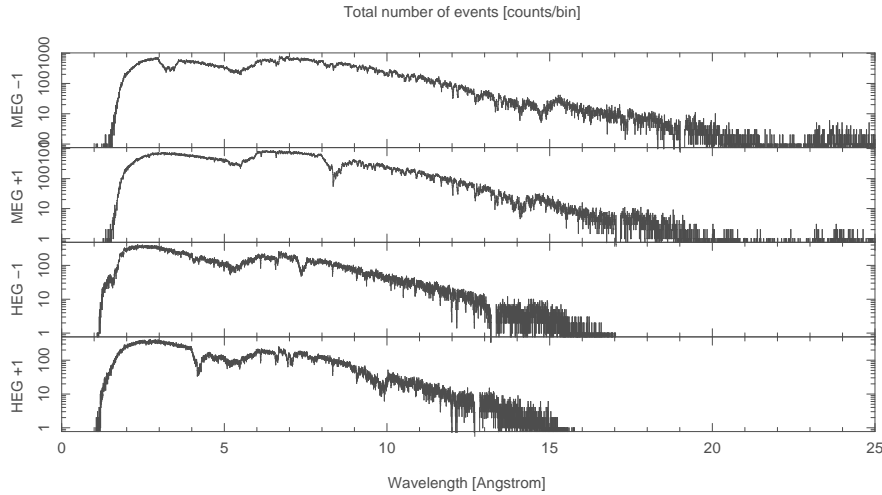


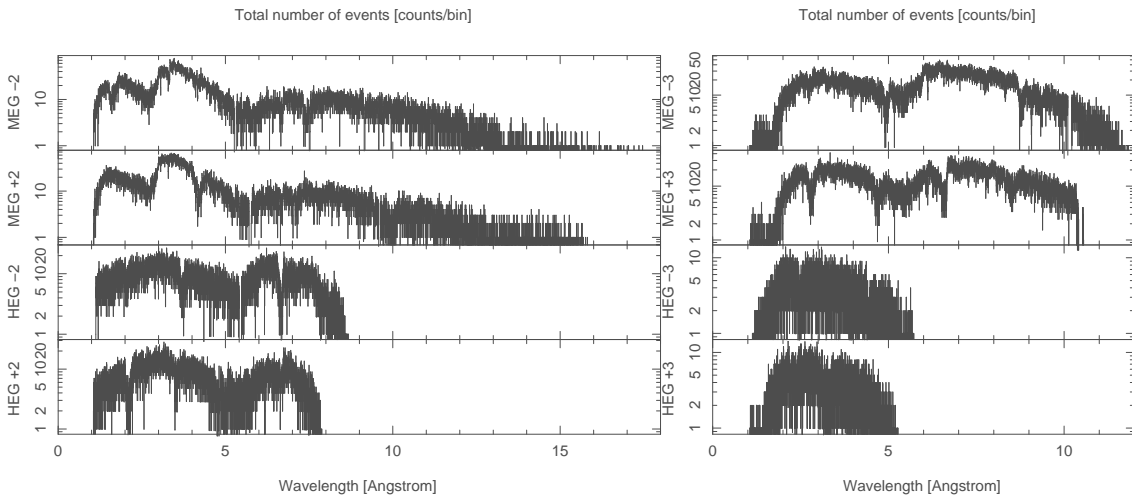
Figure 4.4: Background count rate (lower panel) for different extraction regions: red = default region, orange = 40 pixel width, green = 25 pixel width, blue = 10 pixel width. Unless the region is small enough, the spectra are dominated by the scattering halo, as the count rates are proportional to those of the Cyg X-1 spectrum (shown in the top panel). The plot shows the number of counts in 0.1 \AA bins of each MEG-1 spectrum.

Table 4.2: Events in the different orders of the spectra

order	number of events				
	in the MEG-spectrum	in the HEG-spectrum			
1	+1	992 469	1 918 539	629 099	1 305 022
	-1	926 070		675 923	
2	+2	55 249	11 5 452	42 029	96 060
	-2	60 203		54 031	
3	+3	81 273	183 804	15 760	32 538
	-3	102 531		16 778	
higher unassigned		62 707		13 893	
total unassigned		110 310		82 001	
total		2 390 812		1 529 514	
unassigned		1 434 116			
TOTAL		5 354 442			



(a) \pm first order spectra



(b) higher order spectra

Figure 4.5: Counts in the MEG and HEG spectra (including all events of obs. # 3814).

4.1.2 The light curve

The light curve, i.e., the time-dependent count rate (e.g., Fig. 4.6, showing the $0.5 \dots 7.2$ keV $\equiv 1.7 \dots 25$ Å band), shows several transient absorption dips (cf. Sect. 1.3.4). The dips are most clearly seen in a low energy band – which suggests the interpretation as an enhanced absorption. Therefore, the spectrum hardens during the dips. The quantitative spectral hardness (“X-ray color”) is defined as a ratio of the count rate in a high energy band (e.g., the $2.1 \dots 7.2$ keV $\equiv 1.7 \dots 5.9$ Å band, shown in the second panel of Fig. 4.7) and the count rate in a low energy band (e.g., the $0.7 \dots 1.0$ keV $\equiv 12.4 \dots 17.7$ Å band, shown in the first panel

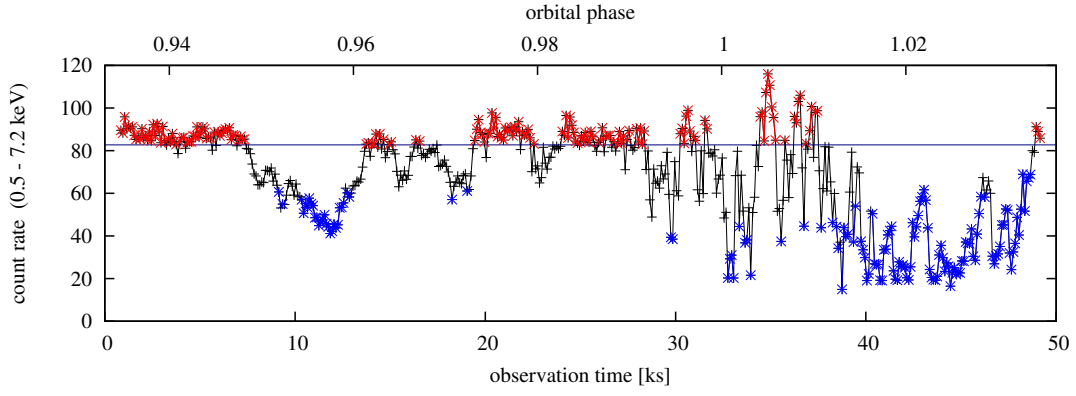


Figure 4.6: Light curve in the energy band of 0.5...7.2 keV.

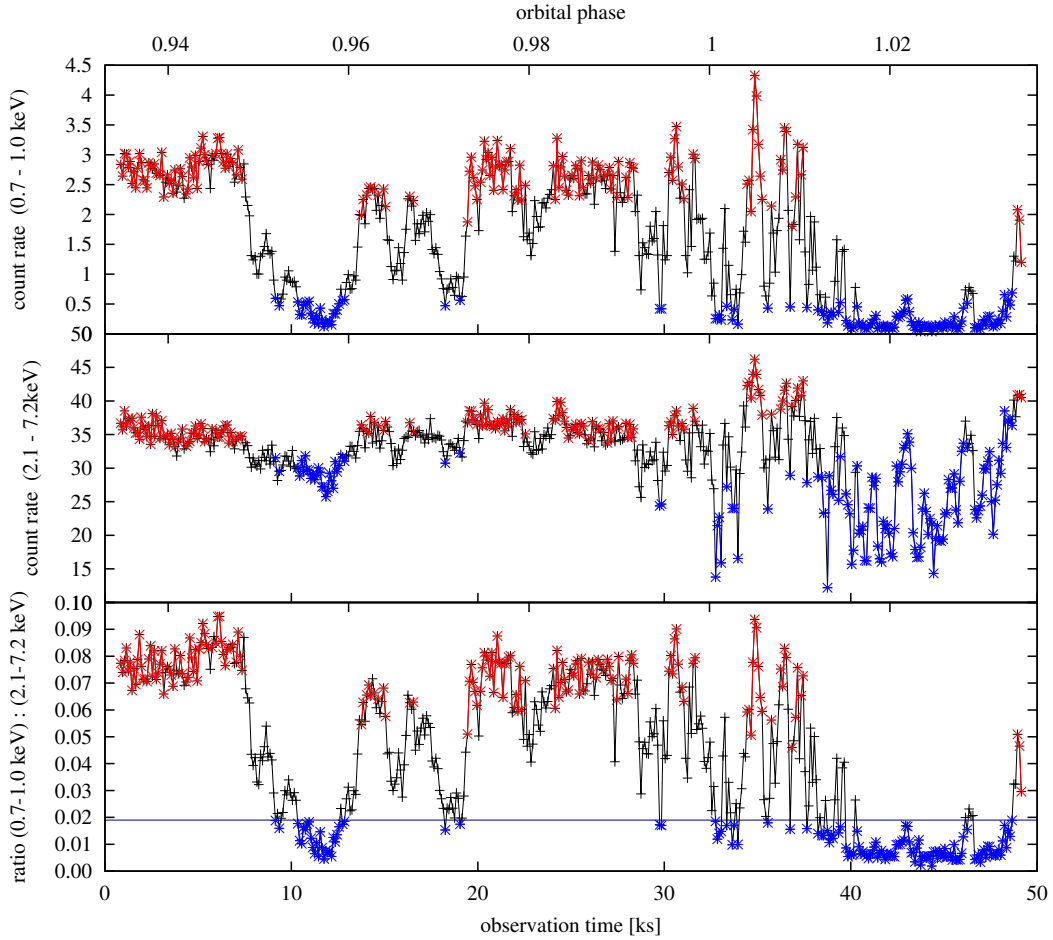


Figure 4.7: Dips in the light curves of different energy bands and their ratio.

of Fig. 4.7). The bottom panel of Fig. 4.7 shows the inverse of such a ratio, which reveals the dips in a similar way as the light curve itself, namely, as decreased “softness”-ratio.

There are two major dips: The first compact dip has a total length of 1 hour, 43 minutes and its deepest and hardest core lasts still 40 minutes. The second dip is deeper and has a duration of more than two hours. The fact that this single observation (great advantage in view of the high variability of Cyg X-1, even on short time scales) shows both the pure source spectrum (‘non-dip’ spectrum) and absorption dips (‘dip’ spectrum) allows to disentangle the effect of the wind material. Following Pottschmidt et al. (2006), three absorption levels, are defined based on a count rate or a hardness ratio. They are also indicated in Figs. 4.6 and 4.7 by colors: Time-intervals where the 0.5...7.2 keV-band count rate extends $82.7 \text{ counts s}^{-1}$ are considered to form the ‘non-dip’ Cyg X-1 spectrum (shown in red), while the ‘dip’ spectrum consists of those times where the ratio $C(0.7...1.0 \text{ keV})/C(2.1...7.2 \text{ keV})$ falls below 0.019 (shown in blue). The remaining events form a ‘transition’ spectrum (shown in black).

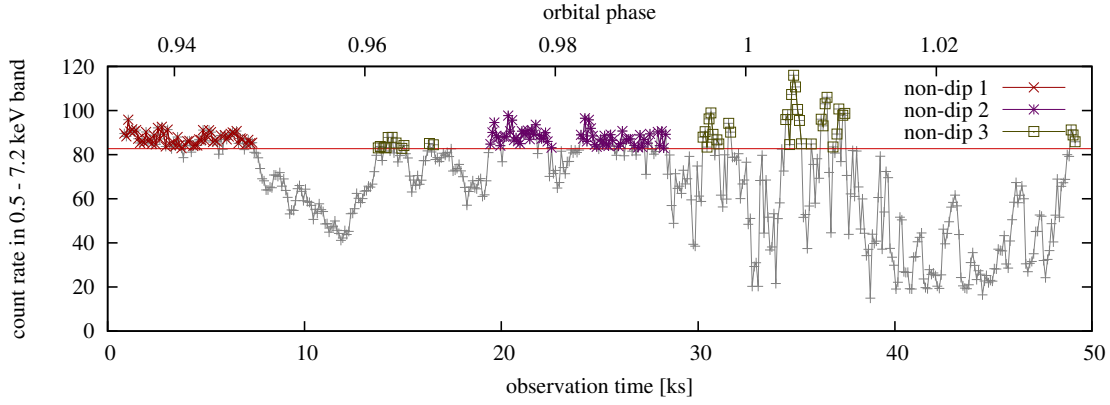


Figure 4.8: Definition of the ‘non-dip’ sub-spectra (see text).

4.2 The ‘non-dip’ spectrum

The ‘non-dip’ Cyg X-1 spectrum is composed from those time-intervals, where the count rate in the 0.5...7.2 keV-band (corresponding to 1.7...25 Å) is larger than 82.7 counts/s. Its total exposure time is 16.1 ks.

4.2.1 Consistency checks

Three subintervals have been defined to check the consistency of this definition of the ‘non-dip’ spectrum (see Fig. 4.8): The ‘non-dip 1’ spectrum uses the continuous 5.8 ks block with constantly high count rate at the beginning of the observation. It is shown in red. After the first large dip in the light curve and two smaller ones, there is a still relatively constant part, which is just interrupted by a small and short dipping event. This defines the 6.2 ks ‘non-dip 2’ spectrum, which is shown in purple. The remaining parts, highly variable and disconnected, form the 4.2 ks ‘non-dip 3’ spectrum, shown in dark yellow.

To check if the sub-spectra are consistent with each other, ISIS’ flux-corrected spectra were divided by the average ‘non-dip’ spectrum. (The count rates alone are not comparable due to the time dependence of the ARFs.) Both MEG±1 have been rebinned by a factor of 4 and both HEG±1 have been rebinned by 8, such that a common bin-size of 20 mÅ was obtained. For each spectrum $s \in \{\text{MEG} \pm 1, \text{HEG} \pm 1\}$, the flux-ratio r_s has been determined as

$$r_s^n(i) = \frac{\tilde{S}_\lambda^{\text{non-dip } n',s}(i)}{\tilde{S}_\lambda^{\text{non-dip}',s}(i)}, \quad \Delta r_s^n(i) = \frac{\Delta \tilde{S}_\lambda^{\text{non-dip } n',s}(i)}{\tilde{S}_\lambda^{\text{non-dip}',s}(i)} + \frac{\tilde{S}_\lambda^{\text{non-dip } n',s}(i) \cdot \Delta \tilde{S}_\lambda^{\text{non-dip}',s}(i)}{\tilde{S}_\lambda^{\text{non-dip}',s}(i)^2} \quad (4.1)$$

The results for ‘non-dip 1’ are shown in Fig. ?? on page ?. The last panel shows the average of the flux-ratios (where $\tilde{S}_s \neq 0$):

$$\langle r_s^n(i) \rangle_s = \frac{1}{|\mathcal{S}^n(i)|} \sum_{s \in \mathcal{S}^n(i)} r_s^n(i) \quad \text{with } \mathcal{S}^n(i) = \{s \mid 0 < r_s^n(i) < \infty\} \quad (4.2)$$

For the ‘non-dip 1’ spectrum, there are deviations from 1, but none is visible in all of the spectra s , as the average flux-ratio is constantly consistent with 1. The large scattering above ~ 12 Å in the HEG spectra and above ~ 16 Å in the MEG spectra is due to the low count rates and therefore high relative statistical errors.

The same analysis with the ‘non-dip 3’ spectrum (Fig. ??) shows that its flux-ratio with the average ‘non-dip’ spectrum is also mostly consistent with 1, although it is formed from discontinuous time-intervals with strongly variable count rates. There are, however, significant deviations, especially in the 12...14 Å wavelength-range, indicating that the deep absorption lines at 12.13 Å and 13.50 Å have still grown deeper, see Fig. ?. Furthermore, the (continuum?) high energy flux up to ~ 4.5 Å is slightly higher. Nevertheless, these effects are considered to be acceptable and the definition of the total ‘non-dip’ spectrum for the following analysis is therefore maintained. (The ‘non-dip 2’ spectrum is supposed to be consistent with the average ‘non-dip’ spectrum, as both ‘non-dip 1’ and ‘non-dip 3’ are.)

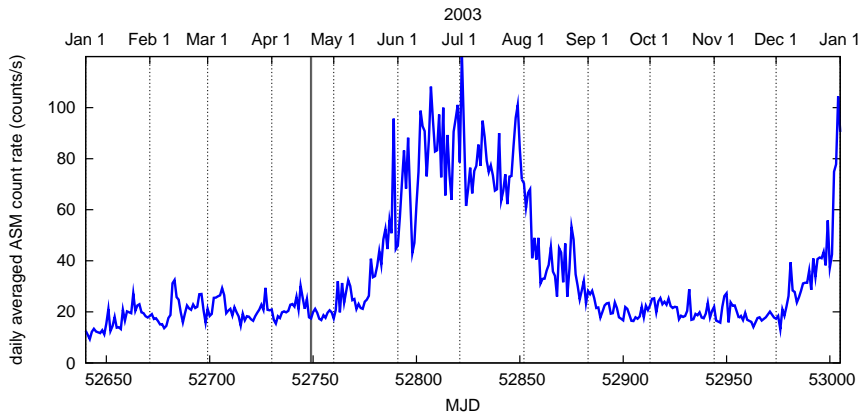


Figure 4.9: RXTE/ASM light curve in 2003. The observation is marked by vertical lines. (after 1.5...12 keV data from <http://xte.mit.edu/XTE/asmlc/srcs/cygx1.html>)

4.2.2 Description of the spectral continuum

At the time of the observation, Cygnus X-1 was still in its hard state (Sect. 1.3.3; cf. also Fig. 1.11), as indicated by the long term light curve (Fig. 4.9) of the *RXTE*/ASM. Therefore, one expects the spectrum to be dominated by a hard power law component. The flux-corrected spectra (Eq. 3.1), especially for the HEG, show that this spectrum of Cyg X-1 can be described just by a photoabsorbed power law. (Photoabsorption bends the power law spectrum down at low energies, see Sect. 2.1.1 and Fig. 2.1.) Fig. 4.10 shows the flux-corrected MEG \pm 1 (i.e., both first order spectra of the MEG) and HEG \pm 1 spectra, after a massive rebinning to ≥ 1000 counts/bin. The HEG spectra can be described quite well by the photoabsorbed power law model, but there is a lack of counts in the MEG spectra, especially in the regions of highest count rate at $6.7 \text{ \AA} \equiv 1.9 \text{ keV}$ (cf. Fig. 4.5.) This indicates that pile-up is an issue for this observation of the bright source Cyg X-1. It is therefore useful to apply `simple_gpiled2` (discussed in Sect. 3.2.2). If a scaling factor is introduced to eventually correct the absolute flux calibrations between the different spectra, the complete fit-function is defined in ISIS via:

```
fit_fun("simple_gpiled2(Isis_Active_Dataset,
                    constant(Isis_Active_Dataset)*powerlaw(1)*phabs(1)
                    )");
```

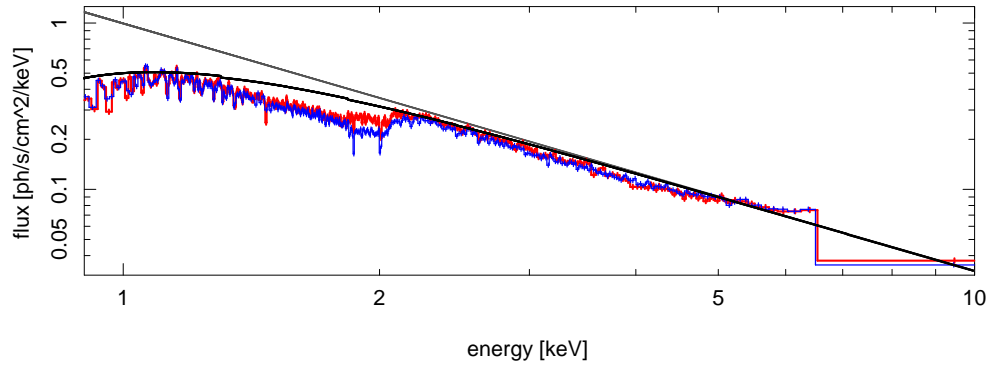
 (4.3)

Besides the separate sets of parameters for the pile-up model and the multiplicative constant (defined by the identifier `Isis_Active_Dataset`, see Sect. 3.2.1), all the MEG \pm 1 and HEG \pm 1 spectra were fitted simultaneously. The parameters are shown in Table 4.3. Due to the inclusion of absorption and emission lines into the model (see below), the best-fit parameters have slightly changed during the analysis. The fitted exponential pile-up scales $\beta_{\text{MEG}} \approx 0.06 \text{ s \AA}$ and $\beta_{\text{HEG}} \approx 0.03 \text{ s \AA}$ are very convincing, as the simple estimate $\beta \approx t_{\text{frame}} \cdot \Delta\lambda$ (Sect. 3.2.2) gives $1.741 \text{ s} \cdot 3 \cdot 11 \text{ m\AA} = 0.057 \text{ s} \cdot \text{\AA}$ for the MEG and the half value for the HEG. A further discussion is given at the end of Section 4.3.2.

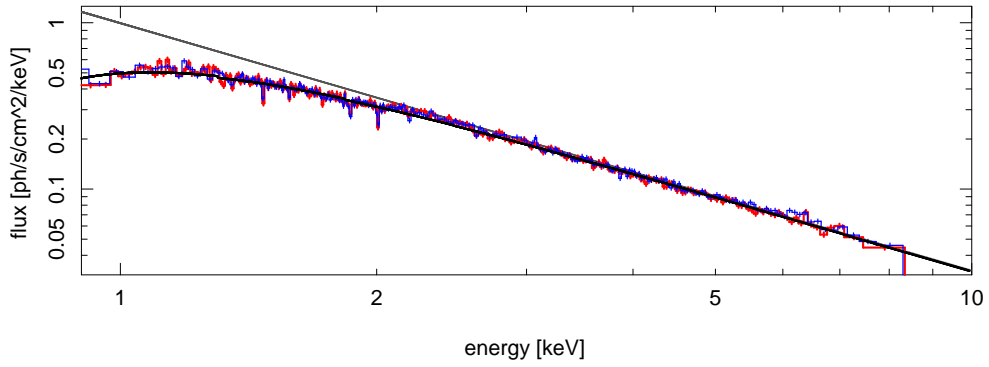
There is a strong correlation between the multiplicative constants and the corresponding pile-up scales, as both lead to a reduced count rate. A χ^2 -contour plot for c_3 and β_3 (in the case of the continuum description without lines) is shown in Fig. 2.9 on page 42.

Modelling of the broad band continuum Bauer (2007) has analyzed the broad band spectrum of Cygnus X-1 obtained with *RXTE* on 2007, April 19; half a day before *Chandra*-observation # 3814. A joint fit of the HEXTE and PCA spectra with the ‘non-dip’ spectrum (see Fig. 4.12) with a (in case of the *Chandra*-spectra pile-up reduced) photoabsorbed broken power law model with high-energy cutoff (cf. Eqs. 3.7, 3.8) gives the parameters $N_{\text{H}} = 0.387(4) \times 10^{22} \text{ cm}^{-2}$, $\Gamma_1 = 1.594(6)$, $E_{\text{break}} = 8.1_{-0.2}^{+0.3} \text{ keV}$, $\Gamma_2 = 1.459(2)$, $E_{\text{cut}} = 24(1) \text{ keV}$ and $E_{\text{fold}} = 183(5) \text{ keV}$.

The *Chandra*-data alone can thus be described by just a single power law with index Γ_1 . Therefore, the results of Table 4.3 are quite consistent with the broad band continuum of Cyg X-1, although the pure *RXTE*-fits give a larger $\Gamma_1 \gtrsim 1.7$, see also Wilms et al., 2006b, datasets # 148–150 of the online material “broken power law fits”.

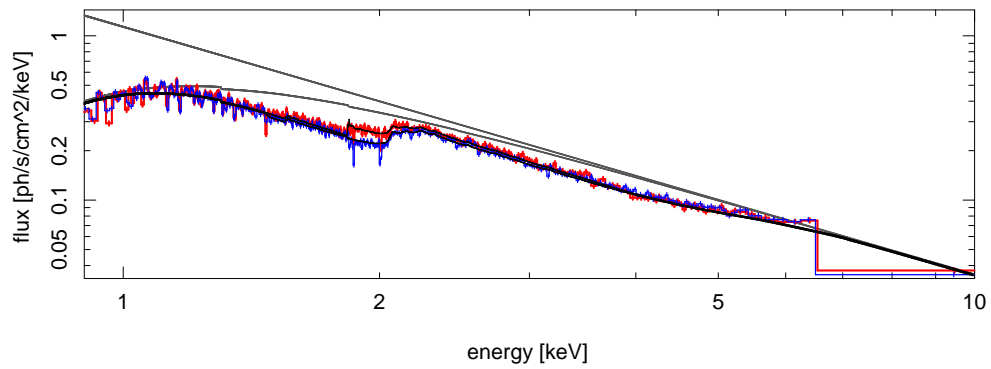


(a) The MEG±1 spectra

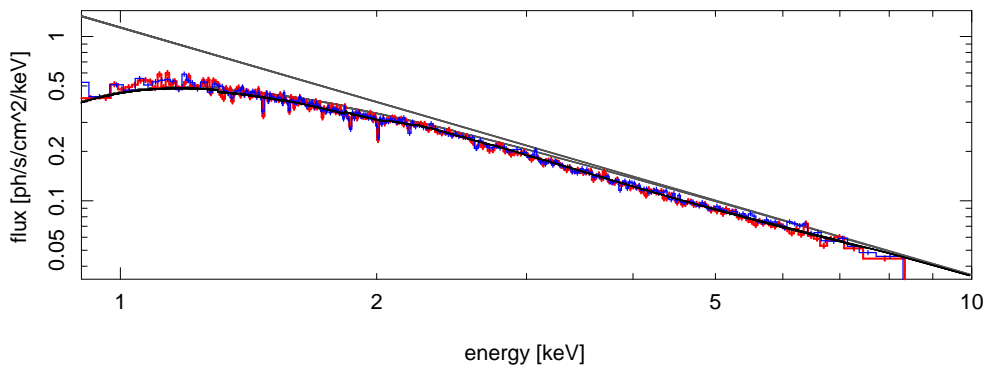


(b) The HEG±1 spectra

Figure 4.10: The flux-corrected spectra (-1^{st} order in blue, $+1^{\text{st}}$ order in red) and a photoabsorbed power law model (black). The gray lines show just the power law model to illustrate the effect of photoabsorption.



(a) The MEG±1 spectra



(b) The HEG±1 spectra

Figure 4.11: As Fig. 4.10, but including the model for pile-up reduction. The un-piled photoabsorbed power law model is also shown in gray.

Table 4.3: Parameters of the ISIS model 4.3 describing the continuum in the ‘non-dip’ spectrum

$$S_E^s(E) = c_s \cdot S_E(1\text{keV}) \cdot \left(\frac{E}{1\text{keV}}\right)^{-\Gamma} \cdot e^{-\sum_Z \sigma_Z(E) \cdot A_Z \cdot N_H}; \quad C_0^{\text{piled},s}(i) = C_0^s(i) \cdot \exp\left(-\beta_s \cdot C_{0,\text{sim}}^{\text{unpiled},s}(i)\right)$$

model	parameter		spectrum	before	after
				line-fitting	
phabspowerlaw	photon index	Γ	all	$1.5512^{+0.0061}_{-0.0060}$	$1.5480^{+0.0059}_{-0.0062}$
	norm	$S_E(1\text{keV})$ [ph.(s cm ² keV) ⁻¹]	all	$1.2341^{+0.0139}_{-0.0136}$	$1.233^{+0.014}_{-0.013}$
phabs	H-column density	N_H [10 ²² cm ⁻²]	all	$0.4139^{+0.0042}_{-0.0041}$	$0.3882^{+0.0041}_{-0.0041}$
simple_gpiled2 (\Rightarrow simple_gpiled)	exponential scale	β_0 [$(\frac{\text{cts}}{\text{s A}})^{-1}$]	} MEG-1	$0.0584^{+0.0012}_{-0.0012}$	$0.0588^{+0.0012}_{-0.0011}$
	(\Rightarrow pile-up fraction	p_0			
	exponential scale	β_1 [$(\frac{\text{cts}}{\text{s A}})^{-1}$]	} MEG+1	$0.0629^{+0.0009}_{-0.0009}$	$0.0617^{+0.0009}_{-0.0009}$
	(\Rightarrow pile-up fraction	p_1			
	exponential scale	β_2 [$(\frac{\text{cts}}{\text{s A}})^{-1}$]	} HEG-1	$0.0311^{+0.0032}_{-0.0033}$	$0.0376^{+0.0031}_{-0.0030}$
	(\Rightarrow pile-up fraction	p_2			
	exponential scale	β_3 [$(\frac{\text{cts}}{\text{s A}})^{-1}$]	} HEG+1	$0.0199^{+0.0035}_{-0.0036}$	$0.0229^{+0.0034}_{-0.0034}$
(\Rightarrow pile-up fraction	p_3	11.4% @ 2.29 Å)			
constant	factor	c_0	MEG-1	$\equiv 1$ (fixed)	
	factor	c_1	MEG+1	$1.0004^{+0.0082}_{-0.0082}$	$0.994^{+0.008}_{-0.008}$
	factor	c_2	HEG-1	$0.972^{+0.011}_{-0.011}$	$0.991^{+0.011}_{-0.011}$
	factor	c_3	HEG+1	$0.943^{+0.011}_{-0.011}$	$0.950^{+0.011}_{-0.011}$

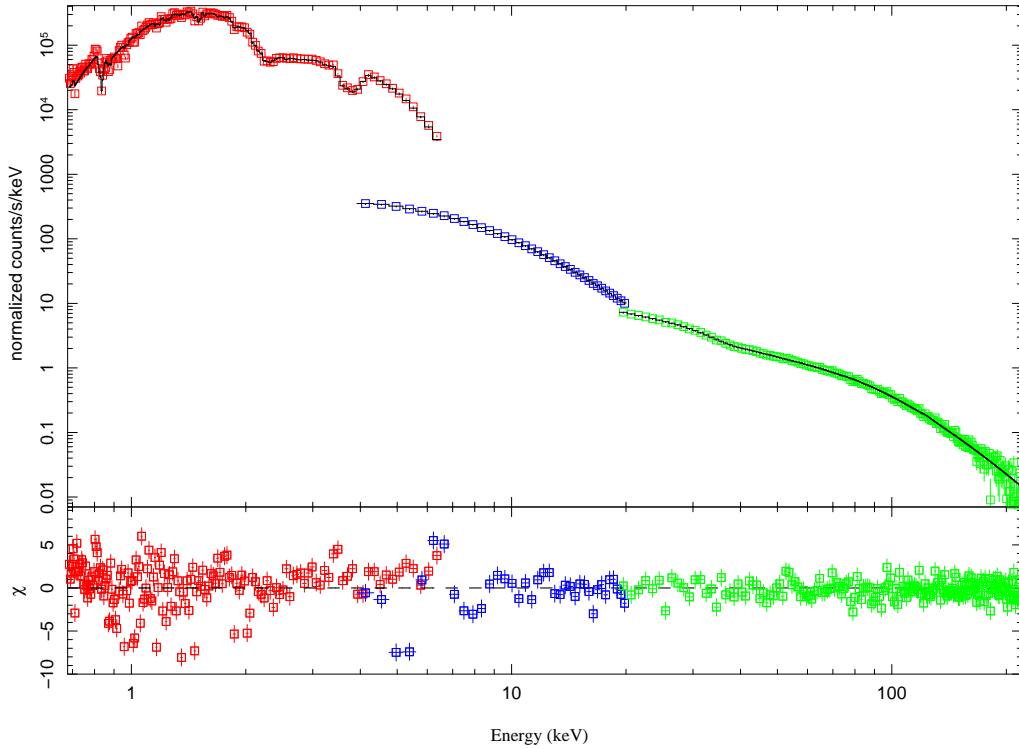


Figure 4.12: Joint fit of the broad band continuum of Cyg X-1 with the ‘non-dip’ MEG-1 (red), PCA (blue) and HEXTE A (green) spectrum with $\chi_{\text{red}}^2 = 3.0$.^a (Bauer, 2007, Fig. 8a)

^a Fitting only *RXTE*-data is possible with $\chi_{\text{red}}^2 \sim 1.0$, but *Chandra* introduces high-resolution features.

4.2.3 Description and identification of absorption and emission lines

As the continuum is now described, lines can be identified as significant residuals from the continuum model that appear in all the MEG±1 and HEG±1 spectra. Therefore, the average residuals $\langle\Delta\chi(i)\rangle$ in bin i are calculated from the number of background-subtracted counts C_0 with (Poisson) error σ_{C_0} and the model counts C_M in all spectra $s = \text{MEG}\pm 1$ and $\text{HEG}\pm 1$:

$$\langle\Delta\chi(i)\rangle = \frac{1}{4} \sum_s \frac{C_0^s(i) - C_M^s(i)}{\sigma_{C_0^s(i)}} \quad (4.4)$$

A deviation of $\langle\Delta\chi(i)\rangle$ from 0 by more than 1 is usually considered significant.

There are almost 220 Gaussian lines included simultaneously (as described in Sect. 3.2.3) to fit the spectrum, although many of them just describe small deviations that could not even be identified with an electronic transition. But it was often necessary to include them, as the fitting routine otherwise preferred to replace a line with a neighboring small deviation by a single, but very broad Gaussian. The decision, whether a line and its identification is finally considered to be trustable, was guided by the following rules:

- Absorption lines should arise from transitions from the ground state.
- Any given line in a series can usually only be trusted if the lower transitions from this series are seen as well.
- Transitions with larger Einstein A -coefficient are more probable within one ion.
- Einstein coefficients of different atoms but similar state of ionization may be compared via their atomic abundances in the interstellar medium, see Table ?? (p. ??).

Table 4.4 lists the position of all lines – sorted by the improvement of the χ^2 statistics. $\Delta\chi^2$ is just the difference of χ^2 (with line) and χ^2 (without line), where the latter has been determined without refitting the continuum. In principle, one has to find the best values of all parameters in any case. But it was found, that this usually does not lead to any differences; the continuum is strongly constrained, especially by all the other lines, such that the fitting routine cannot find a better fit. The usual equivalent width is also included in this table. Emission lines (with $\text{EW} > 0$) are additionally marked by a gray background color. Identifications are given by the ion as far as they are considered to be trustable. A complete list of all parameters and possible identifications within the atomic database is given by Table ?? on page ??.

Table 4.4: List of lines in the ‘non-dip’ spectrum – sorted by χ^2 improvement (see text)

λ [Å]	EW [mÅ]	$\Delta\chi^2$		λ [Å]	EW [mÅ]	$\Delta\chi^2$		λ [Å]	EW [mÅ]	$\Delta\chi^2$	
6.18	-10.31	889	Si XIV	8.42	-11.98	780	Mg XII	12.13	-18.90	736	Ne X
12.28	-14.47	468	Fe XXI	12.83	-17.49	393	Fe XX	13.44	-18.54	301	Ne IX
9.17	-8.97	294	Mg XI	11.77	-10.01	249	Fe XXII	13.50	-17.72	241	Fe XIX
6.65	-6.62	215	Si XIII	10.62	-6.65	164	Fe XXIV	9.71	-8.57	154	Ne X
14.20	-21.96	142	Fe XVIII	9.47	-6.05	131	Ne X	10.24	-4.80	108	Ne X
10.99	-7.05	105	Fe XXIII	4.73	-4.13	93.6	S XVI	13.53	-10.90	88.5	Fe XIX
10.03	-6.85	86.7	Na XI	12.95	-9.91	80.3	Fe XIX	12.85	-7.08	79.7	Fe XX
13.46	-11.81	68.4	Fe XIX	16.00	-20.38	63.1	O VIII	5.04	-3.80	62.7	S XV
7.85	-4.78	62.4	Mg XI	12.27	-5.38	61.8	Fe XVII	1.94	5.00	58.8	Fe K α
5.68	-4.64	58.5	Si XIII	12.81	-5.44	58.1		11.01	-5.69	56.1	Ne IX
12.90	-8.60	55.7		10.66	-5.63	51.4	Fe XXIV	7.11	-2.31	49.6	Mg XII
7.17	-3.04	46.2	Al XIII	6.70	-3.67	45.4		12.11	-4.09	45.2	Fe XVII
8.00	-4.37	43.4		10.64	-3.83	42.7	Ne IX	15.00	-13.12	42.4	Fe XVII
11.09	8.28	42.1		14.25	-11.44	41.6	Fe XVIII	8.98	-2.73	41.6	Fe XXII
11.66	8.85	39.7		18.94	-55.11	38.1	O VIII	11.89	8.81	37.3	
6.72	-2.96	37.2		6.74	2.77	36.1	Si XIII	9.19	-3.35	35.3	Fe XXI
11.53	-3.48	34.7	Fe XVIII	11.70	8.77	34.1		5.22	-4.03	33.5	Si XIV
12.58	-5.68	31.6	Fe XX	13.15	-5.43	31.6		12.92	-4.74	30.6	Fe XX
11.43	-3.96	29.9	Fe XXII	11.59	6.56	28.9		6.78	-1.66	28.7	

Table 4.4: List of lines in the ‘non-dip’ spectrum – sorted by χ^2 improvement (continued)

λ [Å]	EW [mÅ]	$\Delta\chi^2$		λ [Å]	EW [mÅ]	$\Delta\chi^2$		λ [Å]	EW [mÅ]	$\Delta\chi^2$	
10.48	3.49	28.6		11.54	-3.47	28.4	Ne IX	13.15	7.94	28.1	
13.03	-6.46	27.9		11.18	5.78	27.2		14.62	-8.80	27.1	
11.21	5.55	26.4		12.25	-4.27	26.3	Fe XXII	13.42	-4.08	25.2	Fe XIX
13.05	-5.76	25.0	Fe XX	7.48	-1.80	24.9	Fe XXIII	8.01	2.31	24.7	
10.91	3.66	24.7		2.70	-1.64	23.9	Ca XIX	10.94	3.82	23.8	
11.32	-3.10	23.2	Fe XVIII	7.62	2.69	22.9		13.65	-8.11	22.3	Fe XIX
12.15	5.40	21.4		10.72	3.52	21.3		16.39	-24.67	21.2	
9.37	-3.18	21.0	Ne X	11.63	6.30	20.9		10.71	4.76	20.7	
9.99	-2.76	20.4	Fe XX	7.97	2.04	20.3		1.47	-4.43	19.9	
9.51	3.14	19.9		10.28	2.86	19.7		1.45	-4.50	19.3	
1.85	-2.11	18.6	Fe XXV	10.32	2.83	18.0		10.89	3.34	18.0	
10.30	2.55	18.0		9.31	2.45	17.9		13.79	-9.25	17.8	Fe XIX
8.31	-1.72	17.6	Fe XXIII	12.07	5.23	17.0		11.02	-2.24	16.6	Fe XXIII
9.54	2.46	16.6		12.21	5.07	16.2		11.97	-3.06	16.1	Fe XXI
2.29	1.81	16.0		18.63	-33.47	16.0	O VII	12.48	6.15	16.0	
12.57	-3.56	15.9		11.15	4.26	15.8		13.83	-9.17	15.6	Fe XIX
9.82	2.77	15.6		11.48	-3.16	15.4	Fe XXII	14.71	10.14	15.2	
9.28	-1.94	15.0		12.68	7.78	14.9		8.59	2.11	14.9	
11.37	3.25	14.8		1.52	-3.54	14.7	Ni XXVIII	13.63	-5.06	14.5	
1.99	2.28	13.9		9.23	2.02	13.2	Mg XI	2.03	1.77	13.1	
3.93	-1.54	13.0		12.04	3.71	13.0		7.96	1.65	12.9	
15.62	-7.54	12.9		9.91	2.48	12.7		4.30	-3.88	12.4	S XV
2.35	1.48	12.1		7.28	2.06	11.6		4.95	-1.42	11.2	Si XIV
9.40	-1.69	11.0		8.57	-1.75	11.0	Fe XXI	1.55	-3.02	10.9	
9.26	1.85	10.8		5.58	-1.41	10.7		18.74	-14.83	10.3	Ca XVIII
8.05	1.58	10.2		14.53	-5.97	10.1	Fe XVIII	6.76	1.35	9.89	
12.18	3.15	9.85		3.95	-1.11	9.13	Ar XVII	4.10	-1.88	9.11	S XV
8.38	1.53	9.09		9.33	1.94	9.01		10.12	-1.77	8.86	Fe XX
10.74	2.15	8.83		5.40	-1.42	8.68	Si XIII	13.12	4.51	8.64	
8.62	1.32	8.57		5.53	-1.44	8.51		13.76	-4.74	8.45	Fe XX
2.46	1.47	8.39		12.62	3.44	8.29		8.89	1.48	8.16	
10.34	1.94	8.05		3.21	-0.93	8.03	Ar XVII	5.86	-1.11	8.00	
2.69	1.32	7.90		10.82	-1.59	7.52		9.94	2.36	7.45	
16.24	-7.95	7.34		8.93	1.40	7.31		11.84	2.71	7.28	
13.67	-3.38	7.28		12.32	-2.24	7.24		6.06	-1.28	7.03	Al XIII
5.38	-1.42	6.93		9.40	1.46	6.92		7.79	1.46	6.72	Al XII
7.90	-1.30	6.68		1.49	-2.51	6.51	Fe XXV	14.37	-4.49	6.33	Fe XVIII
4.39	-1.09	6.31		3.19	1.01	6.23	Ca XIX	7.35	1.02	6.23	
3.07	-0.85	6.09		7.32	1.17	6.01		8.74	-1.11	5.97	Fe XXII
3.99	-1.73	5.90	S XVI	7.77	-1.15	5.86	Al XII	15.17	-4.71	5.67	O VIII
7.75	-1.09	5.59	Al XII	9.05	1.29	5.41		2.32	1.10	5.38	
8.22	1.13	5.13		8.71	-1.77	5.12		8.40	-0.86	5.02	
16.77	-7.34	4.84	Fe XVII	8.27	1.10	4.69		8.03	0.91	4.40	
2.44	0.82	4.27		10.76	-0.87	4.24	Ne IX	7.82	1.26	4.12	Al XII
3.73	-0.94	4.04	Ar XVIII	8.16	0.95	3.86		1.97	0.93	3.78	
7.93	-0.82	3.71		3.78	-0.64	3.27	S XVI	11.12	1.20	3.08	
3.02	-0.60	3.08	Ca XX	8.79	0.87	3.00		3.37	-0.60	2.79	Ar XVII
8.91	0.96	2.78		4.42	-0.66	2.75		2.98	-0.53	2.64	Ar XVIII
15.26	-3.28	2.49	Fe XVII	9.87	0.93	2.32		13.07	1.77	2.19	
3.19	-0.55	2.19	Ca XIX	5.07	0.77	2.18	S XV	8.10	0.61	2.18	
17.75	-5.83	1.45	Ar XVI	3.14	-0.44	1.36	Ar XVIII	6.32	-0.37	1.28	Al XII
3.70	-0.41	1.24	S XVI	7.88	0.47	1.16	Al XII	8.13	0.44	0.96	
5.10	0.34	0.56	S XV	9.97	-0.19	0.05					

Lines from H-, He-, and Li-like ions and further less-ionized iron ions

The following tables give an overview of the transitions identified in the ‘non-dip’ spectrum: Table 4.5 lists absorption lines of hydrogen-like ions, Table 4.6 describes the He-like triplets (which were found as r-absorption lines and both i- and f-emission lines), Table 4.7 and Table 4.8 show the absorption lines from helium- and lithium-like ions, and Table 4.9 finally compiles further iron absorption lines. Lines definitively seen are listed in with **bold** numbers; those showing only a small signal and not always fitted are marked *slanted*, and those, which are not seen, are ~~stroked out~~. Wavelengths not covered by the spectrum are put in ()-brackets.

Table 4.5: $\lambda/\text{\AA}$ of H-like ions’ absorption lines (as in Table ??) in the ‘non-dip’ spectrum

transition from $1s$	O VIII	Ne X	Na XI	Mg XII	Al XIII	Si XIV	S XVI	Ar XVIII	Ca XX	Fe XXVI	Ni XXVIII
$\rightarrow 2p$ (Ly α)	18.97	12.13	10.03	8.42	7.17	6.18	4.73	3.73	3.02	1.78	1.53
$\rightarrow 3p$ (Ly β)	16.01	10.24	8.46	7.11	6.05	5.22	3.99	3.15	2.55	1.50	1.29
$\rightarrow 4p$ (Ly γ)	15.18	9.71	8.02	6.74	5.74	4.95	3.78	2.99	2.42	1.42	1.23
$\rightarrow 5p$ (Ly δ)	14.82	9.48	7.83	6.58	5.60	4.83	3.70	2.92	2.36	1.39	1.20
$\rightarrow 6p$ (Ly ϵ)		9.36	7.73				3.65	2.88			
$\rightarrow 7p$		9.29					3.62				
$\rightarrow 8p$		9.25									
$\rightarrow 9p$		9.22									

Table 4.6: $\lambda/\text{\AA}$ of He-like ions’ triplets (as in Table ??) in the ‘non-dip’ spectrum: resonance (r) absorption line and intercombination (i) and forbidden (f) emission lines

transition from/to $1s^2$ (1S_0)	O VII	Ne IX	Na X	Mg XI	Al XII	Si XIII	S XV	Ar XVII	Ca XIX	Fe XXV	Ni XXVII
$r_{\text{abs}} 1s2p$ (1P_1)	(21.60)	13.45	11.00	9.17	7.76	6.65	5.04	3.95	3.18	1.85	1.59
$i_{\text{em}} 1s2p$ ($^3P_{2,1}$)	(21.80)	13.55	11.08	9.23	7.80	6.69	5.07	3.97	3.19	1.86	1.60
$f_{\text{em}} 1s2s$ (3S_1)	(22.10)	13.70	11.19	9.31	7.87	6.74	5.10	3.99	3.21	1.87	

Table 4.7: $\lambda/\text{\AA}$ of He-like ions’ absorption lines (as in Table ??) in the ‘non-dip’ spectrum

transition from $1s^2$	O VII	Ne IX	Na X	Mg XI	Al XII	Si XIII	S XV	Ar XVII	Ca XIX	Fe XXV	Ni XXVII
$\rightarrow 1s2p$	(21.60)	13.45	11.00	9.17	7.76	6.65	5.04	3.95	3.18	1.85	1.59
$\rightarrow 1s3p$	18.63	11.54	9.43	7.85	6.63	5.68	4.30	3.37	2.71	1.57	1.35
$\rightarrow 1s4p$	17.77	11.00	8.98	7.47	6.31	5.40	4.09	3.20	2.57	1.50	1.28
$\rightarrow 1s5p$	17.40	10.77	8.79	7.31	6.18	5.29	4.00	3.13	2.51	1.46	1.25
$\rightarrow 1s6p$	17.20	10.64	8.69	7.22	6.10	5.22	3.95	3.10			
$\rightarrow 1s7p$	17.09	10.57	8.63	7.17	6.06	5.19	3.92				
$\rightarrow 1s8p$	17.01	10.51	8.59	7.14	6.03	5.16	3.90				

Table 4.8: $\lambda/\text{\AA}$ of Li-like ions’ absorption lines (as in Table ??) in the ‘non-dip’ spectrum

transition	S XIV	Ar XVI	Ca XVIII	Fe XXIV	Ni XXVI
$[1s^2] 2s \rightarrow [1s^2] 3p$ ($^2P_{1/2}$)	(30.5)	(23.59)	18.73	10.66	9.10
$[1s^2] 2s \rightarrow [1s^2] 3p$ ($^2P_{3/2}$)	(30.4)	(23.55)	18.69	10.62	9.06
$[1s^2] 2s \rightarrow [1s^2] 4p$	(23.0)	17.74	14.09	8.00	6.82
$[1s^2] 2s \rightarrow [1s^2] 5p$	(20.7)	15.93	12.64	7.17	6.11
$[1s^2] 2s \rightarrow [1s^2] 6p$			11.99	6.79	
$[1s^2] 2s \rightarrow [1s^2] 7p$			11.62		

Table 4.9: Further absorption lines of iron (as in Table ??) in the ‘non-dip’ spectrum

(a) Fe xxiii (Be-like ion, as in Table ??)

transition	$\lambda/\text{\AA}$
$[1s^2] (2s^2 ({}^1S_0) \rightarrow 2s3p ({}^1P_1))$	10.98
$[1s^2] (2s^2 ({}^1S_0) \rightarrow 2s3p ({}^1P_1))$	8.30
$[1s^2] (2s^2 ({}^1S_0) \rightarrow 2s5p ({}^1P_1))$	7.47
$[1s^2] (2s^2 ({}^1S_0) \rightarrow 2s3p ({}^3P_1))$	11.02
$[1s^2] (2s^2 ({}^1S_0) \rightarrow 2s4p ({}^3P_1))$	8.32

(b) Fe xxii (B-like ion, as in Table ??)

transition	$\lambda/\text{\AA}$
$[1s^2 2s^2] (2p ({}^2P_{1/2}) \rightarrow 3s ({}^2S_{1/2}))$	12.25
$[1s^2 2s^2] (2p ({}^2P_{1/2}) \rightarrow 3d ({}^2D_{3/2}))$	11.77
$[1s^2 2s^2] (2p ({}^2P_{1/2}) \rightarrow 4s ({}^2S_{1/2}))$	9.06
$[1s^2 2s^2] (2p ({}^2P_{1/2}) \rightarrow 4d ({}^2D_{3/2}))$	8.97
$[1s^2 2s^2] (2p ({}^2P_{1/2}) \rightarrow 5s ({}^2S_{1/2}))$	8.11
$[1s^2 2s^2] (2p ({}^2P_{1/2}) \rightarrow 5d ({}^2D_{3/2}))$	8.09
$[1s^2] 2s 2p (2s ({}^2P_{1/2}) \rightarrow 3p_{3/2})$	11.49
$[1s^2] 2s 2p (2s ({}^2P_{1/2}) \rightarrow 3p_{3/2})$	11.43

(c) Fe xxi (C-like ion, as in Table ??)

transition	$\lambda/\text{\AA}$
$[1s^2 2s^2] 2p (2p ({}^3P_0) \rightarrow 3d ({}^3D_0))$	12.28
$[1s^2] 2s 2p^2 (2s ({}^3P_0) \rightarrow 3p_{3/2})$	11.97
$[1s^2] 2s 2p^2 (2s ({}^3P_0) \rightarrow 3p_{3/2})$	11.95
$[1s^2 2s^2] 2p (2p ({}^3P_0) \rightarrow 4d ({}^3P_1))$	9.48
$[1s^2] 2s 2p^2 (2s ({}^3P_0) \rightarrow 4p_{3/2})$	9.19
$[1s^2 2s^2] 2p (2p ({}^3P_0) \rightarrow 5d_{3/2})$	8.57

(e) Fe xix (O-like ion, as in Table ??)

transition	$\lambda/\text{\AA}$
$[1s^2 2s^2] 2p^3 (2p ({}^3P_2) \rightarrow 3d_{5/2})$	13.79
$[1s^2 2s^2] 2p^3 (2p ({}^3P_2) \rightarrow 3d ({}^3F_3))$	13.64
$[1s^2 2s^2] 2p^3 (2p ({}^3P_2) \rightarrow 3d_{5/2})$	13.55
$[1s^2 2s^2] 2p^3 (2p ({}^3P_2) \rightarrow 3d ({}^3D_3))$	13.52
$[1s^2 2s^2] 2p^3 (2p ({}^3P_2) \rightarrow 3d_{3/2})$	13.50
$[1s^2 2s^2] 2p^3 (2p ({}^3P_2) \rightarrow 3d ({}^3S_1))$	13.46
$[1s^2 2s^2] 2p^3 (2p ({}^3P_2) \rightarrow 3d ({}^1F_3))$	13.42
$[1s^2] 2s 2p^4 (2s ({}^3P_2) \rightarrow 3p_{3/2})$	12.95
$[1s^2] 2s 2p^4 (2s ({}^3P_2) \rightarrow 3p_{3/2})$	12.93
$[1s^2 2s^2] 2p^3 (2p ({}^3P_2) \rightarrow 4d ({}^3D_3))$	10.82
$[1s^2 2s^2] 2p^3 (2p ({}^3P_2) \rightarrow 4d ({}^3F_3))$	10.68
$[1s^2 2s^2] 2p^3 (2p ({}^3P_2) \rightarrow 4d ({}^3D_3))$	10.65
$[1s^2 2s^2] 2p^3 (2p ({}^3P_2) \rightarrow 4d ({}^3P_2))$	10.64
$[1s^2 2s^2] 2p^3 (2p ({}^3P_2) \rightarrow 4d ({}^3S_1))$	10.63
$[1s^2 2s^2] 2p^3 (2p ({}^3P_2) \rightarrow 5d ({}^3D_3))$	9.86
$[1s^2 2s^2] 2p^3 (2p ({}^3P_2) \rightarrow 5d (...))$	9.69

(d) Fe xx (N-like ion, as in Table ??)

transition	$\lambda/\text{\AA}$
$[1s^2 2s^2] 2p^2 (2p ({}^4S_{3/2}) \rightarrow 3s ({}^4P_{1/2}))$	13.96
$[1s^2 2s^2] 2p^2 (2p ({}^4S_{3/2}) \rightarrow 3s ({}^4P_{3/2}))$	13.84
$[1s^2 2s^2] 2p^2 (2p ({}^4S_{3/2}) \rightarrow 3s ({}^4P_{5/2}))$	13.77
	13.06
	12.99
$[1s^2 2s^2] 2p^2 (2p ({}^4S_{3/2}) \rightarrow 3d (...))$	12.97...12.96
	12.92...12.91
	12.86...12.85
	12.83...12.82
	12.76...12.75
$[1s^2] 2s 2p^3 (2s ({}^4S_{3/2}) \rightarrow 3p (...))$	12.58
	12.53
$[1s^2 2s^2] 2p^2 (2p ({}^4S_{3/2}) \rightarrow 4d (...))$	10.13...10.12
	10.04...10.06
	9.99...10.01
$[1s^2] 2s 2p^3 (2s ({}^4S_{3/2}) \rightarrow 4p (...))$	9.73...9.72
	9.20...9.19
$[1s^2 2s^2] 2p^2 (2p ({}^4S_{3/2}) \rightarrow 5d (...))$	9.11...9.10
	9.07...9.06
$[1s^2 2s^2] 2p^3 ({}^4S_{3/2}) \rightarrow ...$	8.82

(f) Fe xviii (F-like ion, as in Table ??)

transition	$\lambda/\text{\AA}$
$[1s^2 2s^2] 2p^4 (2p ({}^2P_{3/2}) \rightarrow 3s ({}^2P_{3/2}))$	16.00
$[1s^2 2s^2] 2p^4 (2p ({}^2P_{3/2}) \rightarrow 3s ({}^2P_{1/2}))$	15.76
$[1s^2 2s^2] 2p^4 (2p ({}^2P_{3/2}) \rightarrow 3d ({}^4P_{1/2}))$	14.60
$[1s^2 2s^2] 2p^4 (2p ({}^2P_{3/2}) \rightarrow 3d ({}^4P_{3/2}))$	14.57
$[1s^2 2s^2] 2p^4 (2p ({}^2P_{3/2}) \rightarrow 3d ({}^2F_{5/2}))$	14.53
$[1s^2 2s^2] 2p^4 (2p ({}^2P_{3/2}) \rightarrow 3d ({}^2D_{5/2}))$	14.37
$[1s^2 2s^2] 2p^4 (2p ({}^2P_{3/2}) \rightarrow 3d (...))$	14.26
$[1s^2 2s^2] 2p^4 (2p ({}^2P_{3/2}) \rightarrow 3d (...))$	14.21
$[1s^2 2s^2] 2p^4 (2p ({}^2P_{3/2}) \rightarrow 3d ({}^2D_{3/2}))$	14.16
$[1s^2 2s^2] 2p^4 (2p ({}^2P_{3/2}) \rightarrow 3d ({}^2P_{1/2}))$	14.14
$[1s^2 2s^2] 2p^4 (2p ({}^2P_{3/2}) \rightarrow 3d ({}^2D_{5/2}))$	13.95
$[1s^2] 2s 2p^5 (2s ({}^2P_{3/2}) \rightarrow 3p_{3/2})$	13.41
$[1s^2] 2s 2p^5 (2s ({}^2P_{3/2}) \rightarrow 3p ({}^2D_{5/2}))$	13.39
$[1s^2] 2s 2p^5 (2s ({}^2P_{3/2}) \rightarrow 3p ({}^2P_{3/2}))$	13.36
$[1s^2] 2s 2p^5 (2s ({}^2P_{3/2}) \rightarrow 3p (...))$	13.32
$[1s^2] 2s 2p^5 (2s ({}^2P_{3/2}) \rightarrow 3p ({}^2S_{1/2}))$	13.18
...	

In the rest of this section, the spectral shape and other notable facts of the lines quoted in this overview will be discussed in detail.

(f) Fe XVIII (F-like ion; continued)

transition	$\lambda/\text{\AA}$
...	
$[1s^2 2s^2] 2p^4 (2p (^2P_{3/2}) \rightarrow 4d_{5/2})$	11.57
$[1s^2 2s^2] 2p^4 (2p (^2P_{3/2}) \rightarrow 4d (\dots))$	11.53
$[1s^2 2s^2] 2p^4 (2p (^2P_{3/2}) \rightarrow 4d (^2F_{5/2}))$	11.42
$[1s^2 2s^2] 2p^4 (2p (^2P_{3/2}) \rightarrow 4d (\dots))$	11.33
$[1s^2 2s^2] 2p^4 (2p (^2P_{3/2}) \rightarrow 4d_{5/2})$	11.31
$[1s^2 2s^2] 2p^4 (2p (^2P_{3/2}) \rightarrow 4d (^2D_{3/2}))$	11.29
$[1s^2] 2s 2p^5 (2s (^2P_{3/2}) \rightarrow 4p_{3/2})$	10.57
$[1s^2] 2s 2p^5 (2s (^2P_{3/2}) \rightarrow 4p_{3/2})$	10.56
$[1s^2 2s^2] 2p^4 (2p (^2P_{3/2}) \rightarrow 5d (\dots))$	10.54
$[1s^2 2s^2] 2p^4 (2p (^2P_{3/2}) \rightarrow 5d (^2D_{5/2}))$	10.45
$[1s^2 2s^2] 2p^4 (2p (^2P_{3/2}) \rightarrow 5d (\dots))$	10.36

(g) Fe XVII (Ne-like ion, as in Table ??)

transition	$\lambda/\text{\AA}$
$[1s^2 2s^2] 2p^5 (2p (^1S_0) \rightarrow 3s (^3P_1))$	17.05
$[1s^2 2s^2] 2p^5 (2p (^1S_0) \rightarrow 3s (^1P_1))$	16.78
$[1s^2 2s^2] 2p^5 (2p (^1S_0) \rightarrow 3d (^3D_1))$	15.26
$[1s^2 2s^2] 2p^5 (2p (^1S_0) \rightarrow 3d (^1P_1))$	15.01
$[1s^2] 2s 2p^6 (2s (^1S_0) \rightarrow 3p (^1P_1))$	13.82
$[1s^2 2s^2] 2p^5 (2p (^1S_0) \rightarrow 4d (^3D_1))$	12.27
$[1s^2 2s^2] 2p^5 (2p (^1S_0) \rightarrow 4d (^1P_1))$	12.12
$[1s^2 2s^2] 2p^5 (2p (^1S_0) \rightarrow 5d (^3D_1))$	11.25
$[1s^2 2s^2] 2p^5 (2p (^1S_0) \rightarrow 5d (^1P_1))$	11.13
$[1s^2] 2s 2p^6 (2s (^1S_0) \rightarrow 4p (^1P_1))$	11.03
$[1s^2 2s^2] 2p^5 (2p (^1S_0) \rightarrow 6d (^3D_1))$	10.77
$[1s^2 2s^2] 2p^5 (2p (^1S_0) \rightarrow 6d (^1P_1))$	10.66
$[1s^2 2s^2] 2p^5 (2p (^1S_0) \rightarrow 7d (^3D_1))$	10.50
$[1s^2] 2s 2p^6 (2s (^1S_0) \rightarrow 5p (^1P_1))$	10.12

Table 4.9: Further iron lines (end)

Oxygen

- O VIII (H-like ion)

Although the $1s \rightarrow 2p$ transition is at a wavelength ($\lambda = 18.97 \text{\AA}$) where the count rate in this observation's HETGS spectra is rather low (≈ 3 counts/bin in MEG-1, ≈ 1 count/bin in MEG+1 and 0 counts in HEG ± 1), MEG-1 shows evidence for an absorption feature at $\lambda \approx 18.95 \text{\AA}$, which stays significant (3σ), even if the spectrum is rebinned. As this is not seen in MEG+1, this transition is not included into the analysis.

The $1s \rightarrow 3p$ transition at $\lambda = 16.01 \text{\AA}$ is clearly seen in both MEG ± 1 spectra. HEG-1's count rate is too low (≈ 1 count/bin) and HEG+1's one is zero. Although this line is a blend with a ground state excitation of Fe XVIII at $\lambda = 16.00 \text{\AA}$ with $A = 1.4 \times 10^{12} \text{ s}^{-1}$, it is attributed to O VIII ($A = 0.7 \times 10^{12} \text{ s}^{-1}$) due to the higher abundance of oxygen (cf. Table ??). At $\lambda \approx 15.17 \text{\AA}$, a weak feature is visible, which might originate from the $1s \rightarrow 4p$ transition. Finally, the $1s \rightarrow 5p$ transition cannot be seen.

- O VII (He-like ion)

The $1s^2 \rightarrow 1s2p$ transitions occur at $\lambda \geq 21.6 \text{\AA}$, where even the count rate in the MEG spectra is too low. There seems to be a signal in the MEG spectra at the $1s^2 \rightarrow 1s3p$ transition's wavelength $\lambda = 18.63 \text{\AA}$, but this blends with Ar XVI lines and cannot be properly fitted. Transitions from $1s^2$ to $1s4p$ (at $\lambda = 17.77 \text{\AA}$) or higher levels are not seen.

Fluorine

The fluorine lines are not included in the atomic database ATOMDB, but in the table of Verner et al. (1996). From the low abundance (cf. Table ??), however, one would not expect to see fluorine lines anyway.

- F IX (H-like ion)

At the wavelengths of the Lyman series – namely 14.98\AA , 12.64\AA , 11.99\AA , 11.70\AA , 11.56\AA , ..., the spectrum shows the following features: At 15.00\AA , there is a relatively deep absorption line. The database transition that matches best is Fe XVII, $1s^2 2s^2 2p^6 \rightarrow 1s^2 2s^2 2p^5 3d$ at 15.014\AA . Near 12.64\AA , there is a large scatter in the count rate, but the continuum seems somehow to be too low. Although the flux is slightly lower at 12.635\AA , there is no clear absorption line nor emission lines in the neighborhood. There is a clear absorption feature at 11.97\AA , which could be due to the Fe XXI, $1s^2 2s^2 2p^2 \rightarrow 1s^2 2s 2p^2 3p$ transition at 11.975\AA . As a result, there is probably no absorption from the F IX Lyman series.

Neon

- Ne x (H-like ion)

Although the strong $1s \rightarrow 2p$ line at $\lambda = 12.13 \text{ \AA}$ overlaps with another line at $\lambda = 12.11 \text{ \AA}$ in the MEG spectra, both can be distinguished and separately modeled with help of the more strongly dispersed HEG spectra. The $1s \rightarrow 3p$ line at $\lambda = 10.24 \text{ \AA}$ is also very strong. The $1s \rightarrow 4p$ line at $\lambda = 9.71 \text{ \AA}$ is clearly visible but might be blended with Fe XIX ground state transitions. Assigning this line entirely to Ne x gives thus an upper limit of the equivalent width. The same holds for the Ly δ line at $\lambda = 9.48 \text{ \AA}$, which overlaps with a Fe XXI ground state transitions. (The same fact has been noticed by [Miller et al. \(2005\)](#), who only confuses Ly γ with Ly δ , or respectively Fe XXI with Fe XIX.) The given equivalent width and therefore column density is thus only an upper limit. Transitions to higher levels are unfortunately not included in the atomic database, but their wavelengths can be calculated from Eq. (2.4). The Ly ϵ ($1s \rightarrow 6p$) line at $\lambda = 9.36 \text{ \AA}$ might be seen, but there are also transitions from the ground state of Ni XX and Ni XXV at this wavelength. The next line of the Lyman series corresponding to the $1s \rightarrow 7p$ transition, should appear at 9.29 \AA . In fact, there is an absorption feature at 9.278 \AA which has no really convincing identification. The $1s \rightarrow 8p$ line at $\lambda = 9.25 \text{ \AA}$ is not so well seen in the spectrum, but this might be due to an improper modeling of the continuum, as two empirical emission lines (without identification) have been included at 9.235 and 9.26 \AA . At last, there is definitely no evidence for the $1s \rightarrow 9p$ transition at 9.22 \AA .

- Ne IX (He-like ion)

The $1s^2 \rightarrow 1s2p$ transition at $\lambda = 13.45 \text{ \AA}$ is definitely seen, but hard to measure quantitatively, as there seem to be at least three overlapping lines next to each other, provided that the line is not yet saturated enough that the line wings become as clearly resolved. (In fact, the other features find explanations in the Fe XIX series.) Although there are some positive fluctuations around 13.55 \AA , there is no significant evidence for the intercombination line. A bold explanation is the coincidence of this emission line with an absorption line of Fe XIX. The forbidden line at 13.70 \AA is not seen as well.

The $1s^2 \rightarrow 1s3p$ transition at $\lambda = 11.54 \text{ \AA}$ overlaps with another line at 11.53 \AA , but they are well enough resolved to be separated. At 11.00 \AA , where the $1s^2 \rightarrow 1s4p$ line is expected, there are (at least) three almost overlapping absorption lines, which are hard to fit separately, and the Ne IX line probably blends with a Na x resonance line. The measured equivalent width is therefore an upper limit. Although there is only little evidence for the $1s^2 \rightarrow 1s5p$ line near 10.77 \AA , the $1s^2 \rightarrow 1s6p$ line at 10.64 \AA is visible much more strongly than expected. It seems that there is even still some evidence for the $1s^2 \rightarrow 1s7p$ transition at 10.57 \AA . There is finally nothing (but a single bin outlier in the HEG-1 at 10.50 \AA) that could be identified with the $1s^2 \rightarrow 1s8p$ line.

Sodium

Sodium lines are not included in the ATOMDB, but in [Verner et al. \(1996\)](#).

- Na XI (H-like ion)

At 10.03 \AA , there is a relatively strong absorption line, which has no convincing interpretation within the atomic database. It is therefore highly likely that this is a Na XI Ly α line. At 8.47 \AA , there is a weak absorption line-like feature in the HEG spectra, which is not so clear in the MEG spectra. (It is not visible at all in the MEG+1.) The continuum near 8.02 \AA is not described very well; 2 “emission lines” are included in the model at 8.01 \AA and 8.03 \AA . (In fact, there are only “emission lines” from 8 \AA to 8.3 \AA .) It is thus much more likely that there is an absorption line at 8.02 \AA ! An absorption line at 7.83 \AA is not visible but only in the HEG+1 spectrum. At 7.73 \AA , no line can be seen at all.

- Na x (He-like ion)

As stated above for the Ne ix $1s^2 \rightarrow 1s4p$ transition at 11.00 Å, three overlapping absorption lines are detected at 10.99 Å, 11.01 Å and 11.02 Å. In comparison with this Ne ix line, the blending Na x $1s^2 \rightarrow 1s2p$ line has the higher oscillator strength (by a factor of 13 Verner et al., 1996), but sodium’s abundance (however, in the ISM) is lower by a factor of 60 than neon’s one (Wilms et al., 2000). If the lines are not saturated and the ionization fractions are comparable, one would expect the Na x line to be stronger by a factor of 4.6. In the region from 11.05 Å to 11.23 Å, the continuum is too low, but no (real, narrow) emission line can be identified, including no intercombination or forbidden line at 11.08 Å and 11.19 Å.

There is almost no evidence for a line near 9.43 Å, where the $1s^2 \rightarrow 1s3p$ transition should occur. For this reason, the strong absorption line at 8.98 Å is much more likely to be from Fe xxii, $1s^2 2s^2 2p \rightarrow 1s^2 2s^2 4d$ than from the $1s^2 \rightarrow 1s4p$ transition. At 8.79 Å, the continuum seems to be unreliable; while there is currently an emission line at 8.786 Å, there could be an absorption at a higher wavelength as well – although the profile of the spectrum is not convincing for either possibility. Higher transitions are definitely not seen.

Magnesium

- Mg xii (H-like ion)

Absorption from the $1s$ ground state was detected into the levels $2p$ (8.42 Å) and $3p$ (7.11 Å), but not into $4p$ (at $\lambda = 6.74$ Å, which is hard to detect due to the blend with the Si xiii forbidden emission line and also calibration difficulties on the Si-edge) or higher: At $\lambda_{Ly\delta} = 6.58$ Å, no line is seen as well.

- Mg xi (He-like ion)

Mg xi is the only ion in this spectrum where the forbidden line (at 9.31 Å) and the intercombination line (at 9.23 Å) can clearly be seen in emission. The recombination line $1s^2 \rightarrow 1s2p$ ($\lambda = 9.17$ Å) could uniquely be identified to be in absorption. The $1s^2 \rightarrow 1s3p$ transition ($\lambda = 7.865$ Å) is also seen quite strong. The $1s^2 \rightarrow 1s4p$ transition at 7.47 Å can clearly be seen, but this line is a blend with a (rather strong) transition of Fe xxiii. The $1s^2 \rightarrow 1s5p$ transition at 7.31 Å is not seen in absorption, there are however emission lines in the vicinity of this wavelength. Higher transitions are not visible.

Aluminum

- Al xiii (H-like ion)

The Ly α line is seen as a strong absorption line. At 6.05 Å, only a weak absorption feature is seen, which is not significant enough to be fitted. Neither the Ly γ or Ly δ line is visible in the spectrum.

- Al xii (He-like ion)

There is an absorption line at 7.76 Å likely corresponding to the resonance transition, which is difficult to fit as there seem to be several separate lines in the vicinity whose signal is not consistent in all four spectra. If, however, only the HEG spectra are considered, two relatively clear absorption lines become visible. If both arise from the first excitation of Al xii, one is red- and one is blue-shifted. The same holds for the intercombination line: There are two nice emission features around 7.80 Å in the HEG spectra. The weak forbidden line at 7.87 Å, shows up, however, as only one component. The $1s^2 \rightarrow 1s4p$ transition at 6.63 Å blends with the strong Si xv resonance line at 6.65 Å, but it seems that they may be separated from the HEG spectra, which show a knee in the line profile. At 6.31 Å, there is a small line feature, which is not very

significant, although it appears in the MEG+1 and both the HEG±1 spectra. The $1s^2 \rightarrow 1s5p$ line at 6.18 Å overlaps with the strongest line of the whole spectrum, Si XIV Ly α , such that there is no way to separate and fit it. Higher transitions are not clearly visible as well.

Silicon

- Si XIV (H-like ion)

The Ly α line at 6.18 Å is in fact the strongest (absorption) line in the whole spectrum. The Ly β and Ly γ lines are clearly visible as well. Ly β appears however quite broad, which might be due to an additional weak contribution from the Si XIII $1s^2 \rightarrow 1s6p$ transition. However the $1s \rightarrow 5p$ transition is not seen. Furthermore, there are two absorption features at 5.53 and 5.58 Å, that might be autoionization resonances.

- Si XIII (He-like ion)

The recombination line is clearly seen in absorption. The intercombination line is not visible as an emission line, but its position coincides with the Si K-edge, where the instrumental calibration might be quite difficult. The forbidden line is detected in emission, again much nicer in the HEG spectra than with the MEG.

Absorption lines from the $1s^2 \rightarrow 1s3p$ and $1s^2 \rightarrow 1s4p$ transitions are detected, while there is only a weak signal near 5.28 Å, that might arise from the $1s^2 \rightarrow 1s5p$ transition. The $1s^2 \rightarrow 1s6p$ transition blends with Si XIV Ly β , but it is also not expected to be still visible. Higher transitions are not seen as well.

Sulfur

- S XVI (H-like ion)

The Ly α line is clearly detected. There are features near Ly β 's 3.99 Å, but they are both neither very significant nor consistent within all four spectra. But one has to notice that this line also blends with the forbidden emission line of Ar XVII. While the Ly γ line at 3.78 Å can only be divined, the $1s \rightarrow 5p$ absorption at 3.70 Å can be seen quite well in the HEG spectra. At the wavelength of Ly ϵ , 3.65 Å, there are only small fluctuations – too tiny to be identified as a line, although it is really tempting that there are similar ‘fluctuations’ at 6.62 Å as well, which should be the position of the next line in the Lyman series.

- S XV (He-like ion)

Both the intercombination and the forbidden line of S XV are present as emission features (at 5.07 Å and 5.10 Å respectively), but not with a clear line-profile. The best fit is therefore quite broad. The resonance line is however detected as a strong absorption line. At the $1s^2 \rightarrow 1s3p$ transition’s wavelength 4.30 Å, one can see a weak absorption-line-like feature in the residuals, which could not be fitted very well, but only by quite a broad Gaussian. The $1s^2 \rightarrow 1s4p$ transition at 4.09 Å is even seen better. The $1s^2 \rightarrow 1s5p$ transition is not found very clearly, there are several fluctuations around 4 Å which are not significant enough. (The absorption feature at 3.99 Å has most likely to be assigned to the S XVI line.) The absorption line at 3.95 Å is certainly due to the transition from the ground state of Ar XVII to its first excited state.

Argon

- Ar XVIII (H-like ion)

The first 3 lines of the Ar XVIII Lyman series are mainly visible in the HEG, although still quite weak. The Ly δ line at 2.92 Å is not seen.

- Ar XVII (He-like ion)

While the $1s^2 \rightarrow 1s2p$ resonance absorption-line can be seen quite well, the intercombination line is not seen as more than a 1σ emission feature in the MEG and the forbidden line is not seen at all. The latter is problematic anyway, as it overlaps with the Lyman β absorption line of S XVI. The line from the $1s^2 \rightarrow 1s3p$ is mainly seen in the HEG, as well as the $1s^2 \rightarrow 1s4p$ line. Near 3.13 Å, there are only small indications in the HEG of a weak feature that might arise from the next line in this series. The $1s^2 \rightarrow 1s6p$ line at 3.10 Å is not seen as well.

- Ar XVI (Li-like ion)

The $1s^22s \rightarrow 1s^23p$ line at 23.6 Å is well above the end of the MEG spectra, but the $1s^22s \rightarrow 1s^23p$ transition at 17.74 Å can be seen quite well. At 15.93 Å, only a 1σ single bin feature appears in the MEG–1 spectrum.

Calcium

- Ca XX (H-like ion)

While the Ly α line at 3.02 Å can be seen, there is no signal at $\lambda_{\text{Ly}\beta} = 2.55$ Å. However, near wavelength 2.42 Å of the Ly γ line, there is an absorption feature in the HEG, although it is not significant enough to be fitted with an absorption line. But this could also be due to the fact that there is a single bin emission at higher energy with a significance of 3σ .

- Ca XIX (He-like ion)

There are absorption and emission features in the HEG spectra immediately below 3.20 Å, which might arise from the resonance and intercombination line of Ca XIX, but they are neither very significant nor consistently line-like shaped.

The $1s^2 \rightarrow 1s3p$ transition is seen quite clearly in the HEG spectra, but the MEG spectra behave contradictory. There is no evidence for absorption lines to higher levels.

At 16.23 Å and 16.28 Å, there are tiny *emission features*, that might be identified with the *Balmer α lines* $3p (^2P_{3/2,1/2}) \rightarrow 2s (^2S_{1/2})$.

- Ca XVIII (Li-like ion)

Despite the low count rate (≈ 3 counts/bin in the whole 16 ks) in the MEG, the 18.73 Å absorption line from the $1s^22s \rightarrow 1s^23p (^2P_{1/2})$ can be seen with a line profile that is as nice as possible with a continuum of 3 counts! At 18.69 Å, where the (stronger) $1s^22s \rightarrow 1s^23p (^2P_{3/2})$ line is expected, there is, however, less signal of an absorption line. The next lines from this series, which are at 14.09 Å and 12.64 Å – and thus in regions of much higher count rate, but unfortunately also bad continuum description – could not be fitted well enough. The two included “emission lines” at 12.62 Å and 12.68 Å might in fact be an absorption line at 12.64 Å. Higher transitions are not seen.

Iron

- Fe XXVI (H-like ion)

Although there is a negative fluctuation at 1.77 Å in the MEG–1 spectrum and some absorption-line-like feature at 1.78 Å in the HEG+1 spectrum, the Ly α at 1.78 Å is not convincingly visible. The Ly β transition at 1.50 Å blends with an Fe XXV line. At 1.42 Å, where the Ly γ transition is expected, there are only very small indications of an absorption feature in the HEG spectra. (The MEG spectra have almost no counts in this wavelength range.)

One might wonder if the *emission-line* like features at both 9.54 Å and 9.58 Å could be assigned to the *Balmer α lines* $3p (^2P_{3/2,1/2}) \rightarrow 2s (^2S_{1/2})$.

- Fe xxv (He-like ion)

There are no indications for intercombination or forbidden lines, but the resonance line is seen as relatively strong absorption line with almost no shift in wavelength. The $1s^2 \rightarrow 1s3p$ transition is expected at 1.57 Å. At this position, there is only a small absorption feature in the HEG+1 spectrum. However, there is a clear absorption at 1.55 Å. Such a large blue shift is surprising, as the resonance line, which is expected to be the strongest of this series (and has in fact a very nice line profile), is almost unshifted. There are also no other absorption lines near 1.85 Å, which could be identified with a strongly shifted r-line. Looking for the $1s^2 \rightarrow 1s4p$ line at 1.50 Å, one only finds a single bin 1σ negative deviation from the continuum. However at 1.49 Å, there is an absorption line which is more significant. The $1s^2 \rightarrow 1s5p$ transition at 1.461 Å is not seen unshifted, but there are two quite clear absorption lines at 1.467 Å and 1.447 Å. None of these two lines can be interpreted as Fe xxv $1s^2 \rightarrow 1s5p$ with certainty, as it would both be surprising if the last transition of this series was red shifted or if it was so strongly blue-shifted. Besides, this line should be weaker than the others due to the lower Einstein coefficient.

- Fe xxiv (Li-like ion)

In contrast to Ca xviii, both $1s^22s \rightarrow 1s^23p$ lines of Fe xxiv are clearly visible separately, and the stronger $^2S_{1/2} \rightarrow ^2P_{3/2}$ transition also appears as stronger line. There is an absorption feature at 7.99 Å, near where the next transition $1s^22s \rightarrow 1s^24p$ is expected. But this one is not so clear to fit convincingly. The next higher transitions at 7.17 Å cannot be detected, as it blends with the strong Al xiii Ly α line, and at 6.79 Å, there is no absorption line as well.

- Fe xxiii (Be-like ion)

The first excitation (in usual dipole approximation) ($1s^22s^2 (^1S_0) \rightarrow 1s^22s3p (^1P_1)$) may be seen at 10.99 Å, which is the assembly of three (or more) lines around 11.00 Å (see Ne ix, Na x). The line at 11.02 Å would match the excitation from the same ground state to the $1s^22s3p (^3P_1)$ state, but as this has to occur via magnetic dipole transition, its transition probability and therefore line strength should be lower. The $1s^22s^2 \rightarrow 1s^22s4p$ line at 8.30 Å is seen, as well as the transition to the $1s^22s5p$ state at 7.47 Å. The latter would blend with a line of Mg xi, but the Fe xxiii is expected to be stronger – because of both the Einstein coefficient and the abundance.

- Fe xxii (B-like ion)

All excitations of the lone $2p$ from the $[1s^2]2s^22p$ ground state with $A > 5 \times 10^{12}/s$, i.e., those at 12.25 Å, 11.77 Å and 8.97 Å, are seen in absorption. For the excitations of one of the $2s$ electrons to a $3p$ level, only the strongest transitions are seen, namely those at 11.49 Å and 11.43 Å.

- Fe xxi (C-like ion)

The $2p \rightarrow 3d$ transition at 12.28 Å is visible as a strong absorption line, overlapping with two other lines at smaller wavelengths, which can be separated in the HEG spectra. The stronger $2s \rightarrow 3p$ line at 11.97 Å is seen, but the weaker one at 11.95 Å appears hardly as an absorption feature. The $2p \rightarrow 4d$ transition at 9.48 Å blends with the Ne x $1s \rightarrow 5p$ line. As the Ly δ line has a (by almost an order of magnitude) lower Einstein coefficient than the Fe xxi line, while the abundance of neon is only 3 times that of iron, it is expected that the latter significantly contributes to the absorption in this line. At 9.18 Å, near the strongest $2s \rightarrow 4p$ transition, there is an absorption feature which has no clear lineprofile and is therefore hard to fit. The $2p \rightarrow 5d$ line at 8.57 Å is seen more clearly, but however very broad, which probably indicates that actually more transitions contribute.

- Fe xx (N-like ion)

From the $[1s^2 2s^2] 2p^3$ ground state's $2p \rightarrow 3s$ transitions, the line at 13.96 Å (to the $^4P_{1/2}$ state) is not seen. However the absorption features between 13.75 Å and 13.85 Å, that may only just be separated in lines, might partly be caused by transitions to $^4P_{3/2}$ and $^4P_{5/2}$ at 13.84 Å and 13.77 Å. At almost all wavelengths of the 12 transitions $2p \rightarrow 3d$ quoted in Table 4.9d, absorption-line features can be seen, which could be identified with those Fe xx lines – the exceptions are at 12.99 Å, where there is only a weak feature, and near 12.75 Å, where no absorption is seen at all. At 12.58 Å, there is a strong absorption feature, which may be identified with two of the $2s \rightarrow 3p$ transitions. However the other line at 12.53 Å is not seen. Concerning the $2p \rightarrow 4d$ transitions, a weak line is seen at 10.125 Å, which even seems to be separated into the 10.12 Å and the 10.13 Å component in the HEG. There might be a line at 10.04 Å, but it certainly blends with the relatively strong Na xi Ly α line. Other lines in the 10.05...10.06 Å range are not seen. At 9.99 Å, there is an absorption line. The $2s \rightarrow 4p$ transitions at 9.72 Å are not seen, but there is a feature at 9.19 Å, which – although in parts overlapping with the Mg xi resonance line – can be well separated in all four spectra. Higher transitions, such as $2p \rightarrow 5d$, are not seen. There is no absorption feature visible at 8.82 Å, where 3 strong (but in parts quite strange) transitions from the ground state occur.

- Fe xix (O-like ion)

At 13.79 Å, an absorption feature is visible in the MEG+1 spectrum. It can only be fitted if the MEG–1 spectrum, which is rather flat, is excluded. The HEG spectra have only ≈ 2 counts/bin in this region, but both tend to show two lines (which are not resolved by the MEG). The 13.64 Å transition seems to be accompanied by two other lines, such that it is hard to fit. No prominent line feature is seen at 13.55 Å, but this might be explained by the Ne ix i-emission line's blending with this Fe xix absorption line. Both the two very strong $2p \rightarrow 3d$ transitions at 13.52 Å and 13.50 Å are seen as deep absorption lines. The next stronger $2p \rightarrow 3d$ transitions at 13.46 Å can explain exactly the further absorption that is seen next to the Ne ix resonance line at 13.44 Å. On the other wing, there might be indications for the weaker transition at 13.42 Å. An absorption line is seen at 12.95 Å, but its identification is not unique, as it has already been considered as a line of Fe xx. No line is seen at 12.93 Å. The absorption at 12.92 Å is more likely due to Fe xx. The $2p \rightarrow 4d$ transition at 10.82 Å is seen as well, the one at 10.68 Å, however, is not. The next transition at 10.65 Å is not seen or at least not very strong, but the line at 10.64 Å (stronger by A as well) is seen quite clearly. The transition at 10.63 Å has a similar Einstein coefficient, but is not detected, which indicates that the 10.64 Å line probably stems from another transition. Finally, none of the $2p \rightarrow 5d$ transitions is seen either.

- Fe xviii (F-like ion)

The $2p \rightarrow 3s$ line at 16.00 Å blends with the Lyman β line of O viii, but it is probably too weak to contribute significantly to this absorption. This is inferred from the fact that nothing is seen from the lines at 15.76 Å, 14.60 Å or 14.57 Å of comparable strength. There is a 2σ hint for the line $2p \rightarrow 3d$ transition at 14.53 Å. The strongest transitions of Fe xix at 14.37 Å (single) and 14.26 Å and 14.21 Å (each double) show up as strong absorption lines. The 14.21 Å line seems to have a deep central core with superimposed broad wings, but this might also be due to the description of the continuum. None of the weak $2s \rightarrow 3p$ transitions ($A < 3.6 \times 10^{12}/s$) is seen. The (double) $2p \rightarrow 4d$ transition at 11.53 Å is seen in the 'non-dip' spectrum, next to the Ne ix $1s^2 \rightarrow 1s3p$ line, but separated in the HEG spectra. The $2p \rightarrow 4d$ transition at 11.42 Å might contribute to the Fe xxii line at 11.43 Å, but it is not separated. Near 11.33 Å, where three other such transitions overlap, a strong absorption line feature is seen in MEG+1 and HEG+1, while the -1^{st} orders do not show such a nice line profile. None of the higher transitions is seen.

- Fe XVII (Ne-like ion)

Most of the lines from the iron XVII series are seen as quite clear absorption lines.

- Further less-ionized iron ions ($\text{Fe} \leq \text{XVI}$)

As already stated in Sect. 2.1.2, Fe XVI and all other less-ionized iron ions have more than 10 electrons, such that the inner two shells ($[1s^2 2s^2 2p^6]$) stay completely filled when the outermost electron is excited. These transitions occur thus at lower energies (or wavelengths above 25 Å), which are not covered by this spectrum.

Nickel

- Ni XXVIII (H-like ion)

There are weak signals in the HEG spectrum at 1.52 Å, and 1.23 Å, which match the wavelengths of the Ni XXVIII Lyman series. One would also expect to see a feature at 1.29 Å, there is a weak signal at 1.28 Å, but this can hardly be fitted. Thus Ni XXVIII absorption is likely present, but its analysis might fail due to the bad statistics.

- Ni XXVII (He-like ion), Ni XXVI (Li-like ion)

None of the lines, neither from the series of Ni XXVII nor from Ni XXVI, is seen convincingly in the spectrum.

Fit-parameters of the lines in the ‘non-dip’ spectrum

The following Table 4.10 lists the parameters of those lines whose identification is really trusted. The fit-parameters of the line are shown in the first block of 4 columns: the position λ , the full width at half maximum FWHM (which is shown with a **green** background color if the upper limit for the error did not converge and with a **red** background color if even the value itself did not converge within a reasonable, allowed range – mostly $[0, 50 \text{ mÅ}]$ or $[0, 75 \text{ mÅ}]$.¹ The allowed range for each wavelength was mostly $\pm 0.02 \text{ Å}$ around the best fit value; in some cases the confidence intervals did not converge in this limit as well, but this is usually not explicitly marked.), the equivalent width EW and the χ^2 -improvement $\Delta\chi^2$ (cf. comments to Table 4.4, page 61). The second block lists the parameters of the identified transition: the ion, the electronic states (ground states are underlined), the rest wavelength λ_0 from the atomic database, the Einstein coefficient A_{ji} and the total absorption oscillator strength f_{ij} . As in Table 4.4, the rows with a **gray** background mark emission lines (with $\text{EW} > 0$). If the rest wavelength is not consistent with the fitted position within the error bars, ()-brackets are put around the identified transitions. They do not mean, however, that this identification is not trusted, as it is not precluded to have Doppler-shifts. The last block of columns reports the deduced parameters, column density (calculated from Eq. 2.41, which holds only if the lines are not saturated and are on the linear part of the curve of growth) and wavelength-shift $\Delta\lambda/\lambda \cdot c$. Using $\Delta\lambda = \lambda - \lambda_0$, red-shifts (towards larger wavelengths) result in positive velocities, while blue-shifts give negative velocities.

Table ?? on page ?? shows the parameters of all lines and possible identifications from the atomic database in a similar way. Trustable identifications are marked by \leftarrow arrows. Figs. ??–?? on pages ??–?? show the fitted spectrum itself.

There is a general trend that higher transitions within a series give larger results for the column density than the first excitations of the considered ion. This indicates, as long as the lines are properly detected, that the first lines are in many cases saturated, i.e., are not on the linear part of the curve of growth (Sect. 2.1.5). For the weakest lines, however, it may mostly be due to the fact that very small equivalent widths W_λ cannot be well determined. Statistical fluctuations or other (still weaker) absorption effects in the proximity of the line of interest usually lead to a too large W_λ . A detailed discussion is given in the next section.

¹It was not possible to allow a too large width in general, as the fitting routine would often prefer one very broad line for several small features.

Table 4.10: List of lines in the ‘non-dip’ spectrum – sorted by ion

λ [Å]	FWHM [mÅ]	EW [mÅ]	$\Delta\chi^2$	ion	i	transition j	λ_0 [Å]	A_{ji} [10^{12}s^{-1}]	f_{ij}	N_i [10^{16}cm^{-2}]	$\Delta\lambda/\lambda \cdot c$ [km/s]
18.9394 ^{+0.0306} _{-0.0094}	55.92 ^{+90.91} _{-22.72}	-55.11 ^{+18.40} _{-116.40}	38.1	O VIII	<u>1s</u>	2p	18.9671	2.52	0.408	4.26 ^{+9.00} _{-1.42}	-438 ⁺⁴⁸³ ₋₁₄₉
16.0002 ^{+0.0051} _{-0.0043}	25.00 ^{+14.56} _{-12.27}	-20.38 ^{+5.40} _{-6.26}	63.1	(O VIII	<u>1s</u>	3p	16.0055	0.67	0.078	11.6 ^{+3.6} _{-3.1}	-99 ⁺⁹⁶ ₋₈₀
15.1721 ^{+0.0082} _{-0.0072}	0.03 ^{+40.38} _{-0.03}	-4.71 ^{+3.24} _{-5.68}	5.7	O VIII	<u>1s</u>	4p	15.1760	0.27	0.028	8.15 ^{+9.82} _{-5.60}	-77 ⁺¹⁶¹ ₋₁₄₂
18.6277 ^{+0.0162} _{-0.0177}	50.00 ^{+0.00} _{-14.23}	-33.47 ^{+14.91} _{-11.47}	16.0	O VII	<u>1s²</u>	1s3p	18.6270	0.93	0.146	7.50 ^{+2.57} _{-3.34}	12 ⁺²⁶¹ ₋₂₈₅
12.1287 ^{+0.0012} _{-0.0009}	19.38 ^{+3.03} _{-2.59}	-18.90 ^{+1.59} _{-1.85}	736.5	(Ne X	<u>1s</u>	2p	12.1321	6.16	0.408	3.57 ^{+0.35} _{-0.30}	-84 ⁺³⁰ ₋₂₃
10.2377 ^{+0.0023} _{-0.0004}	0.26 ^{+2.86} _{-0.26}	-4.80 ^{+0.68} _{-0.48}	108.5	Ne X	<u>1s</u>	3p	10.2385	1.65	0.078	6.68 ^{+0.67} _{-0.94}	-24 ⁺⁶⁸ ₋₁₁
9.7080 ^{+0.0028} _{-0.0020}	23.47 ^{+4.99} _{-5.70}	-8.57 ^{+1.38} _{-1.29}	153.7	Ne X	<u>1s</u>	4p	9.7080	0.67	0.028	36.2 ^{+5.4} _{-5.8}	-1 ⁺⁸⁵ ₋₆₂
9.4745 ^{+0.0023} _{-0.0012}	11.02 ^{+4.74} _{-8.19}	-6.05 ^{+1.12} _{-1.11}	131.3	(Ne X	<u>1s</u>	5p	9.4807	0.34	0.014	55.9 ^{+10.2} _{-10.3}	-195 ⁺⁷³ ₋₃₈
13.4403 ^{+0.0020} _{-0.0021}	19.29 ^{+4.08} _{-4.44}	-18.54 ^{+2.47} _{-2.28}	301.1	(Ne IX	<u>1s²</u>	1s2p	13.4473	8.87	0.721	1.61 ^{+0.20} _{-0.21}	-155 ⁺⁴⁵ ₋₄₆
11.5426 ^{+0.0024} _{-0.0001}	0.01 ^{+7.31} _{-0.01}	-3.47 ^{+1.05} _{-1.03}	28.4	Ne IX	<u>1s²</u>	1s3p	11.5440	2.48	0.148	1.99 ^{+0.59} _{-0.60}	-37 ⁺⁶³ ₋₃
11.0071 ^{+0.0032} _{-0.0031}	17.86 ^{+8.15} _{-6.54}	-5.69 ^{+1.40} _{-1.49}	56.1	(Ne IX	<u>1s²</u>	1s4p	11.0010	1.03	0.056	9.51 ^{+2.49} _{-2.35}	165 ⁺⁸⁶ ₋₈₅
10.7600 ^{+0.0050} _{-0.0025}	0.00 ^{+12.06} _{-0.00}	-0.87 ^{+0.57} _{-1.80}	4.2	(Ne IX	<u>1s²</u>	1s5p	10.7650	0.52	0.027	3.13 ^{+6.48} _{-2.04}	-138 ⁺¹³⁸ ₋₇₁
8.4203 ^{+0.0007} _{-0.0008}	15.23 ^{+2.60} _{-1.66}	-11.98 ^{+0.90} _{-1.12}	780.0	(Mg XII	<u>1s</u>	2p	8.4192	12.8	0.407	4.70 ^{+0.44} _{-0.35}	39 ⁺²⁶ ₋₂₉
7.1050 ^{+0.0025} _{-0.0000}	0.01 ^{+5.89} _{-0.01}	-2.31 ^{+0.43} _{-0.72}	49.6	Mg XII	<u>1s</u>	3p	7.1058	3.41	0.077	6.69 ^{+2.10} _{-1.24}	-33 ⁺¹⁰⁵ ₋₁
9.2350 ^{+0.0000} _{-0.0050}	0.00 ^{+12.46} _{-0.00}	2.02 ^{+1.00} _{-0.95}	13.2	(Mg XI	<u>1s²</u>	1s2p	9.2282	0.000	0.001		222 ⁺⁰ ₋₁₆₂
9.1672 ^{+0.0011} _{-0.0016}	17.02 ^{+4.41} _{-3.44}	-8.97 ^{+1.14} _{-1.18}	293.7	(Mg XI	<u>1s²</u>	1s2p	9.1687	19.5	0.739	1.64 ^{+0.22} _{-0.21}	-52 ⁺³⁷ ₋₅₃
7.8482 ^{+0.0022} _{-0.0025}	14.35 ^{+8.95} _{-6.36}	-4.78 ^{+1.30} _{-1.55}	62.4	Mg XI	<u>1s²</u>	1s3p	7.8503	5.43	0.151	5.84 ^{+1.90} _{-1.59}	-81 ⁺⁸⁵ ₋₉₅
7.4774 ^{+0.0001} _{-0.0049}	0.00 ^{+11.26} _{-0.00}	-1.80 ^{+0.56} _{-0.52}	24.9	Mg XI	<u>1s²</u>	1s4p	7.4730	2.24	0.056	6.49 ^{+1.89} _{-2.01}	175 ⁺⁵ ₋₁₉₆
7.1687 ^{+0.0027} _{-0.0020}	9.91 ^{+7.80} _{-9.90}	-3.04 ^{+0.79} _{-0.99}	46.2	Al XIII	<u>1s</u>	2p	7.1710	17.6	0.407	1.65 ^{+0.54} _{-0.43}	-98 ⁺¹¹³ ₋₈₃
6.0602 ^{+0.0121} _{-0.0093}	14.48 ^{+5.52} _{-14.48}	-1.28 ^{+0.87} _{-1.05}	7.0	Al XIII	<u>1s</u>	3p	6.0526	4.70	0.077	5.11 ^{+4.17} _{-3.47}	376 ⁺⁵⁹⁸ ₋₄₅₉

Table 4.10: List of lines in the ‘non-dip’ spectrum – sorted by ion (continued)

λ [Å]	FWHM [mÅ]	EW [mÅ]	$\Delta\chi^2$	ion	i	transition j	λ_0 [Å]	A_{ji} [10^{12}s^{-1}]	f_{ij}	N_i [10^{16}cm^{-2}]	$\Delta\lambda/\lambda \cdot c$ [km/s]
7.8751 ^{+0.0200} _{-0.0200}	0.02 ^{+49.98} _{-0.02}	0.47 ^{+1.03} _{-0.47}	1.2	Al XII	<u>1s²</u>	1s2s	7.8721	0.000	0.000	112 ⁺⁷⁶² ₋₇₆₂	
7.8150 ^{+0.0092} _{-0.0211}	7.03 ^{+42.97} _{-7.03}	1.26 ^{+1.74} _{-1.04}	4.1	Al XII	<u>1s²</u>	1s2p	7.8070	0.082	0.002	310 ⁺³⁵² ₋₈₀₉	
7.7908 ^{+0.0067} _{-0.0033}	0.00 ^{+39.61} _{-0.00}	1.46 ^{+0.97} _{-0.94}	6.7	(Al XII	<u>1s²</u>	1s2p	7.8070	0.082	0.002	-620 ⁺²⁵⁷ ₋₁₂₇	
7.7676 ^{+0.0049} _{-0.0026}	0.00 ^{+18.45} _{-0.00}	-1.15 ^{+0.78} _{-0.70}	5.9	(Al XII	<u>1s²</u>	1s2p	7.7573	27.5	0.745	0.29 ^{+0.18} _{-0.20}	
7.7532 ^{+0.0056} _{-0.0090}	0.41 ^{+34.00} _{-0.41}	-1.09 ^{+0.75} _{-1.49}	5.6	Al XII	<u>1s²</u>	1s2p	7.7573	27.5	0.745	0.28 ^{+0.38} _{-0.19}	
6.6346 ^{+0.0045} _{-0.0024}	0.88 ^{+10.91} _{-0.88}	-1.81 ^{+1.10} _{-2.12}	0.0	Al XII	<u>1s²</u>	1s3p	6.6350	7.63	0.151	3.08 ^{+3.62} _{-1.87}	
6.3150 ^{+0.0150} _{-0.0050}	0.00 ^{+50.00} _{-0.00}	-0.37 ^{+0.37} _{-0.65}	1.3	Al XII	<u>1s²</u>	1s4p	6.3140	3.14	0.056	1.89 ^{+3.28} _{-1.89}	
6.1810 ^{+0.0005} _{-0.0009}	13.80 ^{+2.31} _{-1.75}	-10.31 ^{+0.78} _{-0.85}	888.9	Si XIV	<u>1s</u>	2p	6.1804	23.7	0.407	7.51 ^{+0.62} _{-0.57}	
5.2193 ^{+0.0077} _{-0.0048}	22.15 ^{+20.59} _{-11.94}	-4.03 ^{+1.41} _{-2.18}	33.5	Si XIV	<u>1s</u>	3p	5.2168	6.32	0.077	21.7 ^{+11.7} _{-7.6}	
4.9518 ^{+0.0032} _{-0.0018}	0.01 ^{+13.26} _{-0.01}	-1.42 ^{+0.69} _{-0.73}	11.2	(Si XIV	<u>1s</u>	4p	4.9468	2.58	0.028	23.2 ^{+11.9} _{-11.3}	
6.7445 ^{+0.0023} _{-0.0019}	7.50 ^{+6.33} _{-7.50}	2.77 ^{+0.94} _{-0.85}	36.1	(Si XIII	<u>1s²</u>	1s2s	6.7403	0.000	0.000	189 ⁺¹⁰² ₋₈₆	
6.6468 ^{+0.0009} _{-0.0010}	9.50 ^{+2.50} _{-2.18}	-6.62 ^{+1.01} _{-1.07}	215.5	(Si XIII	<u>1s²</u>	1s2p	6.6479	37.7	0.749	2.27 ^{+0.37} _{-0.34}	
5.6809 ^{+0.0037} _{-0.0036}	22.02 ^{+14.30} _{-10.29}	-4.64 ^{+1.29} _{-1.47}	58.5	Si XIII	<u>1s²</u>	1s3p	5.6805	10.4	0.151	10.7 ^{+3.4} _{-3.0}	
5.4033 ^{+0.0043} _{-0.0008}	0.01 ^{+25.54} _{-0.01}	-1.42 ^{+0.77} _{-1.05}	8.7	Si XIII	<u>1s²</u>	1s4p	5.4045	4.30	0.056	9.75 ^{+7.22} _{-5.29}	
4.7285 ^{+0.0015} _{-0.0017}	7.78 ^{+9.06} _{-5.76}	-4.13 ^{+0.92} _{-1.18}	93.6	S XVI	<u>1s</u>	2p	4.7274	40.4	0.406	5.15 ^{+1.47} _{-1.15}	
3.9860 ^{+0.0214} _{-0.0181}	37.50 ^{+37.50} _{-37.50}	-1.73 ^{+1.43} _{-1.49}	5.9	S XVI	<u>1s</u>	3p	3.9908	10.8	0.077	16.0 ^{+13.8} _{-13.2}	
3.7801 ^{+0.0061} _{-0.0051}	0.04 ^{+49.96} _{-0.04}	-0.64 ^{+0.58} _{-0.83}	3.3	S XVI	<u>1s</u>	4p	3.7843	4.40	0.028	17.8 ^{+23.2} _{-16.1}	
3.7002 ^{+0.0202} _{-0.0202}	0.00 ^{+75.00} _{-0.00}	-0.41 ^{+0.41} _{-0.59}	1.2	S XVI	<u>1s</u>	5p	3.6958	2.22	0.014	24.9 ^{+36.2} _{-24.9}	

Table 4.10: List of lines in the ‘non-dip’ spectrum – sorted by ion (continued)

λ [Å]	FWHM [mÅ]	EW [mÅ]	$\Delta\chi^2$	ion	i	transition j	λ_0 [Å]	A_{ji} [10^{12}s^{-1}]	f_{ij}	N_i [10^{16}cm^{-2}]	$\Delta\lambda/\lambda \cdot c$ [km/s]
5.1004 $^{+0.0196}_{-0.0204}$	0.22 $^{+49.78}_{-0.22}$	0.34 $^{+0.84}_{-0.34}$	0.6	S XV	<u>1s²</u>	1s2s	5.1015	0.000	0.000	2.23 $^{+0.61}_{-0.53}$	-64 $^{+1151}_{-1199}$
5.0656 $^{+0.0244}_{-0.0156}$	5.27 $^{+44.73}_{-5.27}$	0.77 $^{+0.93}_{-0.77}$	2.2	S XV	<u>1s²</u>	1s2p	5.0631	0.000	0.007		143 $^{+1447}_{-921}$
5.0397 $^{+0.0020}_{-0.0020}$	9.26 $^{+7.70}_{-5.73}$	-3.80 $^{+0.91}_{-1.05}$	62.7	S XV	<u>1s²</u>	1s2p	5.0387	66.7	0.761	2.23 $^{+0.61}_{-0.53}$	61 $^{+120}_{-121}$
4.3019 $^{+0.0211}_{-0.0211}$	74.98 $^{+0.44}_{-64.42}$	-3.88 $^{+2.47}_{-1.82}$	12.4	S XV	<u>1s²</u>	1s3p	4.2990	18.3	0.152	15.6 $^{+7.3}_{-9.9}$	204 $^{+1468}_{-1468}$
4.0984 $^{+0.0088}_{-0.0093}$	20.58 $^{+31.95}_{-20.58}$	-1.88 $^{+1.18}_{-1.24}$	9.1	(S XV	<u>1s²</u>	1s4p	4.0883	7.53	0.057	22.4 $^{+14.7}_{-14.1}$	738 $^{+648}_{-682}$
3.7289 $^{+0.0211}_{-0.0103}$	12.88 $^{+37.12}_{-12.88}$	-0.94 $^{+0.79}_{-1.63}$	4.0	Ar XVIII	<u>1s</u>	2p	3.7311	64.7	0.405	1.89 $^{+3.27}_{-1.59}$	-179 $^{+1697}_{-831}$
3.1427 $^{+0.0213}_{-0.0187}$	0.16 $^{+49.84}_{-0.16}$	-0.44 $^{+0.44}_{-0.54}$	1.4	Ar XVIII	<u>1s</u>	3p	3.1502	17.3	0.077	6.56 $^{+7.99}_{-6.56}$	-713 $^{+2023}_{-1784}$
2.9776 $^{+0.0238}_{-0.0162}$	0.01 $^{+49.99}_{-0.01}$	-0.53 $^{+0.53}_{-0.55}$	2.6	Ar XVIII	<u>1s</u>	4p	2.9873	7.04	0.028	24.2 $^{+24.9}_{-24.2}$	-974 $^{+2389}_{-1625}$
3.9475 $^{+0.0026}_{-0.0026}$	0.03 $^{+18.90}_{-0.03}$	-1.11 $^{+0.54}_{-0.57}$	9.1	Ar XVII	<u>1s²</u>	1s2p	3.9491	109	0.767	1.05 $^{+0.54}_{-0.51}$	-118 $^{+194}_{-201}$
3.3667 $^{+0.0158}_{-0.0067}$	0.00 $^{+0.00}_{-0.00}$	-0.60 $^{+0.59}_{-0.57}$	2.8	Ar XVII	<u>1s²</u>	1s3p	3.3650	30.0	0.153	3.90 $^{+3.74}_{-3.85}$	154 $^{+1405}_{-599}$
3.2075 $^{+0.0025}_{-0.0050}$	0.00 $^{+27.57}_{-0.00}$	-0.93 $^{+0.51}_{-0.49}$	8.0	(Ar XVII	<u>1s²</u>	1s4p	3.2000	12.3	0.057	18.0 $^{+9.5}_{-9.9}$	702 $^{+235}_{-468}$
17.7495 $^{+0.0200}_{-0.0200}$	16.42 $^{+58.58}_{-16.42}$	-5.83 $^{+5.83}_{-11.86}$	1.5	Ar XVI	<u>1s²2s</u>	1s ² 4p	17.7320	0.65	0.092	2.28 $^{+4.64}_{-2.28}$	297 $^{+338}_{-338}$
3.0201 $^{+0.0175}_{-0.0026}$	0.01 $^{+74.99}_{-0.01}$	-0.60 $^{+0.56}_{-0.54}$	3.1	Ca XX	<u>1s</u>	2p	3.0185	98.6	0.404	1.85 $^{+1.67}_{-1.73}$	155 $^{+1734}_{-258}$
3.1942 $^{+0.0033}_{-0.0018}$	0.00 $^{+17.52}_{-0.00}$	1.01 $^{+0.71}_{-0.68}$	6.2	(Ca XIX	<u>1s²</u>	1s2p	3.1891	0.001	0.022		484 $^{+306}_{-165}$
3.1878 $^{+0.0163}_{-0.0306}$	0.00 $^{+50.42}_{-0.00}$	-0.55 $^{+0.55}_{-0.56}$	2.2	Ca XIX	<u>1s²</u>	1s2p	3.1772	170	0.770	0.79 $^{+0.82}_{-0.79}$	1001 $^{+1538}_{-2892}$
2.7000 $^{+0.0025}_{-0.0000}$	0.00 $^{+24.05}_{-0.00}$	-1.64 $^{+0.53}_{-0.50}$	23.9	(Ca XIX	<u>1s²</u>	1s3p	2.7050	46.3	0.152	16.7 $^{+5.1}_{-5.4}$	-554 $^{+277}_{-0}$
18.7387 $^{+0.0074}_{-0.0100}$	0.05 $^{+74.95}_{-0.05}$	-14.83 $^{+7.61}_{-7.43}$	10.3	Ca XVIII	<u>1s²2s</u>	1s ² 3p	18.7320	2.36	0.124	3.86 $^{+1.93}_{-1.98}$	107 $^{+118}_{-160}$
1.9395 $^{+0.0021}_{-0.0020}$	11.51 $^{+6.13}_{-5.28}$	5.00 $^{+1.24}_{-1.18}$	58.8	(Fe	K α		1.9370				385 $^{+331}_{-316}$

Table 4.10: List of lines in the ‘non-dip’ spectrum – sorted by ion (continued)

λ [Å]	FWHM [mÅ]	EW [mÅ]	$\Delta\chi^2$	ion	i	transition j	λ_0 [Å]	A_{ji} [10^{12}s^{-1}]	f_{ij}	N_i [10^{16}cm^{-2}]	$\Delta\lambda/\lambda \cdot c$ [km/s]
1.8499 ^{+0.0029} _{-0.0038}	5.42 ^{+14.13} _{-5.42}	-2.11 ^{+0.90} _{-1.25}	18.6	Fe XXV	<u>1s²</u>	1s2p	1.8504	503	0.775	9.01 ^{+5.35} _{-3.86}	-87 ⁺⁴⁷⁸ ₋₆₂₂
1.4914 ^{+0.0066} _{-0.0041}	0.72 ^{+23.63} _{-0.72}	-2.51 ^{+1.61} _{-2.28}	6.5	Fe XXV	<u>1s²</u>	1s4p	1.4950	56.3	0.057	225 ⁺²⁰⁵ ₋₁₄₅	-713 ⁺¹³¹⁷ ₋₈₁₇
10.6613 ^{+0.0037} _{-0.0035}	19.99 ^{+10.15} _{-8.78}	-5.63 ^{+2.51} _{-1.60}	51.4	Fe XXIV	<u>1s²s</u>	1s ² 3p	10.6630	7.41	0.126	4.44 ^{+1.26} _{-1.19}	-47 ⁺¹⁰⁵ ₋₉₉
10.6207 ^{+0.0010} _{-0.0013}	5.19 ^{+3.91} _{-5.18}	-6.65 ^{+0.87} _{-1.03}	164.0	(Fe XXIV	<u>1s²s</u>	1s ² 3p	10.6190	7.19	0.243	2.74 ^{+0.43} _{-0.36}	47 ⁺³⁰ ₋₃₇
7.9900 ^{+0.0024} _{-0.0032}	0.15 ^{+16.77} _{-0.15}	-1.77 ^{+0.68} _{-0.92}	21.2	(Fe XXIV	<u>1s²s</u>	1s ² 4p	7.9857	3.24	0.094	3.36 ^{+1.74} _{-1.29}	160 ⁺⁸⁹ ₋₁₂₂
11.0225 ^{+0.0033} _{-0.0025}	0.03 ^{+11.44} _{-0.03}	-2.24 ^{+0.83} _{-1.05}	16.6	(Fe XXIII	<u>1s²s²</u>	1s ² 2s3p	11.0190	4.68	0.256	0.82 ^{+0.38} _{-0.30}	96 ⁺⁹⁰ ₋₆₈
10.9871 ^{+0.0019} _{-0.0021}	13.68 ^{+5.10} _{-4.50}	-7.05 ^{+1.30} _{-1.33}	104.5	(Fe XXIII	<u>1s²s²</u>	1s ² 2s3p	10.9810	7.56	0.410	1.61 ^{+0.30} _{-0.30}	167 ⁺⁵¹ ₋₅₈
8.3062 ^{+0.0038} _{-0.0014}	0.02 ^{+19.98} _{-0.02}	-1.72 ^{+0.66} _{-0.60}	17.6	(Fe XXIII	<u>1s²s²</u>	1s ² 2s4p	8.3038	4.66	0.145	1.95 ^{+0.68} _{-0.75}	88 ⁺¹³⁵ ₋₄₉
12.2523 ^{+0.0027} _{-0.0023}	0.07 ^{+13.90} _{-0.07}	-4.27 ^{+1.25} _{-1.21}	26.3	Fe XXII	<u>1s²s²2p</u>	1s ² 2s ² 3s	12.2519	0.91	0.020	15.8 ^{+4.5} _{-4.6}	11 ⁺⁶⁵ ₋₅₇
11.7698 ^{+0.0012} _{-0.0014}	8.77 ^{+3.89} _{-4.92}	-10.01 ^{+0.98} _{-1.94}	248.9	Fe XXII	<u>1s²s²2p</u>	1s ² 2s ² 3d	11.7700	16.3	0.676	1.21 ^{+0.24} _{-0.12}	-6 ⁺³¹ ₋₃₅
11.4789 ^{+0.0059} _{-0.0025}	4.73 ^{+8.91} _{-4.73}	-3.16 ^{+1.47} _{-1.24}	15.4	(Fe XXII	<u>1s²s²2p</u>	1s ² 2s2p3p	11.4900	6.40	0.127	2.15 ^{+0.84} _{-1.00}	-289 ⁺¹⁵⁵ ₋₆₆
11.4264 ^{+0.0036} _{-0.0029}	7.40 ^{+7.17} _{-7.40}	-3.96 ^{+1.15} _{-1.40}	29.9	Fe XXII	<u>1s²s²2p</u>	1s ² 2s2p3p	11.4270	5.85	0.229	1.50 ^{+0.53} _{-0.44}	-17 ⁺⁹⁵ ₋₇₆
8.9775 ^{+0.0002} _{-0.0030}	0.05 ^{+21.73} _{-0.05}	-2.73 ^{+0.67} _{-0.22}	41.6	Fe XXII	<u>1s²s²2p</u>	1s ² 2s ² 4d	8.9748	5.30	0.128	3.00 ^{+0.24} _{-0.73}	89 ⁺⁵ ₋₁₀₀
8.7403 ^{+0.0046} _{-0.0029}	0.00 ^{+17.16} _{-0.00}	-1.11 ^{+0.76} _{-0.63}	6.0	(Fe XXII	<u>1s²s²2p</u>	1s ² 2s2p4p	8.7254	3.54	0.040	4.07 ^{+2.32} _{-2.77}	513 ⁺¹⁶⁰ ₋₉₈
12.2821 ^{+0.0012} _{-0.0008}	12.49 ^{+2.02} _{-4.46}	-14.47 ^{+1.39} _{-0.98}	467.7	(Fe XXI	<u>1s²2s²2p²</u>	1s ² 2s ² 2p3d	12.2840	18.2	1.235	0.88 ^{+0.06} _{-0.08}	-46 ⁺³⁰ ₋₂₀
11.9700 ^{+0.0050} _{-0.0000}	0.00 ^{+9.96} _{-0.00}	-3.06 ^{+1.24} _{-1.21}	16.1	(Fe XXI	<u>1s²2s²2p²</u>	1s ² 2s2p ² 3p	11.9750	3.09	0.199	1.21 ^{+0.48} _{-0.49}	-125 ⁺¹²⁵ ₋₀
9.1918 ^{+0.0032} _{-0.0048}	13.21 ^{+8.85} _{-6.83}	-3.35 ^{+1.28} _{-1.02}	35.3	Fe XXI	<u>1s²2s²2p²</u>	1s ² 2s2p ² 4p	9.1944	2.88	0.109	4.11 ^{+1.25} _{-1.56}	-85 ⁺¹⁰⁵ ₋₁₅₆
8.5748 ^{+0.0061} _{-0.0051}	10.91 ^{+18.46} _{-10.91}	-1.75 ^{+0.90} _{-1.14}	11.0	Fe XXI	<u>1s²2s²2p²</u>	1s ² 2s ² 2p5d	8.5740	2.85	0.094	2.85 ^{+1.86} _{-1.48}	28 ⁺²¹⁴ ₋₁₈₀

Table 4.10: List of lines in the ‘non-dip’ spectrum – sorted by ion (continued)

λ [Å]	FWHM [mÅ]	EW [mÅ]	$\Delta\chi^2$	ion	i	transition	λ_0 [Å]	A_{ji} [10^{12}s^{-1}]	f_{ij}	N_i [10^{16}cm^{-2}]	$\Delta\lambda/\lambda \cdot c$ [km/s]
13.7551 $^{+0.0099}_{-0.0049}$	0.02 $^{+47.63}_{-0.02}$	-4.74 $^{+2.67}_{-2.62}$	8.4	(Fe XX	<u>2s²2p³</u>	2s ² 2p ² 3s	13.7670	1.02	0.044	6.51 $^{+3.60}_{-3.66}$	-259 $^{+215}_{-108}$
13.0522 $^{+0.0051}_{-0.0031}$	11.16 $^{+13.73}_{-11.16}$	-5.76 $^{+1.90}_{-2.52}$	25.0	(Fe XX	<u>2s²2p³</u>	2s ² 2p ² 3d	13.0610	2.62	0.101	3.81 $^{+1.67}_{-1.26}$	-203 $^{+116}_{-71}$
12.9200 $^{+0.0025}_{-0.0000}$	0.01 $^{+21.12}_{-0.01}$	-4.74 $^{+1.42}_{-1.43}$	30.6	(Fe XX	<u>2s²2p³</u>	2s ² 2p ² 3d	12.9120	4.92	0.184	1.74 $^{+0.52}_{-0.52}$	186 $^{+59}_{-1}$
12.8500 $^{+0.0016}_{-0.0021}$	0.36 $^{+13.32}_{-0.35}$	-7.08 $^{+1.38}_{-1.24}$	79.7	(Fe XX	<u>2s²2p³</u>	2s ² 2p ² 3d	12.8460	19.2	0.476	1.02 $^{+0.18}_{-0.20}$	92 $^{+38}_{-48}$
12.8281 $^{+0.0012}_{-0.0016}$	18.73 $^{+4.33}_{-3.22}$	-17.49 $^{+2.14}_{-2.24}$	393.4	(Fe XX	<u>2s²2p³</u>	2s ² 2p ² 3d	12.8240	17.1	0.211	5.71 $^{+0.73}_{-0.70}$	95 $^{+29}_{-37}$
12.5810 $^{+0.0033}_{-0.0042}$	11.62 $^{+12.40}_{-11.62}$	-5.68 $^{+2.07}_{-2.15}$	31.6	(Fe XX	<u>2s²2p³</u>	2s2p2p ³ p	12.5760	4.39	0.104	3.91 $^{+1.48}_{-1.42}$	120 $^{+79}_{-99}$
10.1249 $^{+0.0054}_{-0.0200}$	4.37 $^{+33.85}_{-4.37}$	-1.77 $^{+0.99}_{-2.05}$	8.9	Fe XX	<u>2s²2p³</u>	2s ² 2p ² 4d	10.1203	2.12	0.049	4.01 $^{+4.64}_{-2.24}$	137 $^{+160}_{-592}$
9.9924 $^{+0.0041}_{-0.0030}$	7.10 $^{+10.08}_{-7.10}$	-2.76 $^{+1.05}_{-1.00}$	20.4	(Fe XX	<u>2s²2p³</u>	2s ² 2p2p4d	9.9977	6.56	0.049	6.38 $^{+2.31}_{-2.42}$	-161 $^{+124}_{-89}$
13.8318 $^{+0.0088}_{-0.0085}$	28.25 $^{+17.58}_{-20.33}$	-9.17 $^{+5.40}_{-3.95}$	15.6	Fe XIX	<u>2s²2p⁴</u>	2s ² 2p ² 2p3d	13.8390	1.75	0.050	10.8 $^{+4.7}_{-6.4}$	-155 $^{+190}_{-185}$
13.7914 $^{+0.0116}_{-0.0058}$	26.00 $^{+24.00}_{-19.82}$	-9.25 $^{+4.05}_{-4.96}$	17.8	Fe XIX	<u>2s²2p⁴</u>	2s ² 2p2p ² 3d	13.7950	5.35	0.214	2.57 $^{+1.38}_{-1.13}$	-78 $^{+252}_{-126}$
13.6501 $^{+0.0061}_{-0.0055}$	20.29 $^{+19.29}_{-10.10}$	-8.11 $^{+3.14}_{-3.48}$	22.3	Fe XIX	<u>2s²2p⁴</u>	2s ² 2p ³ 3d	13.6450	2.43	0.095	5.19 $^{+2.23}_{-2.01}$	112 $^{+135}_{-122}$
13.5251 $^{+0.0014}_{-0.0030}$	10.44 $^{+7.45}_{-6.78}$	-10.90 $^{+2.47}_{-1.82}$	88.5	(Fe XIX	<u>2s²2p⁴</u>	2s ² 2p ³ 3d	13.5180	18.7	0.717	0.94 $^{+0.16}_{-0.21}$	156 $^{+31}_{-67}$
13.5026 $^{+0.0019}_{-0.0016}$	17.55 $^{+4.32}_{-4.83}$	-17.72 $^{+2.57}_{-2.18}$	241.5	(Fe XIX	<u>2s²2p⁴</u>	2s ² 2p2p ² 3d	13.4970	12.9	0.353	3.12 $^{+0.38}_{-0.45}$	125 $^{+41}_{-36}$
13.4647 $^{+0.0030}_{-0.0035}$	20.44 $^{+8.49}_{-9.09}$	-11.81 $^{+3.60}_{-2.00}$	68.4	Fe XIX	<u>2s²2p⁴</u>	2s ² 2p ³ 3d	13.4620	14.1	0.231	3.20 $^{+0.54}_{-0.97}$	61 $^{+66}_{-79}$
13.4202 $^{+0.0043}_{-0.0118}$	9.72 $^{+16.28}_{-9.72}$	-4.08 $^{+1.57}_{-2.96}$	25.2	Fe XIX	<u>2s²2p⁴</u>	2s ² 2p ³ 3d	13.4230	5.01	0.190	1.35 $^{+0.98}_{-0.52}$	-61 $^{+97}_{-263}$
12.9538 $^{+0.0025}_{-0.0026}$	14.50 $^{+8.23}_{-5.82}$	-9.91 $^{+2.29}_{-2.52}$	80.3	(Fe XIX	<u>2s²2p⁴</u>	2s2p2p ³ 3p	12.9450	3.11	0.047	14.3 $^{+3.6}_{-3.3}$	204 $^{+58}_{-61}$

Table 4.10: List of lines in the ‘non-dip’ spectrum – sorted by ion (continued)

λ [Å]	FWHM [mÅ]	EW [mÅ]	$\Delta\chi^2$	ion	i	transition j	λ_0 [Å]	A_{ji} [10^{12}s^{-1}]	f_{ij}	N_i [10^{16}cm^{-2}]	$\Delta\lambda/\lambda \cdot c$ [km/s]
14.5301 $^{+0.0099}_{-0.0001}$	0.00 $^{+75.00}_{-0.00}$	-5.97 $^{+3.07}_{-3.02}$	10.1	Fe XVIII	<u>2s²2p⁵</u>	2s ² 2p ⁴ 3d	14.5340	4.05	0.192	1.67 $^{+0.84}_{-0.86}$	-81 $^{+204}_{-2}$
14.3700 $^{+0.0100}_{-0.0050}$	0.00 $^{+26.25}_{-0.00}$	-4.49 $^{+2.94}_{-3.95}$	6.3	Fe XVIII	<u>2s²2p⁵</u>	2s ² 2p ⁴ 3d	14.3730	6.75	0.314	0.79 $^{+0.69}_{-0.51}$	-62 $^{+209}_{-104}$
14.2525 $^{+0.0043}_{-0.0031}$	10.00 $^{+13.77}_{-10.00}$	-11.44 $^{+2.84}_{-4.96}$	41.6	Fe XVIII	<u>2s²2p⁵</u>	2s ² 2p ⁴ 3d	14.2560	12.9	0.197	3.24 $^{+1.40}_{-0.80}$	-74 $^{+91}_{-65}$
14.2010 $^{+0.0029}_{-0.0034}$	26.41 $^{+8.47}_{-7.78}$	-21.96 $^{+4.77}_{-4.27}$	142.4	(Fe XVIII	<u>2s²2p⁵</u>	2s ² 2p ² 2p ³ 3d	14.2080	17.9	0.541)	2.28 $^{+0.44}_{-0.50}$	-148 $^{+62}_{-71}$
11.5312 $^{+0.0013}_{-0.0037}$	0.00 $^{+10.14}_{-0.00}$	-3.48 $^{+1.02}_{-1.01}$	34.7	(Fe XVIII	<u>2s²2p⁵</u>	2s ² 2p ² 2p ² 4d	11.5270	3.55	0.071)	4.20 $^{+1.22}_{-1.23}$	110 $^{+33}_{-97}$
11.3153 $^{+0.0025}_{-0.0005}$	0.08 $^{+9.91}_{-0.08}$	-3.10 $^{+1.04}_{-1.02}$	23.2	(Fe XVIII	<u>2s²2p⁵</u>	2s ² 2p ⁴ 4d	11.3260	4.82	0.046)	5.92 $^{+1.94}_{-1.98}$	-283 $^{+66}_{-13}$
16.7700 $^{+0.0100}_{-0.0049}$	0.00 $^{+23.84}_{-0.00}$	-7.34 $^{+5.71}_{-4.33}$	4.8	Fe XVII	<u>2s²2p⁶</u>	2s ² 2p ⁵ 3s	16.7800	0.90	0.114	2.60 $^{+1.53}_{-2.02}$	-179 $^{+179}_{-88}$
15.2551 $^{+0.0259}_{-0.0259}$	0.00 $^{+26.76}_{-0.00}$	-3.28 $^{+3.28}_{-2.97}$	2.5	Fe XVII	<u>2s²2p⁶</u>	2s ² 2p ⁵ 3d	15.2610	5.87	0.615	0.26 $^{+0.23}_{-0.26}$	-117 $^{+509}_{-509}$
15.0033 $^{+0.0058}_{-0.0026}$	13.76 $^{+9.96}_{-13.75}$	-13.12 $^{+3.16}_{-4.82}$	42.4	(Fe XVII	<u>2s²2p⁶</u>	2s ² 2p ⁵ 3d	15.0140	27.0	2.733)	0.24 $^{+0.09}_{-0.06}$	-214 $^{+116}_{-51}$
12.2650 $^{+0.0025}_{-0.0011}$	0.32 $^{+7.58}_{-0.32}$	-5.38 $^{+1.04}_{-1.23}$	61.8	Fe XVII	<u>2s²2p⁶</u>	2s ² 2p ⁵ 4d	12.2660	4.21	0.285	1.42 $^{+0.32}_{-0.28}$	-24 $^{+60}_{-26}$
12.1141 $^{+0.0014}_{-0.0024}$	1.72 $^{+9.08}_{-1.72}$	-4.09 $^{+1.08}_{-1.07}$	45.2	(Fe XVII	<u>2s²2p⁶</u>	2s ² 2p ⁵ 4d	12.1240	4.83	0.319)	0.99 $^{+0.26}_{-0.26}$	-244 $^{+35}_{-59}$
1.5180 $^{+0.0028}_{-0.0027}$	0.18 $^{+10.71}_{-0.18}$	-3.54 $^{+1.49}_{-1.49}$	14.7	(Ni XXVIII <u>1s</u>		2p	1.5304	379	0.400)	43.5 $^{+18.4}_{-18.3}$	-2422 $^{+555}_{-535}$
1.2146 $^{+0.0070}_{-0.0070}$	27.92 $^{+2.50}_{-15.81}$	-19.84 $^{+8.25}_{-7.53}$	0.0	(Ni XXVIII <u>1s</u>		4p	1.2268	41.2	0.028)	30822	-2984 $^{+1722}_{-1711}$

4.2.4 Spectral analysis with absorption line series

Fitting only single lines leads to several difficulties: Line blends are difficult to analyze and interpret, and a curve of growth has to be constructed from the measured equivalent widths.

It is therefore much easier to fit whole line series at once with the self-developed model described in Sect. 3.2.3. The adequacy of the description of the lines contained in each series and the comparison of the derived parameters with those from the previous section will be discussed in the following list. The results are quoted in Table 4.11, and the collected line profiles of each of the series are shown in Fig. 4.14 at the end of this section.

- O VIII

Though the Ly α line is hardly detected due to the low count rate at $\lambda \approx 19 \text{ \AA}$, an absorption line series for O XVIII is used to describe the Ly β line at 16.01 \AA and the Ly γ line at 15.18 \AA .

The best fit that was found with the line series model has an extremely small v_{therm} . The $N_{\text{O VIII}}$ is thus very high, but has also large uncertainties. One would need to constrain the velocity broadening to get useful limits for the column density.

- O VII

The He-like transitions occur at still larger wavelengths than the H-like ones. Therefore, O VII lines are virtually not seen.

- Ne X

All lines except of the deep Ly α line at 12.13 \AA can be described quite well by an absorption line series. To fit the latter (alone), a much larger blue shift of 245 km/s and a larger Ne X-column density would be required. Furthermore, the residuals of the 9.71 \AA Ly γ line are not fully repaired as well, although Ly β at 10.24 \AA is explained perfectly. This might probably indicate, that there is not only one component in the wind that contributes to the Ne X absorption, but several ones with different velocities.

The result is compatible with what has been found for the single Gaussian absorption lines provided that both the Lyman α and the Lyman β lines are well saturated. If a line is not on the linear part of the curve of growth, Eq. (2.41) predicts too low values for $N_{\text{Ne X}}$ than are actually necessary to produce the observed equivalent widths.

- Ne IX

A good description of all absorption lines is given by a single line series. The contribution of the β line to the strong absorption feature at 11 \AA is only a small part, but it was already discussed that this is a blend of several transitions (probably Na X and Fe XXIII).

The result is also in good agreement with what was found from the single Gaussian lines: Table 4.10 quotes slightly too low values of $N_{\text{Ne IX}}$ for the first two lines, which indicates that they are almost saturated. As already mentioned, the equivalent width (and therefore column density) of the $1s^2 \rightarrow 1s4p$ transition was strongly overestimated in the previous approach.

- Na X

The Na X series mainly accounts for the Ly α line at 10.03 \AA . With the parameters found (Table 4.11), one would not expect to see higher transitions, as it is the case.

- Na IX

Similarly, the only visible feature of the series for the He-like sodium ion is the resonance line at 11.00 \AA . But this one contributes significantly to the line complex near this wavelength. Higher transitions, which are not seen, are not predicted by the model with the parameters given in Table 4.11.

- Mg XII

Both the very strong Ly α line and the strong Ly β line at 8.42 Å and 7.11 Å, respectively, can excellently be described by a line series. The Ly γ line at 6.74 Å, however, cannot account for the absorption features at 6.70...6.73 Å. A larger strength and much larger blue shift would be required. This proves that these features need another explanation.

The result agrees with the results from the single line fitting provided that the Ly α line is slightly saturated.

- Mg XI

In the same way, all lines of Mg XI can be described quite well by a line series.

The column density obtained from the single Gaussian resonance line is much too low, but this is still consistent, as Fig. 4.14g shows directly that this line is saturated.

- Al XIII

The line series fits the Ly α line and explains that no higher transitions should be visible.

The resulting column density is consistent with the values obtained before. It is even possible within the errorbars that the Ly α line is not saturated, as it seems to be.

- Al XII

The same is true for the He-like aluminum ion's line series: The model accounts only for the resonance line, as no higher transitions are detected.

There is also a very good agreement with the column density obtained by fitting a single Gaussian and assuming that the line is on the flat part of the curve of growth.

- Si XIV

All lines of this series can excellently be described by a single model. This is especially notable, as the 6.18 Å Si XIV Ly α is the strongest line in the whole spectrum, but can perfectly be explained.

Though being close to the end of the error bars, the fitted $N_{\text{Si XIII}}$ still agrees with the column density derived from the single Ly α line. The equivalent width of the higher transition seems to be overestimated. It is surprising that a negative shift velocity was found with the line series, although the single lines showed positive shifts, but this may be explained by their large uncertainties.

- Si XIII

Similarly, the He-like Si XIV follows (except small, but still absorption-line-like residuals at 5.68 Å) the predictions of a single series.

As well as for the H-like ion, the derived column density is between the minimal value (for the strongest transition) and the maximum value deduced from the single Gaussians. It is noted that quite high values of v_{therm} have been found for both ions of silicon.

- S XVI

This line series describes all the detected absorption lines (up to Ly δ) very accurately.

As the best fit was found with a very low Doppler broadening, i.e., very small v_{therm} (though still with a large uncertainty), the best fit value for $N_{\text{S XVI}}$ is very high. On the flat part of the curve of growth, those two parameters are strongly correlated: Fig. 4.13 shows the χ^2 -contours in the $N_{\text{S XVI}} - v_{\text{therm}}$ plane, which roughly indicate that higher Doppler velocities lead to lower column densities. (Fig. 4.14l does not give the impression that the line might be saturated, but the small Doppler width is probably not resolved.) Unless the velocity is not constrained by other means, the result for the column density $N_{\text{S XVI}}$ is very dubious.

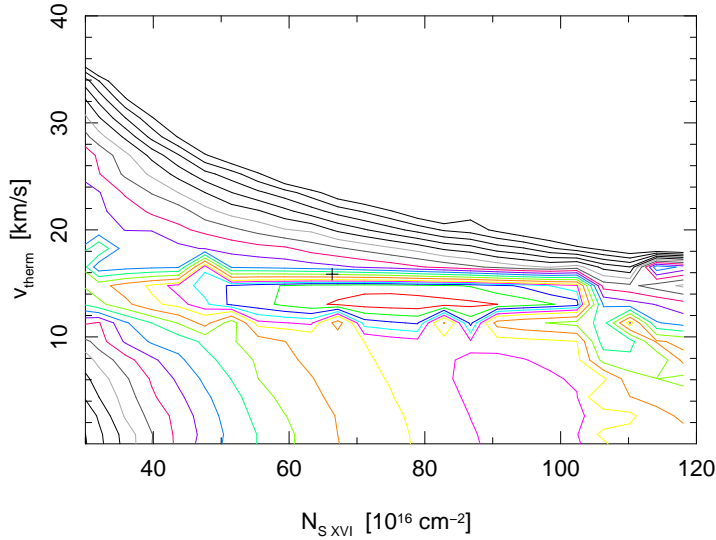


Figure 4.13: χ^2 -contours for column density and Doppler broadening in the S XVI line series.

- S XV

All the detected lines ($1s^2 \rightarrow 1snp$ for $n = 2, 3, 4$, although the $1s^2 \rightarrow 1s4p$ transition is already very weak) can perfectly be described by a single series model. The model also predicts that no higher transitions should be seen.

Again, the consistent description shows that the strongest resonance line is slightly saturated (its measured equivalent width predicts a too small column density by the approximation for the linear part of the curve of growth) and the equivalent width of the weaker lines is overestimated.

- Ar XVIII, Ca XX, Ca XIX

Due to the weakness of the lines of Ar XVIII, it was not possible to fit a series with reasonable parameters. The same is true for the Ca XX and Ca XIX series.

- Ar XVII

Although none of the Ar XVII has a strong and clear profile, a line series was used, which could, however, hardly constrain the parameters.

For this reason, there is also no inconsistency with former parameters, which had enormous uncertainties as well.

- Fe XXVI

Due to *Chandra*'s low effective area at these high energies, no H-like Fe lines are detected.

- Fe XXV

A line series for Fe XXV virtually only describes the resonance line at 1.85 Å.

The inferred column density is twice that obtained from the single Gaussian line, but the resolution at $\lambda < 2$ Å is too low to decide whether the line is saturated or not.

- Fe XXIV

The lines at 10.62 Å, 10.66 Å and 8.00 Å can completely be described by a line series. (In the case of the 10.62 Å line, the MEG spectra still show some residuals and would need a higher $N_{\text{Fe XXIV}}$, but the HEG spectra are perfectly modelled.) The line at 7.17 Å is not fully explained. (The high Mg XI transition could hardly account for it.)

The derived results agree very well with those from the single lines. It is not needed to assume that the lines are saturated. But it will again be necessary to constrain the Doppler velocity to exclude this possibility and thus to set an upper limit for $N_{\text{Fe XXIV}}$.

- Fe XXIII

The strongest transitions of the Fe XXIII series form very nicely the outermost absorption lines at 10.98 Å and 11.02 Å of the quintuplet near 11.00 Å (which may be furthermore explained by Fe XXII, Ne IX and Na X). The parameters are consistent with the weak feature at 8.30 Å. The Fe XXIII transition at 7.48 Å hardly contributes to the absorption feature there, which is dominantly explained by a Mg XI transition.

The line series confirms the results for the parameters already obtained with the single Gaussian lines. As the lines of this series are relatively weak, it is very unlikely (and therefore also not favored by the model fitting) that these lines are saturated. As a result, the uncertainties on the column density are much smaller than, for example, for Fe XXIV.

- Fe XXII

The lines previously identified with Fe XXII transitions cannot be described very well with a single line series. With the latest best fit parameters, there are still absorption line residuals at the strongest line at 11.77 Å, as well as at 8.97 Å. The second strongest line at 11.43 Å is, however, very well explained. The exceptionally high blue-shift of the line at 11.48 Å, as already found for the single Gaussian lines, does, of course, not fit with the line series model either. (As the strength of the predicted line would match the observation, it was worth to check if a wrong wavelength was reported in the ATOMDB. But the CHIANTI database² agrees with those values.) The model does also not account properly for the absorption line at 12.25 Å, as this transition is relatively weak. This means, that probably another identification has to be found for this line. Though not perfectly, the weak single bin line at 8.71 Å can be explained by the series. Higher transitions are neither detected nor predicted.

The fit parameters mostly agree with the previous values. The equivalent width of the weak transition at 12.25 Å is certainly overestimated.

- Fe XXI

The strongest transition at 12.28 Å is described by a very broad line, which does not seem appropriate, as this absorption complex contains more fine structure, especially in the HEG spectra with the double resolution. The second strongest line is described quite well, although there are again additional features. The lines at 11.94 Å and 11.97 Å are not clearly detected, but with the model parameters, namely such a high v_{therm} , they are strongly smeared out. The line at 9.19 Å, which is, however, seen quite well, is not described satisfactorily. For the hardly detected line at 8.57 Å, this is okay again.

From the discussion of the validity of the description by the line series model, it may seem to be dubious to infer parameters from it, but from a statistical point of view, the confidence levels are relatively small and agree with previous values for $N_{\text{Fe XXI}}$.

- Fe XX

Unfortunately, the complex Fe XX line series could not be fitted at all, in the sense that the fit did not converge within several weeks of CPU time.

- Fe XIX

This line series nicely explains the residuals around the Ne IX resonance line at 13.44 Å, most of the absorption complex around 13.50 Å, the tiny features at 13.64 Å and 13.79 Å. The lines at 10.82 Å and 10.64 Å are not fully described by the model.

The parameters are almost consistent with the strongest lines; the higher transitions tend to have overestimated equivalent widths.

² http://wwwsolar.nrl.navy.mil/chianti_linelist.html

- Fe XVIII

The strongest transitions of Fe XVIII appear between 14.1 Å and 14.55 Å. The deepest absorption line is expected at 14.21 Å. There is indeed a relatively strong feature. Its rather unusual shape (deep central core, but superimposed broad wings) is not fully explained by the line series model, but only one of the wings. The lines at wavelengths ≥ 14.4 Å are virtually not seen, probably also due to a bad description of the continuum in this range. This constrains the column density of the line series to a relatively low value. Part of the additional absorption feature next to the Ne IX line at 11.54 Å is described by the line at 11.53 Å. The model also does not account fully for the 11.32 Å line.

As already mentioned, the line series gives probably a too low value for $N_{\text{Fe XVIII}}$.

- Fe XVII

The strongest lines (at 15.01 Å, 15.26 Å, 12.12 Å, 13.82 Å, 12.26 Å) seem to need stronger absorption lines than were actually found with the Fe XVII series.

As the global optimum was probably not yet found, the true $N_{\text{Fe XVII}}$ is considered to be larger than the latest best fit parameter, which is also required by the analysis with single absorption lines.

Discussion

Column densities. The inferred column densities of the ions should be comparable with the column densities expected from the measured photoabsorption and the elemental abundances, which are quoted in Table 4.12. This relies on the assumption, that the continuous photoabsorption is caused by the same material which also produces the absorption lines, i.e., that the contribution of the interstellar medium is negligible. But even if this was the case, photoabsorption by a ionized plasma might require other densities than the neutral photoabsorption which was used to model the continuum (with the `phabs` model). Furthermore, the elemental abundances in the stellar wind of HDE 226868 may significantly differ from the average values in the ISM. Therefore, this is only an order of magnitude estimation. One can anyway only infer relative statements from this comparison, as the detected ions are limited by the transitions, which occur in the accessible wavelength range.

As a result, the column densities for neon, magnesium, and probably argon and iron, measured with the line series are in good agreement with the values expected from photoabsorption. Oxygen and sulfur could not yet be constrained very precisely, and the column density of silicon, and probably aluminum as well, finally might indicate an overabundance.

Doppler broadenings. More precise statements on the column densities and abundances would require to constrain the Doppler broadening within a self-consistent physical model of the absorption region, rather than to fit for all parameters allowed by the data. The velocity parameter v_{therm} is related to the temperature by Eq. (2.26), or, if microturbulence is included:

$$v_{\text{therm}} = \sqrt{\frac{2k_{\text{B}}T}{m_{\text{ion}}} + v_{\text{micro}}^2} \quad (4.5)$$

Wavelength shifts. No strong Doppler shifts are detected. Most of the lines are slightly blue-shifted, i.e., $\Delta\lambda = \lambda - \lambda_0 < 0$, but $\Delta\lambda/\lambda \cdot c \gtrsim -150 \text{ km s}^{-1}$, see Table 4.11.

This gives the important information that the material causing the absorption lines is rather part of the stellar wind of HDE 226868 and moves towards the observer instead of being directly contained in the accretion stream flowing towards the black hole (and thus away from the observer, as this observation was performed during superior conjunction of the black hole). A self-consistent description of the accretion region has to explain this fact. It might be related to the ionization parameter, which is so high in the immediate neighborhood of the source that the material is fully ionized and cannot produce absorption lines.

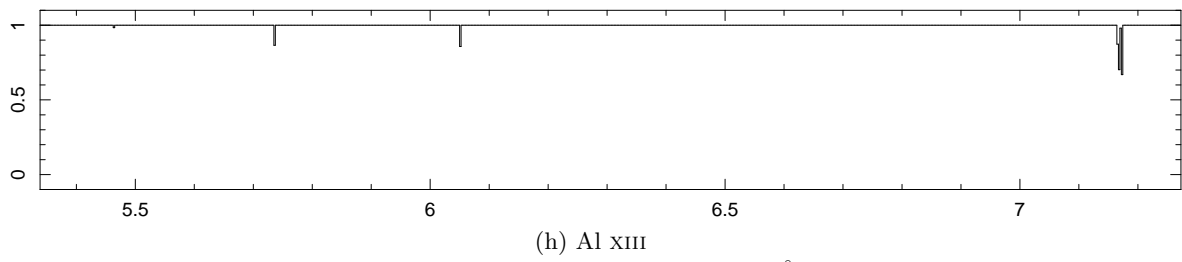
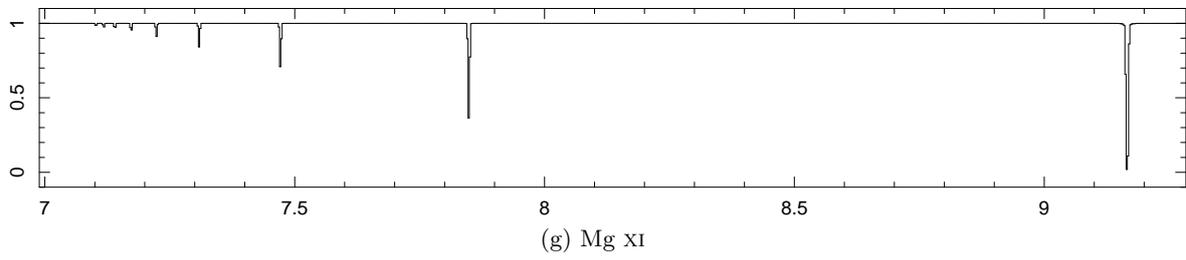
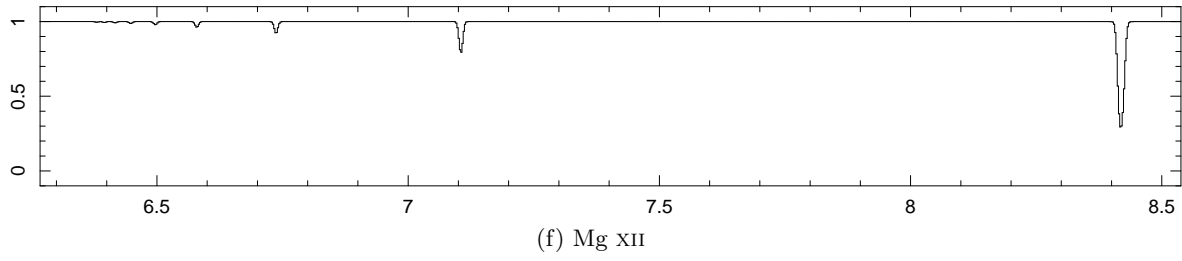
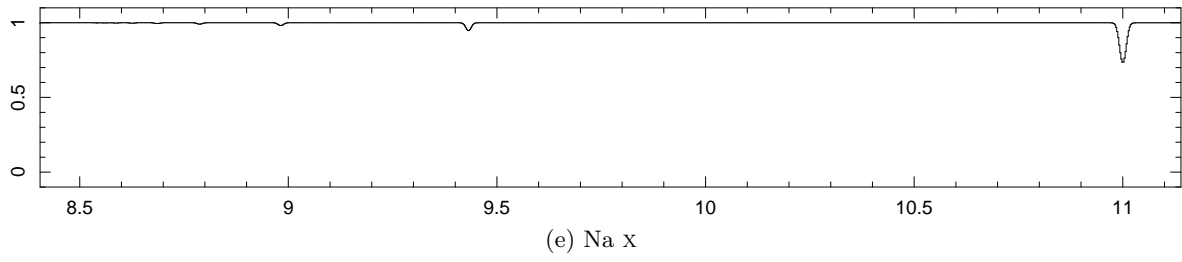
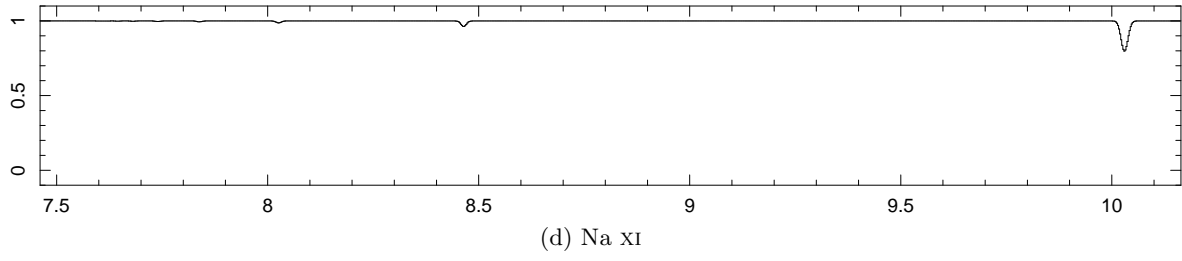
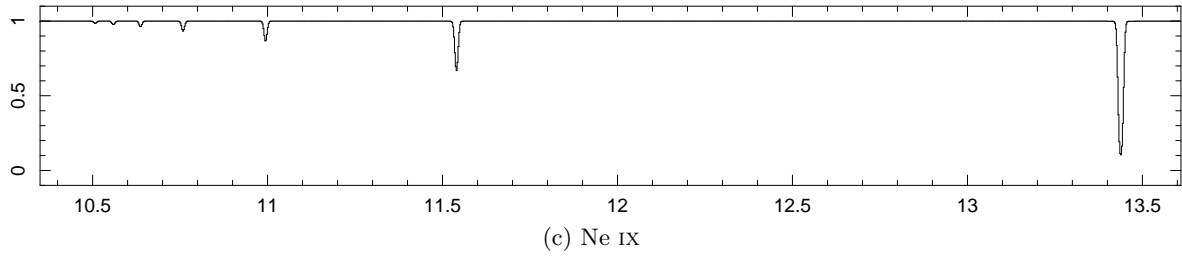
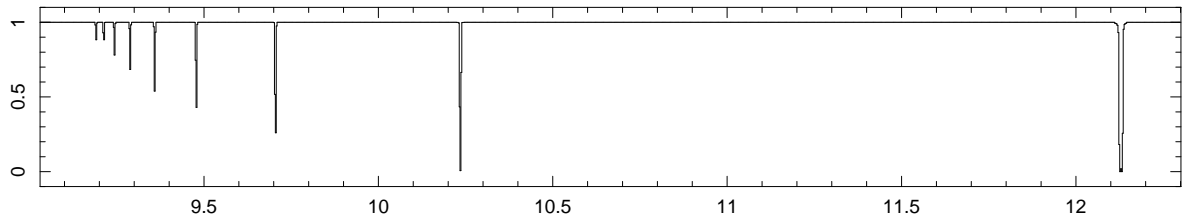


Fig. 4.14: Line profiles of the fitted series vs. wavelength in Å (continued on next pages).

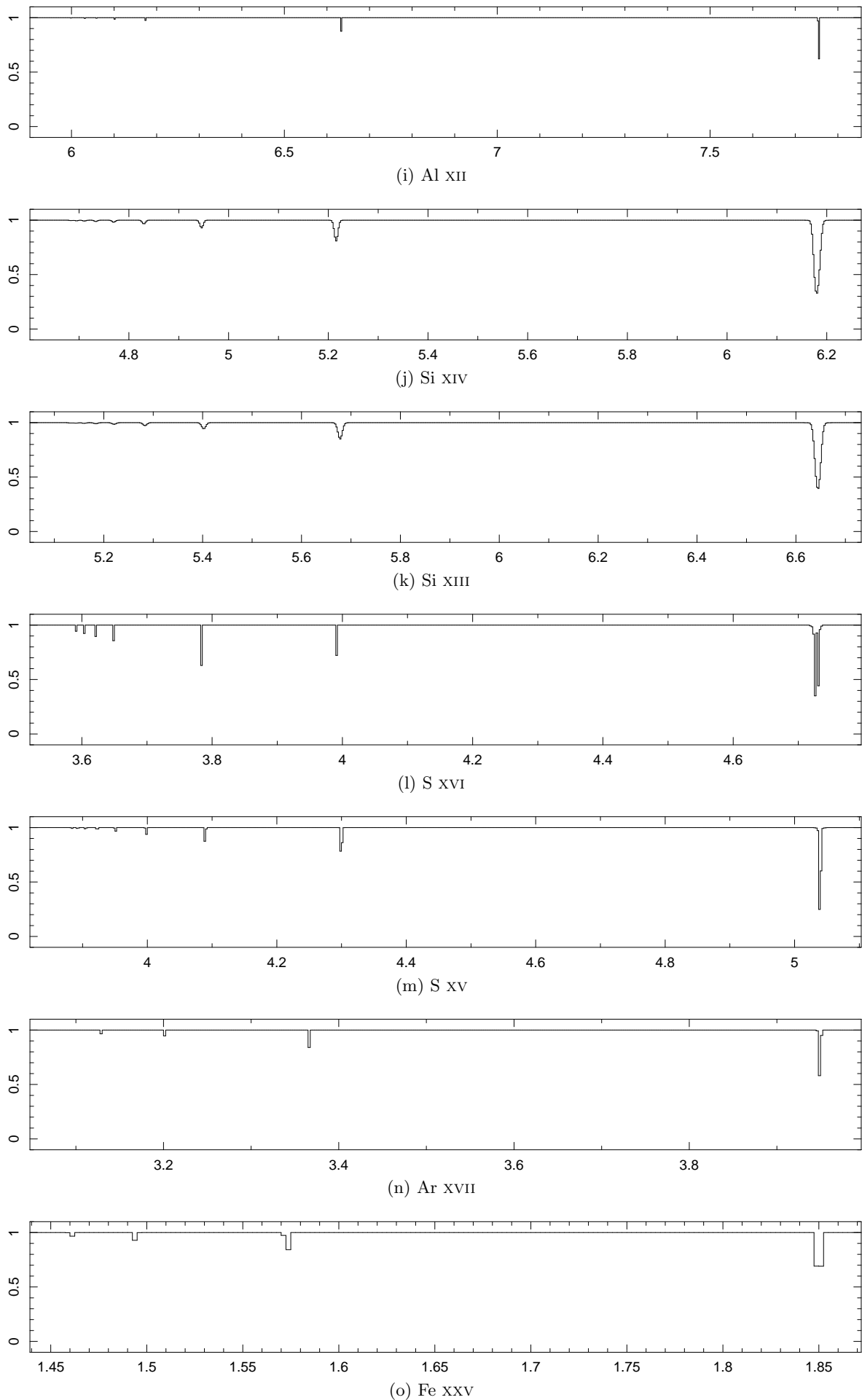


Fig. 4.14: Line profiles of the fitted series vs. wavelength in Å (continued on next page).

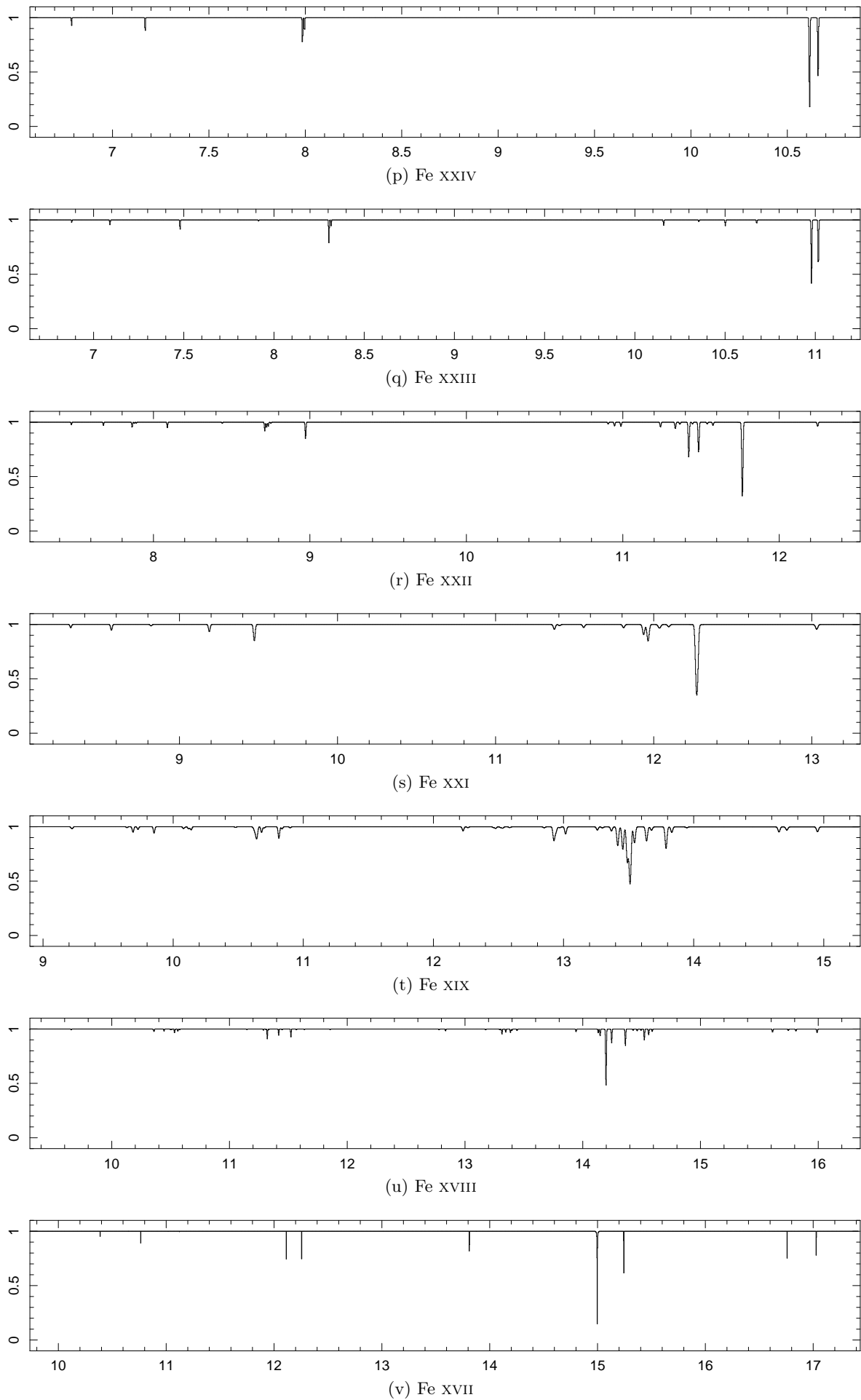


Figure 4.14: Line profiles of the fitted series vs. wavelength in Å.

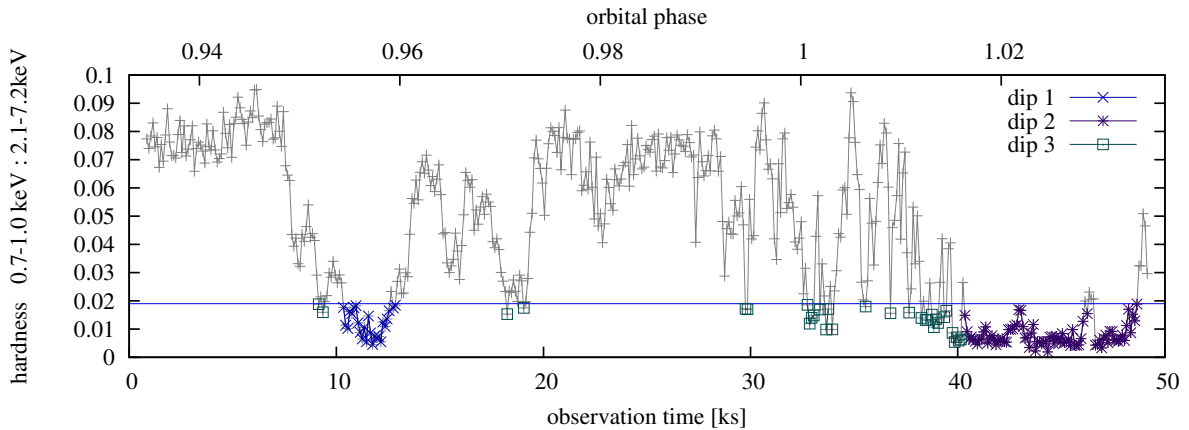


Figure 4.15: Definition of the ‘dip’ sub-spectra (see text).

4.3 The ‘dip’ spectrum

The ‘dip’ spectrum is composed from those time-intervals of the *Chandra*-observation # 3814 where the (inverse) hardness-ratio between the count rates in the 0.7... 1.0 keV-band and in the 2.1... 7.2 keV-band is lower than 0.019. Its total exposure time is therefore 13.3 ks. Due to this definition, spectral properties very different of the ‘non-dip’ spectrum are expected.

4.3.1 Consistency checks

The ‘dip’ spectrum is divided in separate temporal parts just like the ‘non-dip’ spectrum in Sect. 4.2.1. The three sub-spectra are shown in Fig. 4.8: The ‘dip 1’ spectrum, which is shown in blue, uses the first 2.4 ks short dip. There is a long deep dip at the end of the observation (drawn in purple), which will be referred to as ‘dip 2’. Its total exposure is 8.1 ks. The rest of the ‘dip’ events occurring in the remaining 3.0 ks form the ‘dip 3’ spectrum, which is shown as turquoise boxes.

The ratio of each of the (flux-corrected) sub-spectra with the whole (flux-corrected) ‘dip’ spectrum was calculated after a rebinning by a factor of 4 for MEG \pm 1 and 8 for HEG \pm 1 spectra. The plots are shown as Figs. ??, ?? and ?? on page ?. The separate dipping events ‘dip 1’ and ‘dip 2’ show notably different absorption. The ‘dip 1’ spectrum is less absorbed than the average ‘dip’ spectrum, as the ratio shown in Fig. ?? exceeds 1 at higher wavelength, where photoabsorption becomes dominant. For the same reason, the ‘dip 2’ spectrum (Fig. ??) is more strongly obscured, as already expected from the light curve (Fig. 4.6), which shows ‘dip 2’ to be the deepest dip. Finally, the ‘dip 3’ spectrum is mostly consistent with the average ‘dip’ spectrum.

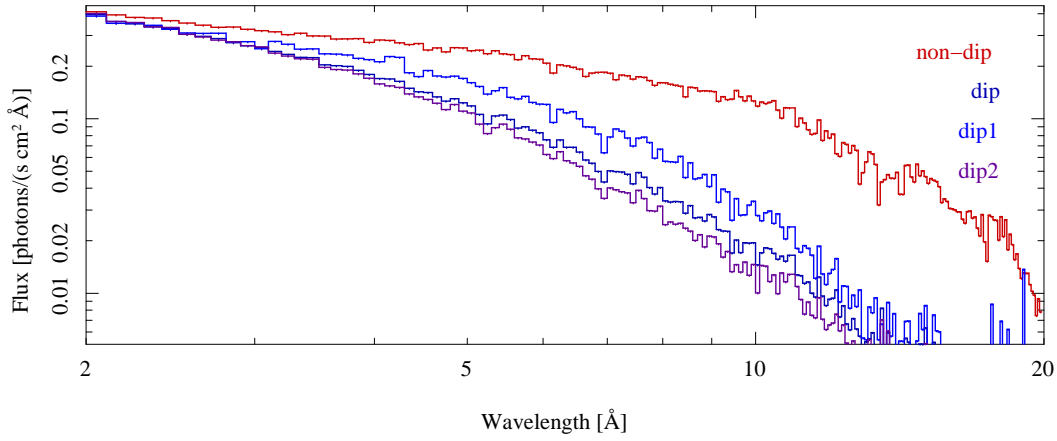
This behavior can also be seen directly in the flux-corrected spectra, Fig. 4.16.

4.3.2 Description of the continuum

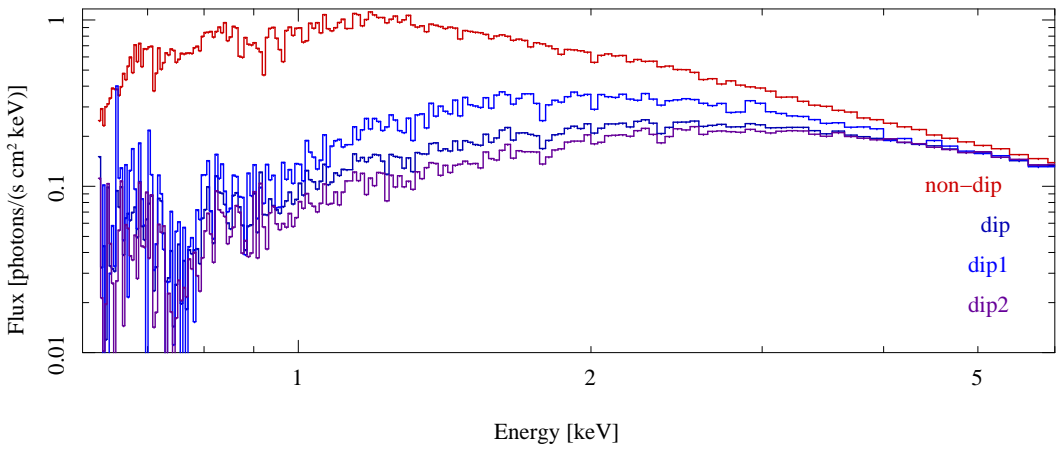
It is necessary to have the proper continuum for the detection of absorption or emission lines.

Comparing the flux-corrected spectra of the ‘non-dip’ spectrum with the ‘dip’ spectra (Fig. 4.16), it is clear that the dips in this observation (both ‘dip 1’ and ‘dip 2’) are of type A according to the nomenclature of Feng & Cui (2002) (see Sect. 1.3.4). The ‘dip’ spectra are reduced with respect to the ‘non-dip’ spectra especially at low energies, probably indicating an increased absorbing column density.

The ‘dip’ spectrum cannot properly be described by the usual continuum model 4.3 (pile-up reduced photoabsorbed power law): The best fit gives a power law with a photon index $\Gamma \approx 0.8$, which is far below the value obtained for the ‘non-dip’ spectrum ($\Gamma_{\text{non-dip}} = 1.55$). One might wonder if this could be due to the inconsistent spectral shape of the sub-spectra (cf. Figs. ?? and ??), but similar problems with inconsistent values of Γ arise in these cases as well (see Table 4.21). It is however expected that the power law spectrum of the source Cyg X-1 rests unchanged during the dipping events and that those only show different levels of photoabsorption.



(a) Wavelength spectrum $S_\lambda(\lambda)$



(b) Energy spectrum $S_E(E)$

Figure 4.16: The ‘non-dip’, ‘dip’, ‘dip 1’ and ‘dip 2’ flux-corrected spectra. (rebinned to 0.1 Å-bins)

Therefore, a slightly different model for the continuum is investigated: a two component photoabsorbed power law with the same pile-up reduction as before, i.e., one power law is divided into two parts with separate absorption – a “partial covering model”. This is realized by two instances of the `powerlaw` model whose photon indices are tied together:

$$\begin{aligned}
 S_E^s(E) &= c_s \cdot \left(\frac{E}{1\text{keV}}\right)^{-\Gamma} \cdot (S_1 \cdot e^{-\sum_Z \sigma_Z(E) \cdot A_Z \cdot N_{H,1}} + S_2 \cdot e^{-\sum_Z \sigma_Z(E) \cdot A_Z \cdot N_{H,2}}) \\
 C_0^{\text{piled},s}(i) &= C_0^s(i) \cdot \exp\left(-\beta_s \cdot C_{0,\text{sim}}^{\text{unpiled},s}(i)\right)
 \end{aligned}$$

```

fit_fun("simple_gpile2(Isis_Active_Dataset,
                constant(Isis_Active_Dataset)
                * (powerlaw(1)*phabs(1) + powerlaw(2)*phabs(2))
                )");
tie("powerlaw(1).PhoIndex", "powerlaw(2).PhoIndex");

```

(4.6)

In order to understand the best fit parameters and put them in a consistent description of all spectra, several dependencies were investigated for the ‘non-dip’ and ‘dip [1/2]’ spectra:

- A) In order to check the consistency within the 4 spectra MEG±1, HEG±1 and to reduce the number of parameters (which will be a problem in the second approach of investigation, especially with view of the correlation between the pile-up scale and the multiplicative constant), the spectra from the different gratings have been fitted separately. Fixed “canonical” pile-up scales ($\beta_{\text{MEG}} = 2 \cdot \beta_{\text{HEG}} = 0.0575 \text{ s } \text{\AA}$; cf. Sect. 4.2.2) have been used,

and multiplicative constants were dispensable, as only one spectrum was considered at a time. The data have been rebinned to contain at least 30 counts per bin. The best fit values of Γ and their 90% confidence intervals are listed in Tables 4.13 & 4.14, 4.15 & 4.16, 4.17 & 4.18 and 4.19 & 4.20. for the ‘non-dip’, ‘dip’, ‘dip 1’ and ‘dip 2’ spectrum with the one & two component model. The corresponding minima of χ^2 and the dependence of the other best fit parameters $S_E(1 \text{ keV})$ and N_H on the fixed value of Γ are shown in Figs. ??, ?? & ??, ?? & ??, and ?? & ?? on pages ??–??.

B) The best fit parameters for Γ , $S_E(1 \text{ keV})$ and N_H depend quite sensitively on the range $[\lambda_1, \lambda_2]$ which is used for fitting. As photoabsorption plays a minor role in the high energy range, the power law parameters should be best determined with the data at lower wavelengths. Therefore the lower boundary of the interval $[\lambda_1, \lambda_2]$, which is used for fitting, was kept fixed at $\lambda_1 = \lambda_{\min(\text{HETGS})} = 1 \text{ \AA}$. The best fit parameters in dependence of λ_2 are shown in Figs. ?? & ??, ?? & ??, ?? & ?? (?? & ??) and ?? & ?? (?? & ??) for the ‘non-dip’, ‘dip’, ‘dip 1’ and ‘dip 2’ spectrum with the one & two component model. (The brackets denote figures where the pile-up scales had been frozen. This was done because best fit scales often gave quite unphysical values and it was found that the other parameters do not depend so much on the pile-up scales. The multiplicative constants often compensate the effect of the corresponding pile-up scales, which shows that these pairs of parameters are strongly coupled.) If one considers larger wavelength intervals $[\lambda_1, \lambda_2]$ to be more convincing than shorter ones, the plots should be read from the right to the left. The “last” results shown for $\lambda_2 < 6 \text{ \AA}$ (implying a $|\lambda_2 - \lambda_1| < 5 \text{ \AA}$ range used for fitting) are certainly not very meaningful.

The values of Γ and the power law’s norm that was used to describe the ‘non-dip’ spectrum in section 4.2.2 are also shown in the plots as dashed lines, as they were expected to be also appropriate for the other spectra. In case of the power law norms of the two component model, the sum of the two norms (which is also shown in the corresponding figures) should be comparable with the previous value.

Parameter dependencies in the ‘non-dip’ spectrum

A) Fig. ?? on page ?? shows the dependence of the best fit parameters for the ‘non-dip’ spectrum on the frozen value of Γ . The dashed lines (which are over-plotted by identical solid lines for low Γ) hold for the one parameter model, which will be discussed first. The third panel shows nice parabolic χ^2 curves around the minima at $\Gamma_{\text{opt}} \approx 1.5$. The statistic is better for the HEG spectra, because the count rates are lower and the relative errors therefore larger than in the MEG spectra. The best fit values for Γ for the different spectra are however not really consistent with each other on the 90% confidence level:

Table 4.13: fitted Γ for the one-component model 4.3 of the ‘non-dip’ spectrum (rebinned to ≥ 30 counts/bin; $[1 \text{ \AA}, 20 \text{ \AA}]$ range noticed)

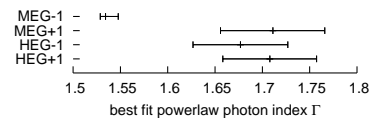
$\Gamma_{\text{opt}}^{\text{MEG-1}} = 1.513 \pm 0.011$	$\Gamma_{\text{opt}}^{\text{MEG+1}} = 1.458 \pm 0.012$	
$\Gamma_{\text{opt}}^{\text{HEG-1}} = 1.509 \pm 0.011$	$\Gamma_{\text{opt}}^{\text{HEG+1}} = 1.489 \pm 0.012$	

The power law norms $S_E(1 \text{ keV})$ rise with Γ from $\approx 0.6 \text{ ph.}(s \text{ cm}^2 \text{ keV})^{-1}$ at $\Gamma = 1$ to $\approx 2 \text{ ph.}(s \text{ cm}^2 \text{ keV})^{-1}$ at $\Gamma = 2$ passing $S_E(1 \text{ keV}) \approx 1.1 \text{ ph.}(s \text{ cm}^2 \text{ keV})^{-1}$ at the best fit $\Gamma_{\text{opt}} \approx 1.5$. This is due to the fact that the largest part of the data is at $E > 1 \text{ keV}$, which needs for increased Γ also an increased norm to fit with a steeper descending power law $\sim E^{-\Gamma}$. The absorbing N_H also increases with Γ , namely from $\approx 0.1 \times 10^{22} \text{ cm}^{-2}$ to $\approx 0.7 \times 10^{22} \text{ cm}^{-2}$ on average.

The best fit parameters of the two component model are for low $\Gamma \lesssim 1.5$ almost identical with those of the one component model, in the sense that the norm S_2 of the second component (lower curves in the top panel of Fig. ??) vanishes. This is *not* due to the fact that the absolute minimum of χ^2 has not been found during the fitting, as one might think, because the same

fit parameters have also been determined by starting at high Γ and constantly decreasing it. Furthermore, quite high absorbing columns $N_{\text{H},2}$ of the (anyway vanishing) second component have been found, which are not related to any starting values. (These high values of N_{H} lead also to the numerical artefacts that the norm of the second component explodes at some points near $\Gamma = 1.5$ – in fact, the second component vanishes in this region.) Above $\Gamma \approx 1.5$, the χ^2 curves do not rise again parabolically, but form new, very flat χ^2 minima, which are shown in the last panel which is a magnified extract of the χ^2 curve. The curves for the MEG spectra use the left axis, while the curves for the HEG spectra are plotted with respect to the right scale. The power law norms of the first components of model 4.6 branch off the corresponding tracks of the power law norms in the single component model, while the norms of the second component begin to rise. From this turn-off point on, the absorbing $N_{\text{H},1}$ does not rise as strong as N_{H} of the one component model any more. The values of $N_{\text{H},2}$ (also shown on the middle panel, but for the righthand axis with a different scale) descend from their previous values, which were unrealistically high – but also not very meaningful, as this just expresses the fact that the second component vanishes in this range. N_{H} achieves now values between 6 and $10 \times 10^{22} \text{ cm}^{-2}$. The best fit values for Γ with the two component model show much larger errors and are – except of the MEG–1 result, which finds its optimum with only one component – consistent with $\Gamma = 1.7 \pm 0.7$, see Table 4.14.

Table 4.14: fitted Γ for the two-component model 4.6 of the ‘non-dip’ spectrum (rebinned to ≥ 30 counts/bin; $[1 \text{ \AA}, 20 \text{ \AA}]$ range noticed)

$\Gamma_{\text{opt}}^{\text{MEG-1}} = 1.534^{+0.013}_{-0.019}$	$\Gamma_{\text{opt}}^{\text{MEG+1}} = 1.71 \pm 0.06$	
$\Gamma_{\text{opt}}^{\text{HEG-1}} = 1.68 \pm 0.05$	$\Gamma_{\text{opt}}^{\text{HEG+1}} = 1.71 \pm 0.05$	

B) The second analysis investigates the dependence on λ_2 , if the range $[1 \text{ \AA}, \lambda_2]$ used for fitting is varied. For the ‘non-dip’ spectrum described with the one component model, Fig. ?? of appendix ?? (p. ??) shows that the photon index Γ is very stable for $\lambda_2 \geq 14 \text{ \AA}$. In the whole tested range of $4 \text{ \AA} \leq \lambda_2 \leq 18 \text{ \AA}$, the best fit photon index Γ varies only within 0.1 in total. The same holds for the power law norm $S_E(1 \text{ keV})$ and the absorbing column density N_{H} , whose evolution with λ_2 is quite parallel to $\Gamma(\lambda_2)$, as can be seen from Fig. ?. Furthermore, the spectrum-dependent constants c_i and the pile-up scales β_i stay for large λ_2 very stable at the values which are also in agreement with the estimation from the frame time and the dispersion of the gratings (see end of Section 4.2.2). This justifies, why these parameters have been chosen to describe the continuum of the ‘non-dip’ spectrum.

The trend that higher values of Γ are preferred within the two component model, which has already been noticed in part A, is also seen in this approach to model 4.6, which is shown in Fig. ?. The implications will be discussed at the end of this section.

Parameter dependencies in the ‘dip’ spectrum

A) Fig. ?? shows the χ^2 curves (in the bottom panel) and the other fit parameters $S_E(1 \text{ keV})$ and N_{H} for the spectra MEG \pm 1 and HEG \pm 1 fitted with the one component power law model 4.3. The trend of the power law norm and absorbing column density is quite similar to the ‘non-dip’ spectrum (except that N_{H} varies from $\approx 0.5 \times 10^{22} \text{ cm}^{-2}$ at $\Gamma = 0.4$ to $\approx 3 \times 10^{22} \text{ cm}^{-2}$ at $\Gamma = 2$), but it is obvious that there is no consistent value of Γ at all; $\Gamma_{\text{opt}}^{\text{MEG+1}}$ and $\Gamma_{\text{opt}}^{\text{HEG+1}}$ differ by more than 20σ (Table 4.15; σ is the error on the 90% CL):

Table 4.15: fitted Γ for the one-component model 4.3 of the ‘dip’ spectrum
(rebinned to ≥ 30 counts/bin; $[1 \text{ \AA}, 20 \text{ \AA}]$ range noticed)

$\Gamma_{\text{opt}}^{\text{MEG-1}} = 0.525 \pm 0.022$ $\Gamma_{\text{opt}}^{\text{HEG-1}} = 0.844 \pm 0.021$	$\Gamma_{\text{opt}}^{\text{MEG+1}} = 0.502 \pm 0.021$ $\Gamma_{\text{opt}}^{\text{HEG+1}} = 0.975 \pm 0.022$	
------------------------------------------------------------------------------------------------------------------	------------------------------------------------------------------------------------------------------------------	--

The results of the same analysis with two component power law model 4.6 are shown in Fig. ?? : The component with the higher absorption (from $\approx 0.5 \times 10^{22} \text{ cm}^{-2}$ to $\approx 9 \times 10^{22} \text{ cm}^{-2}$) is drawn by solid lines, while the dashed curves depict the parameters for the lower absorption (up to $\approx 1.1 \times 10^{22} \text{ cm}^{-2}$). The curves for the power law norm show that the norm of the more strongly absorbed component is at least twice as high as the other norm (independent of Γ), telling that more than 2/3 of the flux is heavily obscured. The χ^2 curves are much broader than in the case of the one component model, which results in larger errors for the best fit values of Γ , see Table 4.16. These are still inconsistent, but not so much as with the one component model ($\Gamma_{\text{opt}}^{\text{HEG+1}} - \Gamma_{\text{opt}}^{\text{MEG-1}} < 7\sigma$). Furthermore, Γ_{opt} is higher than before, which is much more plausible.

Table 4.16: fitted Γ for the two-component model 4.6 of the ‘dip’ spectrum
(rebinned to ≥ 30 counts/bin; $[1 \text{ \AA}, 20 \text{ \AA}]$ range noticed)

$\Gamma_{\text{opt}}^{\text{MEG-1}} = 1.12^{+0.06}_{-0.05}$ $\Gamma_{\text{opt}}^{\text{HEG-1}} = 1.35 \pm 0.05$	$\Gamma_{\text{opt}}^{\text{MEG+1}} = 1.28^{+0.07}_{-0.06}$ $\Gamma_{\text{opt}}^{\text{HEG+1}} = 1.46 \pm 0.05$	
---------------------------------------------------------------------------------------------------------------------	---------------------------------------------------------------------------------------------------------------------	--

B) Figs. ?? and ?? show the dependence of the best fit parameters of the one / two component model for the ‘dip’ spectrum in the range $[\lambda_1 = 1 \text{ \AA}, \lambda_2]$ on λ_2 . If the ‘dip’ spectrum is described by the one component model 4.3, the best fit parameters give a drastically low $\Gamma < 0.8$, which even appears to be stable at high λ_2 . With decreasing λ_2 , the photon index Γ – and $S_E(1 \text{ keV})$ as well as N_H , which are (just as in case of the ‘non-dip’ spectrum) strongly correlated with Γ – rise monotonically over quite a large range, but hardly reach the parameters of the ‘non-dip’ continuum model. Furthermore, the constant factors correcting for the possibly improper absolute flux calibration (relative to $c_{\text{MEG-1}}^{\text{dip}} \equiv 1$) differ further from 1 than in the fits of the ‘non-dip’ spectrum: $c_{\text{HEG-1}}^{\text{dip}} \approx 0.935$ and $c_{\text{HEG+1}}^{\text{dip}}$ even ≈ 0.915 , while $c_{\text{HEG-1}}^{\text{non-dip}} \approx 0.972$ and $c_{\text{HEG+1}}^{\text{non-dip}} \approx 0.943$ was used for the ‘non-dip’ spectrum (Section 4.2.2) At last, the exponential scale $\beta_{\text{HEG+1}}$ was found to vanish for the most values of λ_2 , which is certainly not appropriate, but might be due to problems in finding the absolute minimum of χ^2 with the strong correlation of the multiplicative constant and the pile-up scale (cf. Fig. 2.9, page. 42).

The whole ‘dip’ spectrum can better (in the sense of plausible parameters, not so much what concerns the fit statistic) be described by the two component model 4.6. Fig. ?? shows the best fit parameters with this model in dependence on λ_2 . The values $\Gamma \gtrsim 1.4$ are much more acceptable. The sum of the power law norms approaches the ‘non-dip’ best fit value (dashed line) far better than the best fit norm with the single power law model (Fig. ??).

One might think that it is not necessary to use a two component model, if one treats the sub-spectra ‘dip 1’ and ‘dip 2’ individually, as they clearly show different absorption (Figs. ?? and ??). Therefore, these sub-spectra are analyzed in the following sections as well.

Parameter dependencies in the ‘dip 1’ spectrum

A) The parameters of the ‘dip 1’ spectrum show similar behavior as those of the ‘non-dip’ and ‘dip’ spectrum before: The best fit values of Γ differ more significantly within the one component model than within the two component model, where all best fits of Γ really agree with $1.44 \leq \Gamma \leq 1.49$ on the 90% confidence level. Furthermore, the second model gives larger values of Γ , see Tables 4.17 and 4.18.

Table 4.17: fitted Γ for the one-component model 4.3 of the ‘dip 1’ spectrum
(rebinned to ≥ 30 counts/bin; [1 Å, 20 Å] range noticed)

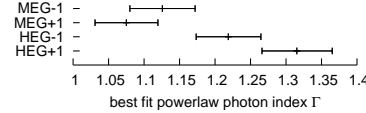
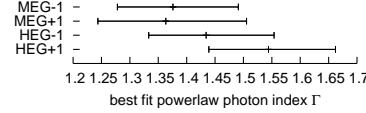
$\Gamma_{\text{opt}}^{\text{MEG-1}} = 1.126 \pm 0.046$	$\Gamma_{\text{opt}}^{\text{MEG+1}} = 1.075^{+0.045}_{-0.044}$	
$\Gamma_{\text{opt}}^{\text{HEG-1}} = 1.219^{+0.046}_{-0.045}$	$\Gamma_{\text{opt}}^{\text{HEG+1}} = 1.315^{+0.051}_{-0.048}$	

Table 4.18: fitted Γ for the two-component model 4.3 of the ‘dip 1’ spectrum
(rebinned to ≥ 30 counts/bin; [1 Å, 20 Å] range noticed)

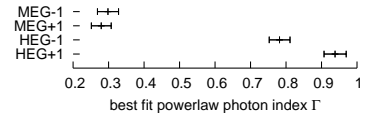
$\Gamma_{\text{opt}}^{\text{MEG-1}} = 1.38^{+0.12}_{-0.10}$	$\Gamma_{\text{opt}}^{\text{MEG+1}} = 1.36^{+0.14}_{-0.12}$	
$\Gamma_{\text{opt}}^{\text{HEG-1}} = 1.43^{+0.12}_{-0.10}$	$\Gamma_{\text{opt}}^{\text{HEG+1}} = 1.54^{+0.12}_{-0.11}$	

B) The analysis of the dependence on λ_2 (the upper bound of the range [1Å, λ_2] used for fitting) is shown in Fig. ?? and Fig. ?? for the one and the two component model respectively. It shows that even the ‘dip 1’ spectrum alone cannot properly be described by a single component absorbed power law. As the pile-up scales β_i have been fitted to quite low values, the analysis has been repeated with frozen values of β (Fig. ?? and Fig. ??), but this has hardly changed the other fit parameters.

Parameter dependencies in the ‘dip 2’ spectrum

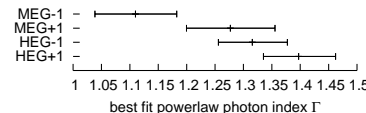
A) Analogous to the ‘dip 1’ spectrum, the ‘dip 2’ spectrum was treated in these ways. Again, the one component model (for the Γ -dependence, see Fig. ??) does not provide an adequate description of the ‘dip 2’ spectrum as well: the values of Γ spread from 0.28 (!) to 0.94:

Table 4.19: fitted Γ for the one-component model 4.3 of the ‘dip 2’ spectrum
(rebinned to ≥ 30 counts/bin; [1 Å, 20 Å] range noticed)

$\Gamma_{\text{opt}}^{\text{MEG-1}} = 0.298 \pm 0.030$	$\Gamma_{\text{opt}}^{\text{MEG+1}} = 0.279 \pm 0.028$	
$\Gamma_{\text{opt}}^{\text{HEG-1}} = 0.782 \pm 0.029$	$\Gamma_{\text{opt}}^{\text{HEG+1}} = 0.938 \pm 0.031$	

The two component model gives for MEG+1 and HEG±1 best fit values of Γ mostly in agreement with $\Gamma \approx 1.35$, see the following Table 4.20:

Table 4.20: fitted Γ for the two-component model 4.6 of the ‘dip 2’ spectrum
(rebinned to ≥ 30 counts/bin; [1 Å, 20 Å] range noticed)

$\Gamma_{\text{opt}}^{\text{MEG-1}} = 1.11 \pm 0.07$	$\Gamma_{\text{opt}}^{\text{MEG+1}} = 1.28 \pm 0.08$	
$\Gamma_{\text{opt}}^{\text{HEG-1}} = 1.32 \pm 0.06$	$\Gamma_{\text{opt}}^{\text{HEG+1}} = 1.40 \pm 0.06$	

Summary of the parameter dependencies and simultaneous fits

In general, the one component power law model

$$S_E^s(E) = c_s \cdot S_E(1 \text{ keV}) \cdot \left(\frac{E}{1 \text{ keV}} \right)^{-\Gamma} \cdot e^{-\sum_Z \sigma_Z(E) \cdot A_Z \cdot N_H} \quad (4.3)$$

constrains the values of Γ to a smaller interval than the two component power law model

$$S_E^s(E) = c_s \cdot \left(\frac{E}{1 \text{ keV}} \right)^{-\Gamma} \cdot \left(S_1 \cdot e^{-\sum_Z \sigma_Z(E) \cdot A_Z \cdot N_{H,1}} + S_2 \cdot e^{-\sum_Z \sigma_Z(E) \cdot A_Z \cdot N_{H,2}} \right), \quad (4.6)$$

which also has two more free parameters. Furthermore, the best fit values of the two component model were found to be higher than those of the other model.

The ‘non-dip’ spectrum can be described by a one component model with $\Gamma \approx 1.5$ which is for lower Γ identical with the best fits of the two component model. The ‘dip’ spectrum and its sub-spectra ‘dip 1’ and ‘dip 2’ however need the two component model 4.6, as the description with model 4.3 lead to inconsistent parameters within the 4 grating spectra MEG \pm 1 and HEG \pm 1. Furthermore, the two component model leads (for the ‘dip’ spectra) to best fit parameters Γ and $S_E(1 \text{ keV})$, which are *much closer* to a consistent description of all spectra. This can also be seen from Table 4.21, which lists the best fit parameters for the simultaneous fit of the 4 spectra each for both models with their 90% confidence intervals.

However, there is still no general agreement on the source parameters Γ and $S_E(1 \text{ keV})$, respectively $S_1 + S_2$. This indicates that the absorption processes in the Cyg X-1 system, especially during these dips, cannot be described as simply as with a single **phabs** or even a partial covering model. The fact that the absorbing material can be highly ionized may be among the possible reasons for this issue.

Table 4.21: Best fit parameters for the one / two absorbing component power law model. All spectra have been rebinned to have ≥ 30 counts/bin and the $[1\text{\AA}, 20\text{\AA}]$ range was used for fitting. (The canonical pile-up scale of $\beta_{\text{MEG}} = 2 \cdot \beta_{\text{HEG}} = 0.05745 \text{ s} \cdot \text{\AA}$ was kept fixed.)

one component model 4.3: $S_E^s(E) = c_s \cdot S_E(1 \text{ keV}) \cdot \left(\frac{E}{1 \text{ keV}}\right)^{-\Gamma} \cdot e^{-\sum_Z \sigma_Z(E) \cdot A_Z \cdot N_H}$				
spectrum	‘non-dip’ (16.1 ks)	‘dip’ (13.3 ks)	‘dip 1’ (2.4 ks)	‘dip 2’ (8.1 ks)
Γ	1.511 ± 0.005	0.743 ± 0.010	1.1876 ± 0.022	0.618 ± 0.015
$S_E(1 \text{ keV}) / \frac{\text{photons}}{\text{s cm}^2 \text{ keV}}$	1.152 ± 0.008	0.2946 ± 0.0047	$0.614^{+0.020}_{-0.019}$	0.241 ± 0.006
$N_H / 10^{22} \text{ cm}^{-2}$	0.3689 ± 0.0034	0.945 ± 0.014	0.973 ± 0.025	$1.097^{+0.022}_{-0.023}$
c_1	0.9788 ± 0.0045	0.994 ± 0.007	$0.987^{+0.015}_{-0.014}$	$1.003^{+0.010}_{-0.009}$
c_2	0.9816 ± 0.0046	0.973 ± 0.007	0.973 ± 0.015	0.976 ± 0.010
c_3	0.9827 ± 0.0048	0.980 ± 0.007	0.985 ± 0.016	0.981 ± 0.010
χ^2/ν	$\frac{21807}{12668-6} = 1.72$	$\frac{14136}{7396-6} = 1.91$	$\frac{3810.4}{3211-6} = 1.19$	$\frac{11066}{5809-6} = 1.91$
two component model 4.6:				
$S_E^s(E) = c_s \cdot \left(\frac{E}{1 \text{ keV}}\right)^{-\Gamma} \cdot (S_1 \cdot e^{-\sum_Z \sigma_Z(E) \cdot A_Z \cdot N_{H,1}} + S_2 \cdot e^{-\sum_Z \sigma_Z(E) \cdot A_Z \cdot N_{H,2}})$				
spectrum	‘non-dip’ (16.1 ks)	‘dip’ (13.3 ks)	‘dip 1’ (2.4 ks)	‘dip 2’ (8.1 ks)
Γ	1.695 ± 0.024	1.335 ± 0.025	$1.443^{+0.057}_{-0.054}$	$1.321^{+0.031}_{-0.030}$
$(S_1 + S_2) / \frac{\text{photons}}{\text{s cm}^2 \text{ keV}}$	1.67 ± 0.08	0.83 ± 0.04	0.95 ± 0.18	0.83 ± 0.05
$S_1 / \frac{\text{photons}}{\text{s cm}^2 \text{ keV}}$	1.307 ± 0.022	0.229 ± 0.012	$0.39^{+0.10}_{-0.11}$	$0.166^{+0.010}_{-0.009}$
$N_{H,1} / 10^{22} \text{ cm}^{-2}$	0.417 ± 0.007	0.612 ± 0.029	$0.69^{+0.10}_{-0.12}$	0.603 ± 0.032
$S_2 / \frac{\text{photons}}{\text{s cm}^2 \text{ keV}}$	$0.36^{+0.06}_{-0.05}$	$0.602^{+0.029}_{-0.028}$	0.56 ± 0.07	$0.662^{+0.039}_{-0.036}$
$N_{H,2} / 10^{22} \text{ cm}^{-2}$	$8.5^{+0.7}_{-0.6}$	$4.02^{+0.16}_{-0.15}$	$2.44^{+0.52}_{-0.44}$	4.38 ± 0.16
c_1	0.9786 ± 0.0045	0.994 ± 0.007	$0.985^{+0.015}_{-0.014}$	1.004 ± 0.009
c_2	$0.9813^{+0.0047}_{-0.0046}$	0.979 ± 0.007	0.977 ± 0.015	0.985 ± 0.010
c_3	0.983 ± 0.005	0.990 ± 0.007	0.990 ± 0.016	0.994 ± 0.010
χ^2/ν	$\frac{21615}{12668-8} = 1.71$	$\frac{10519}{7396-8} = 1.42$	$\frac{3636.8}{3211-8} = 1.14$	$\frac{7663.5}{5809-8} = 1.32$

4.3.3 Lines in the spectrum

Again, as soon as a model describing the continuum to some extent is available, absorption and emission lines can be investigated. This follows the same procedure that was used in Sect. 4.2.3 for the ‘non-dip’ spectrum. Though not expected, the ‘dip’ spectrum is found to be less rich of absorption lines than the ‘pure’ spectrum. The following Table 4.22 shows again the list of lines sorted by χ^2 improvement:

Table 4.22: List of lines in the ‘dip’ spectrum – sorted by χ^2 improvement (see Table 4.4)

λ [Å]	EW [mÅ]	$\Delta\chi^2$		λ [Å]	EW [mÅ]	$\Delta\chi^2$		λ [Å]	EW [mÅ]	$\Delta\chi^2$	
6.92	-10.09	275	Si IX K α	7.00	-8.26	208	Si VIII K α	6.87	-7.81	178	Si X K α
6.85	-6.16	154	Si X K α	5.23	-10.98	153	Si XIV	9.38	-13.22	141	
6.79	-7.64	134	Si XI K α	6.18	-8.83	132	Si XIV	6.94	-4.70	108	Si IX K α
6.74	6.88	79.0	Si XIII	9.23	13.39	72.8	Mg XI	1.94	7.67	69.3	Fe K α
6.65	-5.52	65.2	Si XIII	9.29	-11.18	63.7		9.32	13.46	54.3	
9.50	-7.82	53.1		7.86	-5.79	40.5	Mg XI	5.27	-6.24	40.3	
9.48	-8.69	39.0	Fe XXI	13.54	129.81	39.0	Ne IX	10.69	-8.65	37.4	Fe XIX
5.18	-6.38	36.6		9.52	-7.20	36.5		9.60	-9.94	35.4	
7.05	-3.27	32.7		5.71	4.53	29.8		9.63	-5.43	29.2	
4.72	-4.91	29.0	S XVI	7.47	-3.23	28.2	Mg XI	7.80	6.32	27.4	Al XII
5.69	-4.83	24.7	Si XIII	8.66	-11.31	24.5		3.96	-2.42	24.0	Ar XVII
6.04	-3.22	19.9	Al XIII	9.71	-4.55	19.3	Fe XIX	9.65	-5.06	19.1	
9.73	-6.60	18.2		1.52	-6.26	18.1	Ni XXVIII	11.10	14.75	16.7	
12.47	-14.04	16.6		10.93	16.66	16.3		5.13	-2.51	14.4	
1.85	-2.36	13.9	Fe XXV	10.64	-6.04	13.6	Fe XIX	3.99	-1.83	13.3	S XVI
8.03	-5.00	13.0		6.46	2.45	11.9		5.04	-1.99	11.5	S XV
15.33	138.96	11.4		7.11	-2.05	11.3	Mg XII	12.10	-15.63	10.9	
6.72	-1.96	10.6	Mg XII	1.49	-3.50	10.5	Fe XXVI	9.68	-5.89	10.4	
6.31	-2.35	10.3		8.07	2.70	9.77		10.57	-5.06	9.63	Fe XVIII
10.31	8.89	7.98		3.31	-1.46	7.78		3.74	-1.46	7.76	Ar XVIII
5.79	2.08	7.21		10.55	-4.18	6.96	Fe XVIII	10.52	-4.12	6.80	Fe XVIII
11.21	11.34	6.44		5.82	-2.38	6.32		11.07	-4.77	6.09	
4.31	-1.41	5.97	S XV	10.43	-5.14	5.34		7.18	-1.40	4.86	Al XIII
5.91	-1.40	4.61		5.41	-1.58	4.50	Si XIII	11.57	-5.64	4.24	
3.05	-0.92	4.12		3.35	-0.80	3.18	Ar XVII	11.00	-3.08	2.56	Na X
7.88	1.07	1.71	Al XII	7.16	-0.76	1.29		12.80	-3.94	0.90	

Lines from highly ionized (H-, He- or Li-like) ions and even higher ionized iron

The following Tables 4.23–4.27 give again an overview on the absorption lines from H-like, He-like, Li-like and further iron ions, as well as the He-like triplets in the ‘dip’ spectrum. Lines definitively seen are listed in with **bold** numbers; those showing only a small signal and not always fitted are marked *slanted*, and those, which are not seen, are ~~stroked out~~. If a wavelength is not covered by the ‘dip’ spectrum with a signal to noise ratio high enough for the spectroscopy, it is put in ()-brackets.

Table 4.23: $\lambda/\text{Å}$ of H-like ions’ absorption lines (as in Table ??) in the ‘dip’ spectrum

transition from 1s	O VIII	Ne X	Na XI	Mg XII	Al XIII	Si XIV	S XVI	Ar XVIII	Ca XX	Fe XXVI	Ni XXVIII
2p (Ly α)	(18.97)	12.13	10.03	8.42	7.17	6.18	4.73	3.73	3.02	1.78	1.53
3p (Ly β)	(16.01)	10.24	8.46	7.11	6.05	5.22	3.99	3.15	2.55	1.50	1.29
4p (Ly γ)	(15.18)	9.71	8.02	6.74	5.74	4.95	3.78	2.99	2.42	1.42	1.23
5p (Ly δ)	(14.82)	9.48	7.83	6.58	5.60	4.83	3.70	2.92	2.36	1.39	1.20
6p (Ly ϵ)		9.36	7.73				3.65	2.88			

Table 4.24: $\lambda/\text{\AA}$ of He-like ions' triplets (as in Table ??) in the 'dip' spectrum: resonance (r) absorption line and intercombination (i) and forbidden (f) emission lines

transition	O	Ne	Na	Mg	Al	Si	S	Ar	Ca	Fe	Ni
from/to $1s^2 (^1S_0)$	VII	IX	X	XI	XII	XIII	XV	XVII	XIX	XXV	XXVII
$r_{\text{abs}} 1s2p (^1P_1)$	(21.60)	13.45	11.00	9.17	7.76	6.65	5.04	3.95	3.18	1.85	1.59
$i_{\text{em}} 1s2p (^3P_{2,1})$	(21.80)	13.55	11.08	9.23	7.80	6.69	5.07	3.97	3.19	1.86	1.60
$f_{\text{em}} 1s2s (^3S_1)$	(22.10)	13.70	11.19	9.31	7.87	6.74	5.10	3.99	3.21	1.87	

Table 4.25: $\lambda/\text{\AA}$ of He-like ions' absorption lines (as in Table ??) in the 'dip' spectrum

transition	O	Ne	Na	Mg	Al	Si	S	Ar	Ca	Fe	Ni
from $1s^2$	VII	IX	X	XI	XII	XIII	XV	XVII	XIX	XXV	XXVII
$\rightarrow 1s2p$	(21.60)	13.45	11.00	9.17	7.76	6.65	5.04	3.95	3.18	1.85	1.59
$\rightarrow 1s3p$	(18.63)	11.54	9.43	7.85	6.63	5.68	4.30	3.37	2.71	1.57	1.35
$\rightarrow 1s4p$	(17.77)	11.00	8.98	7.47	6.31	5.40	4.09	3.20	2.57	1.50	1.28
$\rightarrow 1s5p$	(17.40)	10.77	8.79	7.31	6.18	5.29	4.00	3.13	2.51	1.46	1.25
$\rightarrow 1s6p$	(17.20)	10.64	8.69	7.22	6.10	5.22	3.95	3.10			
$\rightarrow 1s7p$	(17.09)	10.57	8.63	7.17	6.06	5.19	3.92				
$\rightarrow 1s8p$	(17.01)	10.51	8.59	7.14	6.03	5.16	3.90				

Table 4.26: $\lambda/\text{\AA}$ of Li-like ions' absorption lines (as in Table ??) in the 'dip' spectrum

transition	S	Ar	Ca	Fe	Ni
	XIV	XVI	XVIII	XXIV	XXVI
$[1s^2] 2s \rightarrow [1s^2] 3p (^2P_{1/2})$	(30.5)	(23.59)	(18.73)	10.66	9.10
$[1s^2] 2s \rightarrow [1s^2] 3p (^2P_{3/2})$	(30.4)	(23.55)	(18.69)	10.62	9.06
$[1s^2] 2s \rightarrow [1s^2] 4p$	(23.0)	(17.74)	14.09	8.00	6.82
$[1s^2] 2s \rightarrow [1s^2] 5p$	(20.7)	15.93	12.64	7.17	6.11

Table 4.27: Further absorption lines of iron (as in Table ??) in the 'dip' spectrum

(a) Fe XXIII (Be-like ion, as in Table ??)

transition	$\lambda/\text{\AA}$
$[1s^2] (2s^2 (^1S_0) \rightarrow 2s3p (^1P_1))$	10.98
$[1s^2] (2s^2 (^1S_0) \rightarrow 2s3p (^1P_1))$	8.30
$[1s^2] (2s^2 (^1S_0) \rightarrow 2s5p (^1P_1))$	7.47
$[1s^2] (2s^2 (^1S_0) \rightarrow 2s3p (^3P_1))$	11.02
$[1s^2] (2s^2 (^1S_0) \rightarrow 2s4p (^3P_1))$	8.32

(b) Fe XXII (B-like ion, as in Table ??)

transition	$\lambda/\text{\AA}$
$[1s^2 2s^2] (2p (^2P_{1/2}) \rightarrow 3s (^2S_{1/2}))$	12.25
$[1s^2 2s^2] (2p (^2P_{1/2}) \rightarrow 3d (^2D_{3/2}))$	11.77
$[1s^2 2s^2] (2p (^2P_{1/2}) \rightarrow 4s (^2S_{1/2}))$	9.06
$[1s^2 2s^2] (2p (^2P_{1/2}) \rightarrow 4d (^2D_{3/2}))$	8.97
$[1s^2 2s^2] (2p (^2P_{1/2}) \rightarrow 5s (^2S_{1/2}))$	8.11
$[1s^2 2s^2] (2p (^2P_{1/2}) \rightarrow 5d (^2D_{3/2}))$	8.09
$[1s^2] 2s 2p (2s (^2P_{1/2}) \rightarrow 3p_{3/2})$	11.49
$[1s^2] 2s 2p (2s (^2P_{1/2}) \rightarrow 3p_{3/2})$	11.43

(c) Fe XXI (C-like ion, as in Table ??)

transition	$\lambda/\text{\AA}$
$[1s^2 2s^2] 2p (2p (^3P_0) \rightarrow 3d (^3D_0))$	12.28
$[1s^2] 2s 2p^2 (2s (^3P_0) \rightarrow 3p_{3/2})$	11.97
$[1s^2] 2s 2p^2 (2s (^3P_0) \rightarrow 3p_{3/2})$	11.95
$[1s^2 2s^2] 2p (2p (^3P_0) \rightarrow 4d (^3P_1))$	9.48
$[1s^2] 2s 2p^2 (2s (^3P_0) \rightarrow 4p_{3/2})$	9.19
$[1s^2 2s^2] 2p (2p (^3P_0) \rightarrow 5d_{3/2})$	8.57

(d) Fe XX (N-like ion, as in Table ??)

transition	$\lambda/\text{\AA}$
$[1s^2 2s^2] 2p^2 (2p (^4S_{3/2}) \rightarrow 3s (^4P_{1/2}))$	13.96
$[1s^2 2s^2] 2p^2 (2p (^4S_{3/2}) \rightarrow 3s (^4P_{3/2}))$	13.84
$[1s^2 2s^2] 2p^2 (2p (^4S_{3/2}) \rightarrow 3s (^4P_{5/2}))$	13.77
	13.06
	12.99
	12.97...12.96
$[1s^2 2s^2] 2p^2 (2p (^4S_{3/2}) \rightarrow 3d (...))$	12.92...12.91
	12.86...12.85
	12.83...12.82
	12.76...12.75
	12.58
$[1s^2] 2s 2p^3 (2s (^4S_{3/2}) \rightarrow 3p (...))$	12.53
	10.13...10.12
$[1s^2 2s^2] 2p^2 (2p (^4S_{3/2}) \rightarrow 4d (...))$	10.04...10.06
	9.99...10.01
	9.73...9.72
$[1s^2] 2s 2p^3 (2s (^4S_{3/2}) \rightarrow 4p (...))$	9.20...9.19
	9.11...9.10
$[1s^2 2s^2] 2p^2 (2p (^4S_{3/2}) \rightarrow 5d (...))$	9.07...9.06
$[1s^2 2s^2] 2p^3 (^4S_{3/2}) \rightarrow ...$	8.82

(e) Fe XIX (O-like ion, as in Table ??)

transition	$\lambda/\text{\AA}$
$[1s^2 2s^2] 2p^3 (2p (^3P_2) \rightarrow 3d_{5/2})$	13.79
$[1s^2 2s^2] 2p^3 (2p (^3P_2) \rightarrow 3d (^3F_3))$	13.64
$[1s^2 2s^2] 2p^3 (2p (^3P_2) \rightarrow 3d_{5/2})$	13.55
$[1s^2 2s^2] 2p^3 (2p (^3P_2) \rightarrow 3d (^3D_3))$	13.52
$[1s^2 2s^2] 2p^3 (2p (^3P_2) \rightarrow 3d_{3/2})$	13.50
$[1s^2 2s^2] 2p^3 (2p (^3P_2) \rightarrow 3d (^3S_1))$	13.46
$[1s^2 2s^2] 2p^3 (2p (^3P_2) \rightarrow 3d (^1F_3))$	13.42
$[1s^2] 2s 2p^4 (2s (^3P_2) \rightarrow 3p_{3/2})$	12.95
$[1s^2] 2s 2p^4 (2s (^3P_2) \rightarrow 3p_{3/2})$	12.93
$[1s^2 2s^2] 2p^3 (2p (^3P_2) \rightarrow 4d (^3D_3))$	10.82
$[1s^2 2s^2] 2p^3 (2p (^3P_2) \rightarrow 4d (^3F_3))$	10.68
$[1s^2 2s^2] 2p^3 (2p (^3P_2) \rightarrow 4d (^3D_3))$	10.65
$[1s^2 2s^2] 2p^3 (2p (^3P_2) \rightarrow 4d (^3P_2))$	10.64
$[1s^2 2s^2] 2p^3 (2p (^3P_2) \rightarrow 4d (^3S_1))$	10.63
$[1s^2 2s^2] 2p^3 (2p (^3P_2) \rightarrow 5d (^3D_3))$	-9.86
$[1s^2 2s^2] 2p^3 (2p (^3P_2) \rightarrow 5d (\dots))$	9.69

(f) Fe XVIII (F-like ion, as in Table ??)

transition	$\lambda/\text{\AA}$
$[1s^2 2s^2] 2p^4 (2p (^2P_{3/2}) \rightarrow 3s (^2P_{3/2}))$	16.00
$[1s^2 2s^2] 2p^4 (2p (^2P_{3/2}) \rightarrow 3s (^2P_{1/2}))$	15.76
$[1s^2 2s^2] 2p^4 (2p (^2P_{3/2}) \rightarrow 3d (^4P_{1/2}))$	14.60
$[1s^2 2s^2] 2p^4 (2p (^2P_{3/2}) \rightarrow 3d (^4P_{3/2}))$	14.57
$[1s^2 2s^2] 2p^4 (2p (^2P_{3/2}) \rightarrow 3d (^2F_{5/2}))$	14.53
$[1s^2 2s^2] 2p^4 (2p (^2P_{3/2}) \rightarrow 3d (^2D_{5/2}))$	14.37
$[1s^2 2s^2] 2p^4 (2p (^2P_{3/2}) \rightarrow 3d (\dots))$	14.26
$[1s^2 2s^2] 2p^4 (2p (^2P_{3/2}) \rightarrow 3d (\dots))$	14.21
$[1s^2 2s^2] 2p^4 (2p (^2P_{3/2}) \rightarrow 3d (^2D_{3/2}))$	14.16
$[1s^2 2s^2] 2p^4 (2p (^2P_{3/2}) \rightarrow 3d (^2P_{1/2}))$	14.14
$[1s^2 2s^2] 2p^4 (2p (^2P_{3/2}) \rightarrow 3d (^2D_{5/2}))$	13.95
$[1s^2] 2s 2p^5 (2s (^2P_{3/2}) \rightarrow 3p_{3/2})$	13.41
$[1s^2] 2s 2p^5 (2s (^2P_{3/2}) \rightarrow 3p (^2D_{5/2}))$	13.39
$[1s^2] 2s 2p^5 (2s (^2P_{3/2}) \rightarrow 3p (^2P_{3/2}))$	13.36
$[1s^2] 2s 2p^5 (2s (^2P_{3/2}) \rightarrow 3p (\dots))$	13.32
$[1s^2] 2s 2p^5 (2s (^2P_{3/2}) \rightarrow 3p (^2S_{1/2}))$	13.18
...	

(f) Fe XVIII (F-like ion; continued)

transition	$\lambda/\text{\AA}$
...	
$[1s^2 2s^2] 2p^4 (2p (^2P_{3/2}) \rightarrow 4d_{5/2})$	11.57
$[1s^2 2s^2] 2p^4 (2p (^2P_{3/2}) \rightarrow 4d (\dots))$	11.53
$[1s^2 2s^2] 2p^4 (2p (^2P_{3/2}) \rightarrow 4d (^2F_{5/2}))$	11.42
$[1s^2 2s^2] 2p^4 (2p (^2P_{3/2}) \rightarrow 4d (\dots))$	11.33
$[1s^2 2s^2] 2p^4 (2p (^2P_{3/2}) \rightarrow 4d_{5/2})$	11.31
$[1s^2 2s^2] 2p^4 (2p (^2P_{3/2}) \rightarrow 4d (^2D_{3/2}))$	11.29
$[1s^2] 2s 2p^5 (2s (^2P_{3/2}) \rightarrow 4p_{3/2})$	10.57
$[1s^2] 2s 2p^5 (2s (^2P_{3/2}) \rightarrow 4p_{3/2})$	10.56
$[1s^2 2s^2] 2p^4 (2p (^2P_{3/2}) \rightarrow 5d (\dots))$	10.54
$[1s^2 2s^2] 2p^4 (2p (^2P_{3/2}) \rightarrow 5d (^2D_{5/2}))$	10.45
$[1s^2 2s^2] 2p^4 (2p (^2P_{3/2}) \rightarrow 5d (\dots))$	10.36

(g) Fe XVII (Ne-like ion, as in Table ??)

transition	$\lambda/\text{\AA}$
$[1s^2 2s^2] 2p^5 (2p (^1S_0) \rightarrow 3s (^3P_1))$	(17.05)
$[1s^2 2s^2] 2p^5 (2p (^1S_0) \rightarrow 3s (^1P_1))$	(16.78)
$[1s^2 2s^2] 2p^5 (2p (^1S_0) \rightarrow 3d (^3D_1))$	15.26
$[1s^2 2s^2] 2p^5 (2p (^1S_0) \rightarrow 3d (^1P_1))$	15.01
$[1s^2] 2s 2p^6 (2s (^1S_0) \rightarrow 3p (^1P_1))$	13.82
$[1s^2 2s^2] 2p^5 (2p (^1S_0) \rightarrow 4d (^3D_1))$	12.27
$[1s^2 2s^2] 2p^5 (2p (^1S_0) \rightarrow 4d (^1P_1))$	12.12
$[1s^2 2s^2] 2p^5 (2p (^1S_0) \rightarrow 5d (^3D_1))$	11.25
$[1s^2 2s^2] 2p^5 (2p (^1S_0) \rightarrow 5d (^1P_1))$	11.13
$[1s^2] 2s 2p^6 (2s (^1S_0) \rightarrow 4p (^1P_1))$	11.03
$[1s^2 2s^2] 2p^5 (2p (^1S_0) \rightarrow 6d (^3D_1))$	10.77
$[1s^2 2s^2] 2p^5 (2p (^1S_0) \rightarrow 6d (^1P_1))$	10.66
$[1s^2 2s^2] 2p^5 (2p (^1S_0) \rightarrow 7d (^3D_1))$	10.50
$[1s^2] 2s 2p^6 (2s (^1S_0) \rightarrow 5p (^1P_1))$	10.12

Table 4.27: Further iron lines (end)

Oxygen

As the ‘dip’-spectrum is strongly absorbed at high wavelengths, it hardly contains any counts in the regime of the O VIII and O VII lines.

Neon

- Ne X (H-like ion)

A Ly α line is hardly visible, this absorption feature is not clearly line shaped. The fact that no Ly β line is visible at all might suggest that the nice absorption line near 9.71 \AA is rather caused by the Fe XIX transition rather than Ne X Ly γ . The Fe XIX line is, however, quite weak, and also no consistent explanation for this line (see below). The same is true for the absorption line at 9.48 \AA , which could as well be caused by a Fe XXI transition.

- Ne IX (He-like ion)

Though already in the limit of very low count rate in both spectra (≈ 5 counts/bin in the combined MEG, ≈ 1 count/bin in the combined HEG spectra), the i-line is visible as

an emission line. The f-line is too weak to be described by a line. The r-line is, however, not seen at all.

Sodium

- Na XI (H-like ion)

Despite slightly line-shaped residuals at 10.02 Å, no significant absorption line is seen that could be identified with the Ly α transition. Higher transitions are not seen either.

- Na X (He-like ion)

The weak r-line is seen in absorption, the i-line as a broad emission feature and the f-line does not show up as a clear line, but there is only as a still broader emission feature – or more probably: several weak, but narrower ones. Furthermore, there is probably a weak absorption signal of the $1s^2 \rightarrow 1s3p$ line, but higher transitions are not seen.

Magnesium

- Mg XII (H-like ion)

The Ly α line does not show up convincingly, if all spectra are considered; there is even emission at 8.415 Å in the HEG+1 spectrum. It still cannot be fitted properly with the MEG–1 spectrum alone, which shows the clearest profile. The combined HEG spectra seem rather to suggest two lines. However, the Ly β line is quite visible. The Ly γ line (overlapping with the much stronger Si XIII f emission line) is hardly seen. The weak absorption feature below 6.73 Å might be a remnant from this line. No $1s \rightarrow 5p$ transition is seen.

- Mg XI (He-like ion)

As in the case of Ne IX, both the intercombination and the forbidden line are detected as emission lines, but the resonance line is almost unseen. The $1s^2 \rightarrow 1s3p$ and $1s^2 \rightarrow 1s4p$ transitions are detected as quite strong absorption lines, in contrast to any higher transition.

Aluminum

- Al XIII (H-like ion)

The Ly α line is hardly visible. Ly β is fitted by a relatively broad and even stronger line. It is most likely, that this fit overestimates the real strength of Al XIII Ly β . There are no indications (except of a single bin scatter in HEG+1 at 5.74 Å) of higher transitions.

- Al XII (He-like ion)

The triplet is visible with the resonance line in absorption, and the intercombination and forbidden line in emission. The profiles appear, however, not very clear, but quite broad; it seems sometimes as if there were two line components. As the $1s^2 \rightarrow 1s3p$ line at 6.63 Å is not seen, it is unlikely, that the absorption features near 6.31 Å, which are not even very clearly line-shaped, are to be identified with the $1s^2 \rightarrow 1s4p$ transition.

Silicon

- Si XIV (H-like ion)

In the MEG spectra, the Ly α is a very strong absorption line. The HEG spectra, probably suffering from the worse statistics, are somehow torn up, but show nevertheless the absorption. Ly β is a nice and strong absorption line in all spectra. The Ly γ line appears as a single-bin feature, but it is not significant enough to be fitted. Higher transitions are not seen at all.

- Si XIII (He-like ion)

While the resonance line is seen as a clear absorption line and the forbidden line as a clear emission line, the intercombination line is not seen. The $1s^2 \rightarrow 1s3p$ line and the $1s^2 \rightarrow 1s4p$ line are detected in absorption. Higher transitions are not clearly seen. There is a broad absorption feature at 5.27 Å, but this cannot be identified with the $1s^2 \rightarrow 1s5p$ line, whose rest-wavelength is 5.29 Å, as the other lines tend rather to be red-shifted. The next transition would anyway overlap with the much stronger Si XIV Ly β line.

Sulfur

- S XVI (H-like ion)

The Ly α absorption line is most clearly visible in the MEG spectra, due to the higher count rate. Around 3.99 Å, the MEG+1 spectrum strongly differs from the others and was therefore excluded for the fitting of the Ly β line. Higher transitions in the S XVI Lyman series are not seen.

- S XV (He-like ion)

The r-absorption line is detected quite clearly. The i-line is not seen, there are small emission features in some of the spectra, but they are not consistent with each other; MEG-1 shows even an absorption feature. The f-line is not seen as well. However, the higher $1s^2 \rightarrow 1s3p$ transition is seen again. The next line appears only very weakly, and still higher transitions are not detected.

Argon

- Ar XVIII (H-like ion)

The Ly α line is most clearly seen in the MEG, but can nevertheless be reasonably fitted with all spectra. However, there are no indications of higher transitions.

- Ar XVII (He-like ion)

The resonance absorption line is clearly detected. The intercombination emission line shows up very weakly, especially in the MEG spectra, but even there only as a one or two bin feature with less than 2σ significance each. It is hardly visible in the HEG spectra. The forbidden line cannot be seen, which is also due to the fact that it blends with the stronger S XIV Ly β absorption line. It is questionable, if the absorption line at 3.35 Å can be identified with the $1s^2 \rightarrow 1s3p$ transition at 3.365 Å. This would correspond to an unusually high blue shift of -940 km/s. It is, however, interesting, that the HEG spectra show very narrow absorption features at all the wavelength of the following three higher transitions, namely, 3.20 Å, 3.13 Å and 3.10 Å.

- Ar XVII (Li-like ion)

The first transitions of the Lithium-like ion are not covered by the strongly absorbed dip spectrum, and the existence of a $[1s^2]$ ($2s \rightarrow 5p$) line at 15.93 Å can be excluded.

Calcium

- Ca XX (H-like ion)

Although there are tiny absorption features that might be connected with Ly α and Ly β , they are not significant enough to be fitted. At 2.42 Å, there is rather a single-bin emission feature than a Ly γ absorption line.

- Ca XIX (He-like ion)

The same is true for the He-like calcium ion: From the triplet, only a weak emission signal is obtained from the i-line. This may in parts also be due to the fact, that the resolution of the HETGS is worse at higher energies.

- Ca XVIII (Li-like ion)

The $[1s^2]$ ($2s \rightarrow 3p$) lines cannot be seen in the ‘dip’ spectrum, as there are almost no counts (not even in the MEG spectrum) in the bins at those large wavelengths.

Iron

- Fe XXVI (H-like ion)

Although there are tiny fluctuations at 1.79 Å in the MEG+1 spectrum and, to a weaker extent, in the HEG-1 spectrum as well, that might resemble the Ly α line, this is not consistent with the other spectra. Furthermore, one might be tempted to identify the Ly β line in the HEG spectra, as there seems to be a nice line shaped absorption feature in the combined spectra, but this is neither consistent with the non-existence of the α -line nor is it visible in the single HEG \pm 1 spectra, which have, moreover, only 15 counts/bin at these high energies. The same holds for the higher transitions, which would probably not even be expected to be seen.

- Fe XXV (He-like ion)

The resonance line of Fe XXV, however, is clearly detected in the HEG spectra. Emission from the i- or f-transition are not resolved, as well as higher absorption lines are not seen.

- Fe XXIV (Li-like ion)

There are two absorption features at 10.64 Å and 10.69 Å (which may still be blends). An identification with red shifted $[1s^2]$ ($2s \rightarrow 3p$) transitions (at 10.62 Å and 10.66 Å) is not considered to be appropriate, as the $^2S_{1/2} \rightarrow ^2P_{1/2}$ transition, which is at higher wavelength, should be only half as strong as the $^2S_{1/2} \rightarrow ^2P_{3/2}$ transition, but its equivalent width is in fact larger by a factor of 1.4. Furthermore, the required Doppler velocities are significantly different. Also no higher transitions are seen.

- Fe XXIII (Be-like ion)

None of the strongest lines of Fe XXIII is clearly visible: The absorption feature at 7.47 Å may be explained by a Mg XI transition, the line at 11.00 Å is more likely due to the sodium resonance transition.

- Fe XXII (B-like ion)

Likewise, Fe XXII absorption lines are not detected as well: At 9.06 Å, there is rather an emission feature, and at 8.09 Å, there seems to be an absorption line in the HEG spectra (especially HEG+1), which is, however, contradictory with the MEG spectra (which have a larger number of counts).

- Fe XXI (C-like ion)

No lines of this series, except of the one at 9.48 Å, can be seen in the ‘dip’-spectrum, which opens the question again if it should not rather be attributed to the Ne X transition.

- Fe XX (N-like ion)

The transitions at high wavelength cannot be seen as there are hardly counts in the strongly absorbed ‘dip’-spectrum, even in the MEG. Sometimes, there are tiny indications, but none of them was significant enough to be fitted. (There is a slightly stronger absorption feature at 9.73 Å, but its fit is very broad. Furthermore, it is not likely that only this line of the Fe XX series, which is by far not the strongest one, should be seen.)

- Fe XIX (O-like ion)

There most transitions do not show up as absorption lines. At 10.68 Å and 10.64 Å, however, there are clear line profiles, which also match two transitions of Fe XIX. As these are the strongest transitions in this wavelength range, this interpretation is

quite convincing. The transition at 9.71 Å, which was a questionable other identification than Ne x Ly γ for the observed line, seems, however, to be too weak to cause this absorption.

- Fe XVIII (F-like ion)

At 14.57 Å, 14.26 Å and 14.16 Å, there are tiny indications of absorption lines, which probably suffer only from the low count rate. It was tried to fit the line at 11.57 Å, which resulted only in a rather broad Gaussian. As it is most strongly seen in the HEG spectra, but not in the MEG, this line is likely not significant. The nice absorption lines at 10.57 Å, 10.55 Å and 10.52 Å, however, may be identified with strong transitions within the Fe XVIII series.

- Fe XVII (Ne-like ion)

There is no strong evidence for lines of the Fe XVII series.

Nickel

- Ni XXVIII (H-like ion)

There is an absorption feature near 1.53 Å in the HEG, that might be identified with the Ly α transition of Ni XXVIII. Near 1.29 Å, there are negative fluctuations in the HEG, but at such high energies, the signal to noise ratio is very bad. As a conclusion, there is no strong evidence for H-like nickel.

- Ni XXVII (He-like ion)

One might wonder if there are small absorption features in the HEG spectra that correspond to the resonance and $1s^2 \rightarrow 1s3p$ transition.

- Ni XXVI (Li-like ion)

No transitions of Li-like nickel are detected.

K α lines of lower ionized silicon

There are some strong, new absorption lines in range from 6.75 Å to 7.1 Å, which show up only in the ‘dip’ spectra and for which there is no good explanation within the `atomdb`. In a table by House (1969) on K α -type X-ray lines, it was found that the detected lines would match these K α lines of lower ionized silicon ($\lambda_{K\alpha(\text{Si VIII})} = 7.007$ Å, $\lambda_{K\alpha(\text{Si IX})} = 6.947$ Å, $\lambda_{K\alpha(\text{Si X})} = 6.882$ Å, $\lambda_{K\alpha(\text{Si XI})} = 6.813$ Å). K α lines are often seen as fluorescent emission lines: They are produced when the vacancy created by a hard X-ray photon’s knocking out an electron of the innermost K-shell, which is then replaced by an electron of the next shell (K α line) or respectively a higher shell (K β , ...). It has to be investigated, if it is also likely to see those lines from a optically thick medium as absorption lines, which requires a large enough population of states with vacancies in the $2p$ shell, such that a $1s$ could be excited. For this investigation, atomic data like Einstein A -coefficients and oscillator strengths (see Sect. 2.1.3) are needed, which are not reported by House (1969).

As the dips are assumed to be produced by dense clumps in the accretion flow, the detected presence of lower ionized material gives important hints on their actual nature.

The lines around 6.86 Å and 6.93 Å are in fact resolved by the HEG into two lines each. If both lines in the two cases may be identified with the same transition, they correspond to notably different shifts in wavelength, of course. Though no detailed analysis will be presented in this work, it is noted that the two different shifts are related to the fact that the ‘dip’-spectrum comprises two distinct major dips, namely ‘dip 1’ and ‘dip 2’, according to the convention of Section 4.3.1.

Fit-parameters of the lines in the ‘dip’-spectrum

As in the prior section describing the ‘non-dip’ spectrum, the trusted lines are listed in the following Table 4.28. The fit-parameters of each line are shown in the first block of 4 columns: the position λ , the full width at half maximum FWHM, the equivalent width EW and the χ^2 -improvement $\Delta\chi^2$ (cf. comments to Table 4.4, page 61). The second block lists the parameters of the identified transition: the ion, the electronic states (ground states are underlined), the rest wavelength λ_0 from the atomic database, the Einstein coefficient A_{ji} and the total absorption oscillator strength f_{ij} . As in Table 4.4, the rows with a gray background mark emission lines (with $EW > 0$). If the rest wavelength is not consistent with the fitted position within the error bars, ()-brackets are put around the identified transitions. They do not mean, however, that this identification is not trusted, as it is not precluded to have Doppler-shifts. The last block of columns reports the deduced parameters column density (calculated from Eq. 2.41, which holds only if the lines are not saturated and are on the linear part of the curve of growth) and wavelength-shift $\Delta\lambda/\lambda \cdot c$. Again, the convention $\Delta\lambda = \lambda - \lambda_0$ is used, which means that red-shifts (towards larger wavelengths) result in positive velocities, while blue-shifts give negative velocities.

The complete list of lines are given by Table ?? on page ?.?. The spectrum itself is finally shown in Figs. ??-?? on pages ??-??.

Conclusions

The modelling of the ‘dip’ spectrum requires further investigations. As there are only few (sometimes just one or two) transitions of a given ion detected, it is difficult to estimate the exact physical parameters from these single Gaussian lines. No modelling with the self-developped model for complete line series in the module `lineProfile` (see Sects. 3.2.3 and 4.2.4) has yet been performed, which would probably give the most accurate constraints. The parameters have therefore to be inferred from Table 4.28.

A brief discussion is given in the following section.

Table 4.28: List of lines in the ‘dip’ spectrum – sorted by ion

λ [Å]	FWHM [mÅ]	EW [mÅ]	$\Delta\chi^2$	ion	i	transition j	λ_0 [Å]	A_{ji} [10^{12}s^{-1}]	f_{ij}	N_i [10^{16}cm^{-2}]	$\Delta\lambda/\lambda \cdot c$ [km/s]
$13.5398^{+0.0058}_{-0.0049}$	$31.33^{+12.61}_{-12.19}$	$129.81^{+36.46}_{-35.78}$	39.0	(Ne IX	$\underline{1s^2}$	$1s2p$	13.550;	0.000	0.001		-231^{+128}_{-109}
$8.4220^{+0.0151}_{-0.0149}$	$42.69^{+0.00}_{-0.00}$	$-8.28^{+0.00}_{-0.00}$	0.0	Mg XII	$\underline{1s}$	$2p$	8.4192	12.8	0.407	$3.25^{+0.00}_{-0.00}$	99^{+537}_{-532}
$7.1080^{+0.0047}_{-0.0030}$	$0.21^{+20.25}_{-0.21}$	$-2.05^{+0.99}_{-1.18}$	11.3	Mg XII	$\underline{1s}$	$3p$	7.1058	3.41	0.077	$5.93^{+3.43}_{-2.86}$	95^{+196}_{-126}
$6.7243^{+0.0009}_{-0.0045}$	$0.09^{+21.23}_{-0.09}$	$-1.96^{+0.98}_{-1.18}$	10.6	(Mg XII	$\underline{1s}$	$4p$	6.7378	1.39	0.028	$17.3^{+10.4}_{-8.6}$	-598^{+41}_{-202}
$9.2311^{+0.0026}_{-0.0016}$	$7.16^{+5.39}_{-7.16}$	$13.39^{+3.29}_{-2.25}$	72.8	Mg XI	$\underline{1s^2}$	$1s2p$	9.2312	0.034	0.001		-3^{+86}_{-52}
$7.8550^{+0.0040}_{-0.0038}$	$17.84^{+11.35}_{-8.58}$	$-5.79^{+1.73}_{-1.79}$	40.5	(Mg XI	$\underline{1s^2}$	$1s3p$	7.8503	5.43	0.151	$7.06^{+2.18}_{-2.11}$	180^{+151}_{-146}
$7.4700^{+0.0025}_{-0.0000}$	$0.00^{+6.59}_{-0.00}$	$-3.23^{+0.97}_{-0.95}$	28.2	(Mg XI	$\underline{1s^2}$	$1s4p$	7.4730	2.24	0.056	$11.7^{+3.4}_{-3.5}$	-120^{+100}_{-0}
$7.1762^{+0.0038}_{-0.0062}$	$0.01^{+17.29}_{-0.01}$	$-1.40^{+1.03}_{-1.17}$	4.9	Al XIII	$\underline{1s}$	$2p$	7.1710	17.6	0.407	$0.75^{+0.63}_{-0.56}$	218^{+157}_{-259}
$6.0442^{+0.0048}_{-0.0045}$	$14.82^{+10.15}_{-8.86}$	$-3.22^{+1.24}_{-1.36}$	19.9	(Al XIII	$\underline{1s}$	$3p$	6.0526	4.70	0.077	$12.9^{+5.4}_{-5.0}$	-417^{+240}_{-225}
$7.8776^{+0.0224}_{-0.0176}$	$0.02^{+49.98}_{-0.02}$	$1.07^{+1.36}_{-1.07}$	1.7	Al XII	$\underline{1s^2}$	$1s2s$	7.8721	0.000	0.000		210^{+852}_{-672}
$7.8024^{+0.0057}_{-0.0056}$	$25.11^{+13.65}_{-11.32}$	$6.32^{+2.28}_{-2.19}$	27.4	Al XII	$\underline{1s^2}$	$1s2p$	7.8070	0.082	0.002		-175^{+217}_{-214}
$7.7750^{+0.0171}_{-0.0097}$	$0.00^{+23.68}_{-19.88}$	$-2.08^{+2.45}_{-2.90}$	0.0	(Al XII	$\underline{1s^2}$	$1s2p$	7.7573	27.5	0.745	$0.52^{+0.73}_{-0.62}$	684^{+662}_{-373}
$6.7867^{+0.0020}_{-0.0021}$	$17.89^{+5.97}_{-4.72}$	$-7.64^{+1.31}_{-1.41}$	134.3	(Si XI	$\text{K}\alpha$		6.8130				-1158^{+89}_{-92}
$6.8536^{+0.0016}_{-0.0013}$	$9.96^{+4.04}_{-9.96}$	$-6.16^{+1.73}_{-1.00}$	154.5	(Si X	$\text{K}\alpha$		6.8820				-1239^{+68}_{-56}
$6.8659^{+0.0016}_{-0.0016}$	$15.57^{+4.95}_{-3.60}$	$-7.81^{+1.17}_{-1.24}$	178.4	(Si X	$\text{K}\alpha$		6.8820				-702^{+70}_{-71}
$6.9236^{+0.0014}_{-0.0013}$	$16.74^{+3.67}_{-3.74}$	$-10.09^{+1.28}_{-1.22}$	274.7	(Si IX	$\text{K}\alpha$		6.9470				-1010^{+60}_{-58}
$6.9400^{+0.0025}_{-0.0001}$	$0.02^{+8.26}_{-0.02}$	$-4.70^{+0.74}_{-0.67}$	107.9	(Si IX	$\text{K}\alpha$		6.9470				-302^{+106}_{-2}
$6.9981^{+0.0013}_{-0.0012}$	$10.87^{+4.53}_{-4.30}$	$-8.26^{+1.26}_{-1.35}$	207.6	(Si VIII	$\text{K}\alpha$		7.0070				-380^{+58}_{-52}
$7.0550^{+0.0003}_{-0.0029}$	$0.07^{+7.53}_{-0.07}$	$-3.27^{+0.99}_{-0.90}$	32.7	(Si VII	$\text{K}\alpha$		7.0630				-341^{+13}_{-122}

Table 4.28: List of lines in the ‘dip’ spectrum – sorted by ion (continued)

λ [Å]	FWHM [mÅ]	EW [mÅ]	$\Delta\chi^2$	ion	i	transition j	λ_0 [Å]	A_{ji} [10^{12}s^{-1}]	f_{ij}	N_i [10^{16}cm^{-2}]	$\Delta\lambda/\lambda \cdot c$ [km/s]
$6.1814^{+0.0027}_{-0.0026}$	$24.59^{+6.87}_{-6.05}$	$-8.83^{+1.52}_{-1.59}$	132.5	Si XIV	$\underline{1s}$	2p	6.1804	23.7	0.407	$6.43^{+1.16}_{-1.11}$	46^{+130}_{-127}
$5.2297^{+0.0020}_{-0.0020}$	$19.38^{+5.13}_{-4.34}$	$-10.98^{+1.74}_{-1.82}$	153.3	(Si XIV	$\underline{1s}$	3p	5.2168	6.32	0.077	$58.8^{+9.7}_{-9.3}$	740^{+117}_{-117}
$6.7426^{+0.0024}_{-0.0010}$	$1.02^{+6.56}_{-1.02}$	$6.88^{+1.35}_{-1.44}$	79.0	(Si XIII	$\underline{1s^2}$	1s2s	6.7403	0.000	0.000		103^{+106}_{-45}
$6.6461^{+0.0026}_{-0.0027}$	$11.50^{+7.78}_{-5.60}$	$-5.52^{+1.36}_{-1.58}$	65.2	Si XIII	$\underline{1s^2}$	1s2p	6.6479	37.7	0.749	$1.89^{+0.54}_{-0.47}$	-81^{+119}_{-120}
$5.6875^{+0.0054}_{-0.0065}$	$20.66^{+22.18}_{-18.27}$	$-4.83^{+1.91}_{-2.43}$	24.7	(Si XIII	$\underline{1s^2}$	1s3p	5.6805	10.4	0.151	$11.2^{+5.6}_{-4.4}$	369^{+285}_{-343}
$5.4075^{+0.0053}_{-0.0052}$	$0.05^{+47.10}_{-0.05}$	$-1.58^{+1.21}_{-1.88}$	4.5	Si XIII	$\underline{1s^2}$	1s4p	5.4045	4.30	0.056	$10.8^{+12.9}_{-8.3}$	167^{+292}_{-288}
$4.7240^{+0.0057}_{-0.0061}$	$25.65^{+14.98}_{-12.44}$	$-4.91^{+1.74}_{-1.86}$	29.0	S XVI	$\underline{1s}$	2p	4.7274	40.4	0.406	$6.13^{+2.32}_{-2.17}$	-215^{+360}_{-386}
$3.9940^{+0.0000}_{-0.0042}$	$0.37^{+7.84}_{-0.37}$	$-1.83^{+0.82}_{-0.76}$	13.3	S XVI	$\underline{1s}$	3p	3.9908	10.8	0.077	$16.8^{+7.0}_{-7.5}$	239^{+1}_{-316}
$5.0375^{+0.0050}_{-0.0025}$	$0.00^{+20.22}_{-0.00}$	$-1.99^{+0.89}_{-1.16}$	11.5	S XV	$\underline{1s^2}$	1s2p	5.0387	66.7	0.761	$1.17^{+0.68}_{-0.52}$	-73^{+297}_{-149}
$4.3063^{+0.0200}_{-0.0200}$	$0.66^{+74.97}_{-0.66}$	$-1.41^{+0.94}_{-1.26}$	6.0	S XV	$\underline{1s^2}$	1s3p	4.2990	18.3	0.152	$5.68^{+5.06}_{-3.79}$	511^{+1395}_{-1395}
$3.7350^{+0.0072}_{-0.0056}$	$8.89^{+17.25}_{-8.89}$	$-1.46^{+0.90}_{-1.07}$	7.8	Ar XVIII	$\underline{1s}$	2p	3.7311	64.7	0.405	$2.92^{+2.15}_{-1.80}$	313^{+578}_{-450}
$3.9566^{+0.0051}_{-0.0035}$	$5.91^{+19.24}_{-5.91}$	$-2.42^{+0.96}_{-1.68}$	24.0	(Ar XVII	$\underline{1s^2}$	1s2p	3.9491	109	0.767	$2.29^{+1.58}_{-0.91}$	569^{+389}_{-266}
$3.3545^{+0.0055}_{-0.0145}$	$0.00^{+76.27}_{-0.00}$	$-0.80^{+0.74}_{-0.69}$	3.2	(Ar XVII	$\underline{1s^2}$	1s3p	3.3650	30.0	0.153	$5.27^{+4.54}_{-4.86}$	-939^{+493}_{-1290}
$1.9405^{+0.0049}_{-0.0032}$	$23.96^{+17.37}_{-8.89}$	$7.67^{+2.18}_{-1.81}$	69.3	(Fe	K α		1.9370				536^{+755}_{-492}
$1.4924^{+0.0026}_{-0.0032}$	$0.33^{+11.44}_{-0.33}$	$-3.50^{+1.78}_{-2.96}$	10.5	(Fe XXVI	$\underline{1s}$	3p	1.5024	75.2	0.076	233^{+197}_{-118}	-1981^{+511}_{-648}
$1.8521^{+0.0052}_{-0.0046}$	$9.01^{+11.42}_{-9.01}$	$-2.36^{+1.24}_{-1.30}$	13.9	Fe XXV	$\underline{1s^2}$	1s2p	1.8504	503	0.775	$10.0^{+5.5}_{-5.3}$	280^{+839}_{-748}
$9.4794^{+0.0043}_{-0.0131}$	$18.05^{+11.98}_{-8.94}$	$-8.69^{+2.62}_{-2.80}$	39.0	Fe XXI	$\underline{1s^2 2s^2 2p^2}$	$\underline{1s^2 2s^2 2p^4 d}$	9.4797	6.12	0.247	$4.43^{+1.43}_{-1.34}$	-11^{+138}_{-413}

Table 4.28: List of lines in the ‘dip’ spectrum – sorted by ion (continued)

λ [Å]	FWHM [mÅ]	EW [mÅ]	$\Delta\chi^2$	ion	i	transition	λ_0 [Å]	A_{ji} [10^{12}s^{-1}]	f_{ij}	N_i [10^{16}cm^{-2}]	$\Delta\lambda/\lambda \cdot c$ [km/s]
10.6897 ^{+0.0007} _{-0.0030}	0.09 ^{+8.30} _{-0.09}	-8.65 ^{+2.30} _{-2.29}	37.4	(Fe XIX	<u>2s²2p⁴</u>	2s ² 2p ³ 4d	10.6840	2.28	0.055	15.7 ^{+4.2} _{-4.2}	160 ⁺¹⁸ ₋₈₅
10.6402 ^{+0.0054} _{-0.0037}	4.39 ^{+16.07} _{-4.39}	-6.04 ^{+2.70} _{-3.61}	13.6	Fe XIX	<u>2s²2p⁴</u>	2s ² 2p ³ 4d	10.6414	5.20	0.088	6.86 ^{+4.09} _{-3.06}	-34 ⁺¹⁵² ₋₁₀₅
9.7116 ^{+0.0026} _{-0.0018}	0.10 ^{+12.34} _{-0.10}	-4.55 ^{+1.69} _{-1.90}	19.3	(Fe XIX	<u>2s²2p⁴</u>	2s2p ² 2p ² 4p	9.7061	0.015	0.000	30822	170 ⁺⁷⁹ ₋₅₅
10.5525 ^{+0.0075} _{-0.0000}	0.00 ^{+14.78} _{-0.00}	-4.18 ^{+2.60} _{-2.77}	7.0	(Fe XVIII	<u>2s²2p⁵</u>	2s2p ² 2p ³ 4p	10.5640	1.58	0.040	10.7 ^{+7.1} _{-6.7}	-326 ⁺²¹³ ₋₀
10.5734 ^{+0.0064} _{-0.0060}	0.45 ^{+24.33} _{-0.45}	-5.06 ^{+2.72} _{-2.49}	9.6	(Fe XVIII	<u>2s²2p⁵</u>	2s2p ² 2p ³ 4p	10.5640	1.58	0.040	13.0 ^{+6.4} _{-7.0}	266 ⁺¹⁸⁰ ₋₁₇₀
10.5225 ^{+0.0075} _{-0.0051}	0.01 ^{+28.98} _{-0.01}	-4.12 ^{+2.53} _{-1.93}	6.8	(Fe XVIII	<u>2s²2p⁵</u>	2s ² 2p ⁴ 5d	10.5364	2.60	0.065	6.50 ^{+3.05} _{-3.99}	-396 ⁺²¹⁴ ₋₁₄₄
1.5199 ^{+0.0058} _{-0.0070}	15.00 ^{+0.00} _{-4.46}	-6.26 ^{+2.44} _{-2.41}	18.1	(Ni XXVIII	<u>1s</u>	2p	1.5304	379	0.400	76.8 ^{+29.5} _{-29.9}	-2049 ⁺¹¹⁴⁴ ₋₁₃₇₇

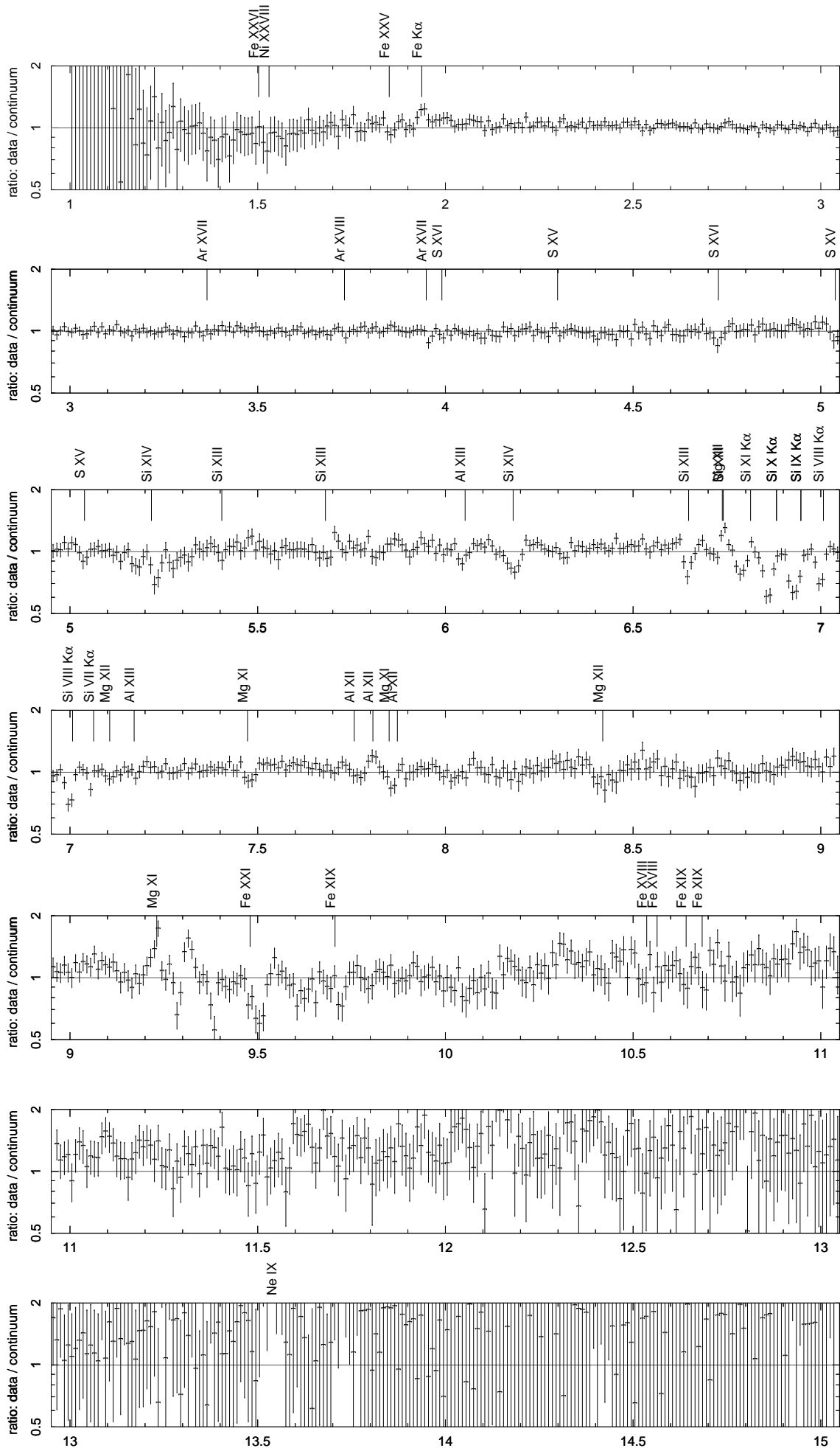


Figure 4.18: Normalized 'dip'-spectrum (data/continuum-ratio) vs. wavelength in Å.

4.4 Comparison of ‘dip’ and ‘non-dip’ spectrum

Figures 4.17 and 4.18 allow a direct comparison of the ‘non-dip’ and the ‘dip’ spectrum: All spectra $s \in \{\text{MEG} \pm 1, \text{HEG} \pm 1\}$ have been rebinned to 0.01 Å bins and combined:

$$C(i) = \sum_s C_s(i) \quad , \quad \sigma_C(i) = \sqrt{\sum_s \sigma_{C_s}(i)^2} \quad (4.7)$$

The plots show the normalized spectra, i.e., the combined data C divided by the folded continuum model C_M . This is just to get the rough shape of the spectra for an overview, the detailed plots are shown as Figs. ?? and ?? in appendix ?. The line identifications obtained in Sects. 4.2.3 and 4.3.3, respectively, are also indicated by the position of the rest-wavelength.

Because the ‘dip’-spectra are more strongly absorbed, it was expected that they also show more absorption lines. As already mentioned, this is, however, not the case.

A first inspection of the parameters for Mg XII/XI and Si XIV/XIII, which seem to give consistent parameters, might indicate that the relative column density of lower ionized ions is larger in the ‘dip’ spectrum than in the ‘non-dip’ spectrum. This may be a bold extrapolation of data with large uncertainties, but gives already first hints on the origin of the dips – namely that they originate from dense clumps in the focussed wind, which are colder and therefore less ionized than the other wind material.

An even stronger observational evidence will be obtained by a detailed modelling of the $K\alpha$ lines of lower ionized silicon, which arise in the ‘dip’ spectra between 6.75 Å and 7.1 Å, but have not been seen in the ‘non-dip’ spectrum at all.

4.5 Outlook

Although the spectral line features have been described very adequately, both for the ‘non-dip’ and the ‘dip’ spectrum, there are still further investigations necessary, which will be performed in the near future, but are beyond the scope of this work.

The final goal is to constrain the accretion geometry in Cygnus X-1. Therefore, it is also necessary to determine exactly where these absorption lines have been formed. For this purpose, detailed simulations of the ionization structure in the focussed wind near the black hole will be necessary. First hints have already been given at the end of Sect. 4.2.4, where the fit-parameters of the line-series used for the ‘non-dip’ spectrum were discussed.

Furthermore, the form of the continuum during the dips needs a better understanding, as indicated at the end of Sect. 4.3.2. Photoabsorption in the ionized plasma has to be considered and a self-consistent model has to be found for the partial covering.

In order to find answers to the questions which are still open and to derive more constraints on the accretion processes in the Cygnus X-1 system, more observations of this kind have to be studied. Therefore, the next chapter gives an overview on other *Chandra* observations.

5 Other observations of Cygnus X-1

Chapter 4 presented a spectroscopic analysis of Cygnus X-1. Besides all reported results, many questions are still open. As concluded in the last section, the analysis of further observations is necessary.

The *Chandra* X-ray observatory provides with the HETGS the best resolution to study atomic transitions in the low energy X-ray regime. In fact, RGS-data of *XMM-Newton* can also be considered, see Sect. 5.3. Not every observation, however, is qualified for such a high-resolution spectroscopy; a certain minimum exposure time is necessary to obtain a sufficiently large signal-to-noise ratio not only for the continuum, but also in the lines.

There are some further observations of Cygnus X-1 in the *Chandra* data archive, and most of them have already been analyzed. Many of them cannot directly be compared with the observation analyzed in this work, as the source Cyg X-1 was in a different spectral state.

5.1 Comparison of all *Chandra* observations

5.1.1 Overview

Table 5.1 lists all *Chandra* observations of Cygnus X-1 that have been performed up to now and whose data is already freely available from the CXC archive. There is one further 50 ks imaging observation # 7501 of Heinz carried out just on 2007 Mar 11, which is intended to investigate a shocked radio shell around Cyg X-1 and possibly confirm its jet-origin. This data will only be released one year after. Finally, our group (Wilms et al.) has gained a new $\phi = 0$ observation # 8525 (not yet scheduled), see Sect. 5.3.

5.1.2 Summary of published results

This section gives a brief summary of the previous results reported by other groups.

Table 5.1: *Chandra* observations of Cyg X-1 (all with the HETGS)

obs. ID	start date	ϕ_{orbital}	state	t_{exp}/ks	data mode	principal investigator
107	1999-10-19 19:16:33	0.73	transitional	13.96	GRADED	Canizares
1511	2000-01-12 08:14:13	0.83	low/hard	12.57	CC33_GRADED	Canizares
2415	2001-01-04 06:02:43	0.74	intermediate	30.15	CC33_GRADED	Miller
3407	2001-10-28 16:13:52	0.85	trans. \rightarrow soft	30.00	CC33_GRADED	Cui
2741	2002-01-28 05:33:28	0.20		4.49	GRADED	Zhang
2742	2002-01-30 01:22:27	0.53		4.75	GRADED	Zhang
2743	2002-04-13 20:51:58	0.71		5.23	GRADED	Zhang
3724	2002-07-30 17:26:13	0.97	high/soft	26.40	CC33_GRADED	Feng
3815	2003-03-04 15:45:02	0.71	(low/hard)	55.85	CC33_GRADED	Lewin
3814	2003-04-19 16:46:27	0.93	low/hard	48.33	GRADED	Pottschmidt

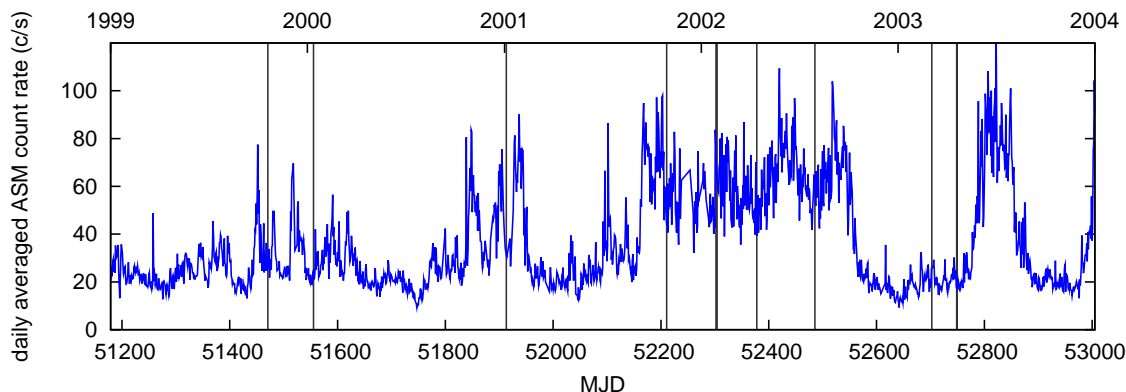


Figure 5.1: ASM light curve of Cyg X-1 with indicators of the *Chandra* observation times.

Observation # 107

The observation # 107 was performed in a time when Cyg X-1 showed much flaring activity (cf. Fig. 5.1) and was in a state similar to the transition between hard and soft state. Schulz et al. (2002) have analyzed this first high-resolution X-ray spectrum of Cygnus X-1 mainly with view of absorption edges, which allow a direct measurement of the different elements' column densities: The height of an absorption edge is given by (cf. Eq. 2.3 and Sect. 2.1.1)

$$\lim_{\Delta E \rightarrow 0} \frac{S_E(E_{\text{ion}}^Z + \Delta E)}{S_E(E_{\text{ion}}^Z - \Delta E)} = e^{-\sigma_{\text{ion}}^Z(E_{\text{ion}}^Z) \cdot N_Z} \quad (5.1)$$

An equivalent column density of $N_{\text{H}} = 6.2 \times 10^{21} \text{ cm}^{-2}$ and relative abundances roughly consistent with the ISM have been found. The continuum was described by multicolor disk model with $k_{\text{B}}T = 0.2 \text{ keV}$ and a power law with $\Gamma = 1.95$. Some emission and absorption lines are seen, but only tentative identifications are given.

Cui et al. (2002) present a spectroscopic survey of persistent black hole candidates, where this observation of Cyg X-1 is compared with those of LMC X-1, LMC X-3 and GRS 1758-258.

Furthermore, this observation (as well as observations # 3407 and # 3724) has been used by Juett et al. (2004, 2006) to study the absorption in the interstellar medium.

Observation # 1511

Marshall et al. (2001) found in observation # 1511 highly ionized absorption in the X-ray spectrum of Cyg X-1, mainly from Ly α lines, with an average redshift of 460 km/s. The continuum described by a power law with $\Gamma = 1.73$ has still a soft excess from a disk.

This observation was furthermore used by Yao et al. (2003) to resolve the X-ray halo.

Observation # 2415

During this observation, Cyg X-1 showed \approx twice the usual hard state luminosity (see Fig. 5.1). This allowed Miller et al. (2002) to resolve the composite Fe K α emission line for the first time. The continuum was described by a multicolor disk and a $\Gamma \approx 1.8$ -power law spectrum, a narrow and a broad iron line. Furthermore, this observation revealed the focused companion wind in Cygnus X-1 (Miller et al., 2005) by presenting ~ 35 absorption lines of H- and He-like Ne, Na, Mg and Si. He-like i- and f-lines are seen in emission, as well as in observation # 3814 presented in this work.

This observation also contains a 500 s dip.

Observation # 3407

Observation # 3407, triggered by a transition from the hard to the soft state, has recently been analyzed by Chang & Cui (2007). They report a spectral continuum (constrained with a joint *RXTE* observation) to be a broken power law with $\Gamma_1 \sim 2.1$, $E_{\text{break}} \sim 10 \text{ keV}$ and $\Gamma_2 \sim 1.7$ with a high-energy cutoff above $E_{\text{cut}} = 20 \dots 21 \text{ keV}$ with a folding energy $E_{\text{fold}} = 120 \dots 130 \text{ keV}$ (cf. Sect. 4.2.2). No significant disk component can be inferred from the (rather high energy) data. From these spectral properties, Chang & Cui conclude that the true high/soft state was not yet reached. Furthermore, they perform a high resolution spectral analysis and identify a large number of absorption lines in the first period of their observation. In the second period, however, most of these lines weaken significantly or even cannot be detected at all, which shows the dramatic variability of X-ray absorption lines in Cyg X-1. According to Chang & Cui, a possible explanation is related to the complete ionization of the wind due to a sudden density decrement. The lines are mostly redshifted, but not by a globally consistent single velocity. The average velocity is lower than expected from the focussed wind scenario of Miller et al. (2005).

Observations # 2741–2743

According to the *chaser* publication list, no articles are associated with these observations. It is noted that each observation of this sequence has only ~ 5 ks exposure time.

Observation # 3724

Feng et al. (2003) used this observation to probe the inflow/outflow and accretion disk in the high state. They report the detection of asymmetric absorption lines with more extended red wings, especially for the transitions of highest ionized ions. A qualitative explanation (according to Feng et al. (2003), “comprehensive studies of the absorption lines will be reported elsewhere”) is consistent with the focussed wind, inflowing towards the black hole: Closest to the latter, both the highest red-shifts and ionization parameters are reached. The non-detection of recombination emission lines is interpreted as a hint that the accreted material falls directly through the corona into the event horizon rather than cooling down and joining the disk. Furthermore, trials of fitting a broad iron line emission feature are reported.

Observation # 3815

No publications are associated with this observation.

It might be suited to perform another high-resolution spectroscopy of Cygnus X-1 in the hard state as it has a comparable exposure time. The observation was, however, performed at another binary phase; it is thus not clear if the fingerprints of the focussed wind can be seen.

Observation # 3814

This observation (and # 107) has been used by Xiang et al. (2005) to probe the spatial distribution of the interstellar dust medium by studying the X-ray halo.

Up to now, nobody else has performed a spectroscopic analysis with this observation. Therefore, the publication of the results of this work is in progress.

5.2 Miller’s *Chandra* observation # 2415

Observation # 2415 is especially interesting for several reasons: As described above, Miller et al. (2005) has performed the first high-resolution spectroscopy similar to the here presented one. It might be interesting to check their result with probably other methods. Furthermore, the other detector mode was used to avoid pile-up problems:

Miller’s observation # 2415 of Cygnus X-1 was performed on 2001 January 4 for 32 ks with the HETGS in continuous-clocking (CC) mode to prevent photon pile-up. Additionally, there was a 100 row blocking window put over the zero-order image of the bright source to reduce the amount of data that had to be telemetered.

As there is no HEG and MEG arm visible in a one dimensional CC mode ‘image’ (Fig. 5.3), it is quite hard to reconstruct the zero-order position. First attempts of fitting the center of energy or number of counts vs. x plots didn’t give results that were accurate enough.



Figure 5.2: Detector image of observation # 2415 (CC mode).



Figure 5.3: “Sky-image” of observation # 2415 (CC mode).

The goodness of a trial zero-order position can be checked by comparing the resulting + and – first order spectra $S_{\lambda}^{+}(\lambda)$ and $S_{\lambda}^{-}(\lambda)$ of, e.g., the MEG via a cross-correlation function

$$\text{CCF}(\delta) = \int_{\lambda_{\min}}^{\lambda_{\max}} d\lambda \quad S_{\lambda}^{+}(\lambda) \cdot S_{\lambda}^{-}(\lambda - \delta) \quad (5.2)$$

$\text{CCF}(\delta)$ reaches its maximum when $S_{\lambda}^{+}(\lambda)$ is most similar to $S_{\lambda}^{-}(\lambda - \delta)$; the cross-correlation function allows thus to determine relative shifts in different but similar spectra (or other curves).

5.3 Future work

5.3.1 The joint *XMM-Chandra* observation (# 8525)

There will be a new *Chandra* observation to continue the study of the accretion in Cygnus X-1. In fact, it will even be a joint observation, together with the second major X-ray observatory which is able to perform a high-resolution spectroscopy, namely the X-ray multi-mirror mission *XMM-Newton*. Like the *Chandra* observation # 3814 presented in Chapter 4, it will be performed during superior conjunction of the black hole to study the spectrum during absorption dips. The observation time will also be 50 ks with each observatory, with at least 30 ks overlap of the *Chandra*-exposure with that of *XMM*. These strong constraints are necessary, as the source Cyg X-1 is highly variable, even on short timescales, as could already be seen in Sect. 4.1.2. Of course, this is especially crucial, when it is just the dips which one wants to study.

But *XMM-Newton* does not only contain the reflection grating spectrometer, which is similar to *Chandra*'s HETGS. There are also the EPIC CCDs, which allow to measure the flux in the iron line region, from ~ 2 keV to ~ 12 keV, with a very high time-resolution.

In addition, the source will most likely be observed simultaneously with *RXTE*, which should be available via the biweekly monitoring campaign of Cyg X-1 by Wilms et al. (see, e.g., Wilms et al., 2006b). *RXTE* provides the broad band spectrum up to >150 keV, which is necessary to constrain the continuum. It was shown in Sect. 4.3.2 how difficult it is to determine the parameters of the continuum with data at low energies alone. And an appropriate continuum-description is essentially necessary to measure absorption or emission lines.

5.3.2 Outlook

As indicated above, an analysis of the other *Chandra* observations of Cyg X-1 in the public data archive will be performed, as some of them might give results comparable with those obtained in this work.

Analysis with *XMM*'s reflection grating spectrometer

There are also some observations of Cygnus X-1 with the X-ray multi-mirror mission *XMM-Newton*, which have to be analyzed, if they allow for similar investigations. In any case, at least the new observation (Sect. 5.3.1) definitely will, as it is planned to do so.

In order to learn the analysis with the instruments on *XMM*, I performed a three month traineeship at the European Space Astronomy Center, where the *XMM* Science Operations Centre is located. During a research project on the wind accretion in Vela X-1, another high mass X-ray binary system, I could both learn the data reduction and also investigate the physical processes in systems of this kind.

Simulation of the accretion region

To translate the observed parameters from the absorption lines into a physical description of the Cyg X-1 system, simulations of the radiative transfer, the response of the ionized plasma

to the hard X-ray spectrum, will have to be performed. The derived results will be compared with the actual observational data.

5.3.3 Final conclusions

For me, this work has provided insights in X-ray astronomy, the fascinating physics of black holes in general and in particular in X-ray binaries, and especially in the Cygnus X-1 system. I have developed techniques in spectral analysis, which I can use for future studies. Besides its own results, this thesis is also a starting point for further investigations.

Although Cyg X-1 is the best studied black hole, it still contains many mysteries that have to be resolved. – *There's a lot to find out, let's get started!*

References

- Abramowitz M., Stegun I.A., 1972, Handbook of Mathematical Functions, New York: Dover
- Arnaud K., Dorman B., Gordon C., 2007, XSPEC Users Guide, HEASARC, NASA/GSFC, <http://heasarc.gsfc.nasa.gov/docs/xanadu/xspec/>
- Aschenbach B., 1985, Reports of Progress in Physics 48, 579
- Asplund M., Grevesse N., Sauval A.J., 2005, In: Barnes, III T.G., Bash F.N. (eds.) Cosmic Abundances as Records of Stellar Evolution and Nucleosynthesis, Vol. 336. Astronomical Society of the Pacific Conference Series, p.25
- Balbus S.A., Hawley J.F., 1998, Reviews of Modern Physics 70, 1
- Bałucińska-Church M., Church M.J., Charles P.A., et al., 2000, MNRAS 311, 861
- Bałucińska-Church M., Takahashi T., Ueda Y., et al., 1997, ApJ 480, L115
- Bauer C., 2007, Investigating the continuum spectrum of Cygnus X-1: a joint fit of Chandra and RXTE data, research project
- Bevington P.R., Robinson D.K., 1992, Data reduction and error analysis for the physical sciences, New York: McGraw-Hill, 1992, 2nd ed.
- Blondin J.M., Stevens I.R., Kallman T.R., 1991, ApJ 371, 684
- Bolton C.T., 1972, Nat 240, 124
- Bowyer S., Byram E.T., Chubb T.A., Friedman H., 1965, Science 147, 394
- Brocksopp C., Fender R.P., Larionov V., et al., 1999a, MNRAS 309, 1063
- Brocksopp C., Tarasov A.E., Lyuty V.M., Roche P., 1999b, A&A 343, 861
- Brown G.E., Lee C.H., Rho M., 2005, ArXiv Nuclear Theory e-prints
- Burgio G.F., Baldo M., Sahu P.K., et al., 2002, Physics Letters B 526, 19
- Carter B., 1971, Physical Review Letters 26, 331
- Cash W., 1979, ApJ 228, 939
- Castor J.I., Abbott D.C., Klein R.I., 1975, ApJ 195, 157
- Chandrasekhar S., 1931a, MNRAS 91, 456
- Chandrasekhar S., 1931b, ApJ 74, 81
- Chang C., Cui W., 2007, Dramatic Variability of X-ray Absorption Lines in the Black Hole Candidate Cygnus X-1, arXiv:0704.0452 [astro-ph]
- Charles P., Fabian A., 2001, Astronomy and Geophysics 42, 11
- Charles P.A., Seward F.D., 1995, Exploring the X-ray universe, Cambridge, New York: Cambridge University Press, 1995
- Cui W., Feng Y.X., Zhang S.N., et al., 2002, ApJ 576, 357
- CXC 2006, The Chandra Proposers' Observatory Guide, <http://cxc.harvard.edu/proposer/POG/>
- Dolan J.F., 1972, Ap&SS 17, 472
- Doty J.P., 1994, The All Sky Monitor for the X-ray Timing Explorer, Technical report, MIT <http://xte.mit.edu/XTE.html>
- Drake G.W.F., Dalgarno A., 1969, ApJ 157, 459
- Ebisawa K., Ueda Y., Inoue H., et al., 1996, ApJ 467, 419
- Eckart A., Genzel R., Ott T., Schödel R., 2002, MNRAS 331, 917
- Ehle M., Breittellner M., González Riestra R., et al., 2006, XMM-Newton Users' Handbook, <http://xmm.vilspa.esa.es/external/xmm-user-support/documentation/uhb/index.html>
- Einstein A., 1916, Annalen der Physik 354, 769
- Einstein A., 1917, Phys. Z. 18, 121
- Ergma E., van den Heuvel E.P.J., 1998, A&A 331, L29
- Fender R.P., Pooley G.G., Durouchoux P., et al., 2000, MNRAS 312, 853
- Feng Y.X., Cui W., 2002, ApJ 564, 953
- Feng Y.X., Tennant A.F., Zhang S.N., 2003, ApJ 597, 1017
- Fisher P.C., Jordan W.C., Meyerott A.J., et al., 1968, ApJ 151, 1
- Forman W., Jones C., Cominsky L., et al., 1978, ApJ 38, 357
- Friedman H., Byram E.T., Chubb T.A., 1967, Science 156, 374
- Friend D.B., Castor J.I., 1982, ApJ 261, 293
- Fruscione A., McDowell J.C., Allen G.E., et al., 2006, In: Observatory Operations: Strategies, Processes, and Systems, Vol. 6270. Proc. SPIE, p. 62701V
- Gabriel A.H., Jordan C., 1969, MNRAS 145, 241
- Gallo E., Fender R., Kaiser C., et al., 2005, Nat 436, 819
- Gehrels N., 1986, ApJ 303, 336
- Ghez A.M., Morris M., Becklin E.E., et al., 2000, Nat 407, 349
- Giacconi R., Gursky H., Paolini F.R., Rossi B.B., 1962, Phys. Rev. Let. 9, 439
- Gies D.R., Bolton C.T., 1982, ApJ 260, 240
- Gies D.R., Bolton C.T., 1986, ApJ 304, 371
- Gies D.R., Bolton C.T., Thomson J.R., et al., 2003, ApJ 583, 424
- Glæssner T., 2004, Ph.D. thesis, Universität Tübingen
- Golian S.E., Krause E.H., Perlow G.J., 1946, Phys. Rev. 70, 223
- Gruber D.E., Blanco P.R., Heindl W.A., et al., 1996, A&AS 120, C641
- Haensel P., 2003, In: Motch C., Hameury J.M. (eds.) EAS Publications Series, Vol. 7., p. 249
- Herrero A., Kudritzki R.P., Gabler R., et al., 1995, A&A 297, 556

- Hilborn R.C., 2002, ArXiv Physics e-prints, <http://adsabs.harvard.edu/abs/2002physics...2029H>
- Hjellming R.M., Wade C.M., 1971, *ApJ* 168, L21+
- Hjellming R.M., Wade C.M., Hughes V.A., Woodsworth A., 1971, *Nat* 234, 138
- Houck J.C., 2006, ISIS 1.0. Technical Manual, <http://space.mit.edu/cxc/isis/manual.html>
- Houck J.C., Denicola L.A., 2000, In: Manset N., Veillet C., Crabtree D. (eds.) *Astronomical Data Analysis Software and Systems IX*. ASP Conf. Ser. 216, p. 591
- House L.L., 1969, *ApJ* 18, 21
- Humphreys R.M., 1978, *ApJ* 38, 309
- Hutchings J.B., 1978, *ApJ* 226, 264
- Ishibashi K., 2006, An algorithm for finding zeroth order position, http://space.mit.edu/cxc/docs/memo_fzero.1.3.ps, updated in 2007: <http://space.mit.edu/cxc/analysis/findzo/>
- Israel W., 1967, *Phys. Rev.* 164, 1776
- Jackson J.D., 1975, *Classical electrodynamics*, 92/12/31, New York: Wiley, 1975, 2nd ed.
- Jahoda K., Swank J.H., Giles A.B., et al., 1996, In: Siegmund O.H., Gummin M.A. (eds.) *EUUV, X-Ray, and Gamma-Ray Instrumentation for Astronomy VII*, Vol. 2808. Presented at the Society of Photo-Optical Instrumentation Engineers (SPIE) Conference, p.59
- Jonauskas V., Bogdanovich P., Keenan F.P., et al., 2005, *A&A* 433, 745
- Juett A.M., Schulz N.S., Chakrabarty D., 2004, *ApJ* 612, 308
- Juett A.M., Schulz N.S., Chakrabarty D., Gorczyca T.W., 2006, *ApJ* 648, 1066
- Kalemci E., Tomsick J.A., Rothschild R.E., et al., 2006, In: *VI Microquasar Workshop: Microquasars and Beyond*.
- Kelley R., 2006, In: *American Astronomical Society Meeting Abstracts*, Vol. 208. *American Astronomical Society Meeting Abstracts*, p. #32.02
- Kerr R.P., 1963, *Phys. Rev. Let.* 11, 237
- Kotani T., Ebisawa K., Dotani T., et al., 2000, *ApJ* 539, 413
- Kruskal M.D., 1960, *Physical Review* 119, 1743
- Lampton M., Margon B., Bowyer S., 1976, *ApJ* 208, 177
- Lang K.R., 1999, *Astrophysical formulae*, K.R. Lang. New York : Springer, 1999. (Astronomy and astrophysics library, ISSN0941-7834)
- LaSala J., Charles P.A., Smith R.A.D., et al., 1998, *MNRAS* 301, 285
- Laughlin C., 1978, *Journal of Physics B Atomic Molecular Physics* 11, L391
- Li K.F., Clark G.W., 1974, *ApJ* 191, L27
- Lightman A.P., White T.R., 1988, *ApJ* 335, 57
- Liu Q.Z., van Paradijs J., van den Heuvel E.P.J., 2006, *A&A* 455, 1165
- Lund N., Budtz-Jørgensen C., Westergaard N.J., et al., 2003, *A&A* 411, L231
- Lyford N.D., Baumgarte T.W., Shapiro S.L., 2003, *ApJ* 583, 410
- Markoff S., Nowak M.A., Wilms J., 2005, *ApJ* 635, 1203
- Marquardt D., 1963, *SIAM J. Appl. Math.* 11, 431
- Marshall H.L., Schulz N.S., Fang T., et al., 2001, In: Yaqoob T., Krolik J.H. (eds.) *X-ray Emission from Accretion onto Black Holes*.
- Mas-Hesse J.M., Giménez A., Culhane J.L., et al., 2003, *A&A* 411, L261
- Mason K.O., Hawkins F.J., Sanford P.W., et al., 1974, *ApJ* 192, L65
- Mewe R., Gronenschild E.H.B.M., van den Oord G.H.J., 1985, *A&AS* 62, 197
- Mihalas D., 1978, *Stellar atmospheres /2nd edition/*, San Francisco, W. H. Freeman and Co., 1978. 650 p.
- Miller J.M., Fabian A.C., Wijnands R., et al., 2002, *ApJ* 578, 348
- Miller J.M., Wojdowski P., Schulz N.S., et al., 2005, *ApJ* 620, 398
- Morrison I.A., Baumgarte T.W., Shapiro S.L., 2004, *ApJ* 610, 941
- Müller A., 2004, Ph.D. thesis, University of Heidelberg
- Müller A., 2007, *Schwarze Löcher – Das dunkelste Geheimnis der Gravitation*, http://www.mpe.mpg.de/~amueller/astro_sl.html
- Murdin P., Webster B.L., 1971, *Nat* 233, 110
- Nelder J.A., Mead R., 1965, *Computer Journal* 7, 308
- Newman E.T., Couch E., Chinnapared K., et al., 1965, *J. Math. Phys.* 6, 918
- Ninkov Z., Walker G.A.H., Yang S., 1987, *ApJ* 321, 425
- Nowak M.A., Juett A., Yao Y., et al., 2007, *The Black Hole Candidate 4U 1957+11 (V1408 Aql) in a ‘Pure Disk State’: Simultaneous Chandra-HETG, RXTE and optical observations*, in prep.
- Nowak M.A., Wilms J., Heinz S., et al., 2005, *ApJ* 626, 1006
- Oppenheimer J.R., Volkoff G.M., 1939, *Physical Review* 55, 374
- Penrose R., Floyd G.R., 1969, *Riv Nuovo Cim* 1, 252
- Penrose R., Floyd G.R., 1971, *Nat* 229, 177
- Petterson J.A., 1978, *ApJ* 224, 625
- Porquet D., Dubau J., 2000, *A&AS* 143, 495
- Porquet D., Mewe R., Raassen A.J.J., et al., 2001, In: Giacconi R., Serio S., Stella L. (eds.) *X-ray Astronomy 2000*, Vol. 234. *Astronomical Society of the Pacific Conference Series*, p. 121
- Postnov K.A., Yungelson L.R., 2006, *Living Rev. in Relativity* 9, 6

- Pottschmidt K., Nowak M.A., Wilms J., 2006, Chandra-HETGS Observations of Dipping Events in Cygnus X-1, poster on the 207th meeting of the American Astronomical Society, 8-12 Jan 2006
- Pravdo S.H., White N.E., Becker R.H., et al., 1980, *ApJ* 237, L71
- Press W.H., Teukolsky S.A., Vetterling W.T., Flannery B.P., 1992, Numerical recipes in C. The art of scientific computing, Cambridge: University Press, —c1992, 2nd ed.
- Remillard R.A., Canizares C.R., 1984, *ApJ* 278, 761
- Remillard R.A., McClintock J.E., 2006, *ARA&A* 44, 49
- Reynolds C.S., 1998, ArXiv Astrophysics e-prints, <http://adsabs.harvard.edu/abs/1998astro.ph.10018R>
- Rowan T., 1990, Ph.D. thesis, Univ. Texas at Austin
- Rybicki G.B., Lightman A.P., 1979, Radiative processes in astrophysics, New York, Wiley-Interscience, 1979. 393 p.
- Schödel R., Ott T., Genzel R., et al., 2002, *Nat* 419, 694
- Schulz N.S., Cui W., Canizares C.R., et al., 2002, *ApJ* 565, 1141
- Schulze H.J., Polls A., Ramos A., Vidana I., 2006, *Phys. Rev. C* 73, 058801
- Schutz B.F., 1985, A First Course in General Relativity, A First Course in General Relativity, by Bernard F. Schutz, pp. 392. ISBN 0521277035. Cambridge, UK: Cambridge University Press, February 1985.
- Schwarzschild K., 1916, *Pr. Akad. Wiss.* 1916, 189
- Shapiro S.L., Teukolsky S.A., 1983, Black holes, white dwarfs, and neutron stars: The physics of compact objects, Research supported by the National Science Foundation. New York, Wiley-Interscience, 1983, 663 p.
- Smith R.K., Brickhouse N.S., Liedahl D.A., Raymond J.C., 2001, *ApJ* 556, L91
- Spitzer L., 1978, Physical processes in the interstellar medium, New York Wiley-Interscience, 1978. 333 p.
- Srinivasan G., 2002, *A&A Rev.* 11, 67
- Stirling A.M., Spencer R.E., de la Force C.J., et al., 2001, *MNRAS* 327, 1273
- Sunyaev R.A., Titarchuk L.G., 1985, *A&A* 143, 374
- Takahashi T., Abe K., Endo M., et al., 2007, *PASJ* 59, 35
- Tananbaum H., Gursky H., Kellogg E., et al., 1972, *ApJ* 177, L5+
- Ubertini P., Lebrun F., Di Cocco G., et al., 2003, *A&A* 411, L131
- Vedrenne G., Roques J.P., Schönfelder V., et al., 2003, *A&A* 411, L63
- Verner D.A., Verner E.M., Ferland G.J., 1996, Atomic Data and Nuclear Data Tables 64, 1
- Verner D.A., Yakovlev D.G., 1995, *A&AS* 109, 125
- Walborn N.R., 1973, *ApJ* 179, L123
- Webster B.L., Murdin P., 1972, *Nat* 235, 37
- Wilms J., 1998, Ph.D. thesis, Universität Tübingen
- Wilms J., 2006, *Nat* 444, 699
- Wilms J., Allen A., McCray R., 2000, *ApJ* 542, 914
- Wilms J., Juett A., Schulz N., Nowak M., 2006a, In: AAS/High Energy Astrophysics Division, Vol. 9., p. #13.60
- Wilms J., Nowak M.A., Pottschmidt K., et al., 2001, *MNRAS* 320, 327
- Wilms J., Nowak M.A., Pottschmidt K., et al., 2006b, *A&A* 447, 245
- Wolter H., 1952, *Annalen der Physik* 445, 286
- Xiang J., Zhang S.N., Yao Y., 2005, *ApJ* 628, 769
- Yao Y., Zhang S.N., Zhang X., Feng Y., 2003, *ApJ* 594, L43
- Ziólkowski J., 2005, *MNRAS* 358, 851